8-2012

Thermo-Mechanical Modeling of the Electrically-Assisted Manufacturing (EAM) Technique During Open Die Forging

Wesley Salandro
Clemson University, wsaland@clemson.edu

THERMO-MECHANICAL MODELING OF THE ELECTRICALLY-ASSISTED MANUFACTURING (EAM) TECHNIQUE DURING OPEN DIE FORGING

A Thesis
Presented to
the Graduate School of
Clemson University

In Partial Fulfillment
of the Requirements for the Degree
Doctor of Philosophy
Automotive Engineering

---

by
Wesley A. Salandro
August 2012

Accepted by:
Dr. Laine Mears, Committee Chair
Dr. Thomas Kurfess
Dr. Randy Collins
Dr. Mica Grujicic

ABSTRACT

This thesis contains all of the steps which allow the Electrically-Assisted Manufacturing (EAM) technique to be experimentally explored and analytically modeled for an electrically-assisted forging operation. *Chapter 1* includes the problem statement, proposed solution, and literature reviews on EAM. *Chapter 2* describes a thorough background on the EAM technique, highlights prior EAM research, and explains the research approach taken for this thesis. The coupled thermo-mechanical modeling strategy, along with the introduction of the Electroplastic Effect Coefficient (EEC) is provided in *Chapter 3*. *Chapter 4* explains the two different approaches to determine the EEC profiles when modeling a particular metal. The simplified EAF mechanical model for electrically-assisted forging is presented in *Chapter 5*. Also in this chapter, the same modeling methodology (*i.e.* thermo-mechanical, EEC, etc.) is used to predict loads for an electrically-assisted bending (EAB) process.

The following chapters explore how different material- and process-based parameters affect the EAF technique. *Chapter 6* examines how different workpiece contact areas affect EAF effectiveness, along with an exploration of how well different metal forming lubricants perform with EAF. *Chapter 7* explores if there is a difference in the thermal or mechanical profiles of specimens undergoing EAF forging tests with different average grain sizes. *Chapter 8* examines the same effects as the previous chapter on specimens with varying levels of prior cold work. The materials- and process-based simplifications and sensitivities of the proposed modeling strategy are outlined in *Chapter 9*. *Chapters 10-14* include the science behind the electroplastic effect, conclusions, future work, broader impacts, and intellectual merit, respectively. The overall intention of this thesis is to show the candidate's ability to take an idea for a new manufacturing process, prove that it works, and then understand and model the process such that it may be competitive within relevant industries.

DEDICATION

My family and friends have influenced me towards a career in engineering and further into pursuing a Ph.D. I would like to dedicate this thesis to my mother, father, and brother for all of their positive influences on me. I was raised in a blue-collar hard working family, where nobody achieved a secondary education. I learned mechanics from working with my father as a youth, and the importance of focusing on school and learning from my mother. My brother and I raced motocross where we traveled, raced, and worked on our bikes together, which taught us both responsibility and discipline.

Additionally, I would also like to dedicate a portion of this work to Derek Benedict, a childhood friend who passed on May 4, 2012. We grew up together and we both wanted to becomes engineers. Although Derek did not end up becoming an engineer, he was a good friend who was always proud of my accomplishments.

ACKNOWLEDGEMENTS

The following people outside of my research committee have impacted/inspired my research in the following ways:

Individuals:

Dr. John T. Roth was my undergraduate research advisor at Penn State University. I approached him about undergraduate research during my junior year and he inspired me to begin EAM research. Over the next two years, I worked under his guidance and as a result, I published several journal and conference proceedings, and one textbook as an undergraduate. His guidance showed me what it takes to become a world-class researcher, teacher, mentor, and friend.

Dr. Cristina Bunget is a post-doctoral researcher at CU-ICAR, with a strong background in mathematics and metal forming. Since beginning at ICAR, Cristina and I have collaborated on many research papers on EAM. I can always rely on Cristina for advice on EAM and metal forming in general.

Jon Jarvais is my current supervisor at BMW Manufacturing LLC. As a manager at an international automotive company, Jon realizes the need and importance of research like mine that can greatly impact the automotive industry. Jon tries to align my duties at work such that I can get an all-inclusive view of the industry which my research will affect.

Dr. Henry Rack is my materials science professor at Clemson University. He has strong international industrial ties with the automotive and aerospace industries, both industries which my research will directly impact. I want to acknowledge Dr. Rack for the periodic informational discussions on the direction of my Ph.D. research, and where I can make the most impact.

Robin Rickman was my mentor when I worked at Westinghouse Nuclear LLC as a design engineer. Even though I was a young engineer at the time, Robin provided and challenged me with various projects including design of new nuclear power plant components as well as design of components for re-fueling outages. This provided me with a great experience and a very thorough understanding of the nuclear power industry.

Gary Mathis is the technical support specialist at CU-ICAR. I would like to acknowledge Gary for his priceless advice to me when I am fabricating fixtures, dies, and specimens for my EAM research. His many years of industrial experience make him a valuable resource with realistic answers that would be acceptable in the real-world.

Dave Mann is a research associate specialist at CU-ICAR. I would like to thank Dave for his support and advice with setting up my testing equipment. Additionally, his vast knowledge of electricity kept me informed about the dangers of electrical current.

Dr. David Bodde is my entrepreneurship class professor. I would like to thank him for providing me with countless ideas of how my research can be used or marketed.

Industrial Support:

BMW Plant 10 Associates who have supported me in my research and classwork over the years, and who continue to support me in my Quality Engineer position at the plant.

Aggressive Grinding Services Inc. has provided centerless and surface grinding services for help with specimen and tooling fabrication for several of my research tasks.

Insulfab Plastics Inc. has provided me with countless pieces of reinforced plastics that are used as insulation components for fixtures and dies for my research.

Westinghouse Nuclear LLC. Associates provided a brief, but good learning experience of how a large corporate company operated, and this is where I began developing myself as an engineer.

Ionic Technologies Inc. has heat treated or hardened many fixtures and dies for my EAM research.

Fuchs Lubricants has provided several of the top metal forming lubricants to be used in comparison studies with EAM.

Koyo Bearings has provided instrumentation that was used during specific EAM testing. Additionally, Koyo has run material property tests on my research material in their measurements and instrumentation laboratory.

Specialty Steel Inc. has provided me with numerous rods of various materials in order for me to run experimental EAM testing.

Southeastern Industrial Services Inc. has assisted with manufacturing specimens for many of the experiments in this proposal.

TABLE OF CONTENTS

Page #

LIST OF TABLES

Page #

LIST OF FIGURES

Page #

EXECUTIVE SUMMARY

The overall objective of this Ph.D. research is to test the hypothesis that direct electron-dislocation interactions occur within a metal during Electrically-Assisted Manufacturing (EAM) to reduce the apparent flow stress of the metal workpiece. If the electroplastic effect of the EAM technique can be successfully modeled, EAM has the potential to improve essentially every metal forming process.

Metal forming is a key manufacturing process in the automotive industry, an industry which comprises 4% of the US Gross Domestic Product (GDP) [1]. Traditional sheet and bulk forming for automotive and aircraft components is limited by a number of design and physical factors, most notably achievement of formability by elongation (achievable strain before tearing or buckling failure) which restricts allowable strain in design, and elastic recovery (springback), thus complicating the die design and process repeatability.

Due to the absence of predictive manufacturing models and the limited formability of new lightweight alloys, innovative process design is limited. Liewald et al. give a comprehensive historical overview of techniques for characterizing sheet deformation behavior, and states that new testing methods and modeling approaches are necessary to better understand and design for deformation behavior [2]. Work continues across the field to better characterize formability through improving approaches to the Forming Limit Diagram (FLD).

Electrically-Assisted Manufacturing (EAM) is a new manufacturing technique that has the potential to improve the cost-efficiency of essentially every metal forming process, and enable greater process capabilities, thus resulting in deformation of new, stronger materials at a lower cost. In this process, electricity is applied (in a closed loop) to a metal workpiece while it is undergoing deformation. The formability improvements due to the electricity (*i.e.* reduced forming forces, increased achievable deformation displacements, and reduced springback) are

collectively categorized as the electroplastic effect.

Although shown to be effective experimentally, researchers have not developed an accepted theory explaining electricity's ability to enhance a metal's formability (*i.e.* the electroplastic effect), and because of this, past researchers have not been successful in accurately modeling and predicting EAM effects for process control. While previous EAM modeling works have helped to disprove the common misbelief that EAM's effect is due solely to increased temperature of the workpiece, they emphasized the fact that EAM theory is not fundamentally understood and EAM effects cannot be effectively predicted. As will be discussed in this document, the candidate considers the electroplastic effect differently than previous researchers, by assuming direct electrical effects as well as thermal effects from the applied electricity.

The Ph.D. research completed herein aims to create a thermo-mechanical predictive model for EAM, using the theory that the applied electrical power is divided into a portion that assists deformation (*i.e.* creates the electroplastic effect) and a portion that contributes towards resistive heating (*i.e.* thermal softening). The model is used to analyze how material- and process-based parameters, such as real contact area, lubrication, starting grain size, and cold working affect the efficiency of the applied electrical power (or how well it was utilized to enhance the part formability). The contact area research shows that the roughness of the contact points between the die/workpiece were negligible plastic deformation took place. The tribology section shows that roughness is affected by EAF. The grain size work depicts little change to the thermal and mechanical profiles. Finally, the percent cold work section helps to prove that the excess dislocations led to a hotter profile and also affected the forces. These and other sensitivities and simplifications are discussed. This is all concluded with future work, and broader impacts are also described.

1. Introduction

Within this chapter, an introduction into the motivation and background for this Ph.D. thesis on Electrically-Assisted Manufacturing (EAM) is presented. Specifically, a problem statement is provided, which describes the current state and issues with EAM. Then, the proposed solution to solve these issues is given. To follow up on the proposed solution, clear concise research statements are noted. Then, relevant background information (*i.e.* lightweighting, current forming technologies and limitations, EAM explanation, literature review, and past EAM theory and modeling) are documented to show the extensive work which has been performed on EAM in the past 10-20 years.

1.1. Problem Statement

The Electrically-Assisted Manufacturing (EAM) technique has been proven to produce elongations of up to 400% and transform brittle metals into formable materials under small-scale laboratory conditions [3]. However, one must be able to understand the theory behind the electroplastic effect before it can be modeled, and ultimately used within metal forming industries. The particular aspects to be modeled are the temperature and force profiles of an EA-forging process, because both are critical design criteria for selecting machinery, dies, and materials suitable for EAM processes. Additionally, once the EAM process is able to be modeled, process planning and cost optimizations could be performed by the potential end-user as part of the design process.

Currently, trial-and-error is the only way to select EAM parameters. Because there is a specific "threshold" current density or flux (*i.e.* Current/Area) where EAM starts to have a beneficial effect on the forming process, this type of methodology would require time-consuming testing to find appropriate parameters each time a new machine setup, design change, or machine

re-start was made. This could include reworking die designs and spending time varying material and process parameters. Further, forming dies can range in cost from $25,000 to over several million dollars, so remaking and extensive reworking of this equipment is simply prohibitive because of the huge capital costs. From the perspective of potential industries (*e.g.,* the automotive and aerospace markets), the benefits of EAM currently do not outweigh the required money and time investment for this manufacturing technique because of this. Specifically, industry would rather use less-effective, but predictable manufacturing techniques, such as those described in sub-section *1.4.2: Current Forming Technologies*, until EAM is predictable and controllable.

Overall, the main *Research* and *Industrial* issues with the current state of the EAM technique are that:

- It has only been proven successful in small-scale laboratory settings, but not used in industry, contrary to the techniques in sub-section *1.4.2: Current Forming Technologies* (*Industrial*).
- There is no clear fundamental understanding of the formability-enhancing mechanisms of EAM, which are theorized in sub-section *1.4.6: EAM Theory and Modeling* (*Research*).
- The EAM technique is currently not able to be successfully modeled (thermally/mechanically) (*Research*).
- A costly trial-and-error methodology is currently the only way to design/setup an EAM process, making it an undesirable procedure in its current state (*Industrial*).

1.2. Proposed Solution: Create a Thermo-Mechanical Predictive Model

The proposed solution to the current unpredictability and inability to understand and model EAM, as explained in the *Problem Statement* sub-section, is to create a thermo-mechanical

predictive model that is capable of accurately producing both temperature and force profiles for an electrically-assisted forging (EA-Forging) test. Then, the model can potentially used or updated to develop an understanding of how real contact area, tribology, grain size, and cold work affect the efficiency of EAM, as well as test the theory that electrons and dislocations interact when electricity is applied, thus causing the electroplastic effect. In addition, contact area, tribology, grain size, and prior cold work experiments will be run to identify relations and to help explain the theory of electrons and dislocations interacting during EAM. This has been theorized by several early EAM researchers, including Kravechenko [4], Klimov [5], and Conrad [6].

1.3. Research Statement

The overall objective of this Ph.D. research is to test the hypothesis that direct electron-dislocation interactions occur within a metal during EAM to reduce the apparent flow stress, and to use this theory to be able to produce force/temperature profiles of an EAF test successfully. In addition, the specific effects of contact area, tribology, grain size, and cold work will be examined and used to optimize or simplify the model. The theory explains that, as electricity is applied, the electrons impact the dislocations and give them the "push" needed to continue deformation, thus reducing deformation forces and increasing the achievable forming distance before fracture. The contact area relationship to the resistance of the system is investigated, as a small contact area increases the voltage and ultimately the power of the system, and also contributes to excessive heating. The tribology section verifies if different compositions of lubricants react differently with EAM. The grain size section investigates if the difference in grain size (determining the amount of grain boundaries a dislocation must surpass) will have an effect on EAM. The pre-existing cold work in a metal determines the number of dislocations

already existing in the material before plastic deformation even starts, and this could affect the temperature and mechanical profile of the workpiece.

1.4. Relevant Background

Before research on EAM can be understood, an exploration into EAM, as well as the motivation for a manufacturing customer to want to use this technique, must first be explained. This section contains several sub-sections which cover: 1.) a description of the different automotive approaches to lightweighting, 2.) current formability-enhancing technologies, 3.) the limitations of these technologies, 4.) a description of the Electrically-Assisted Manufacturing (EAM) technique, 5.) an in-depth history of the effects of electricity on metals and on EAM, and 6.) a review of previous unsuccessful attempts at modeling an EAM process.

1.4.1. Lightweighting

US-based automotive Original Equipment Manufacturers (OEM's) are an integral part of the United States economy, responsible for nearly one million automotive-related jobs [7]. Meanwhile, stringent legislation continues to be passed, which requires further limitations on both fuel consumption and CO_2 gas emissions for this industry. The concept of vehicle lightweighting is a major focus for all US and foreign automotive manufacturing OEM's, due to strict regulatory standards for the emissions of carbon dioxides and the minimization of fuel consumption. To enforce the importance of this statement, the following are quotes from several automotive OEM's about their commitment towards vehicle weight reduction:

- "The use of advanced materials such as magnesium, aluminum, and ultra-high strength boron steel offers automakers structural strength at a reduced weight to help improve fuel economy and meet safety and durability requirements." – Ford Motor Company [8]

- "Light weight design can be achieved by engineering light weight, manufacturing light weight and material light weight design." – BMW AG [9]
- "Lightweight design is a key measure for reducing vehicle fuel consumption, along with power train efficiency, aerodynamics and electrical power management." – VW [10]
- "Excess weight kills any self-propelled vehicle…Weight may be desirable in a steam roller but nowhere else." – Henry Ford [11]

Figure 1 shows the weight trends for US light duty vehicles from 1975 until 2009 [12]. A statement from General Motors claims that about 20-40% of this weight increase is due to the content increase (*i.e.* navigation, electronics, etc.) in newer vehicles [13]. It can be estimated that another reason for the increase in vehicle weight is simply because of the interest in large vehicles that Americans have been known to like. Regardless, the increase in weight leads to a decrease in efficiency of these vehicles, even if powertrains have improved over the years. Figure 2 shows the US CAFE fuel economy standards for the next decade [14]. As can be seen, there is a steep increase in fuel economy expected. Automotive OEM's realize that consumers want more efficient vehicles without compromising; hence this has led to a focus on a number of lightweighting techniques.

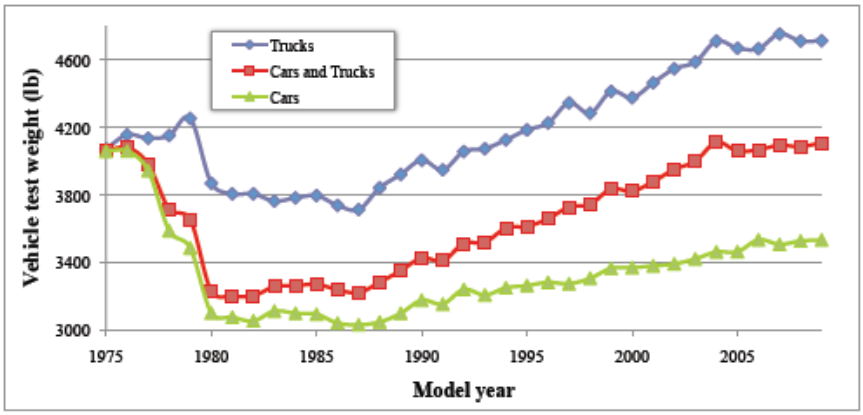

Figure 1. US light duty vehicle weight trends [12]. Since the early 1980's, US vehicle weights have increased significantly.

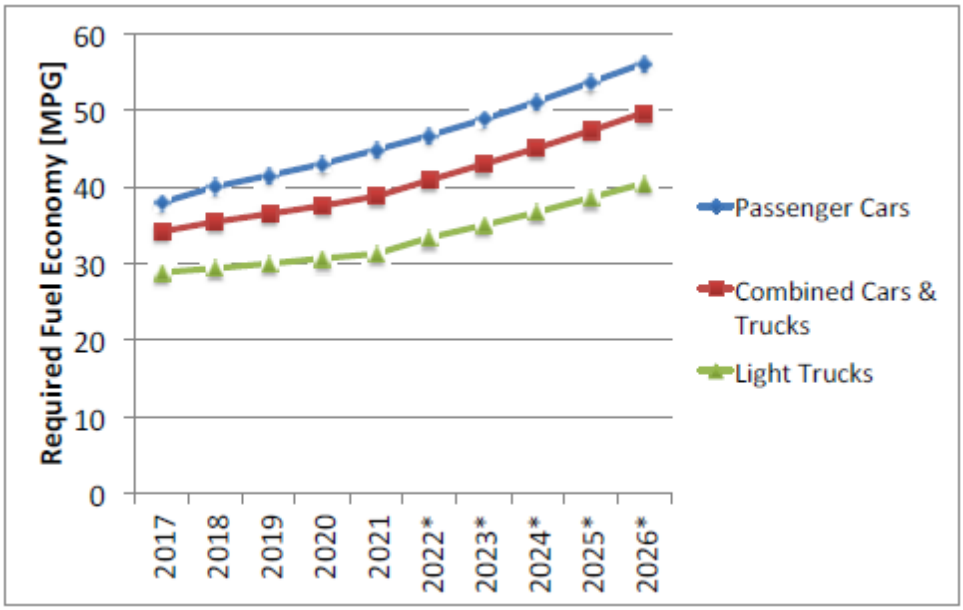

Figure 2. US CAFE economy standards (*proposed) [14]. There is a steep increase in average fuel economy for all types of US vehicles expected in the near future.

The procedure of lightweighting can be done using two approaches: 1.) using new alloys with high strength-to-weight ratios (*i.e.* magnesium and titanium), or 2.) using creative design strategies (*i.e.* stainless steels with ribbed designs vs. carbon steel or plastic). Some case studies of creative design approaches are explained below and can be seen in Figure 3. Some of the

lightweighting metals may not be as strong as the heavier metals that they are replacing, so a combination of both lightweighting techniques will commonly be used. The following examples show how different lightweight materials and creative design strategies were used to reduce weight in a vehicle without compromising strength.

- For an automobile bumper, a 20% weight reduction was achieved using stainless steel versus carbon steel, when the C1000 Stainless Steel design included "ribs" for strengthening rather than a large cross-section of the carbon steel [16].
- For an automotive fuel tank, a 4% capacity increase and a 20% weight reduction was accomplished by using stainless steel as the tank material compared to conventional plastic used in fuel tanks, because the tank wall thickness could be decreased [17].

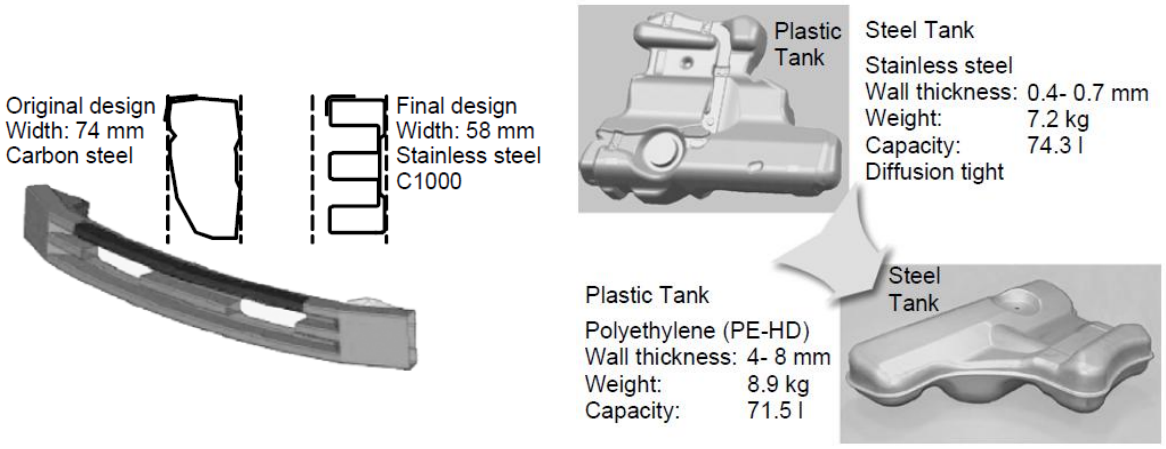

a.) Stainless steel bumper beam [16] b.) Plastic vs. steel gas tank [17]

Figure 3. Lightweight design strategies [15]. Using lightweight materials or creative design strategies are two main methods for lightweighting. (a) A stainless steel ribbed bumper beam design saves weight compared to a carbon steel design, (b) The reduced thickness of a stainless steel gas tank decreased the weight and allowed for greater capacity compared to a plastic tank.

Aside from the two examples shown above, the overall material content used in vehicle production as a whole has changed dramatically over the last century. Figure 4 illustrates this trend. Specifically, larger amounts of high/medium strength steels, aluminum, polymers, and even some magnesium are being integrated into all components of the vehicle (*i.e.* body panels,

trim, engine, etc.) to reduce weight [18]. An example of this is with the BMW X6 Sport-Activity Vehicle, which received the "Great Designs in Steel, Automotive Excellence Award" from the Automotive Applications Council of AISI's Steel Market Development Institute (SMDI) for utilizing Ultra-High Strength Steels (UHSS) to enforce strength without increasing weight [19]. Also from the figure, it can be realized how rapidly the materials used in vehicle production have changed, as wood was the primary automobile component about 100 years ago.

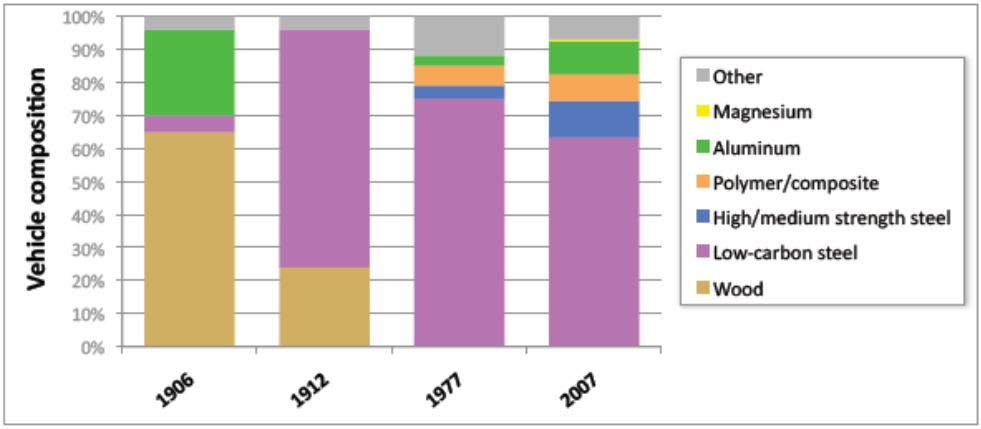

Figure 4. US vehicle material composition trends [18]. Larger amounts of lightweight materials (*i.e.* high/medium steels, aluminum, polymers, and magnesium) are now integrated into the vehicles to contribute to lightweighting.

Overall, there is a greater amount of aluminum and magnesium being implemented into the vehicles. With the limited formability of these metals compared to current automotive metals, there is the need for an efficient metal forming technique capable of making components from these and other comparable metals in place of the current metals. Previous experimental EAM research has shown EAM's successfulness in forming both of these metals, as will be seen in *Ch.2: Previous EAM Experimental Work*.

1.4.2. Current Forming Technologies

There are numerous techniques used in manufacturing plants today which help to improve a metal's formability. Within this sub-section, several of the most common techniques are described and their advantages/disadvantages discussed.

Hot working is defined as the deformation of a material at an elevated temperature. As part of this process, the metal is heated above its recrystallization temperature, thus increasing the formability of the material. Advantages to hot working include decreased flow stress and increased ductility. This is one of the simplest manufacturing methods because all that is required is a heat source, such as a heater or furnace. In many cases, however, these benefits come at the expense of part quality. One key disadvantage includes lower dimensional accuracy, due to uneven thermal expansion resulting from temperature gradients within the material. Moreover, a rougher surface finish (resulting from an oxide layer developing on the outside of the part) is another consequence of using this process. Also, as the size of the workpiece increases, larger furnaces will be needed, proving to be more costly and taking up a larger footprint on the shop floor. Further, energy use is much higher for this technique. Regardless of the minor fluctuations in part quality and cost, this relatively simple and effective process makes it a desirable choice when holding rough tolerances where secondary finishing operations will likely follow.

Using the stress vs. strain graph in Figure 5, the effects of hot working can be compared to a room-temperature (*i.e.* cold forming) compression test when forging Ti-6Al-4V. Due to hot working, the compressive flow stress was decreased and the amount of achievable compressive displacement prior to fracture was increased when compared to cold-working conditions.

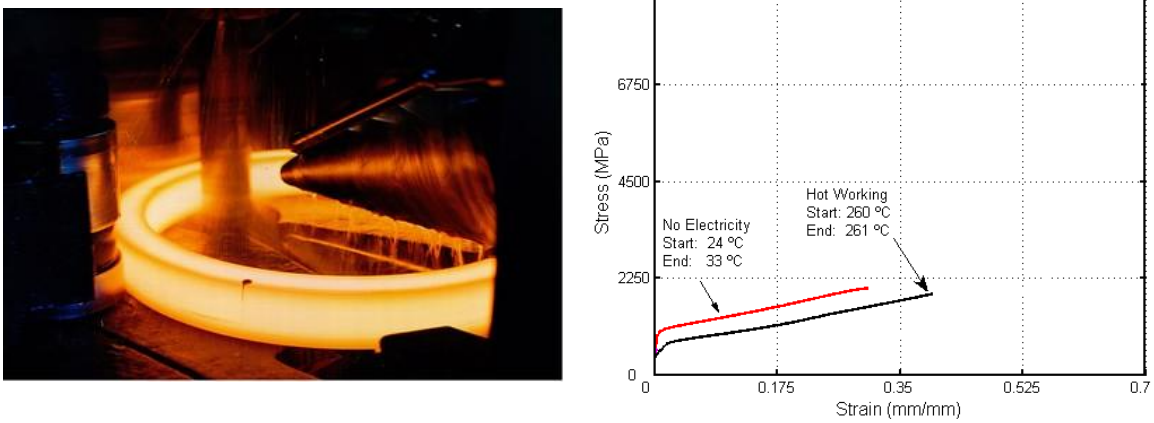

a.) Hot ring rolling [20] b.) Ti-G5 hot working [21]

Figure 5. Hot working [20], [21]. Parts are bulk heated to induce thermal softening, then formed at high temperature with lower forces. (a) Ring being hot rolled to increase diameter, (b) Stress-strain curve for Grade 5 Titanium showing cold working (upper curve) vs. hot working (lower curve) stress profiles.

Incremental forming (IF) is a type of manufacturing process in which a metallic part is deformed in small steps with a minor heat treatment (*i.e.* a process anneal) performed in between steps [22]. Figure 6 shows a schematic diagram of the incremental forming process, along with a graphic of a blank at different stages of the IF process. This type of manufacturing is especially beneficial when forming brittle sheet metals and is used in the automotive and aircraft industries. The major advantages to this process are the large amounts of deformation and the decrease in the required deformation forces that can be obtained. These advantages are possible because of the minor heat treatments performed in between the increments of deformation. The treatments eliminate the effects of cold work or strain hardening by causing recrystallization to occur during each process anneal, thus resulting in a new, overall weaker material. Aside from the benefits, this process does have its disadvantages. A big downfall is the potential for low dimensional accuracy, since the part must be continuously removed and re-fixtured before and after the heat treatments. The decreased accuracy arises from the fact that the part may not be fixtured in the exact fashion each time it is removed and reinstalled. Also, this process can be very time

consuming, depending on the variables such as the number of heat treatments and their respective durations, as well as the depth of the desired deformations. Using this technique, production times are greatly increased, hence, incremental forming may not be an optimum process for high production or high precision manufacturing, however, materials can be formed to great distances and complex shapes can be achieved.

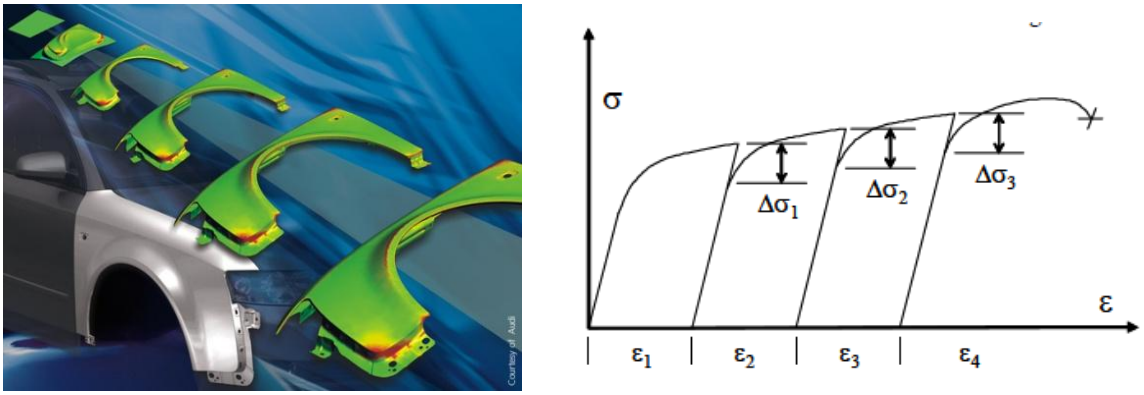

a.) Stages of a blank during IF [23] b.) Schematic of the IF process [22]

Figure 6. Incremental forming (IF) [22], [23]. Parts are deformed in small increments, with a minor heat treatment usually performed offline in between steps. (a) the various stages of an IF process, (b) a stress-strain schematic of an IF process.

Superplastic forming (SPF) involves heating a material to extremely high temperatures (roughly two-thirds of its melting temperature) when deforming, as seen in Figure 7. This process can produce tremendous elongations of up to 2000%, coupled with greatly reduced flow stress [24]. Other advantages include being able to form precise complex shapes in which minimal or no residual stresses are present. Also, lower strength tooling and fixtures can be used since the required forces for deformation are minimized. This process can be used to form complex shapes because of the very low forming forces; however, it also has its disadvantages. First, the superplastic forming process is only applicable for very fine-grained alloys (less than 10 to 15 μm), such as some aluminum (5083-FG and 7475), titanium (Ti-6AL-4V), and magnesium

alloys (Mg-AZ31B). These small grains allow for GBS (grain boundary sliding) to occur at elevated temperatures, which is the primary SPF deformation mechanism responsible for the huge elongation increases. Another consequence of this process is that extremely slow strain rates must be used (10^{-4}/s to 10^{-2}/s). Similar to the incremental forming technique, the superplastic technique may not be practical for many high production manufacturing applications, and can be classified as a batch-forming process. Neglecting the limited number of applicable materials and the slow strain rate that is required, this process is capable of producing precise complex geometrical parts with little or no finishing operations needed. Vehicle manufacturers, such as Porsche and Aston Martin, have used SPF to form components for their low production exotic cars.

Figure 7. Superplastic forming [25]. A part is heated to roughly two-thirds of its melting temperature and formed to allow for great elongations and a formed part with very few residual stresses.

When using Tailor Welded Blanks (TWB's), different sheets of material (*i.e.* differences in material grade, thickness, or coating) are mechanically or automatically welded together before the forming process [26]. This allows the manufacturers to produce custom blanks, where strong, lightweight materials are placed where they are needed, while utilizing more formable steels in other areas, thus allowing for a relatively strong and easily formable part. However, this process

can be time consuming, costly, and can result in reduced part accuracy because of all the extra manufacturing steps and associates required to prepare the blanks. An example of a tailor-welded floor pan can be seen in Figure 8, with arrows pointing to the different materials used in the part.

Figure 8. Tailor welded blanking (TWB) [27]. TWB is a method of using different materials (*i.e.* grades, thicknesses, coatings, etc.) within the same component to strategically place specific properties where they are desired.

1.4.3. Limitations of Current Technologies

The goal of any manufacturing engineer is to produce quality parts as efficiently and cost-effectively as possible. For many common engineering metals, this can be accomplished rather easily, however, it has proven challenging with some of the stronger, more lightweight metals which are being implemented into today's manufacturing processes. These materials, such as high-strength aluminum-, magnesium-, copper-, and titanium-based alloys, all possess high strength-to-weight ratios, but their limited formability makes them impractical for use in many real-world applications which require complex part geometries. The main downfall in using these materials to make complicated shapes is the fact that, with current technology, the forming capability is insufficient, such that the forming process is extremely time consuming and some very complex shapes may not even be able to be formed at all. In this case, numerous simpler

parts must first be formed and then attached using screws, rivets, or welds, which can significantly increase the overall cost and useable life-cycle of the products.

High production costs and poor part quality issues can result from attaching smaller, simpler parts together, making the disadvantages of using these materials outweigh their great strength-to-weight characteristics. To this end, formability enhancing techniques are used to increase the overall efficiency of the manufacturing process, thus increasing the applicability of these materials and allowing more complex part geometries to be formed from single blanks rather than attaching many smaller components together. Formability-enhancing techniques must be devised and employed on current manufacturing methods to make them more applicable for forming lightweight metals. Experts say that extensive research, which couples materials and manufacturing engineering, is the key towards further developing lightweight engineering [28]-[29]. Not only do novel manufacturing techniques need to be created and proven, but Computer-Aided Engineering (CAE), analytical modeling, and simulations of these novel processes must be further developed in order to gain industry acceptance for a specific formability-enhancing technique.

1.4.4. Electrically-Assisted Manufacturing (EAM)

Electrically-Assisted Manufacturing (EAM) is a recently-introduced metal forming technique capable of enhancing a metal's formability during deformation and reducing springback after deformation (note that only the formability-enhancing effect of EAM will be of focus in this dissertation). In this technique, electricity is applied to a metal blank while it is deformed, without stopping the deformation. EAM is a general term used for the technique of applying electricity to any manufacturing process. Electrically-Assisted Forming (EAF) is a specific type of EAM, where electricity is applied to metal-forming processes (*i.e.* bulk

deformation or sheet metal forming). A schematic of an EAF (forging) test setup can be seen in Figure 9. The key components of the test setup include a controllable power supply to generate the electricity, a DAQ system to collect mechanical data, a thermal camera to collect thermal data, and insulation to isolate the die/workpiece and machinery from the applied electricity.

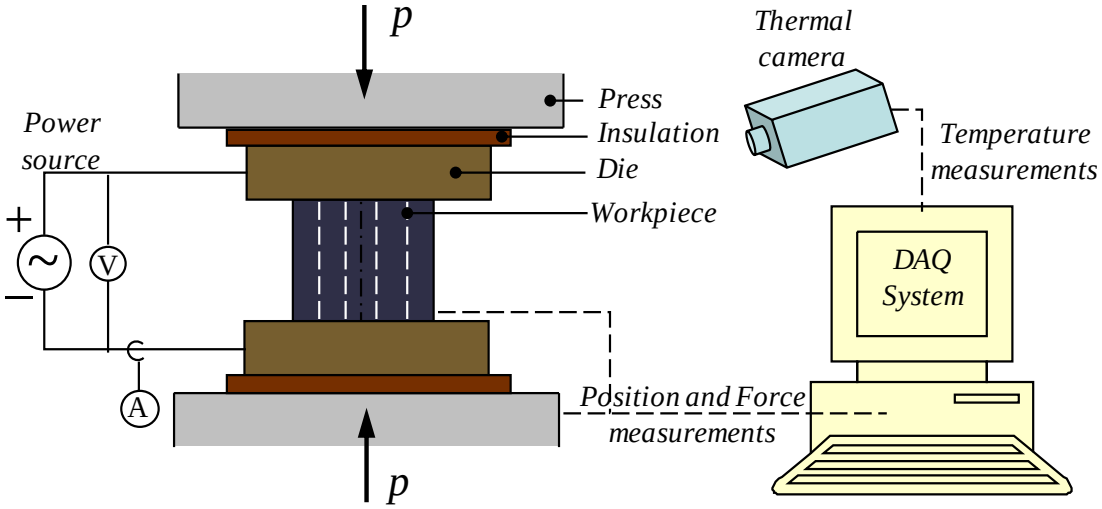

Figure 9. Schematic of an EAF test setup. During EAF, electricity is applied to a metal while it is deformed, thus increasing the overall formability of the metal and producing the electroplastic effect.

The multiple benefits generated from the applied electricity are collectively known as the electroplastic effect. The three main benefits of the electroplastic effect are:

- A reduction in the flow stress required to continue plastic deformation
- Increased achievable part deformation prior to failure
- Reduction/elimination of springback effects in formed parts

Figure 10 illustrates the electroplastic effect, by showing EAM's ability to transform strong and brittle Ti-6Al-4V into a highly formable material. In Part *a*, a specimen compressed under conventional conditions, with no applied electricity, is shown. After a minimal amount of

deformation, the HCP material failed due to brittle shear fracture. Part *b* shows a specimen compressed under EAM conditions, where the electricity was applied for the duration of the forging operation. Due to EAM, the part was able to be completely formed to its desired height without failure.

a.) Conventional Forming b.) Continuous EAF

Figure 10. EAF formability improvement (Ti-G5). EAF increases the achievable amount of part displacement before failure. (a) conventional forming of a Ti-G5 slug led to almost instantaneous shear failure, (b) EAM forming of the same material enabled the slug to be deformed to its desired distance.

However, like all processing techniques, EAM has some disadvantages and challenges that exist within the process and its implementation towards industrial use. First, in order for the electricity to reach the part, there must be some type of electrical applicator in contact with the conductive workpiece at all times. For manufacturing processes where the workpiece is stationary, like forging or stamping, this can be done rather easily. Conversely, when implementing the EAM technique on manufacturing processes with workpieces of relative motion, like friction welding two workpieces together, an applicator system which is in continuous contact with the workpiece while not becoming entangled in the part, must first be designed. In addition, since the workpiece is subjected to electrical flow, all personnel and machine components should be insulated from the electricity. It must be noted that extreme caution should always be used when working with electricity. Isolating the electricity, however, can prove to be a challenging task in some cases, since most machinery components are

comprised of conductive metals and the common insulating materials (*e.g.*, nylons, rubbers, ceramics, or plastics) cannot withstand the mechanical demands placed on these components (*i.e.* too soft or too brittle). Outweighing these issues, in most cases, are the energy reduction benefits, such as decreased flow stress, increased ductility, and reduced springback, that can be accomplished using the EAM method. Some tooling designs devised to overcome issues with EAM tooling and equipment is described in the appendix as sub-section *15.1.3: EAM Tool Design*.

1.4.5. EAM Literature Review

Research investigating how electricity affects materials can be traced back to the mid 20th century in Russia. Towards the later part of this century, this research slowly began in the United States. Now, there are an increased number of universities and national labs which have begun to focus on some portion of the EAM technique. An in-depth explanation into the history of EAM research will be provided below.

In 1959, Machlin et al. examined electricity's effect on group 1A salts (NaCl), determining that an applied electric current significantly affected the material's ductility, flow stress, and yield strength [30]. Later, Nabarro discussed electricity's effect on metals as part of his book in 1967 [31]. In 1969, Troitskii et al. studied how electrons influence dislocation motion and reproduction in different alloys of zinc, tin, lead, and indium, concluding that pulsed electricity could lower the flow stress within the materials [32]. Years later, in 1982, Klimov et al. explained that the effects on a metal's structure from electricity are unrelated to those caused by Joule heating [5]. Moving forward, in 1988, a microstructure analysis was conducted by Xu et al., and it was discovered that a continuous electric current in titanium materials caused the recrystallization rate and the grain size of the materials to increase [33]. Next, Chen et al.

developed a relationship between electric flow and the formation of intermetallic compounds (Sn/Cu and Sn/Ni systems) [34]-[35]. Afterwards, in 2000, Conrad et al. determined that very high current density/short duration electrical pulses can affect the plasticity and phase transformations of metals and ceramics [6], [36]-[37]. In 2005, Heigel et al. examined the microstructural alterations in Al6061 resulting from direct current [38].

Within the past few years, much experimental research has been performed to establish how electricity affects the mechanical behavior of different metallic alloys. In 2007, Andrawes et al. was able to conclude that electrical current can significantly reduce the energy needed for uniaxial tensile deformation of Al6061-T6511without greatly heating the workpiece [39]. Perkins et al. studied the effects of a continuously applied electric current on various alloys undergoing an upsetting process and found that the electricity increased the amount of allowable compressive deformation prior to fracture, and lowered the required compressive forces [40]. Again in 2007, Ross et al. examined the application of a continuously supplied electric current on tensile specimens, only to conclude that, although deformation forces were reduced, the achievable elongation was decreased, leading to premature failure [41].

The problem of decreased elongation in EAM-tensile processes was overcome in 2008, when Roth et al. achieved elongation increases of nearly 400% by applying pulsed (rather than continuous) current to Al5754 tensile specimens [3]. Following this, Salandro et al. examined the effect of pulsed electricity on three different heat treatments of two 5xxx Aluminum Alloys (5052 and 5083) [42]. Moreover, in 2009, Salandro et al. discovered a linear relationship between current density and pulse duration in MgAZ31B-O tensile specimens that could be used to reliably achieve intended elongations for a variety of pulsing conditions [43]. Research by McNeal et al. examined microstructural alterations in the same MgAZ31B-O tensile specimens [44]. Green et al. determined that springback in Al6111 sheet specimens could be completely

eliminated with a single high current, short duration electrical pulse [45]. From work by Jones et al., achievable compressive displacements of the same Mg alloy were increased by over 400%, and the electricity even led to strain weakening effects [46]. Additionally in 2009, Salandro et al. found that, by applying electric pulses to Al5052 while undergoing highly localized channel formation, the achievable channel depth could be increased while reducing the required machine forces [47]. Siopis et al. examined how different microstructure properties affect the effectiveness of EAM in micro-extrusion experiments. Specifically, it was concluded that a finer-grained material, with more grain boundaries, enhanced the electroplastic effect, whereas a larger-grained material, with fewer grain boundaries, lessened the effect [48]. Another work by Siopis et al. determined that the effectiveness of EAF increased as the dislocation density within the metal also increased, as a result of cold-working prior to EAF experiments [49]. A work by Dzialo et al. examined the effect of current density and zinc content during electrical-assisted forming of copper alloys [50]. A more in-depth overview of the development of EAM can be found in [51]. Additionally, several recent EAM patents were found as a part of the EAM literature review [52]-[56].

Overall, the effort and number of researchers studying EAM in the US have increased tremendously since Roth began experimentally analyzing EAM in the mid-2000's. Shown in Figure 11 is a timeline displaying both the researchers and universities that are involved in some type of EAM research (note the exponentially increasing trend).

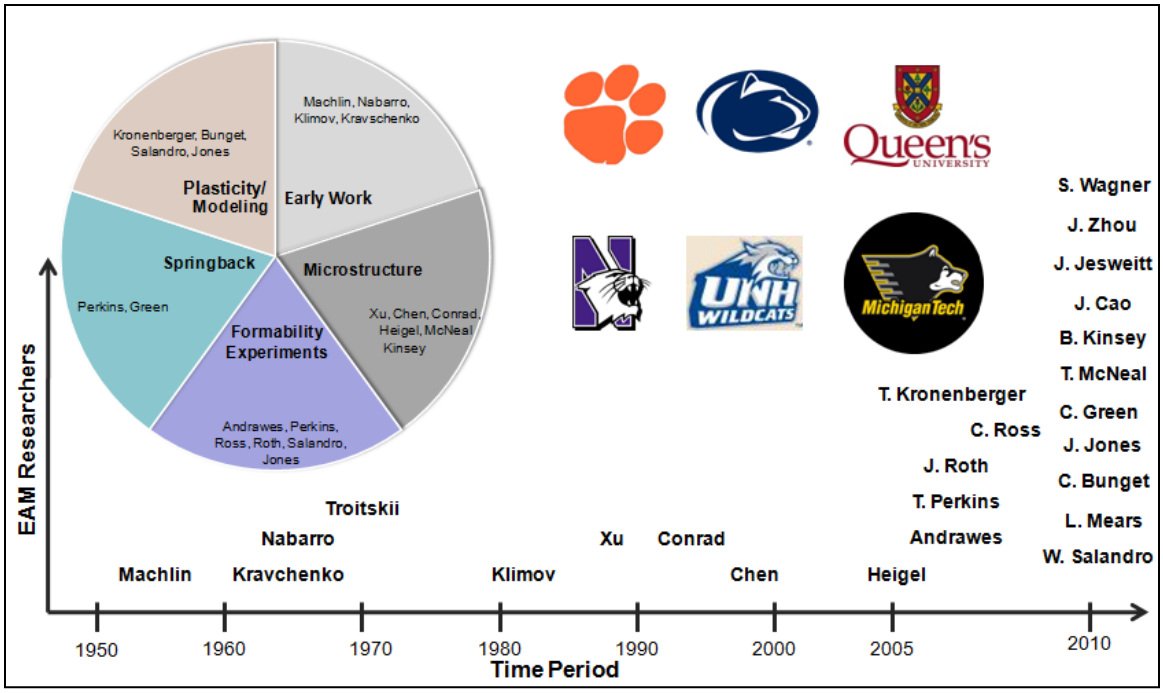

Figure 11. EAM research timeline. The number of researchers and universities investing time and money into different aspects of EAM research has increased exponentially over the past decade.

1.4.6. EAM Theory and Modeling

Due to the lack of knowledge about the electroplastic effect, past researchers have been unsuccessful in accurately modeling and predicting EAM effects for process control. However, from the previous work in this field, a multi-part postulated theory can be explained. Please note that these conclusions were drawn by previous research in the EAM field and not solely by the Ph.D. candidate. At the microstructure level, metals are held together by metallic bonds, consisting of clouds of electrons, which surround ion cores containing protons and neutrons. Because of this, it is realistic that the application of electricity (*i.e.* the application of flowing electrons) to any metal will have noticeable effects. Specifically, when electricity is applied to a metal during deformation, a few phenomena occur simultaneously, thus transforming the material

into an easier-to-deform state, known as the electroplastic effect. This effect can be due to the following aspects:

- *Localized atomic-level resistive heating effects* that are enhanced by the resistivity of the material (*i.e.* electrons scatter off of interfacial defects within the lattice, such as voids, impurities, grain boundaries, etc) [3]. It is important to remember that this heating occurs on the atomic level (within the metal's lattice), and although this contributes towards the overall heating of the workpiece, this temperature increase is not the same as the bulk temperature increase that is witnessed at the part's surface (known as global or bulk heating). Specifically, the bulk temperature of a metal is the result of all the atomic-level heating locations. This effect expands the local lattice and allows for easier dislocation motion (*i.e.* plastic deformation) by way of enhanced diffusion. The resistive heating effects are dependent upon resistivity, hence, a material with a greater resistance will experience larger amounts of localized resistive heating and will potentially achieve greater formability benefits when the EAM technique is applied.
- *Direct dislocation-electron interaction* takes place when the flowing electrons impact the dislocation lines, assisting in "pushing" the dislocation lines and further enhancing plastic deformation and material ductility [57]. Kravchenko, in his explanation of electroplasticity, succinctly stated this effect when he explained that, if there is an electric current flowing and the electrons are traveling at a faster rate than the dislocations within the lattice, the energy from the electrons is transferred to the dislocations, thus making the plastic flow easier [4]. The overall impact of this effect can be significant or minimal, depending on the direction of the flowing electrons and the direction of deformation. This aims to explain why the temperature of an EAM test, where electricity is applied during deformation, is less than a stationary-electrical test, where the electricity is applied when

no deformation takes place. In the EAM test, some of the energy is used to assist plastic deformation, instead of fully contributing towards resistive heating.

- The *addition of excess electrons* to the metal's microstructure is an important aspect. Since the electron clouds control how strongly a metal is bonded and essentially act as the "glue" which holds a metal together, the excess electrons (obtained from applying the electricity) will assist in breaking and reforming bonds by reducing the bond strength between electrons. As the metallic bonds are able to break and reform easier, the ductility of the metal is improved, hence it becomes more workable [58].

Figure 12 displays a schematic describing the three main pillars of the electroplastic effect explaining the EAM theory.

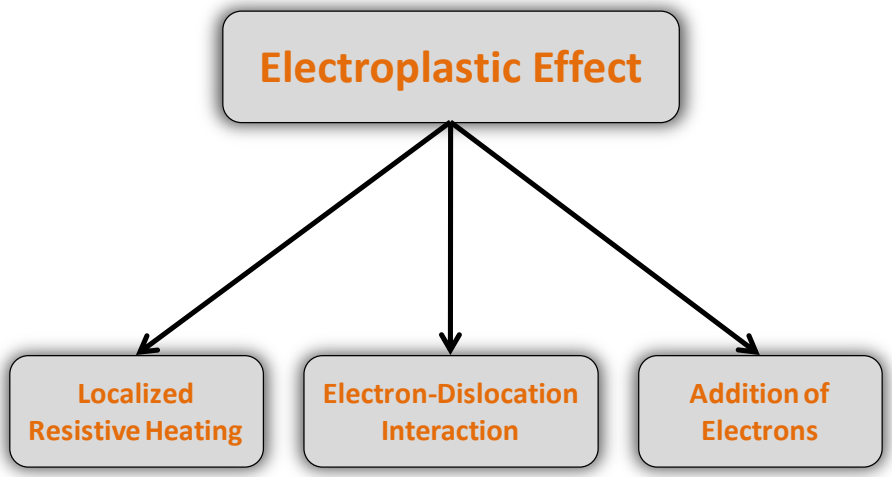

Figure 12. EAM research theory summary. From the previous research performed on EAM, the three effects listed above are theorized to produce the electroplastic effect in metals.

As previously stated, there have been several unsuccessful attempts at modeling EAM, however, these attempts have helped to bring a better understanding to EAM. In [59], a FE

model, capable of accurately predicting resistive heating and isothermal forming effects, was considerably unsuccessful in simulating material behavior in an EAM compression test, as shown in Figure 13. Additionally, in [21], isothermal compression tests were run at temperatures above the maximum temperature reached during EAM tests, concluding that the isothermal tests accounted for about only 10% of the formability improvement witnessed in the EAM tests (Figure 14). While these works helped to disprove the common misbelief that EAM's effect is due solely to temperature, they emphasize the fact that the EAM theory is not fundamentally understood and EAM effects cannot be effectively predicted.

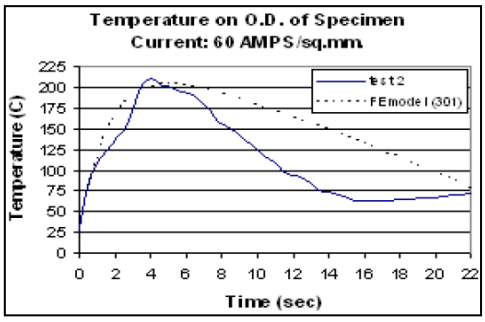

a.) Resistive heating profile modeling

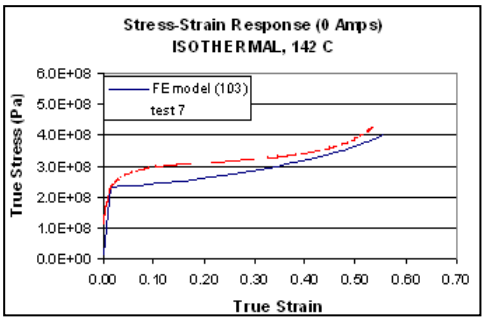

b.) Isothermal stress-strain modeling

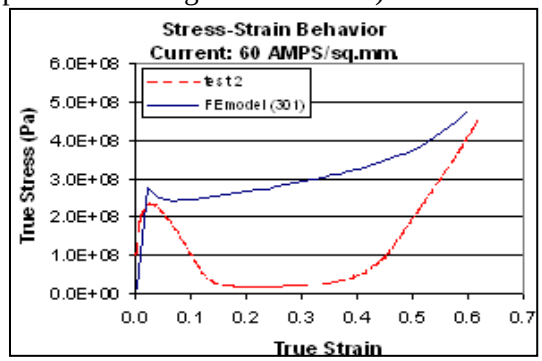

c.) Unsuccessful EAM modeling

Figure 13. FEA modeling of EAM [59]. In previous research, generic FEA modeling of EAM proved unsuccessful. (a) the FEA program was capable of predicting resistive heating temperature profiles, (b) the FEA model proved capable of predicting a stress-strain profile for an isothermal test, (c) the FEA model, which accounted solely for resistive heating, was shown to be highly inaccurate when trying to predict an EAM stress-strain profile.

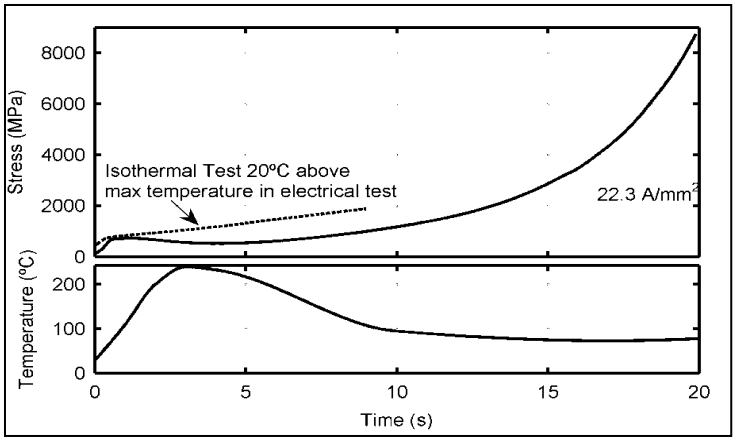

Figure 14. Experimental EAM modeling [21]. A previous research work proved that the stress-strain profiles for an EAM test, and an isothermal test run at the maximum temperature reached during the EAM test, were considerably different. Additionally, this confirmed that the effects of EAM were not solely contributable to resistive heating or thermal softening.

2. Previous EAM Experimental Work

This section contains several sub-sections of experimental EAM works which highlight particular aspects of the EAM technique. Specifically, various types of deformation processes are examined on numerous metals under various conditions. From this, justifications for specific EAM material-based and process-based parameters can be provided, which will be used to investigate these influences throughout this thesis.

2.1. EAM Compression Results on Various Metals

In the work by Perkins et al., EAM compression tests were run on various types of metal alloys, including Aluminum Alloys (Al6061-T6511, Al7075-T6, Al2024-T4, -T351), Copper-based Alloys (C11000, 360 Brass, 464 Brass), Ferrous-based Alloys (304 Stainless Steel, A2 Steel), and Titanium Alloy [40]. In addition, the work explored two different specimen sizes for several of the metals mentioned above. The specimens were compressed 6.4mm (a 60% height reduction) with a platen speed of 25.4mm/min, while various starting current densities were applied to the specimens constantly throughout each test. Figure 15 shows stress-strain curves for the Titanium Alloy at different starting current densities.

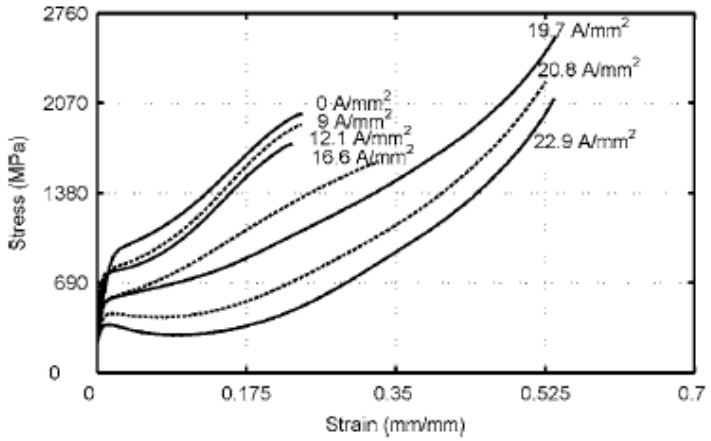

Figure 15. Threshold effect (Ti-G5) [40]. Once a particular current density level is reached, which is specific to each metal alloy, a significant force/stress reduction due to EAM will take place. This current density level is denoted as the "electrical threshold" level at the particular electrical settings.

Conclusions from this work are as follows:

- There is an "electrical threshold" where electroplastic effects are produced, which is specific to each material.
- The electrical threshold is a function of the starting current density, die speed, and material.
- At the same die speed, some metals in this work expressed a low threshold current density, while others showed a higher threshold current density (up to 4-times higher than others).
- The EAM technique produced similar results on two different size specimens, leading to the conclusion that the effects are related to current density and not current amplitude.

2.2. EAM Application Methods for Different Deformation Processes

In 2007, Ross et al. studied the effect of a continuous current on the same metals as Perkins, now for uniaxial tension tests [41]. It could be concluded that the yield strength, flow

stress, and elastic modulus were all reduced. Also, because of strain weakening, the overall energy of deformation was decreased. However, one important finding of this research was that, due to the continuously applied current, the achievable elongations of the specimens decreased (an opposite effect of using continuously applied current in compression), as shown in Figure 16. This led to experimentation with pulsed electricity, rather than leaving it applied continuously, for tensile applications.

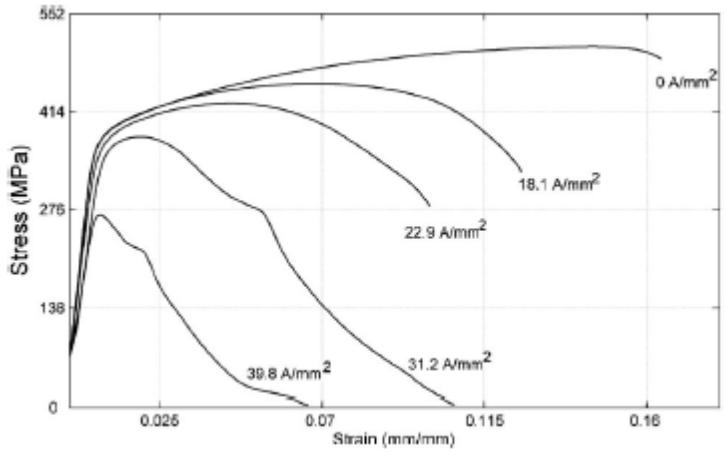

Figure 16. Al2024-T4 EAM stress-strain tensile profiles [41]. When the electricity is applied to a tensile deformation process continuously (as is done with compression tests), the larger amounts of electrical power will produce decreased elongations. Hence, this is why electrical pulsing is performed on EAM tensile processes.

The conclusions from this work are:

- If electricity is applied continuously during a tensile deformation process, the forces will be reduced, however, the achievable elongation will also be reduced.
- The difference in the specimen conditions throughout tensile and compressive tests explains the reasoning for the continuously-applied electricity causing a detrimental effect on the tensile process. Specifically, the cross-sectional area of the workpiece will increase in compression (the current density will decrease over the test), and the cross-

sectional area of the workpiece in tension will decrease (which will increase the current density of the specimen over the test).

2.3. Effects of Different Die Speeds on EAM Effectiveness

Work by Jones et al. [46] determined that the electroplastic effect is strain rate dependent. More specifically, in this work, Mg AZ31B-O specimens were compressed while a constant current was applied. As the die speed was increased, while the current remained constant, the magnitude of the electroplastic effect decreased, as shown in Figure 17.

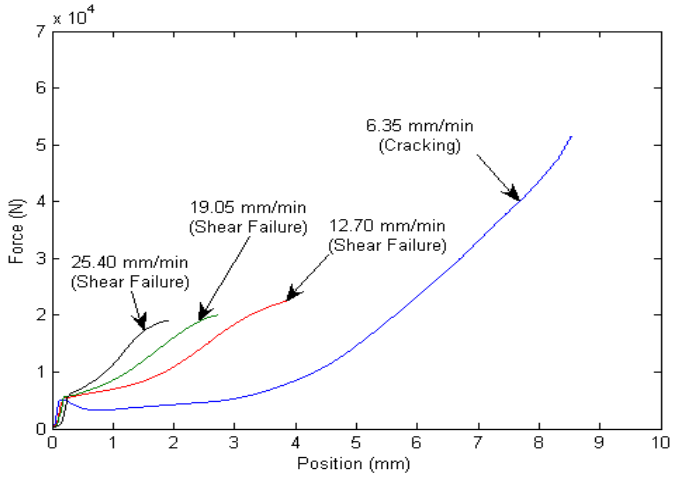

Figure 17. EAM die speed dependence (CD=20A/mm^2) [46]. For the same electrical settings, as the die speed is increased, the amount by which EAM has an effect on the metal's formability becomes reduced.

Conclusions from this work are as follows:

- The higher current densities produced greater formability improvements, however, the same benefits could be produced from lower current densities if the platen speed was slowed down.

- A threshold current density was noticed where the formability was considerably improved compared to the other lower current densities.
- The EAM technique in compression was found to be strain-rate dependent.

2.4. Effects of Electrical Application Parameters on Formability Improvements

This research work explored the effects of particular EAM pulsing parameters (current density and pulse duration) on the formability of Mg AZ31B-O specimens undergoing uniaxial tensile deformation [43] and [60]. As a part of investigating these effects, various current density and pulse duration combinations (*i.e.* high current/short duration or low current/long duration) are examined. An important outcome of this work was the development of a linear inverse relationship between current density and pulse duration, which allows accurate elongation predictions to be made from respective parameter combinations (Figure 18). This relationship could also be represented in 3-D as a "formability ridge", specifying expected elongation for different current density and pulse duration combinations, as shown in Figure 19.

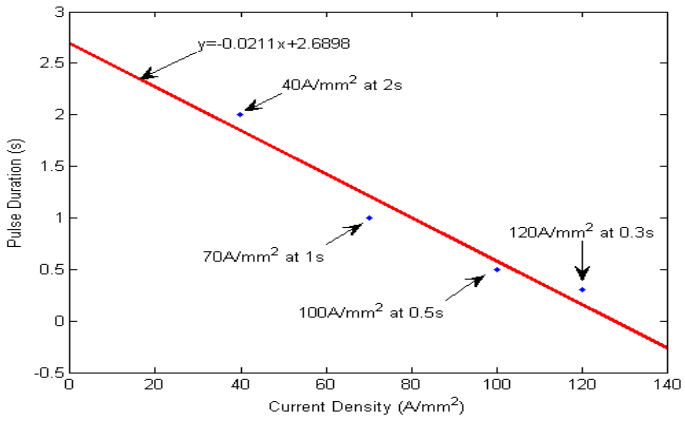

Figure 18. Inverse linear relationship between current density and pulse duration [43]. This chart depicts a line of optimum elongation. Specifically, to maintain optimum elongations, longer pulse durations must be coupled with lower current densities, and shorter pulse durations must be paired with higher current densities.

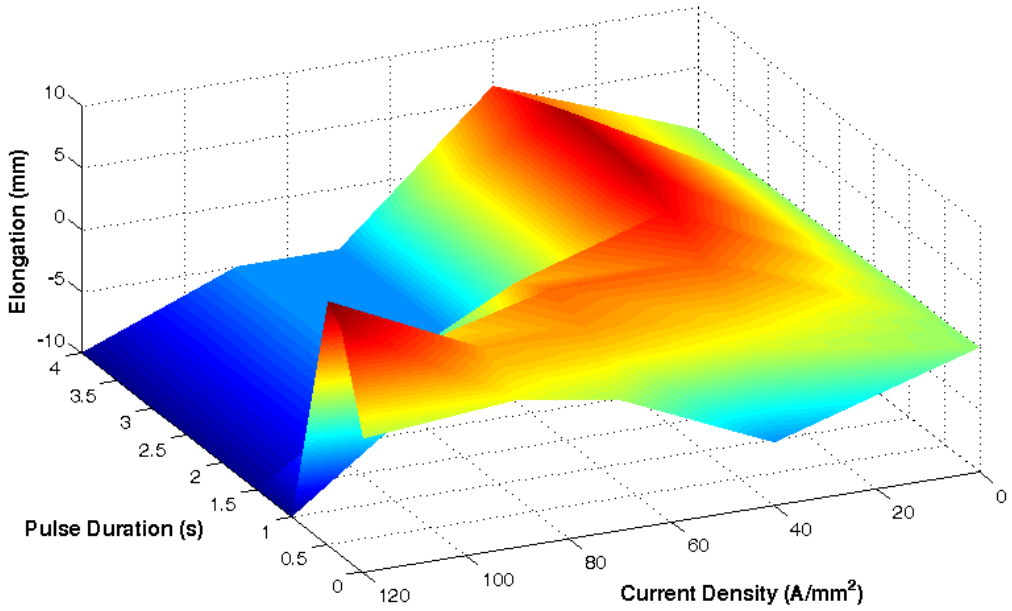

Figure 19. 3-D EAM formability ridge for Mg AZ31B-O [60]. This is a 3-D representation that shows that pulse duration and current density magnitudes must be "balanced" to reach maximum allowable elongation levels. Not meeting this requirement will result in reduced elongation levels, away from the peaks of the ridge.

Conclusions from this work are as follows:

- EAM produced the most optimum formability improvements with high current density/short pulse duration and low current density/long pulse duration combinations.
- In cases where this inverse relationship was violated, such as low current/short duration, the formability remained unchanged.
- In parameters with high current/long durations, the specimens failed prematurely due to the overly powerful combination of electricity, leading to extensive and undesirable heating effects.
- The electrical power input into an EAM process needs to be considered because an under powerful or overly powerful combinations of input parameters (starting current density, pulse duration, and pulse period) can decease the formability of the part.

- The efficiency of the applied electrical parameters must be considered because the same amounts of formability improvements may be possible from less powerful electrical input parameter combinations.

2.5. EAM Post-forming Microstructure Investigation

On the same specimens used for the previous work, the post-forming characteristics of the EAM-formed specimens were studied by performing a microstructure examination [44] and [60]. The microstructure analysis focused on how EAM affected grain size, grain orientation, and twinning. Twinning was examined because the Mg alloy (HCP crystal structure) had limited slip planes and deformation had to be accompanied by twinning. Therefore, if twinning was minimized or eliminated, this would prove that EAM affects the actual deformation mechanisms of the alloy. The microstructure of the following different specimen types will be compared: a.) deformed EAM specimens, b.) deformed non-pulsed baseline specimens, and c.) undeformed non-pulsed "as received" specimens. This work concluded that:

- As the pulse duration lengthened, the average grain size of the post-formed metal increased, and the grain size became more sensitive to variations in current density (Figure 20).
- As the current density increased, the average grain size increased, and the grain size became more sensitive to varying pulse durations (Figure 21).
- At some current density/pulse duration combinations, twinning was completely eliminated within the microstructure of the magnesium alloy, leading to the conclusion that the material's deformation mechanisms could be affected by EAM (Figure 22).

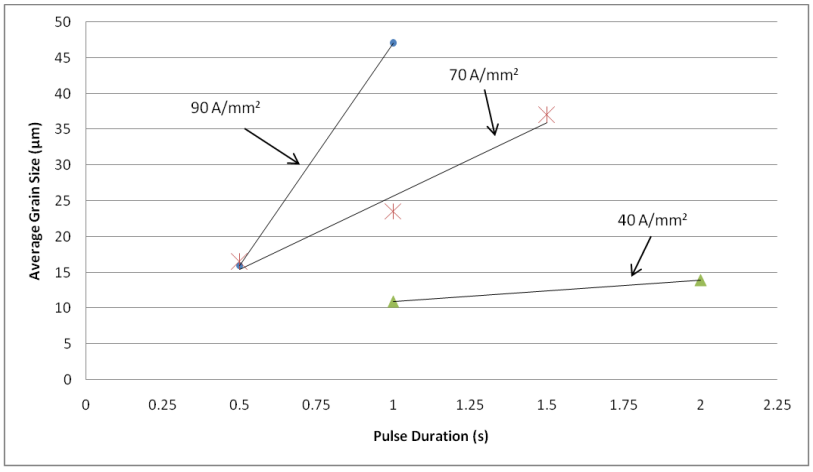

Figure 20. Average grain size vs. pulse duration [44], [60]. The average grain size of Mg AZ31B-O alloy increased as the duration of the electrical pulses increased. Additionally, this relationship became more sensitive as current density was increased.

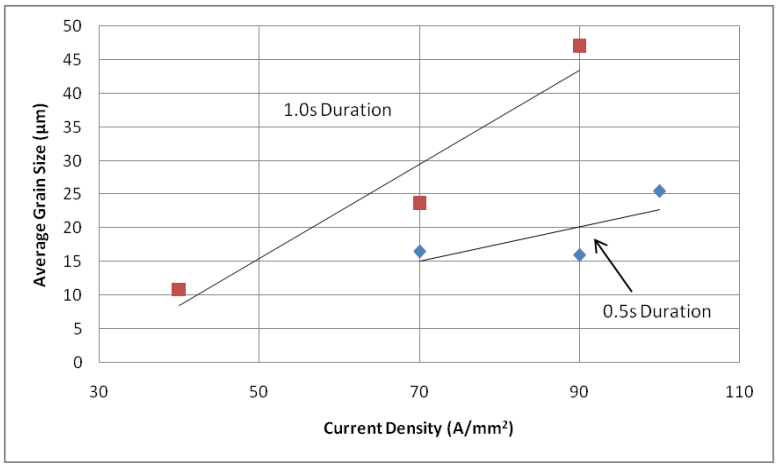

Figure 21. Average grain size vs. current density [44], [60]. The average grain size of Mg AZ31B-O alloy increased as the current density magnitude increased. Additionally, this relationship became more prominent as the duration of the electrical pulses lengthened.

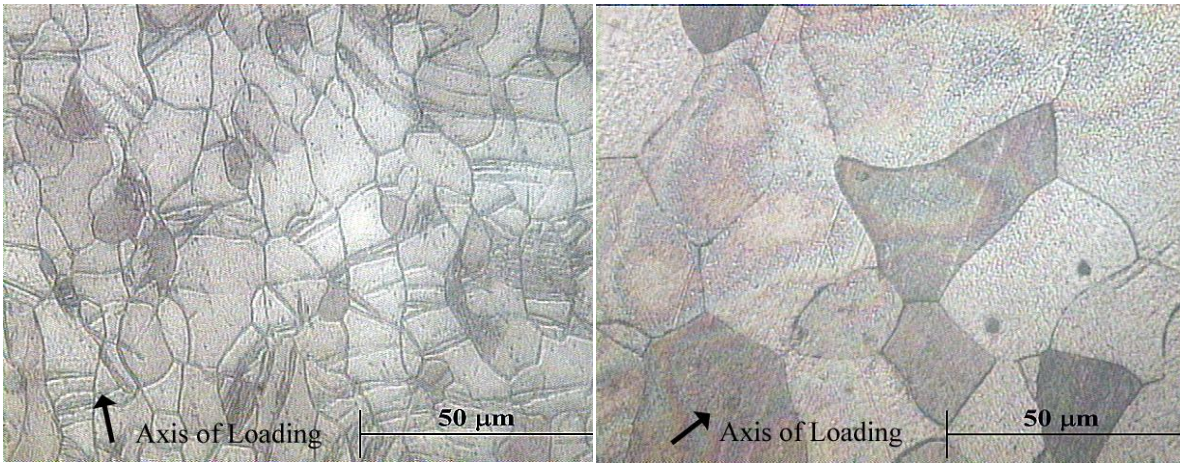

a.) Baseline (non-pulsed) - Twinning b.) EAM – No Twinning

Figure 22. Elimination of twinning using EAM [44], [60]. It is proposed that the application of EAM to the forming of Mg AZ31B-O will result in a variation of the deformation mechanisms in the metal. (a) Baseline deformation of the metal results in twinning as a deformation mechanism, (b) EAM deformation did not require twinning in order to deform the material.

2.6. Effects of Heat Treatments on EAM in Tension

In 2008, the effect of different heat treatments on EAM for two different Al alloys were tested [42], [61]. Two Aluminum Alloys (Al 5052 and Al 5083) were electrically pulsed using two different electrical parameter sets (*i.e.* combinations of current density, pulse duration, and pulse period settings). Additionally, specimens from each alloy were subjected to three different heat treatments (As Is, 398°C, and 510°C). The analysis focuses on establishing the effect the electrical pulsing had on the aluminum alloy's various heat treatments by examining the displacement of the material throughout the testing region of the dogbone shaped specimens. Figure 23 shows the experimental setup. The results from this research show that pulsing significantly increased the maximum achievable elongation of the aluminum (when compared to the baseline tests conducted without electrical pulsing), as well as reduced the engineering flow stress. The electrical pulses also caused the aluminum to deform non-uniformly, such that the material exhibited a diffuse neck where the minimum deformation occurs near the ends of the

specimen (near the clamps) and the maximum deformation occurs near the center of the specimen (where fracture ultimately occurs). This diffuse necking effect is similar to what can be experienced during superplastic deformation, but on a smaller scale. Figure 24 and Figure 25 display the general force reductions, elongation improvements, and diffuse necking effects compared to the non-pulsed baseline tests.

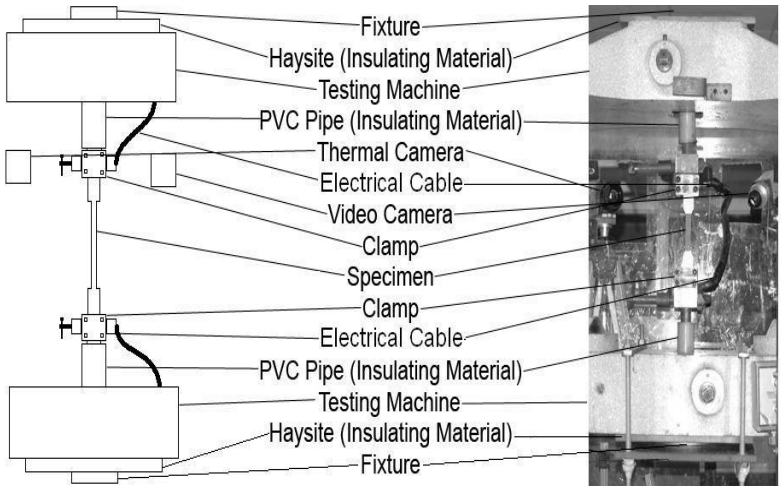

Figure 23. Experimental EAM setup [42], [61]. This EAM testing setup includes conductive metal dies with rigid insulation materials placed in between the dies and the testing machine, to ensure that the electricity only flows through the workpiece.

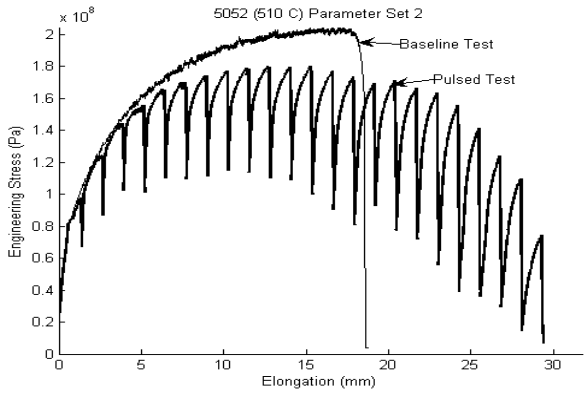

Figure 24. EAM force reduction and elongation increase [42], [61]. The application of electrical pulses (*i.e.* the steep drop-offs in the EAM profile) proved to reduce the overall engineering stress-elongation profile and increase elongation compared to the non-pulsed baseline test.

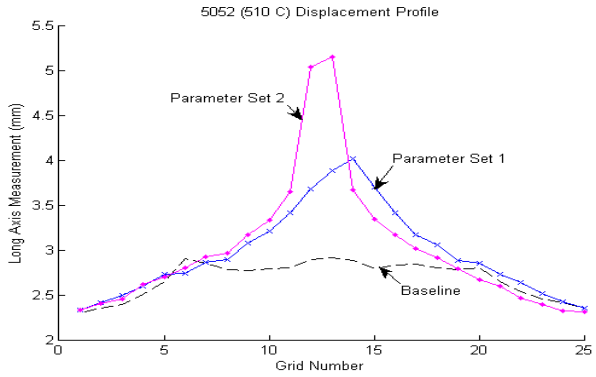

Figure 25. Diffuse necking effect (baseline vs. EAM) [42], [61]. The two EAM tests produced much more defined diffuse necks than the non-EAM baseline test.

The conclusions from this work are as follows:

- The effectiveness of the pulsed electricity is dependent on both the alloy and its heat-treatment.
- The size of the diffuse neck resulting from electrical pulsing was found to be irrespective of the material pulsed, but dependent on the parameter set used for pulsing.

- In any aluminum alloy/heat-treatment combination, the greater pulsing frequency of Parameter Set 2 developed a larger diffuse neck compared to the greater magnitude of pulses in Parameter Set 1.
- The formability of both Aluminum Alloys was improved by EAM, but Al5083 had the greatest elongation increases and flow stress reductions due to EAM.

2.7. Non-uniform Deformation Using EAM

Until now, EAM research was conducted on processes where uniform and uniaxial deformations were taking place. However, the candidate also researched the effect of the EAM technique on a non-uniform channel formation process using Al5052-O sheet strip specimens [47]. The experimental setup can be seen in Figure 26, including the custom insulated EAM channel die supplied by the Ford Motor Company.

The EAM variables which were examined in this work are: current density, pulse duration, pulse period, and die speed. Specifically, the Al5052 sheet strip specimens were formed into channels using the EAM technique and experiments were run with different combinations of the variables mentioned above.

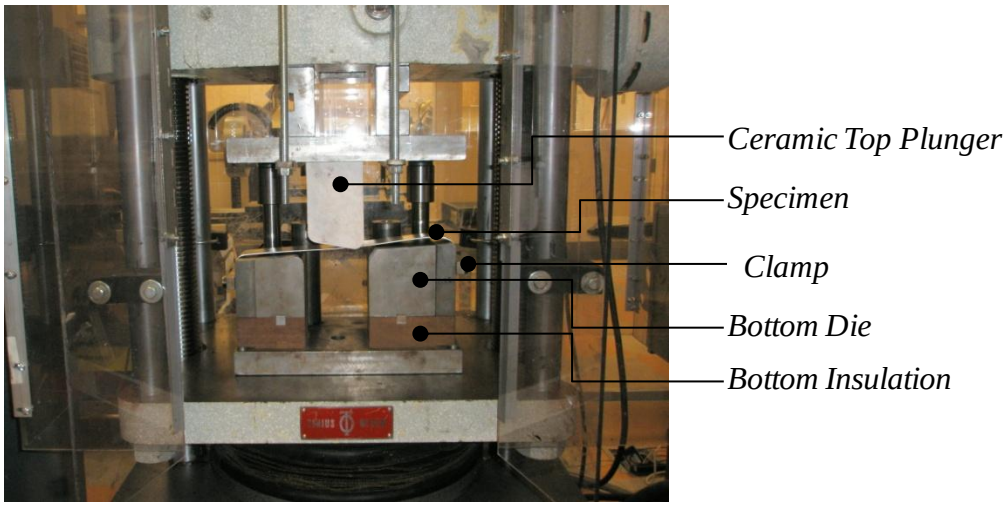

Figure 26. EAM channel formation experimental test setup [47]. This setup included a 2-part channel die, composed of a top ceramic plunger and a metal bottom portion with insulation integrated into the base structure.

Engineering Stress vs. Elongation plots examining the effects of either pulse period or pulse duration can be seen in Figure 27 (parts a and b). In part a for this particular current density magnitude, it can be seen that the length of the pulse period had little effect on the increased elongation. However, in part b, a longer pulse duration (2 seconds) proved to be overly powerful and led to premature failure compared to non-EAM baseline channel forming.

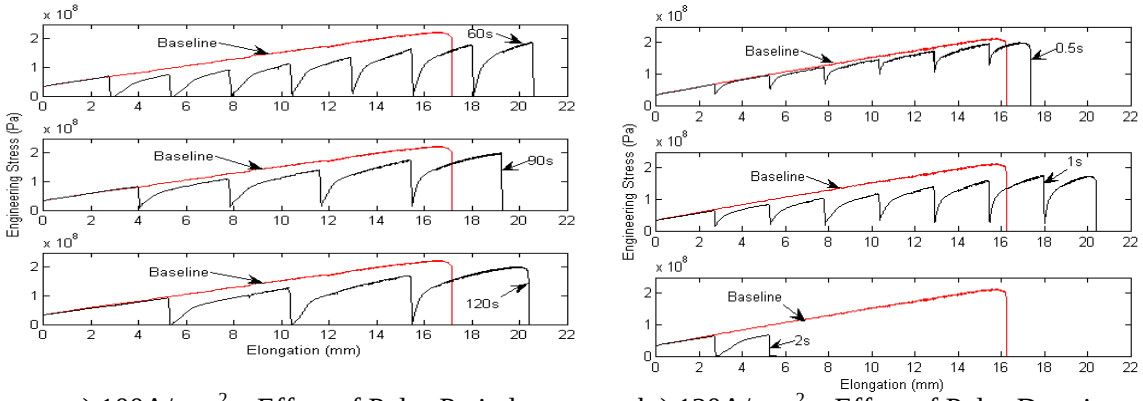

a.) 100A/mm^2 – Effect of Pulse Period b.) 120A/mm^2 – Effect of Pulse Duration

Figure 27. EAM channel formation formability results [47]. EAM was not as effective with channel forming as uniaxial tension, because channel forming caused localized deformation regions whereas uniaxial tension consisted of uniform deformation. (a) Engineering stress-elongation profiles for CD=100A/mm^2 with varying pulse periods, (b) Engineering stress-elongation profiles for CD=120A/mm^2 with varying pulse durations.

Conclusions from this work are as follows:

- EAM parameter combinations above the threshold can improve the part elongation and reduce the forming forces.
- Additionally, the magnitude of each of the electrical variables must be proportionally "balanced" for best results.
- When dealing with localized strain regions, such as with channel forming, it is no longer optimum to apply the electricity throughout the entire part, but rather to devise a method to divert the electricity to primarily the regions of localized strain, which need it most.
- When examining the effects of die speed, it can be concluded that there is a relationship between the strain rate sensitivity of the Al 5052-O Alloy and the electricity's sensitivity.
- As the current density is increased, the longer durations and more frequent pulse periods can be detrimental to the overall formability of the specimen, even if they do reduce required deformation forces in the process.

2.8. Electrical Threshold and how it is Affected by Material Resistivity

As seen in the work by Perkins et al., for a specific die speed, each material has a specific electrical threshold (*i.e.* a current density where significant formability improvements due to the applied electrical power are observed) [40]. Table 1 shows several lightweight material properties (crystalline structure and resistivity), along with the electrical thresholds, which were experimentally determined using data from works by Perkins et al. and Jones et al. [40] and [46]. Figure 28 shows the relationship between the material resistivity and the electrical threshold current density. The calculated electrical thresholds for each of these materials are from [40] and [46], where the specimens were deformed at 25.4mm/min. It can be noted that, as the material resistivity is increased, the electrical threshold current density decreases. This supports the theory of localized heating from electrons scattering off of lattice obstacles and allowing the lattice to expand easier. Also noted in the figure are the crystalline structures of the specific materials. It can be seen that, for these four metals, there is not a relation between the crystalline structure and the electrical threshold.

Table 1. Lightweight materials and respective electrical thresholds [62]-[65].

Material	Electrical Threshold (A/mm^2)	Crystalline Structure	Resistivity (Ωm)	Threshold Reference	Specimen Size (mm)	Def. Rate (mm/min)
Al 6061-T6511	60	BCC	3.99E-08	Perkins et al.	9.5 x 6.4 (dia)	25.4
Mg AZ31B-O	30	HCP	9.20E-08	Jones et al.	12 x 7.5 (dia)	25.4
304 SS	18	BCC	7.20E-07	Perkins et al.	9.5 x 6.4 (dia)	25.4
Ti-6Al-4V	20	HCP	1.78E-06	Perkins et al.	9.5 x 6.4 (dia)	25.4

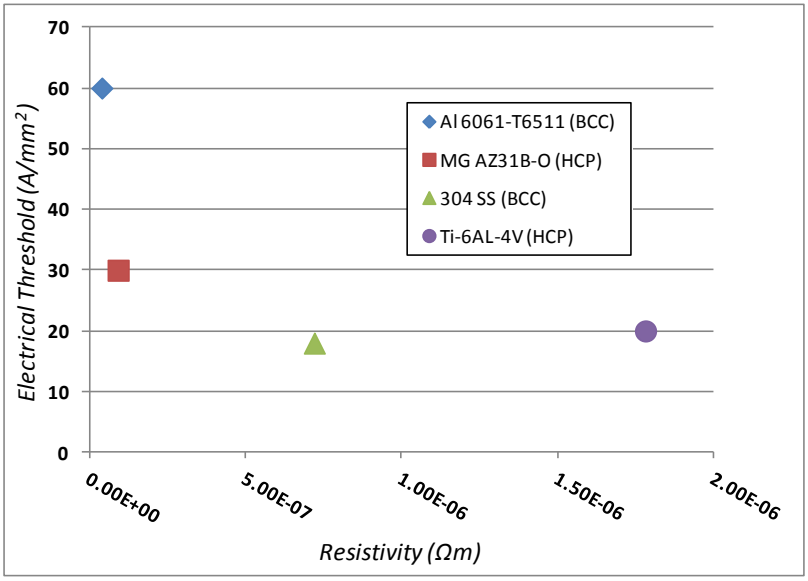

Figure 28. Electrical threshold vs. material resistivity comparison for several lightweight metals. The figure depicts that, as the material resistivity is increased, the electrical threshold decreases.

2.9. Potential Important EAM Modeling Variables from Experimentation

The previous experimental works on EAM highlight the important material- and process-related parameters for EAM. The following lists of important variables are derived from the experimental works on EAM, as well as from conversations with experts in related fields who have shared their opinions on the electroplastic effect.

The material properties of importance to an EAM process are: 1: Thermal conductivity (k), 2: Density (ρ), 3: Specific Heat (C_p), 4: Heat transfer coefficient (h), 5: Starting strength coefficient of the material (C), 6: Strain hardening exponent of the material (n), 7: Resistivity *(r)*, and 8: the initial grain structure of the metal. Each of the material-based properties is significant when modeling any heat transfer or thermodynamic phenomenon, or performing any mechanical modeling. The effects/relations of these inputs will be described below:

- The thermal conductivity (k), density (ρ), specific heat (C_p), heat transfer coefficient (h), and resistivity *(r)* all affect the heat transfer, and ultimately the stress-strain

characteristics of the EAM process. Additionally, each of these variables changes as a function of temperature, so depending on the temperatures reached during an EAM process, these variables could have weighted effects. These intrinsic properties are not only important for the workpiece, but it is also critical to know these properties for the forming dies as well.

- The strength coefficient (*C*) and strain hardening exponent (*n*) are intrinsic properties that determine the magnitude and shape of the forming load profile of an EAM test (and any forming test in general). Further, both are affected by the temperature of the workpiece and forming dies in the process. Any type of metal deformation modeling would need to include the effects of both the strength coefficient and strain hardening exponent at a minimum.
- The initial grain structure (*i.e.* grain size, grain direction, etc.) of a material can affect the heating and mechanical characteristics of a workpiece during EAM. The grain size dictates how often moving dislocations must pass through grain boundaries which cause dislocation pile-ups and can limit achievable deformation. In addition, the applied electrons must also pass through the grain boundaries and the grain size (dictating the number of boundaries) will potentially cause the workpiece to become hotter (more boundaries) or cooler (less boundaries).
- The resistivity has a direct correlation with the electrical threshold current density, as seen in Figure 28. For the same die speed, metals with a higher resistivity require a lower electrical threshold to produce significant formability improvements. This could be related to the first part of the electrical theory, where the flowing electrons scatter off of the lattice obstacles and cause localized atomic heating. A material with a higher resistivity will have a greater number of lattice obstacles, and will result in a greater

amount of localized heating around these obstacles, which ultimately lowers the electrical thresholds of these metals.

The process-related variables to be presented are: 1: Initial dimensions of the workpiece (r_o and h_o), 2: Deformation speed (*i.e.* die speed), 3: Current density (Amps/Area), 4: Applied voltage (V), 5: workpiece/die contact area, 6: electrical application method, and 7: initial percent cold-work.

- The initial dimensions of the workpiece determine the magnitude of current needed for EAF. It was determined that the electroplastic improvements are a function of current density, and not current magnitude, so the current density will determine the appropriate current magnitude to use.
- The deformation speed is important because the EAM technique is strain rate-dependent, and therefore, the electrical application parameters (starting current density) must be adjusted if the die speed is increased or decreased.
- The current density and applied voltage make up the applied electrical power to the process. In an EA-forging process where the electricity is applied continuously, these variables must be adjusted to produce a desired amount of electrical power. Let it be known that the power supply used is a constant current/variable voltage supply, so the voltage will vary in order to hold the current constant.
- The effect of the actual contact area between the workpiece and die was not previously explored experimentally, however, since the dies and workpiece are separate parts, are composed of different materials, and must both transfer electricity during the EAF process, this variable is to be explored. Additionally, the roughness between surfaces is a widely-studied topic in the field of electrical connectors.

- Electricity can be applied to a deformation process in many ways. The work by Ross et al. showed that the electricity must be applied differently for compressive and tensile processes. Since this thesis focuses on a forging operation, the electricity will be applied continuously throughout each EAF process. Let it be known that when a current density value is provided within this document, the value is the starting current density. As the specimen cross-section increases throughout the compression tests, the current density will decrease.
- The percent cold work within a metal generally determines the dislocation density within that metal. As the dislocation density is increased, there are more dislocation pile-ups and the achievable deformation can become limited. It is theorized that the flowing electrons directly affect the dislocations within the metal's lattice.

2.10. Research Approach

The overall objective of this Ph.D. research is to test the hypothesis that direct electron-dislocation interactions occur within a metal during EAM to reduce the apparent flow stress, and use this theory to be able to produce force/temperature profiles of an EAF test successfully. In addition, the specific effects of contact area, tribology, grain size, and cold work are examined and used to understand their specific effects on EAF and will be used optimize the model when applicable. The theory explains that, as electricity is applied, the electrons impact the dislocations and give them the "push" needed to continue deformation, thus reducing deformation forces and increasing achievable forming distance before fracture. The contact area relationship to the resistivity of the system is investigated, as a small contact area increases the voltage and ultimately the power of the system, also contributing to excessive heating. The tribology work explores if different lubricant compositions react differently with EAF. The grain size of the

material determines how many grain boundaries a dislocation will have to pass through during plastic deformation. The pre-existing cold work in a metal denotes the number of dislocations already existing in the material before plastic deformation even starts and these dislocations act as obstacles for the flowing electrons during EAM.

The basic research approach is outlined in Figure 29. First, a modeling concept, which incorporates thermal and mechanical effects, is established. Next, methods for quantifying the electroplastic effect are devised. Then, a simplified EAF model is created. After that, specific experiments are designed and run to generate data on contact area, tribology, grain size, and percent cold work. This data is evaluated and both variables strategically integrated into the simplified model to create an inclusive EAF model. As discrepancies between the model and experiments arise, revisions are fed back to the model. Finally, information on any simplifications that could be made to the modeling strategy, or any notable sensitivities are provided.

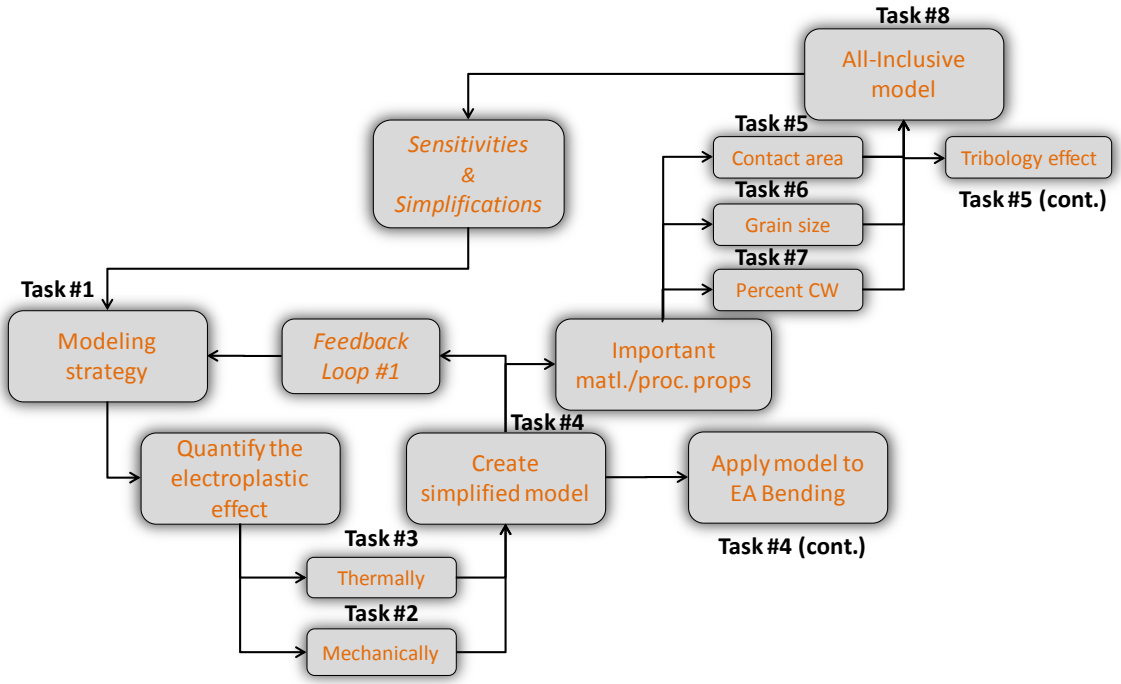

Figure 29. Ph.D. research approach. The flow chart outlines the main steps for completing the proposed Ph.D. research objectives.

3. Definition of an EAF Modeling Strategy (Task #1)

The first task in creating a thermo-mechanical model is to define how EAF could be modeled, with the optimization of current metal forming equations by creating new coefficients to capture electricity's effects. As is explained below, an Electroplastic Effect Coefficient (EEC) is created to help account for the direct electrical effects on the forming process [66]. The objective of this work is to establish a closed-form solution describing the flow stress of a material which is plastically deformed under a compressive load while direct electric current is applied through the dies. Equations predicting the effective stresses are derived from balancing the input and output energies of the system. These energy-based equations are aimed at predicting the effective stresses and strains of the system, and the forming loads for different parameters of the applied current. It is expected that this model may be beneficial in the preliminary determination of the feasibility of electrically-assisted forging a part based on formability improvement. Specifically, the model would determine process input requirements for given formability improvements, and the user could be able to determine if these inputs were worth the costs. An analytical model will bring a better understanding of the electroplastic deformation mechanism and will open new avenues for derivation of analytical solutions for more complicated manufacturing processes.

The derivation begins by establishing expressions for the effective stresses and strains acting on a plastically deformed billet without current in the classical cylindrical upsetting test using the upper bound analysis. This approach utilizes key metal forming relations derived from works by [67]-[70]. The material is assumed to follow the power law as shown in eq.(1)**:**

$$\bar{\sigma} = C\bar{\varepsilon}^{n} \qquad (1)$$

where $\bar{\sigma}$ is the flow stress, C is the strength coefficient, $\bar{\varepsilon}$ is the effective strain, and n is the strain hardening exponent. After the equations for stress and strain are established, the next step is to include the effects of the electrical current applied to the part. Two aspects are considered: (a) the applied electrical energy, and (b) the electroplastic effect on the material's behavior and on the efficiency of the process. The analytical model is verified with results (force and position data) from EAM compression tests run on Al6061-T6511 specimens, by Perkins et al. [40]. Finally, the potential applications of the developed analytical model are discussed.

3.1. Analysis of an Electrically-Assisted Compression Process

An experimental schematic of an electrically-assisted compression test can be seen in Figure 30. A power source provides electricity and a variable resistor controls the magnitude of current flowing through the dies. Insulation is placed between the dies and the machinery, thus to ensure all electricity flows through the workpiece. Electrons flow through the workpiece from anode to cathode; material flow is shown schematically in Figure 30. Friction is present at the workpiece/die interfaces, thus causing the part to bulge into a specific barrel shape. This barreling effect is neglected in the initial EAM modeling analysis.

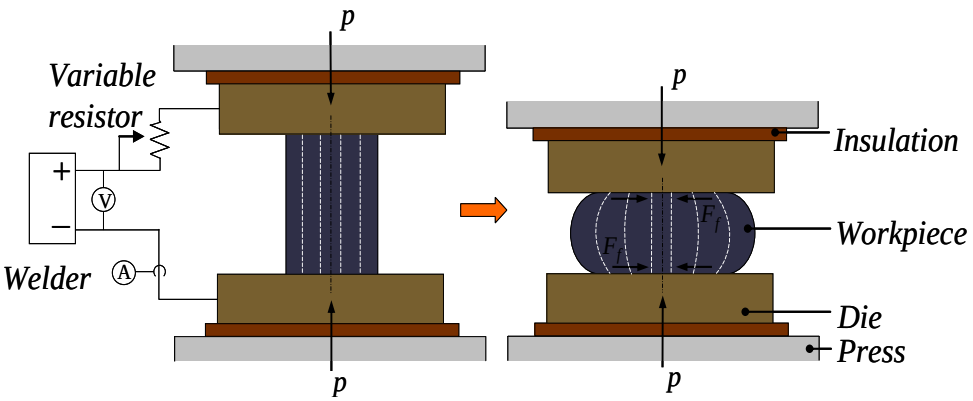

Figure 30. EAM compression test schematic. Main components include a controllable power supply, a thermal camera, and insulation placed between the dies.

The following major simplifications and assumptions are used throughout the derivations in this study:

- The material is homogeneous and isotropic.
- The elastic deformation is negligible and the power law is used for the flow stress of the material.
- The von Mises yield criterion is applied.
- The friction of the workpiece/die interfaces follows Coulomb's friction law. Sliding friction conditions assumed and barreling is ignored.
- The specific heat/resistivity of the material are assumed independent from temperature.
- The strain rate sensitivity is neglected since previous experimental investigations found that the temperature rise is not high enough for the process to be considered hot forming.
- Volume constancy is valid throughout the deformation process.
- The lubrication regime is assumed unaffected by the presence of electricity.

3.2. Effective Stress and Effective Strain – Classical Compression Test

The energy of a process is the total work needed to perform that process. The power of a process relates the required work to a particular speed at which the work is performed. The power needed to plastically deform a cylindrical billet is found by employing the upper bound analysis method as presented by [71]. The objective of this method is to determine the strain rate field that minimizes eq.(2):

$$J^* = \dot{W}_i + \dot{W}_s + \dot{W}_b + \dot{W}_k + \dot{W}_p + \dot{W}_\gamma \qquad (2)$$

where J^* is the upper bound on power, $\dot{W}_i$ is the internal power of deformation, $\dot{W}_s$ is the shear power given by the discontinuity of velocity, $\dot{W}_b$ is the power to overcome opposing external forces (back-stress), $\dot{W}_k$ is the inertia power due to the inertia forces, $\dot{W}_p$ is the pore opening power, usually neglected under the volume constancy assumption, and $\dot{W}_\gamma$ is the surface power which includes the rate of introduction of new surfaces in the deformation process. This component can also be assumed negligible in bulk deformation, but will be of more importance as this method is extended to sheet metal forming. The power components were computed by [71] for the ideal case where no bulge is formed, and the shape of the billet is assumed to remain cylindrical throughout the deformation process, unaffected by the interface friction. Using the average pressure approximation, where the pressure on the workpiece is assumed to be constant across the cross-section, the following equation for total power needed for compression can be derived as eq.(3):

$$J^* = \pi r_{inst}{}^2 \bar{\sigma} \dot{u} \left(1 + \frac{2\mu r_0}{3h_{inst}} \right) = F\dot{u} \qquad (3)$$

where r_{inst} and h_{inst} are the instantaneous radius and height of the workpiece, $\bar{\sigma}$ is the effective flow stress of the material, $\dot{u}$ is the velocity of the compressive die, r_0 is the initial radius of the billet, and F is the forming load. When the applied load and die velocity are known, the pressure exerted by the die is determined as eq.(4):

$$p = \frac{F}{\pi r_{inst}^{\ 2}} = \bar{\sigma}\left(1 + \frac{2\mu r_0}{3h_{inst}}\right) \tag{4}$$

The power law will be used to formulate the relation between the effective stress and strain, thus the pressure will be given by eq.(5):

$$p = C\bar{\varepsilon}^{n}\left(1 + \frac{2\mu r_0}{3h_{inst}}\right) \tag{5}$$

By employing the slab analysis method and simple balance of forces in the axial direction, along with the von Mises criterion, the compressive and effective stresses are determined from eq.(6):

$$\begin{aligned} &\sigma_z = p,\ \sigma_\theta = \sigma_r = p - \bar{\sigma}, \\ &\varepsilon_z = -2\varepsilon_\theta = -2\varepsilon_r, \\ &\bar{\varepsilon} = -\varepsilon_z = \ln\left(\frac{h_0}{h_{inst}}\right), \end{aligned} \tag{6}$$

where $\sigma_z, \sigma_\theta, \sigma_r$ and $\varepsilon_z, \varepsilon_\theta, \varepsilon_r$ are the principal stresses and strains in axial, hoop, and radial direction, respectively, and h_0 is the initial height of the billet.

3.3. Effective Stress and Strain – Electrically-Assisted Compression Test

The flow stress required to deform a specimen to a desired strain is lowered by applying electric current during the process. In this section, the effective electrical energy utilized in reducing this stress is formulated.

When electricity is applied during deformation, a part of the electrical energy is imparted into the mechanical deformation process. Thus the total power consumed by the process will be given by eq.(7):

$$J^* = J_m^* + J_e^* \tag{7}$$

where J_m^* is the mechanical component given by the product of the forming load and the die velocity, and J_e^* is the effective (usable) electrical power, as shown in eq.(8):

$$J_e^* = \xi \cdot P_e \tag{8}$$

where ξ is defined as the Electroplastic Effect Coefficient (EEC), and P_e is the power of the electrical current passing through the workpiece. It is known from previous experimental research that the EEC is a new material property coefficient introduced here, and it reflects the ratio of the electrical power that contributes towards plastic deformation to the total input electrical power. Research Tasks #2 and #3 explain several different methods for obtaining the specific EEC profile for a material/electrical parameter combination. The Electroplastic Effect Coefficient, ξ, depends on the material, applied current density and time, and can be determined through the tests defined below. Electric current will also increase the part temperature, thereby lowering the flow stress of the material and contributing to decreased required work.

Through resistive heating, the electric current results in thermal softening of the material, thereby decreasing flow stress as represented by the strength coefficient C in eq.(5). In our analysis, a stepwise approach is used, whereby the material is strained by $d\varepsilon$, the contribution of

electrical energy to the deformation work calculated, the remaining electrical energy converted to heat, then the material workpiece temperature rise and subsequent effect on strength coefficient derived. The process is repeated to the final desired strain.

When the electric current passes through the metallic workpiece, heat is generated and the temperature of the part rises. Heat transfer and thermodynamics knowledge was gathered from [72]-[73] to derive the thermal equations for this section. The temperature rise can be determined from an energy balance conforming to eq.(9):

$$\frac{\partial \rho U}{\partial t} + \frac{\partial}{\partial x_j}\left(\dot{Q}_{conv} + \dot{Q}_{cond}\right) = Q_{rad} + (1-\xi)P_e \qquad (9)$$

where $\frac{\partial \rho U}{\partial t}$ is the rate of change of the internal energy of the part, $\frac{\partial}{\partial x_j}\left(\dot{Q}_{conv} + \dot{Q}_{cond}\right)$ are the convective and conduction components of the heat flux, Q_{rad} is the radiation heat, and $(1-\xi)P_e$ is heat generated in the part from the electric energy dissipated. Using constitutive equations for each component, the heat equation to be solved for, that determines the temperature rise for particular electric parameters is eq.(10):

$$\rho V_v C_p \frac{\partial T}{\partial t} = -A_s[h(T - T_\infty)] - 2kA_c \frac{\partial^2 T}{\partial x_j^2} - A_s \varepsilon \sigma_{SB}\left(T^4 - T_\infty^4\right) + (1-\xi)VI \qquad (10)$$

where ρ is the density of the material, V_v is the volume of the part, C_p is the specific heat of the material, T is the temperature, t is time, A_s is the lateral surface of the part, h is the convection heat transfer coefficient, T_∞ is the surrounding temperature, k is thermal conductivity of the die

material, A_c is the cross-sectional area, x_j are coordinates, ε is radiative emissivity for the part, σ_{SB} is the Stefan-Boltzmann constant, V is the electric voltage, and I is the intensity of the current, given by the product of the current density and cross-sectional area.

The local heating of the workpiece influences the flow of the material. At room temperature, the flow is given by the power law presented earlier, but as the temperature rises, the flow curve depends strongly on the temperature. If the temperature is higher than the temperature at which recovery and recrystallization take place, then the flow depends also on the strain rate of the process, conforming to eq.(11):

$$\bar{\sigma} = C\bar{\varepsilon}^{n}\dot{\bar{\varepsilon}}^{m} \tag{11}$$

where C is the strength of the material, $\dot{\bar{\varepsilon}}$ is the effective strain rate, and m is the strain rate sensitivity. The investigations conducted by previous researchers indicated a maximum temperature of the part between 100ºC and 200ºC (which is far below the recovery temperature), thus the strain rate dependency may be neglected, but the influence of the temperature on the strength of the material is still significant, since the higher temperatures favor the climbing of the dislocations, thus the deformation process.

3.4. Current Density Relationship during Compression

Work by Ross et al. (in section *2.2: EAM Application Methods…*) shows that the electricity in an EAF process had to be applied differently for different forms of metal deformation [41]. Specifically, Ross et al. determines that applying EAF continuously for a tensile process caused detrimental effects. This is due to the increasing current density

throughout a tensile process, due to the shrinking cross-sectional area. Conversely, the cross-sectional area of a workpiece in a compression-based process increases, leading to a decreasing current density over the duration of the test.

The term "current density" will be used frequently throughout this document. When used, it represents the starting current density, not the instantaneous current density. For the forging experiments in this thesis, the current density will decrease since the cross-sectional area of the workpiece will increase during deformation. Eq.(12) shows this relation as:

$$CD_{act} = CD_{nom} \cdot \left(\frac{A_o}{A_f} \right) \tag{12}$$

where CD_{act} is the actual current density during the deformation process, CD_{nom} is the nominal current density (*i.e.* the starting current density), A_o is the initial cross-sectional area, and A_f is the final cross-sectional area. As $\left(\frac{A_o}{A_f} \right)$ decreases, the current density decreases as well. Eq.(12) can be re-written in terms of strain as eq.(13):

$$CD_{act} = CD_{nom} \cdot \left(\frac{1}{e^{\varepsilon}} \right) = CD_{nom} \cdot e^{-\varepsilon} \tag{13}$$

where ε is the material strain.

Figure 31 shows the change in current density over the duration of an electrically-assisted forging test. The specific tests in the figures are of 304SS specimens (7.154mm x 4.761mm diameter) that were deformed at dies speeds of 12.7mm/min and 25.4mm/min. From the figure,

the ending current density is about 41% of the starting current density, hence there is a significant change in the current density over the duration of the EAF tests if current is held constant. Let it be known that the current density is not specifically used in any modeling done as part of this thesis. The modeling includes electrical power, which is obtained by the current (which is held constant in all tests). The starting current density value of any EAF test is used purely as a classification mechanism and not as a modeling variable, because it is dependent on the cross-section of the part and this is constantly changing.

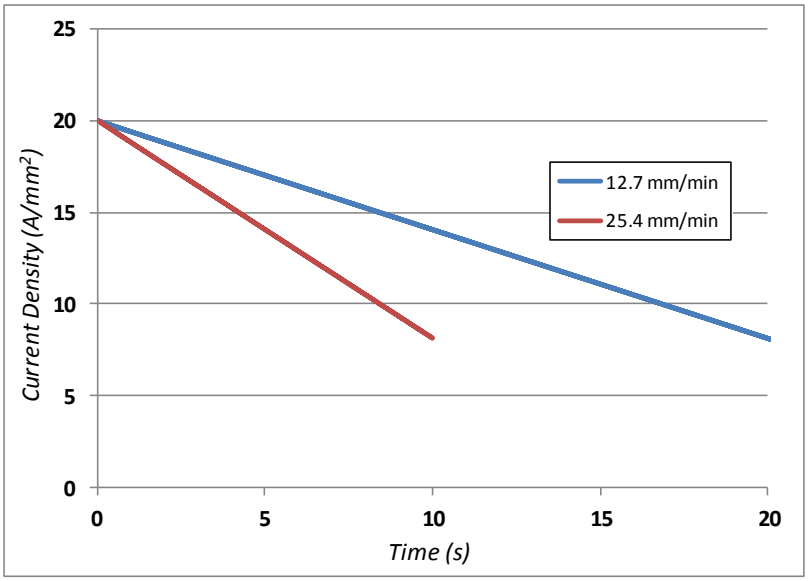

Figure 31. Current density decrease during an EA-Forging test. Since the cross-sectional area increases in compression, the current density will decrease over the duration of the test.

3.5. Strain and Temperature Effect on Resistance and Current

By virtue of strain and material heating, the resistance of the sample and ultimately the induced current, is affected. Referring to Figure 30, the DC source is a voltage source; the current is set through adjustment of the voltage and a variable resistor as shown. During

deformation, the resistance is affected by the workpiece geometry and the material resistivity according to eq.(14).

$$R[\Omega] = \rho \frac{L}{A} \tag{14}$$

For Al6061-T6, the resistivity *(r)* is given by eq.(15):

$$r = 4 \cdot 10^{-8} \left(1 + 0.0039T\right)[\Omega m] \tag{15}$$

For specimens at different nominal applied current densities, the reduction in resistance of the specimens is plotted in Figure 32. We observe that the geometric effects dominate, and that the specimen resistance decreases up to 87% in the test data. However, the overall system resistance is dominated by the variable resistor, so this effect is negligible.

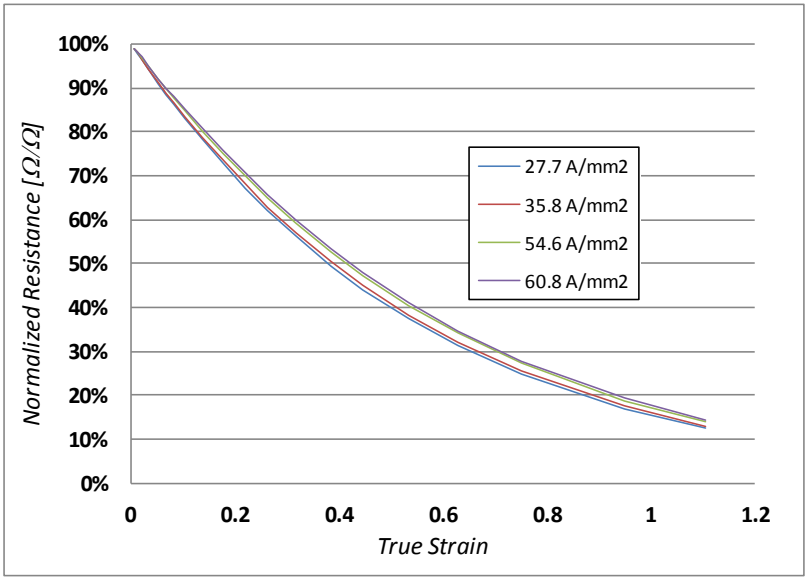

Figure 32. Specimen resistance change with respect to strain and temperature [66]. Although the overall normalized resistances change with the strain (because of the decreasing specimen height), there is no notable difference in resistance change in relation to the specimen temperature (different current densities).

3.6. Analytical Model for Electrically-Assisted Compression

The proposed thermo-mechanical analytical model is based on the stress-strain equations presented for the classical test, but adapted to take into consideration the various effects of the electrical energy on the deformation mechanism. Thus, eq.(16) represents the amount of electrical energy contributing to the deformation, as presented in eq.(7) and eq.(8), is introduced in eq.(3)-eq.(6).

$$J^* = F\dot{u} + \xi \cdot P_e = \bar{\sigma}\left(1 + \frac{2\mu r_0}{3h_{inst}}\right)\pi r_{inst}{}^2 \qquad (16)$$

where the effective stress will be given by eq.(11). Thus, eq.(17) can be written as follows:

$$F\dot{u} + \xi VI = C\bar{\varepsilon}^{n}\dot{\bar{\varepsilon}}^{m}\left(1+\frac{2\mu r_0}{3h_{inst}}\right)\pi r_{inst}{}^{2} \tag{17}$$

where V and I are the voltage and current intensity. The current is given by eq.(18):

$$I = \pi r_{inst}{}^{2} C_d \left[=\right]\left(mm^2\right)\cdot\left(\frac{Amps}{mm^2}\right) \tag{18}$$

with C_d being the current density (*i.e.* current/cross-sectional area) and $\pi r_{inst}{}^{2}$ being the cross-sectional area of the workpiece. Eqns.(10), (17), and (18) constitute the analytical model for an electrically-assisted compression test.

3.7. Overall Solution Schematic

A MATLAB program was implemented to numerically solve the equations derived for the model. The model is solved incrementally. By imposing the material and initial dimensions of the part, the model is used to determine the effective strain and stress for different current density values. The solution schematic is given in Figure 33. A mechanical power step, ΔP_m, is preset such that P_m increases incrementally throughout the test. Specifically, the overall mechanical power profile is divided into a given number of steps, at which mechanical forces will be determined. More steps will produce higher modeling accuracy, however, it may increase modeling time. At step i, eq.(10) is solved to determine the temperature rise, and then used to find the corresponding strength coefficient, C. The new value is used in eq.(15) and the height of the billet is calculated. The stroke, effective strain and stress, and the complete state of stress and

strain can be determined if desired. The iteration continues until deformation reaches the desired value of the stroke, or a failure criterion, such as the fracture limit, is reached.

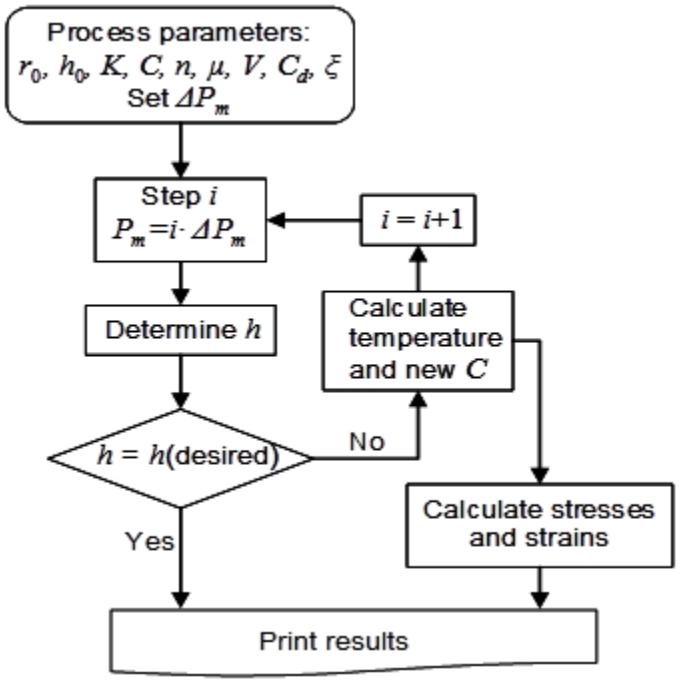

Figure 33. Solution scheme for solving the analytical model [66]. The EAF model is set such that all important variables are established first, and then the desired compression stroke is divided into increments at which the model will output data for each increment.

3.8. EAM Modeling Approach Summary

This chapter presents an energy-based approach to analyze electrically-assisted forming. The input electrical energy is separated into the useful energy that assists the mechanical deformation process, while the remaining energy is converted to heat, causing thermal softening by way of resistive heating. The Electroplastic Effect Coefficient (EEC) is created to account for the ratio of "useable" electricity compared to the overall magnitude of applied electricity. More information about the EEC and different methods to determine this coefficient will be provided in the next chapter.

4. Quantification of the Electroplastic Effect (Tasks #2 and #3)

The electroplastic effect is not novel, since it has been researched for several decades [74]-[79]. Now that the EEC has been introduced into the modeling strategy in the previous chapter, methods by which to determine this EEC profile must be discussed. The EEC is simply a ratio of the amount of electricity contributing towards plastic deformation vs. the total amount of electricity applied to the process. There is also the assumption that whatever applied electrical power that does not contribute towards plastic deformation will contribute towards resistive heating. With this being said, the EEC profile can be determined by utilizing either the mechanical power profiles or the thermal profiles of EAF and non-EAF tests. This chapter is divided into three sections. First, an explanation of the mechanical-based approach for determining the EEC is described. The EEC is not a constant value, but it is a function of the time of the forming process. In the following sections, the EEC will be considered a profile and not a constant value. Next, the thermal-based EEC determination strategy is explained. Finally, a comparison between the two methods is provided.

4.1. Mechanical-based approach to determining the EEC

In the same research paper as discussed in *Chapter 3*, one can understand the mechanical-based approach for determining the EEC [66]. This ratio represents the difference between the power required for a non-pulsed baseline test and the power required for each EAM test using a different current density. This fraction of power is assumed to be converted into mechanical work with respect to time, thus aiding the deformation (*i.e.* imparting energy onto the dislocations and facilitating their movement by providing enough energy to overcome lattice obstacles). The specific steps to solve for the EEC using the mechanical-based method are as follows. Within the

following sub-sections, these steps will be carried out using EAF compression tests on Al6061-T6511.

- Run a conventional and an EAF compression test. Note that these tests need to be run at the same parameters (*i.e.* die speed, deformation stroke, initial pre-load, and starting specimen size), with the exception of the applied current for the EAF test. It is also recommended to run up to three replicates of each test to verify that the results are repeatable (in the past, with the CU-ICAR testing setup, it was determined that these tests were repeatable such that one test could be used to represent the batch of tests at each particular setting).
- Plot the mechanical power vs. time profiles. In Figure 51, four different starting current densities were tested, therefore, four different sets of EAF tests and one set of conventional compression tests were needed to construct the profiles.
- Determine the difference between the two power profiles and normalize it with respect to the conventional forming power profile.

4.1.1. Experimental Setup and Procedure

The experiments for this sub-section involved running conventional compression tests and EAF compression tests at several starting current densities. The experimental data used in determining the EEC is from EAM compression tests run on Al6061-T6511 specimens, by Perkins et al. [40]. The initial billets had a diameter of 6.4 mm, and a height of 9.5 mm. The compression tests were deformed to a maximum stroke of 6.4 mm at a speed of 25.4 mm/min. The material parameters and the friction conditions were determined by solving the model for a classical test. After fitting the data, the following values were determined: $C = 348\,\text{MPa}$, $n = 0.04,$ and $\mu = 0.08.$ The influence of the temperature on the strength coefficient, $C,$ is

assumed to follow the same trend as for technical pure aluminum, as shown in Figure 203 in the appendix.

4.1.2. Mechanical-Based EEC Determination Procedure

In determining the EEC using this method, the mechanical power profiles of conventional compression and EAF compression tests are needed. As mentioned, the EEC is a ratio between the useable applied electrical power and the overall applied electrical power. Further, any portion of the overall applied electrical power that is not utilized to assist plastic deformation is assumed to contribute directly towards heating the workpiece. The EEC can be described in equation form as eq.(19):

$$\xi = \frac{\left(P_{conv} - P_{EAF}\right)}{P_{conv}} \tag{19}$$

where P_{conv} is the mechanical power profile of a conventional compression test and P_{EAF} is a mechanical power profile of an EAF test. The difference between the mechanical power profiles of a conventional and EAF test provides the magnitude of electrical power which contributed towards aiding the plastic deformation. Figure 34 shows the mechanical power profiles for the mentioned compression tests, where Al6061 specimens (9.5mm height x 6.4mm diameter) were compressed at 25.4mm/min to a final displacement of 6.4mm. Please note that the "Baseline" and "EAM" tests in the figure have the exact same test parameters, with the exception of the "EAM" test having a current density of 20A/mm^2 applied to the specimen during deformation. The Baseline/EAM mechanical power profiles cannot be compared unless the following test parameters are the same: stroke, die speed, starting specimen size, and pre-load.

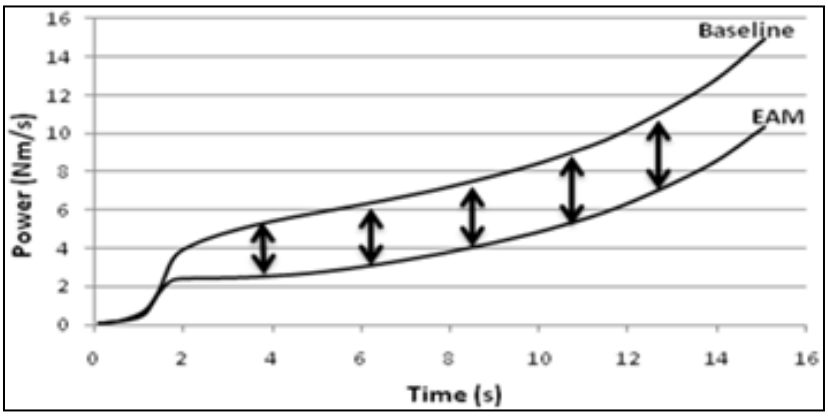

Figure 34. Determination of the Electroplastic Effect Coefficient (EEC) [66]. In this figure, the differences in the mechanical power profiles are used to determine the ratio of "useable" applied electricity, quantified by the EEC.

The next step is to determine the Electroplastic Effect Coefficient. In the initial stages of this research, an average value approximation to quantify the EEC was used. To determine an average EEC, a coefficient profile was created by plotting the coefficient vs. time for each respective current density, as shown in Figure 35. Once the coefficient profile was established, an average coefficient for each current density was determined using a flat-line approximation approach. This type of approximation is sufficient for initial model verification, and is fairly accurate except with the 60.8A/mm^2 test. As the research into this task progressed, it was determined that the EEC was a function of time and that a profile, rather than a straight-line approximation, was more accurate. To create an EEC profile as a function of time, the same EEC profiles in Figure 35 can be used, where a power law trend line can be fit to each profile as a function of the testing time. In later chapters of this thesis, EEC profiles will be used, instead of straight-line approximations.

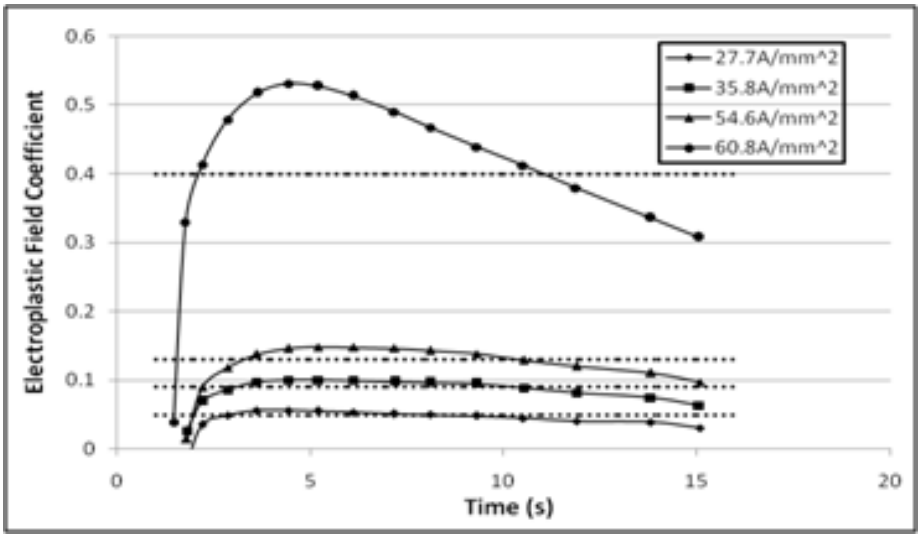

Figure 35. Electroplastic Effect Coefficient (EEC) profiles [66]. The EEC profiles are shown, along with a straight-line approximation.

4.1.3. Mechanical-Based EEC Conclusions

There is an unmodeled time- or strain-dependent effect of the electrical influence on deformation. Previous work has highlighted a "threshold effect" whereby electrical application benefits are negligible until a critical current density is reached [40]. Figure 35 supports this threshold effect since the 60.8A/mm^2 test has an EEC profile that is much higher than the other three current densities. However, this does not mean that the electrical threshold is 60.8A/mm^2, but this was just one of the current densities tested. In this case, the threshold is somewhere between 54.6A/mm^2 and 60.8A/mm^2.

Following the steps presented earlier in the solution scheme in Figure 33, the model was solved for three different current densities (27.7A/mm^2, 35.8A/mm^2, and 60.8A/mm^2) primarily using eqns.(10), (17), and (18). For this model, the straight-line approximated EEC values were used. Figure 36 compares the model predictions with stress-strain profiles of experimental compression tests at the same current densities. It can be observed that the predictions agree very well for two of the cases. The differences can be attributed to the simplifications and assumptions

made in the model. Next steps could be to refine the model to account for factors that were neglected, *i.e.* strain rate sensitivity, and also to conduct specific experiments targeting accurate measurements of material properties included in the analytical model, such as the material strength and EEC.

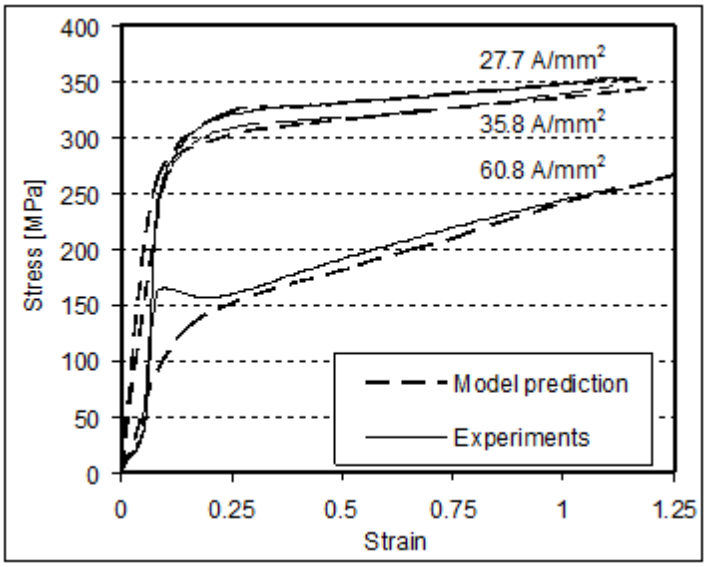

Figure 36. EAM model verification [66]. The actual experiments and the EAM compression model, using the generated EEC's, are very similar.

4.2. Thermal-Based Approach to Determining the EEC

The thermal-based approach to determining the EEC was highlighted in [80]-[82]. The objective of this section is to establish a methodology for quantifying the Electroplastic Effect Coefficient using thermal profiles. From the conservation of energy and empirical observations, an analytical model able to predict the temperature rise in the specimen due to the electricity that was applied while subjected to deformation must be completed before being able to determine the EEC. The Electroplastic Effect Coefficient is dependent on the magnitude of current applied to the workpiece. This can be seen from the differences in the EEC profiles at different current

densities in Figure 35. Since the purpose of this section was to develop a preliminary model and propose a thermal-based procedure for determining the Electroplastic Effect Coefficient, only one current magnitude (300A) was used. The EEC is dependent on the applied current, so the effect of different magnitudes of current will be indirectly linked into the thermal model by way of different EEC profiles resulting from the different currents.

To determine the EEC, the variation of the temperature of the specimen in time is solved from eq.(21) and eq.(23), and combined with experimental thermal measurements and with geometrical changes occurring during the deformation process. The procedure is described below:

1. Solve the model for a stationary-electrical test. This is a test when the part is clamped between the dies and pre-loaded, and electricity is applied. The dies are stationary, thus no plastic deformation occurs and the dimensions of the part are not changed.
2. Validate the model by comparing with thermal measurements from experiments (*i.e.* strictly resistive heating).
3. Solve eq.(21) and eq.(23) for an electrically-assisted deformation test. Note that just the temperature rise component due to the application of electricity is considered. Initially assume the Electroplastic Effect Coefficient to be $\xi = 0$.
4. Compare the solution from the previous step with the thermal measurements. At this step, the increase in temperature due to electricity is separated from the increase due to plastic deformation by subtracting the temperature increase recorded during conventional compression experiments. As will be shown in the results section, there will be a significant thermal profile difference between the experiment and the model. This difference proves the concept of the Electroplastic Effect Coefficient.

5. Determine the Electroplastic Effect Coefficient, ξ, in order to match the model with the experimental thermal profile, and propose a formulation for this coefficient for the different materials studied.
6. Further refine the Electroplastic Effect Coefficient and the model to account for prior cold work.

The analytical model is solved and validated in the next sections, followed by investigations of influencing parameters initially assumed constant, such as material properties as a function of temperature, and contact pressure.

4.2.1. Building a Thermal Model

The Electroplastic Effect Coefficient depends on specific material properties, such as heat capacity, electric resistivity, electric field characteristics and the current magnitude. The next sections will investigate all these aspects. The simplifying assumptions which were used to facilitate the derivation of the model are as follows:

- The material is homogeneous and isotropic.
- The increase in temperature due to friction at the workpiece/die interface is negligible. This assumption is valid for the small dimensions and low relative speeds in the compression tests.
- The barreling effect due to friction is neglected when the model is solved.
- In the initial calculations, the material properties that are assumed constant with temperature are C_p and r. The influence of material property changes is discussed in *Section 9.1*.

- The temperature distribution in the part is considered uniform. In reality, contact resistance under low loading causes an increase in the temperature at the contact points between the specimen and the dies at the beginning of application, followed rapidly by homogeneous heat generation as the load increases and contact resistance effect becomes negligible. The die/specimen interfaces will also have a different temperature distribution, and these boundary conditions will be taken into consideration when the solution for the model is calculated.
- The voltage in the specimen is assumed constant and it is determined for the initial dimensions of the specimen at room temperature. However, the voltage will vary during the test, since the power supply is a variable-voltage source (*i.e.* constant current). On one hand the decrease of the ratio of height over cross-sectional area results in lower resistance, thus lower voltage, while the increase in temperature will increase the resistivity, thus resistance and voltage increase. Overall, the present work assumes that these effects cancel each other. The specimen resistance change with respect to strain and temperature is shown in Figure 32. Here the change in resistance is proven negligible.

The temperature rise and its distribution during an electrical test are illustrated in Figure 37 during a stationary-electrical test, where electricity is applied without plastic deformation. It can be seen that the specimen quickly heats up for about the first 14 seconds with almost all the heat going exclusively into the workpiece. Then, the heat from the specimen conducts into the compression dies for the remaining half of the stationary-electrical test.

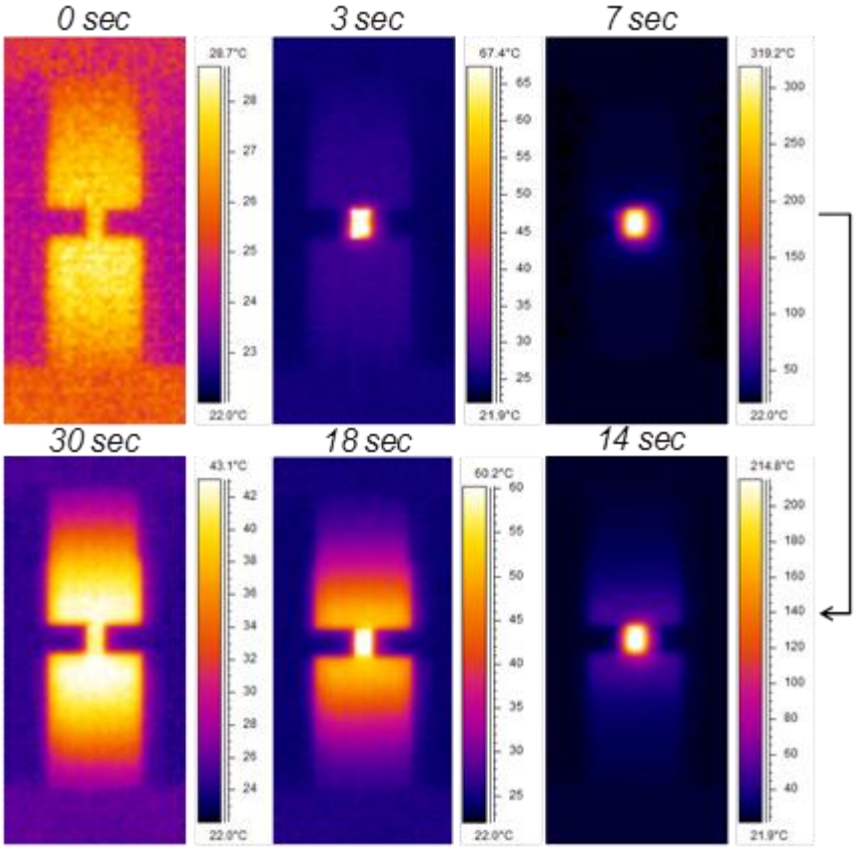

Figure 37. Heating and cooling sequence during a stationary-electrical test [80], [82]. During the first half of the test, the specimen holds the majority of the heat generated, and then the heat is transferred to the dies through conduction for the second half of the test.

When examining only the specimen, the specific temperature profile will also change throughout the test. More specifically, the temperature of the die/workpiece contact points at the beginning of the test will be much hotter than the rest of the specimen (because the actual contact area will be less, leading to a higher overall electrical power at these points). This will be further discussed in *Chapter 6*, which focuses on contact area effects. However, as the part is compressed and the asperities are crushed, the temperature profile inverts and the middle of the specimen is the hottest (since the asperities crush and the contact area increases, leading to a decrease in the electrical power at these points). In addition, the heat generation is reduced to a

point that it cannot keep up with conduction into the dies. The estimated thermal profiles of an EAF test are schematically illustrated in Figure 38.

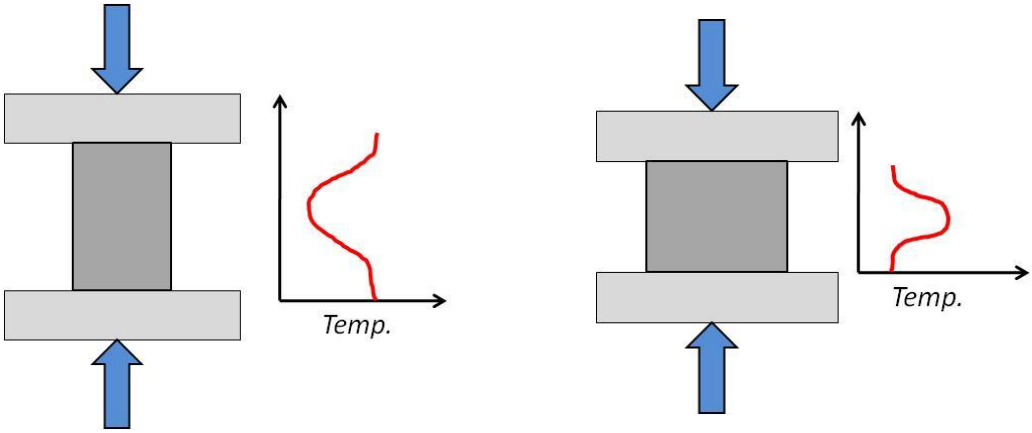

a. Temperature profile at the beginning of an electrically-assisted compression test

b. Temperature profile towards the end of an electrically-assisted compression test

Figure 38. Specimen thermal profiles at the beginning and end of an electrically-assisted compression test [82]. The specimen is hottest at the die/workpiece interfaces at the beginning of the EAF test, while the center of the specimen is hottest at the end of the EAF test.

For a better understanding of the electroplastic effect, the thermal aspects must be isolated. When the electric current passes through the metallic workpiece, heat is generated and the temperature of the part rises. The temperature increase is determined from the energy balance, illustrated in Figure 39.

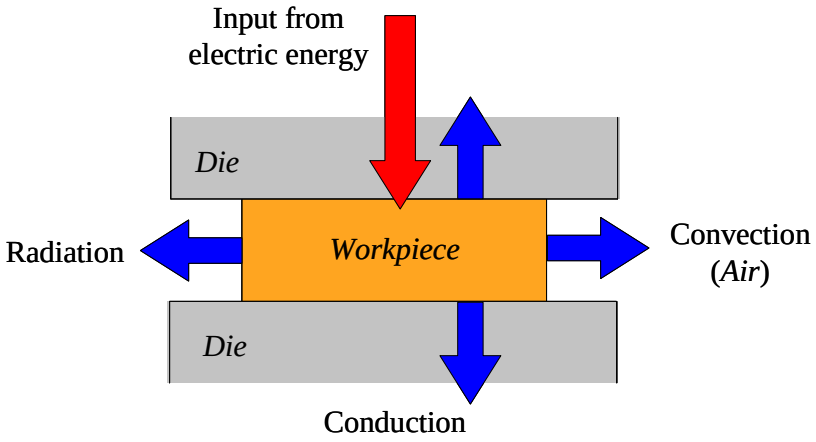

Figure 39. Heat flux energy balance [80]-[82]. All three heat transfer modes (conduction, convection, and radiation) are accounted for in the thermal model.

The general form of the energy conservation is expressed on a rate basis as eq.(20):

$$\begin{aligned} \dot{E}_{part} &= \dot{E}_g - \dot{E}_{out}, \\ \dot{Q} &= \dot{Q}_e - \dot{Q}_{cond} - \dot{Q}_{conv} - \dot{Q}_{rad}, \end{aligned} \qquad (20)$$

where $\dot{E}_{part}$ is the rate of change of the energy content in the part analyzed ($\dot{Q}$), $\dot{E}_g$ is the rate of heat generation due to the electric resistive heating ($\dot{Q}_e$), and $\dot{E}_{out}$ is the rate of energy leaving the part due to conduction into the dies in the contact zone ($\dot{Q}_{cond}$), convection ($\dot{Q}_{conv}$) and radiation from the surface ($\dot{Q}_{rad}$). To clarify, $\dot{E}_g$ has only one contributor ($\dot{Q}_e$), whereas $\dot{E}_{out}$ has three contributors ($\dot{Q}_{cond}, \dot{Q}_{conv}, \dot{Q}_{rad}$) which are the three forms of heat transfer. After developing each component, the heat equation can be written in one dimension as eq.(21):

$$\rho V_v C_p \frac{\partial T}{\partial t} = -A_s[h(T - T_\infty)] - 2kA_c \frac{\partial T}{\partial x} - A_s \varepsilon \sigma_{SB}\left(T^4 - T_{surr}^4\right) + \eta(1-\xi)VI \qquad (21)$$

where ρ is the density of the material, V_v is the volume of the part, C_p is the specific heat of the material, T is the temperature, t is time, A_s is the lateral surface area of the part, h is the convection heat transfer coefficient, T_∞ = T_{surr} is the surrounding temperature, k is thermal conductivity for the die material, A_c is the cross-sectional area, x is coordinate, ε is radiative emissivity for the part, and σ_{SB} is the Stefan-Boltzmann constant. The input from electricity was taken from eq.(22).

$$P_e = P_{heat} + P_{def} = \eta(1-\xi)VI + \eta\xi VI \tag{22}$$

where P_e is the electric power (I·V), η is the efficiency, and ξ is the Electroplastic Effect Coefficient. P_{heat} represents the amount of electric power that will dissipate into heat through resistive heating of the workpiece. P_{def} is the electrical power component that will aid the plastic deformation.

The changes in geometry are calculated assuming compression at constant speed, as well as volume constancy, as given by eq.(23):

$$\frac{\partial h}{\partial t} = -\dot{u};\ \frac{\partial D}{\partial t} = \sqrt{\frac{V_v}{\pi}}\frac{\dot{u}}{h\sqrt{h}} \tag{23}$$

where D and h are instantaneous dimensions of the workpiece, and $\dot{u}$ is the compression speed. The second equation was determined from the volume constancy condition $(V_v = \pi D^2 h/4)$.

The change in temperature solely due to the portion of electrical power that did not contribute towards plastic deformation can be shown in the integral in eq.(24).

$$T_f - T_o = \frac{\eta VI}{mC_p} \int_0^{t_f} (1-\xi)\, dt \tag{24}$$

where m is the mass of the workpiece. The EEC profile with respect to time can be shown in eq.(25).

$$\xi = \xi_0 * t^b \tag{25}$$

where ξ_0 is an initial value, which is dependent on specific material properties and the magnitude of the applied current, *t* represents time, and *b* is an exponential term. The ξ_0 value is similar to the *C*-term in the power law equation, where it is dependent on the specific material (*i.e.* its strength, crystal structure, etc.). Although the Electroplastic Effect Coefficient does not simply vary in time, the term 'time' is related to the deformation parameters. Eq.(25) can be re-written in terms of strain, as shown in eq.(26), where ε is the material strain and $\dot{\varepsilon}$ is the strain rate (*i.e.* the deformation speed).

$$\xi = \xi_0 * \left(\frac{\varepsilon}{\dot{\varepsilon}}\right)^b \tag{26}$$

4.2.2. Experimental Setup and Procedure

The main experimental objective of this work was to measure the thermal profile during the EAF test and use it to generate an EEC profile. Figure 40 displays the experimental setup. An Instron Model 1332 hydraulic testing machine was used to compress the specimens. Machined, hardened, and insulated dies, made from A2 tool steel, were installed in the Instron machine (note that insulation was used such to isolate the electricity from the test machine). For thermal measurements, a FLIR A40M thermal camera, with a temperature capacity of 550°C, resolution of 0.1°C, and sample frequency of 50 Hz was utilized. All force and position data was gathered using an on-board data acquisition system at 1500 Hz sampling frequency.

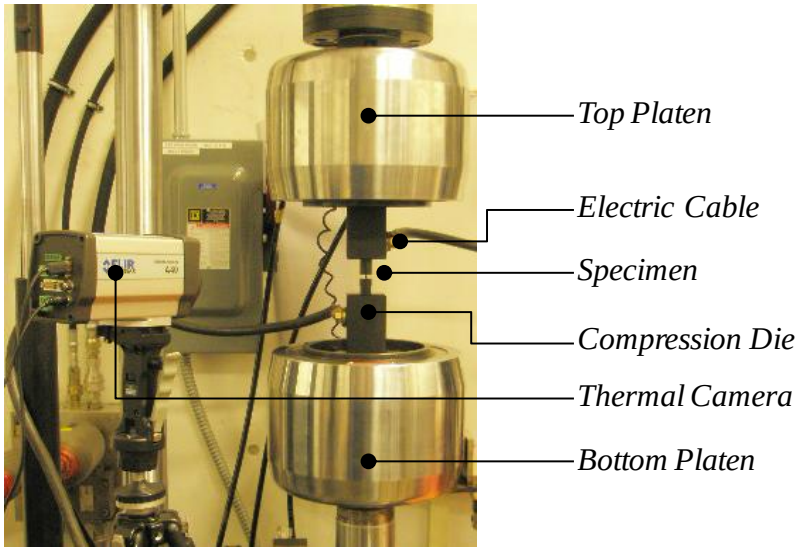

Figure 40. EAF test setup [80]-[82]. This test setup consisted of the mechanical testing machine, dies, and a thermal camera.

The materials tested were two grades of titanium: Grade 2, which is a single phase polycrystalline material, and Grade 5 (Ti-6Al-4V), a dual-phase alpha-beta alloy. The initial dimensions of the specimens are summarized in Table 2. A displacement speed of 12.7mm/min was used for all tests and a constant DC current of 300A was utilized for all the EAF tests. Please

note that, since the cross-sectional areas between the specimens of the three levels of deformation will be different, the resulting current densities will also be different. Considering the size of the "as-is" specimens, the current density supplied to the workpieces is about 26A/mm^2, which is above the threshold current density of about 20A/mm^2 determined by Perkins et al. [40].

Table 2. Specimen dimensions [80]-[82].

Def. Level	Diameter [mm]	Height [mm]	Description
L_0	3.81	5.72	"As-is"
L_1	4.32	4.45	Machined or Deformed to dimensions
L_2	5.11	3.18	Machined or Deformed to dimensions

Two types of tests were performed in this work. First, deformation tests were run, where the specimens were deformed at a constant die speed from an initial height of L_0 to deformation levels of L_1 or L_2, with and without electricity applied (note: electricity applied at 300A). Stress-strain and thermal profiles were created from these tests. Second, stationary-electrical tests were performed, where electricity was applied to a specimen without plastic deformation. Specifically, the dies were in contact with the specimen such to prevent hot spots at the contact interfaces and to allow electricity to flow, but without causing plastic deformation in the sample. Thermal profiles were gathered from these tests and were used in comparison with each other and with the thermal profiles from the deformation tests, as will be shown in the following sub-sections. The different test combinations and corresponding specifications can be seen in Table 3.

Table 3. Test combinations and specifications [80]-[82].

Grade	Deformed/Stationary	EAF/Conv.	Displ.	Prev. Strucutre	% CW
2	Def.	EAF	L_0-L_2	As-Is	-
2	Def.	Conv.	L_0-L_2	As-Is	-
5	Def.	EAF	L_0-L_2	As-Is	-
5	Def.	Conv.	L_0-L_2	As-Is	-
2	Def.	EAF	L_1-L_2	Init. Def. to L_1	22
2	Def.	Conv.	L_1-L_2	Init. Def. to L_1	22
2	Def.	EAF	L_1-L_2	Init. mach. to L_1	-
2	Def.	Conv.	L_1-L_2	Init. mach. to L_1	-
2	Stationary	EAF	L_1	Init. Def. to L_1	22
2	Stationary	EAF	L_1	Init. mach. to L_1	-
2	Stationary	EAF	L_2	Init. Def. to L_2	44
2	Stationary	EAF	L_2	Init. mach. to L_2	-
5	Stationary	EAF	L_1	Init. Def. to L_1	22
5	Stationary	EAF	L_1	Init. mach. to L_1	-
5	Stationary	EAF	L_2	Init. Def. to L_2	44
5	Stationary	EAF	L_2	Init. mach. to L_2	-

4.2.3. EEC Thermal-Based Determination

Within this section, true stress-strain plots and temperature plots are used to emphasize several EAF relations and effects. First, the reductions in flow stress due to EAF are shown. Of note is that since this work focused on modeling EAF, only one current was used, so the reductions in flow stress from EAF could be much greater if larger currents were utilized. Second, the model prediction process and accompanying experimental results are discussed. The steps required for model prediction are outlined in the previous section. From the creation of the model and analysis of several of the main input variables, EAF can be better understood and more accurately predicted through this variety of influencing factors.

Force Reduction due to EAF

From many experimental works over the last several years, it has been shown that EAF reduces a metal's flow stress compared to conventional forming [3]. Figure 41 and Figure 42

show the true stress-strain profiles of a conventional compression test (at room temperature) and an EAF test for Ti-G2 and Ti-G5, respectively. A die speed of 12.7mm/min was used and a constant current of 300A was applied during the EAF test. Both figures show that the flow stress was reduced significantly due to EAF. In Figure 41, one can see that the difference in the flow stress is offset by about 150-200MPa throughout the test. Conversely, in Figure 42, the difference in flow stress increased slightly as the test progressed. Additionally, the Ti-G5 in the conventional compression test failed before the end of the test. However, in the electrically-assisted compression test, the material was able to be completely formed without failure (see specimens in Figure 10). The results in Figure 42 are comparable to EAF compression test results of the same alloy run by [40]. Specifically, a small amount of strain weakening is apparent at the beginning of the test, and in both works, the elongation of Ti-G5 is increased using EAF.

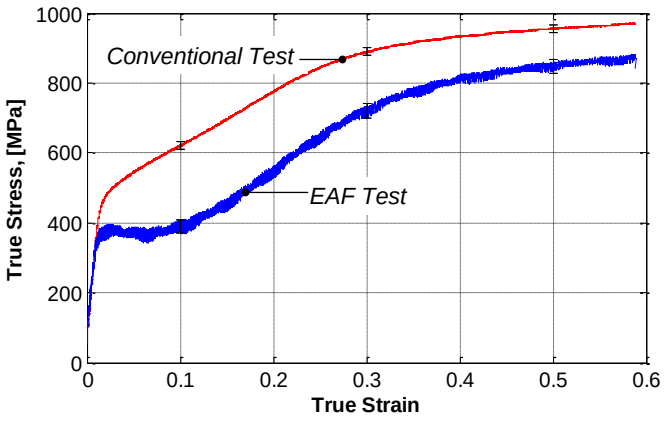

Figure 41. Flow stress reduction due to EAF (Ti-G2) [80]-[82]. The flow stress was notably reduced in comparison to the conventional stress-strain profile.

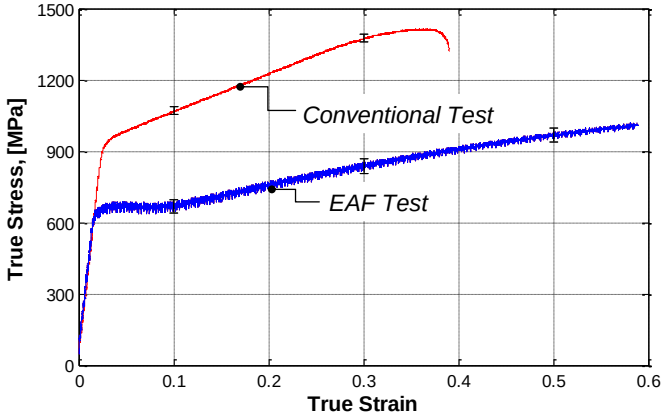

Figure 42. Flow stress reduction due to EAF (Ti-G5) [80]-[82]. The flow stress was reduced to EAF, and the specimen was able to be completely formed to the desired length without failure, unlike with the conventionally formed test.

Although the displacement varies linearly in time due to a constant die speed, the force for the EAF test showed some variation ('noise'). The frequency analysis of the data indicated a frequency response at ~22.29 Hz and its multiples for G2, and 1.02 Hz and its multiples for G5, which are not found in the conventional tests. The behavior observed may be due to a cyclic softening/hardening phenomenon present during EAF. It is hypothesized that the input of electric energy may result in alternating of electroplastic softening of the material (thus reduction in the forming load), and hardening of the material due to deformation (thus increase in load). This effect is discussed in further detail in section *9.4: EEC Frequency Analysis*.

Model Prediction and Experiments

When the electric current passes through a metallic workpiece, heat is generated and the temperature of the part rises. For a better understanding of the electroplastic effect, the thermal aspect needs to be isolated. All Ti (grade 2 and 5) specimens used in this section were machined from the same 6.35mm-diameter rod of each respective material. Two types of tests were

performed in this section. While multiple tests were run for each set of conditions, only a single representative test is plotted for each condition, since all tests represented sufficient repeatability. First, deformation tests were run, where the specimens were deformed at a constant die speed of 12.7mm/min to deformation levels L_1 or L_2. For EAF deformation tests, 300 Amps was the only current used (note that this current coupled with the cross-sectional area of the specimen produced a current density that was above the electrical threshold of $20A/mm^2$ for Ti [40]). Force and temperature profiles were created from these tests. Second, stationary tests were performed, where electricity was applied to a specimen at any deformation level (L_0, L_1, or L_2), without plastic deformation. Specifically, the dies were in contact with the specimen such to allow electricity to flow, but without causing plastic deformation in the sample. Thermal profiles were gathered from these tests and were used in comparison with each other and with the thermal profiles from the deformation tests, as will be shown in the following sections. The different test combinations and corresponding specifications can be seen in Table 4.

Table 4. Test combinations and specifications [80]-[82].

Ti Grade	Deformed/Stationary	EAF/Conv.	Displ.	Prev. Strucutre	% CW	Test Length (s)
2	Def.	EAF	L_0-L_2	As-Is	-	12
2	Def.	Conv.	L_0-L_2	As-Is	-	12
5	Def.	EAF	L_0-L_2	As-Is	-	12
5	Def.	Conv.	L_0-L_2	As-Is	-	12
2	Def.	EAF	L_1-L_2	Init. Def. to L_1	22	6
2	Def.	Conv.	L_1-L_2	Init. Def. to L_1	22	6
2	Def.	EAF	L_1-L_2	Init. mach. to L_1	-	6
2	Def.	Conv.	L_1-L_2	Init. mach. to L_1	-	6
2	Stationary	EAF	L_1	Init. Def. to L_1	22	12
2	Stationary	EAF	L_1	Init. mach. to L_1	-	12
2	Stationary	EAF	L_2	Init. Def. to L_2	44	12
2	Stationary	EAF	L_2	Init. mach. to L_2	-	12
5	Stationary	EAF	L_1	Init. Def. to L_1	22	12
5	Stationary	EAF	L_1	Init. mach. to L_1	-	12
5	Stationary	EAF	L_2	Init. Def. to L_2	44	12
5	Stationary	EAF	L_2	Init. mach. to L_2	-	12

The first step in the model prediction process is to compare the model to a simple stationary-electrical test, to isolate the resistive heating effects and validate that the heat transfer relationships within the model are correct. Figure 43 displays both an experimental test and the model output for a stationary-electrical test on Ti-G2. The model tends to slightly underestimate the temperatures in the middle of the test, but is accurate at the beginning and end of the test. Additionally, the heating profile of the model is slower than that of the experiments.

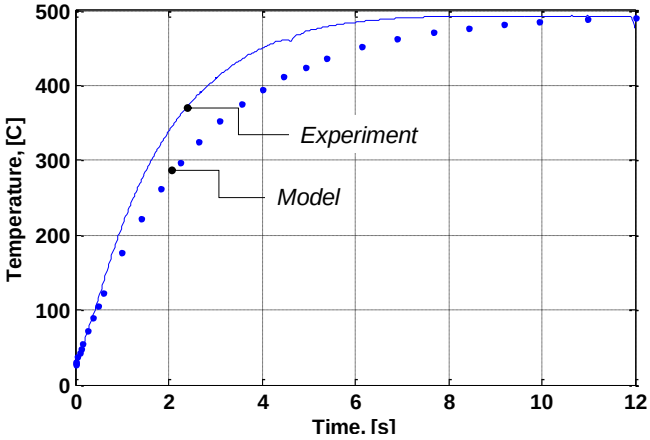

Figure 43. Stationary-electrical test at L0 (Ti-G2) [80], [82]. The model is predicting the temperature profile based solely on the assumption that all the applied electricity contributes towards resistive heating.

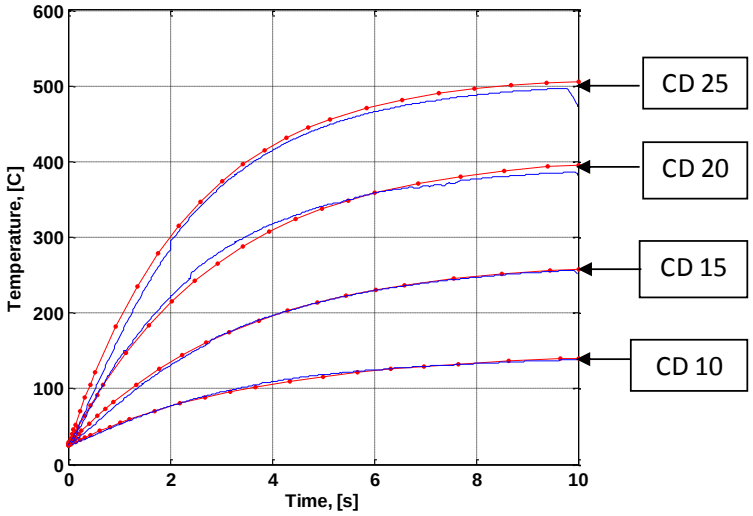

Figure 44. Stationary-electrical modeling tests at different starting current densities for 304SS. The resistive heating thermal model was tested on different materials with different starting current densities before integrating the effect of plastic deformation into the model.

Figure 43 shows the modeled thermal profile of a stationary-electrical test for only one specific starting current density. Please note that prior to incorporating plastic deformation into the model, the resistive heating-only model was verified at different starting current densities. Figure 44 shows the model results of four different starting current densities for 304SS. Now that

the model can effectively predict resistive heating effects, the effect of plastic deformation must now be included to represent an actual EAF test. The temperatures recorded are presented in Figure 45 for Ti-G2. The EAF deformation test is compared with the stationary tests for intermediate stages of deformation, *i.e.* 6sec for L_1 and 12sec for L_2 (the test durations are list in Table 4). The temperatures generated during stationary-electrical tests due to resistive heating are greater than the EAF deformation tests. The difference cannot be explained simply by the very small difference in the cross-sectional area (the machined specimens do not have barreling), but by the difference in the dislocation density. Moreover, during the EAF deformation test, a significant portion of the electric power goes toward assisting plastic deformation, rather than direct resistive heating. Knowing this, the EEC can be determined from the difference in thermal profiles of the model and experimental EAF tests, after deducting the temperature profile for the conventional forming test.

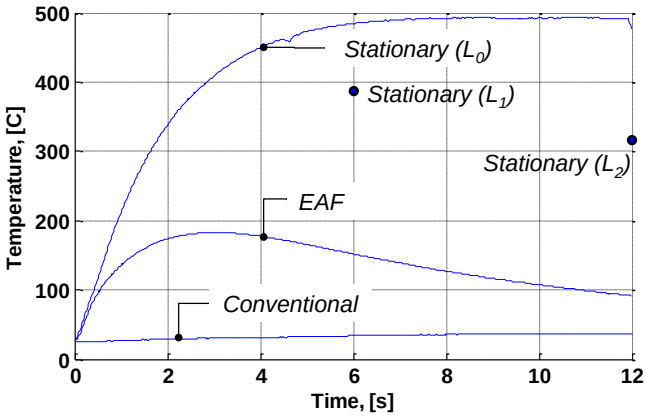

Figure 45. Temperature profiles (Ti-G2) [80]-[82]. The temperature profiles for a conventional compression, EAF compression, and stationary-electrical test are displayed. The maximum temperatures reached with stationary-electrical tests at L_1 and L_2 are designated by single points in the figure.

After experimenting with different EEC relations, the model and experimental EAF thermal profiles were matched using a power law function (eq.(25)) to represent the EEC, as shown in Figure 46.

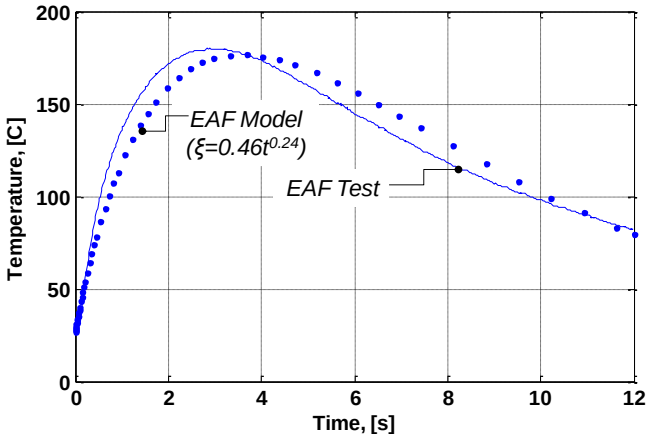

Figure 46. L_0 to L_2 model with EEC [80], [82]. The model's power law function was adjusted until the thermal model agreed with the corresponding experiments.

The same temperature model prediction process procedure was followed for Ti-G5. The model and experimental results for the stationary-electrical test are shown in Figure 47. For this test, a specimen machined to L_2 dimensions was used in the experiments. The model and experiments matched closer than for Ti-G2.

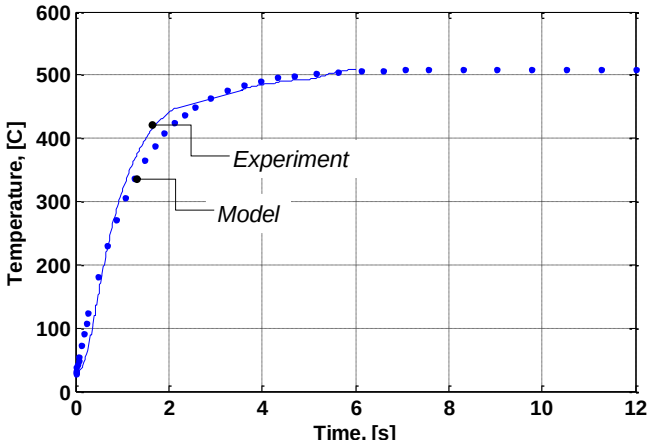

Figure 47. Stationary-electrical test at L_2 (Ti-G5) [80], [82]. The thermal model for a stationary-electrical test assumes that 100% of the applied electricity contributes towards resistive heating.

As was done for Ti-G2, an EEC function was developed to match the model and experimental EAF thermal profiles, shown in Figure 48. For this material, the model produced roughly the same peak temperature as the experiments, but the model showed a slightly slower heating profile, as was also seen for Ti-G2.

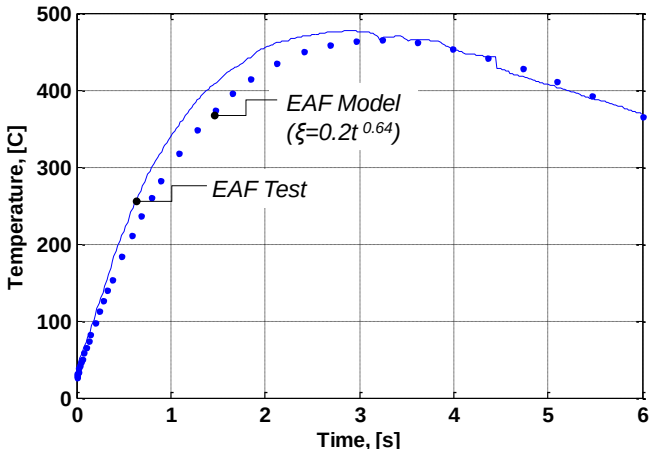

Figure 48. L_0 to L_1 EAF test with EEC contribution (Ti-G5) [80], [82]. The model profile was adjusted using a power law relation.

Figure 49 displays the EEC profiles for an EAF test from L_0 to L_2 (0s to 12s). Of note is that the Ti-G5 profile ends at 6s, while the Ti-G2 profile extends to 12s. This is because the Ti-G5 specimens failed after L_1 and were not able to be conventionally formed to L_2 without fracture. The coefficients were found to be non-linear, and were approximated using the power law.

From Figure 49, the EEC for each Ti-grade is different, due to differences in the electrical, thermal, and microstructure properties of the two materials. Specifically, the Ti-G2 EEC increased rapidly in the first few seconds of deformation, hence the larger ξ_0 value, whereas the Ti-G5 EEC increased more consistently throughout the length of the test, hence the larger *b*-value.

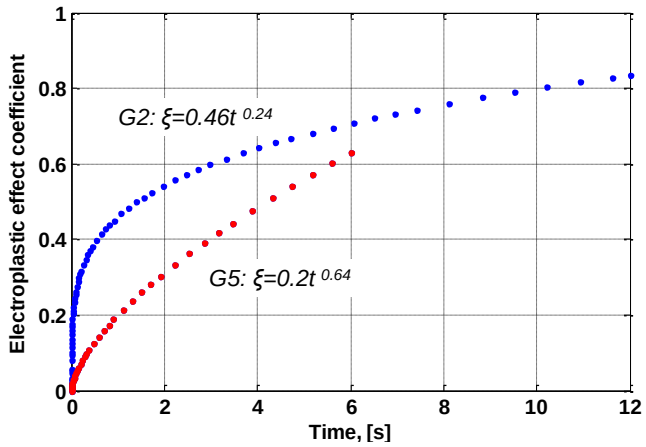

Figure 49. L_0 to L_2 EEC profiles (Ti-G2 and Ti-G5) [80], [82]. The different grades of titanium have different EEC profiles, where the Grade 2 metal has its EEC increase rapidly at the beginning of the test.

The difference between model predictions and experiments was computed, and the maximum and minimum differences as compared to the experimental measurements of the temperature are presented in Figure 50. For most of the tests, the model predicted the temperatures with less than 12% error, while one of the tests underestimated some of the values

with about -20%. Overall, the model predictions agree well with the measurements, but refinement will be needed for greater accuracy.

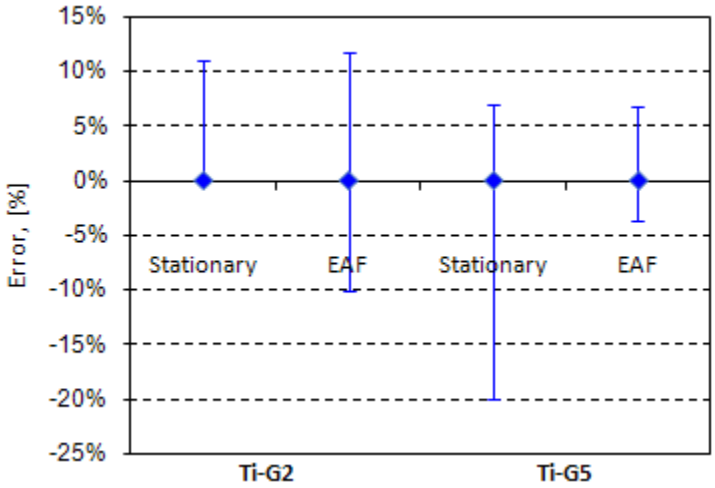

Figure 50. Percent error between model predictions and experiments [80], [82]. The magnitude of the percent error varied between the material type and the test type.

4.2.4. Thermal-Based EEC Conclusions

This chapter analyzed the thermo-mechanical aspects of the electroplastic effect. A thermal model, accounting for material properties specifically for titanium alloys various levels of plastic deformation, was verified using experimental EAF tests. The conclusions from this work are as follows:

- EAF reduced the flow stress in both Ti-G2 and Ti-G5. Although just one current was used, 300A DC, based on previous work, similar results are expected for different currents.
- To account for varying differences in thermal profiles between the conventional/EAF tests, a new electroplastic effect coefficient (EEC) was introduced, which was defined by a power law relation.

- The EEC's for the two Ti-grades were significantly different. This could be because the grades of titanium were different. Ti-G2 is a single phase polycrystalline material, and Ti-G5 is a dual-phase alpha-beta alloy. For Ti-G2, the electrons were able to travel easier because they only had to move through one phase. This can be seen by noticing the steeper and higher EEC for Ti-G2 compared to Ti-G5.

4.3. Comparison between the Different EEC Determination Approaches

Because each of the EEC-determination methods is essentially the inverse of the other (*i.e.* one is based off of the difference in mechanical power and the other is based off the difference in temperature), the resulting EEC profiles should be consistent. EEC profiles are calculated using both methods and then compared to each other [83]-[84].

4.3.1. Overview of Each EEC Determination Method

The first method for calculating the EEC is to utilize mechanical power profiles of the baseline and EAF tests. Figure 51 displays the power profiles for all of the current densities run at a die speed of 12.7mm/min. To generate the EEC profiles, the difference in power between the baseline and each respective EAF test will be normalized using the baseline power profile for a series of discrete times throughout each forming test. Of note is that, as the test time progresses, the difference between the baseline and EAF mechanical power profiles becomes greater. This is the inverse of what was seen when performing this same analysis on Ti-G2/G5 specimens, where the power difference decreased over the duration of the test [82]. The specific procedure to solve for the EEC using the mechanical method is:

- Run a conventional and an EAF compression test. Note that these tests need to be run at the same parameters (*i.e.* die speed, deformation stroke, initial pre-load, and starting

specimen size), with the exception of the applied current for the EAF test. It is also recommended to run up to three replicates of each test to verify that the results are repeatable (in the past, with the CU-ICAR testing setup, it was determined that these tests were repeatable such that one test could be used to represent the batch of tests at each particular setting.

- Plot the mechanical power vs. time profiles. In Figure 51, four different starting current densities were tested, therefore, four different sets of EAF tests and one set of conventional compression tests were needed to construct the profiles.
- Determine the difference between the two power profiles and normalize it with respect to the conventional forming power profile.

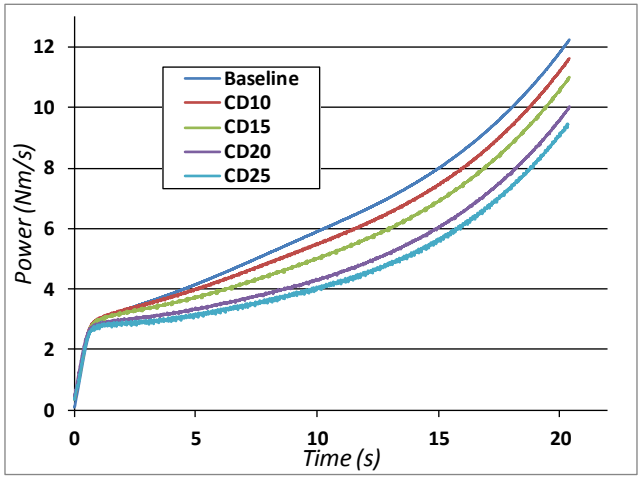

Figure 51. Mechanical power profiles (12.7mm/min) [83]. The mechanical power profiles decrease in magnitude as a higher current density is applied.

The second EEC-calculation method utilizes the stationary-electrical tests, the EAF model with no EEC, and the EAF model with the correct EEC, where all are shown in Figure 52. This is an opposing method compared to the previous method. Specifically, it is assumed that all

electrical effects provide mechanical deformation assistance or resistive heating. This method focuses on quantifying the resistive heating profiles of EAF tests, and then utilizes them to provide an EEC for the "useful" amount of applied electricity (*i.e.* amount that does not contribute towards resistive heating). The specific procedure to solve for the differences between the stationary-electrical test and the EAM test (*i.e.* to determine the EEC) are listed below:

1. Use the thermal model to predict the pure resistive heating profile (only heat transfer). - *Part a*
2. Plot the temperature profiles for a conventional compression test, an EAM test, and the model prediction assuming pure resistive heating. - *Part b*
3. Match the model thermal profile to the experimental EAM profile by estimating the EEC using a power law correlation. - *Part c*
4. The resulting EEC is a time-dependent variable that represents the efficiency of the electricity throughout the test. Therefore, the EEC is reported in this thesis as a function of time.

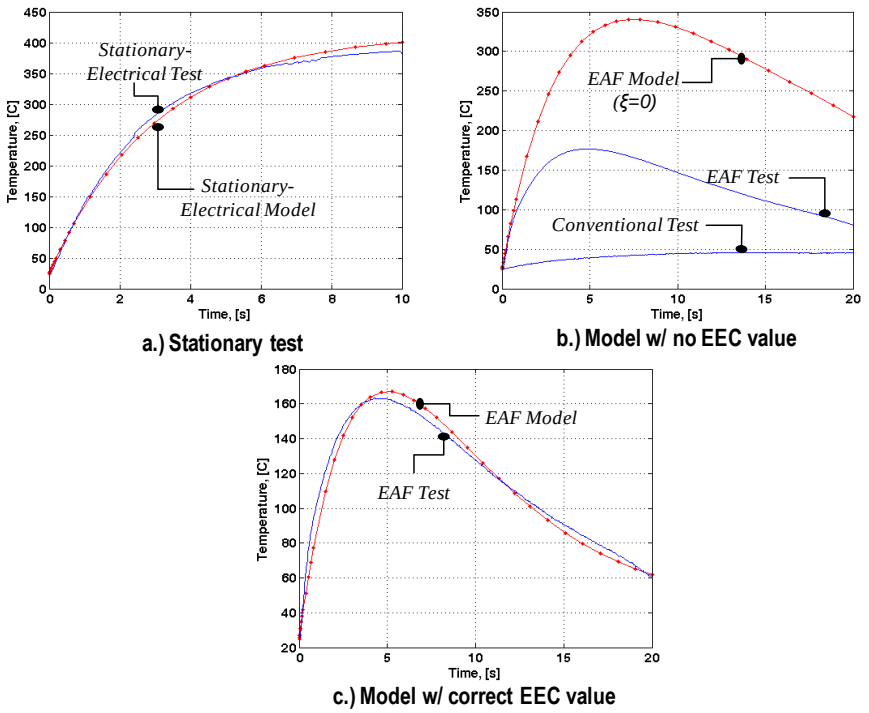

Figure 52. Thermal-based method (CD20, 12.7mm/min) [82]-[84]. The thermal-based method for determining the EEC consists of modifying the power law relation in the model to achieve satisfactory fit in accordance with the experiments.

4.3.2. SS304 Electroplastic Effect Coefficient Profiles

In this sub-section, EEC profiles derived from the previously-described mechanical and thermal methods will be described, and the effects of different die speeds will also be examined. Table 5 shows the different tests required to generate the EEC profiles using both of the methods. Specifically, there was a batch of conventional compression, and an EAF compression tests for each respective current density and die speed combination. In addition, there was a stationary-electrical test batch run for each respective current density. All tests are described in the table. Figure 53 and Figure 54 display mechanical and thermal EEC profiles for tests run at 12.7 and 25.4mm/min with starting current densities of 15 and 25A/mm^2. Because two different die speeds are analyzed in each figure (and the tests are different time lengths), the x-axis was chosen

to represent the percent of the compressive stroke completed rather than time, to allow for ease of comparison between all four tests.

Table 5. Deformed and stationary-electrical tests for determining EEC profiles for 304SS [83]-[84].

Deformed/Stationary	Conv./EAF	Current Density (A/mm^2)	Die Speed (mm/min)
Deformed	Conv.	-	12.7
Deformed	EAF	15	12.7
Deformed	EAF	25	12.7
Deformed	Conv.	-	25.4
Deformed	EAF	15	25.4
Deformed	EAF	25	25.4
Stationary	EAF	15	-
Stationary	EAF	25	-

In Figure 53, a starting current density of $15A/mm^2$ is explored. Please note that the x-axis on this figure and the following figure is in terms of "% Stroke Completed". This is due to the fact that there are two different deformation speeds and by using this unit for the x-axis, the EEC profiles for both speeds can be compared. The same EEC profiles are plotted as a function of time and as a function of strain in the appendix as Figure 195 to Figure 202. Since the EEC was determined to be time-dependent, the EEC vs. time graphs are shown in the appendix, such that they could be used in the future by other researchers if desired. From the figure, both methods of determining the EEC are extremely accurate with respect to each other, for both die speeds. The EEC profile for the slower die speed (12.7mm/min) is higher than the faster die speed profile after about 25% of the desired compressive stroke is completed. This can be expected, since previous works have proven the EAM technique to be strain rate dependent [46].

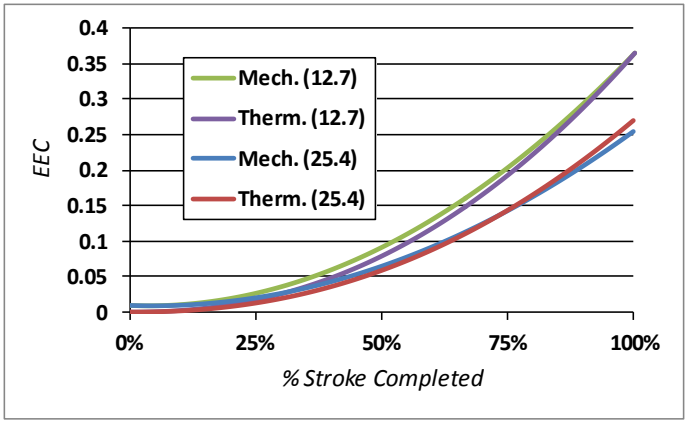

Figure 53. EEC profiles (CD15, 12.7 and 25.4 mm/min) [83]. The mechanical and thermal EEC profiles are similar for each respective speed. Additionally, the slower speed produced a higher EEC value at this particular current density.

The EEC's for a starting current density of 25A/mm^2 are shown in Figure 54. As was the case in Figure 53, both EEC-calculation methods are consistent throughout the entire compressive stroke for both die speeds. For the case of current density of 25A/mm^2, the EEC for the die speed of 25.4mm/min was on average 12% higher than for the case of 12.7mm/min, with a maximum difference of 17% at the end of stroke. Please understand that the EEC is not solely based on the reduction in mechanical power, but that it is determined from the power reduction with respect to the magnitude of electrical power input required to create that reduction. This will be discussed in further detail in sub-section *5.1.6: Electrical Efficiency Analysis*.

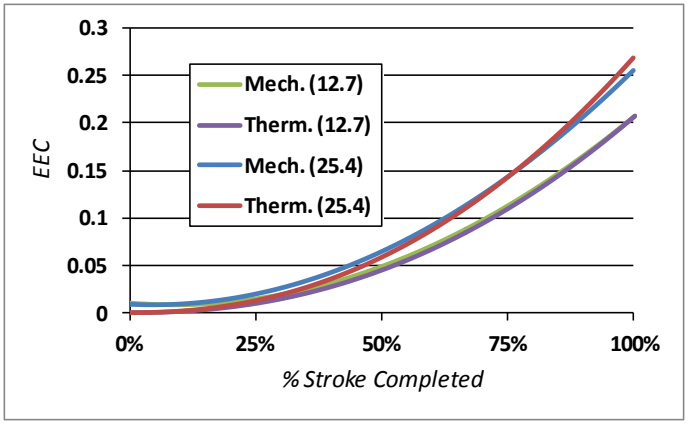

Figure 54. EEC profiles (CD25, 12.7 and 25.4 mm/min) [83]. The faster deformation speed produced a higher EEC value when coupled with this particular current density.

4.3.3. EEC Profile Conclusions

This chapter analyzed two methodologies for quantifying the Electroplastic Effect Coefficient. An experimental upper bound approach and a thermal analytical approach were utilized to determine the EEC profiles. The conclusions from this work are as follows:

- EAF reduced the flow stress in the 304 Stainless Steel specimens for both die speeds.
- The EEC profiles determined using both methods were consistent to each other throughout the entire stroke range for both die speeds.
- The mechanical-based approach to determining the EEC only required force vs. position data to generate the EEC's, whereas the thermal-based approach required there to be thermal data taken, which required the use of a thermal camera.
- The mechanical-based approach does not solely isolate the effects of thermal softening, since there will be some extent of thermal softening contributing to the mechanical power reduction of the EAF tests due to the increased temperature.

5. Simplified EAF Model (Task #4)

In this chapter the modeling strategy and different methods for determining EEC's is combined to produce a simplified EAF relationship model. This model predicts stress-strain profiles and will be compared to experimental conventional/EAF compression tests to verify accuracy. In addition to modeling an EA-Forging process, the same modeling strategy is employed to predict forming loads for an electrically-assisted bending (EA-Bending) process. It will be shown in this chapter that the same modeling strategy could also be implemented on other metal manufacturing processes as well.

5.1. EAF Forging Stress-Strain Model

In this section and proceeding sub-sections, an explanation of the simplified EAF forging model is described and compared to experimental results. Specifically, this section includes an overview of the simplified modeling strategy, an explanation of the experimental setup and procedures used to calibrate the model for accuracy, a discussion of the experimental/analytical results, an efficiency analysis comparing the magnitude of applied electrical power to the decreases in the forming stress, and finally conclusions on the EA-Forging model [85]. Within this document, the resulting stress-strain profiles, after the EEC values are fed into the thermo-mechanical model, and then will be displayed and explained. Additionally, the efficiency of applying electricity to the deformation process and the benefits gained will be explained.

5.1.1. Modeling Strategy Overview

The objective of Task #4 was to describe a hybrid thermo-mechanical modeling strategy and use it to effectively show stress-strain profiles for an electrically-assisted forming operation [83]. As part of the modeling strategy, an Electroplastic Effect Coefficient (EEC) was previously

created to represent the efficiency of the applied electricity (*i.e.* how much of the applied electrical power contributes towards plastic deformation vs. how much contributes towards resistive heating). Electrically-Assisted Forming (EAF) tests were performed on SS304 specimens, while varying the die speed and the starting current density (*i.e.* the current magnitude was held constant throughout each test, and density varied according to the instantaneous cross-sectional area). Throughout this thesis document, the phrase "current density" will be used. In all cases, the current density value will be based on the initial cross-sectional area of the specimen. As the part is deformed, the cross-section will increase. However, in this thesis, the current magnitude (*i.e.* the current selected at the beginning of the test in order to produce a particular starting current density) will remain constant throughout the test. This means that the current density will decrease as deformation takes place and the workpiece diameter increases. In the previous chapter, the results from these experiments were used to determine the EEC for Stainless Steel using the mechanical- and thermal-based approaches, and the results from both methods were compared. Now, the EEC's will be fed into a thermo-mechanical model in order to predict stress-strain profiles comparable to the experiments.

The hybrid modeling strategy introduced by Bunget et al. in 2010, accounts for the thermal, mechanical, and coupled thermo-mechanical aspects of the direct electrical effects witnessed during EAF [66]. Further, the EEC was conceptualized to quantify the "useable" direct electrical effects. The interrelations between the thermal and mechanical aspects of EAM, and how they relate to the workpiece temperature and force profiles are depicted in Figure 55.

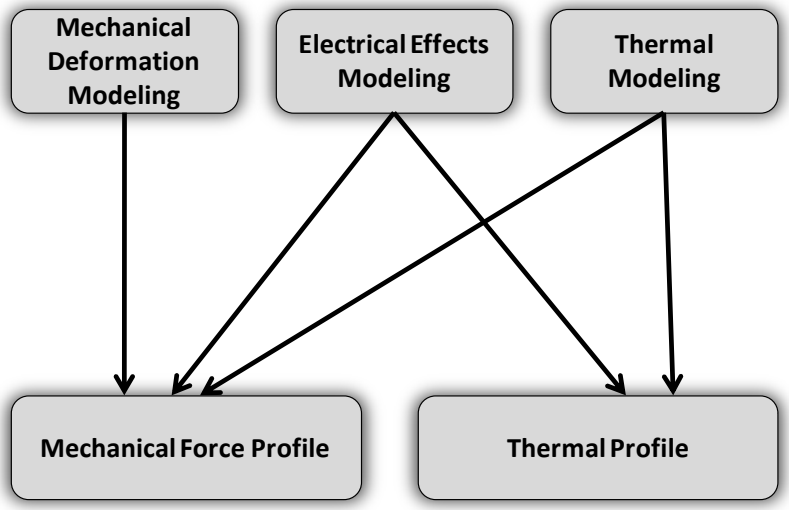

Figure 55. Coupled relations of EAM modeling. The following modeling aspects specifically contribute to the mechanical force profile, the thermal profile, or both. The candidate assumes that, from the entire amount of electricity applied to the process, a portion contributes towards plastic deformation, and the remainder contributes towards resistive heating, which increase the temperature of the part and also contributes towards thermal softening.

5.1.2. Coupled Thermo-Mechanical Modeling

As stated, the electroplastic effect is the fraction of electrical power imparted into the plastic deformation process, as shown below in eq.(27):

$$P_e = P_{heat} + P_{def} = \eta(1-\xi)VI + \eta\xi VI \qquad (27)$$

where P_e is the electric power (I·V), η is the efficiency, and ξ is the EEC [80]. P_{heat} represents the amount of electric power that will dissipate into heat through resistive heating of the workpiece. P_{def} is the magnitude of the reduction of the required mechanical power to deform, due to the total applied electrical power. Figure 56 shows that the magnitude of the thermal softening effect is highly dependent on the specific metal being formed, as well as the actual

temperatures reached during the manufacturing process. Of note, in the thermo-mechanical model, the material strength coefficient, $C(T)$ is adjusted to one constant value or to a temperature-dependent profile representative of the temperatures reached for specific EAF processes. As a result, the decrease in the force needed for the same deformation as in a conventional test, is controlled by two mechanisms: (i) thermal softening, thus lower flow stress, and (ii) facilitating deformation due to the energy provided by the electrons to the dislocations.

Within eqns.(28) and (29), the strength coefficient of the material is included in the mechanical modeling of the EAF technique. Figure 56 below shows the relationship between the strength and temperature for several metals that were tested with EAF throughout the research (Al6061-T6511, 304SS, and Ti-G5). From the figure, each metal's strength has a different response as temperature is increased. Additionally, there are temperature regions where the strength is unaffected by the change in temperature (*i.e.* 200°C to 400°C for Ti-G5), and other regions where the strength significantly decreases as temperature is increased (*i.e.* 150°C to 200°C for Al6061-T6511). With this said, the sole impact of increased temperature (without direct electrical effects) has the potential to have an impact on the overall mechanical profile of the process, depending highly on the material and specific temperatures reached during the process. However, the thermal effects on the mechanical profile are small compared to the direct electrical effects, as can be seen from the work by Ross et al. (Figure 14) [41]. Figure 45 also supports this claim. In this figure are the thermal profiles of a conventional compression test, an EAF compression test, and a stationary-electrical test on Ti-G2. The stationary-electrical test temperature was about 500°C (note that this could have been hotter but the maximum temperature for the thermal camera was 500°C), whereas the maximum temperature reached for the EAF compression test at the same settings was approximately 180°C. This difference of over two times between the temperatures shows that a large portion of the applied electrical power

contributed towards plastic deformation rather than towards heating. From the significant differences in the resistive heating model and isothermal experiments when compared to their respective EAF tests, it can be noted that the effect of thermal softening is minimal when evaluating EAF.

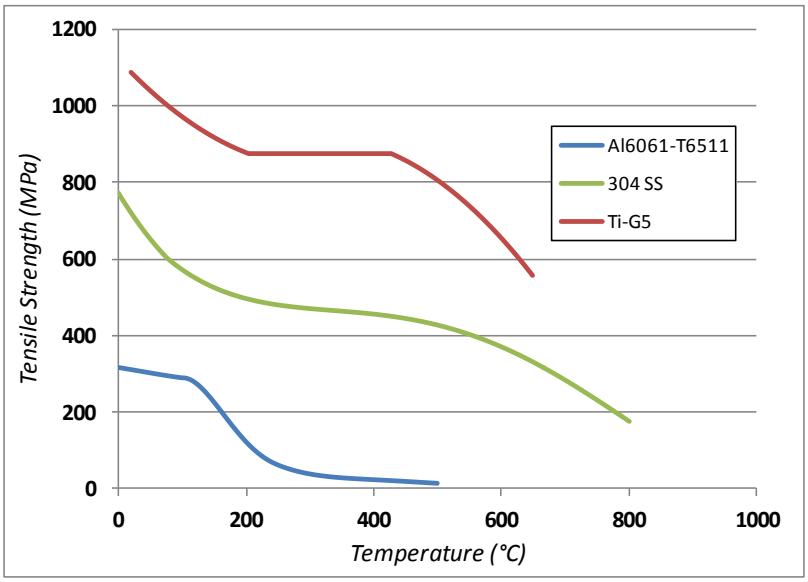

Figure 56. Tensile strength vs. temperature for various metals [86]-[88]. Tensile strength vs. temperature profiles show that the strength is reduced by different magnitudes as the temperature is increased for Al6061-T6511, 304SS, and Ti-G5.

Eqns.(28) and (29) are used for calculating the flow stress of a conventional and an EAF test, respectively.

$$\sigma_{conv} = C\varepsilon^{n}\left(1+\frac{2\mu r_o}{3h_{inst}}\right) = C\cdot\ln\left(\frac{h_{inst}}{h_o}\right)^{n}\cdot\left(1+\frac{2\mu r_o}{3h_{inst}}\right)\ [\text{MPa}] \qquad (28)$$

$$\sigma_{EAF} = C\varepsilon^{n}\left(1+\frac{2\mu r_o}{3h_{inst}}\right)-\left(\frac{\left(\frac{\eta\xi IV}{10^6}\right)}{\pi r_{inst}{}^2\dot{u}}\right) \text{ [MPa]} \quad (29)$$

where is C is the strength coefficient, ε is the material strain, n is the strain hardening exponent, μ is the friction coefficient, r_o is the starting specimen radius, h_o is the starting specimen height, h_{inst} is the instantaneous specimen height, ξ is the EEC, I is the electrical current, V is the electrical voltage, and $\dot{u}$ is the die speed.

5.1.3. Assumptions of the Thermo-Mechanical Model

The following are the major assumptions for the model (more general assumptions can be found in [66] and [80]):

- The material is homogeneous, isotropic, and the density is uniform throughout the specimen.
- The increase in temperature due to friction at the die/workpiece interfaces can be neglected.
- Barreling effect due to friction is neglected.
- Specific heat and resistivity are assumed constant with temperature.
- Conduction die length is estimated from thermal camera images.
- The workpiece and dies are divided into three Zones, as shown in Figure 57, where:
    - Zone 1 is equivalent to Zone 3.

- The real contact area $\leq$ 80% of the apparent contact area for Zones 1 and 3, and has a length of L_c which depends on the surface aspect (asperity peaks).
- The real contact area is equal to the apparent contact area in Zone 2.

- One voltage value is used in the thermal/mechanical calculations, but it is comprised of proportioned voltages from each zone (V_{z1}, V_{z2}, and V_{z3}), as shown below. The value used for L_c in eq.(30) was 1.27mm. This was about 20% of the total specimen height. This was an estimation based on the thermal videos, where excessive heating was apparent at these locations when electricity was applied.

$$V_{Total} = \left[\left(\frac{L_c}{L_{Total}}\right)\cdot V_{Z1}\right] + \left[\left(\frac{L_w}{L_{Total}}\right)\cdot V_{Z2}\right] + \left[\left(\frac{L_c}{L_{Total}}\right)\cdot V_{Z3}\right] \qquad (30)$$

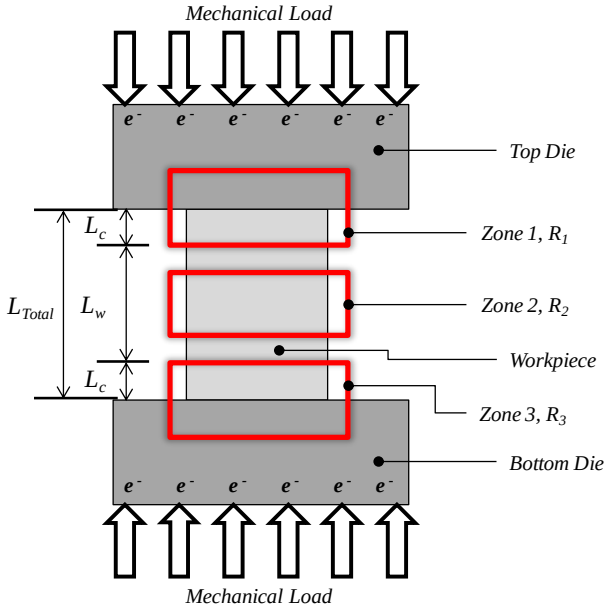

Figure 57. Die and workpiece zones [83]-[84]. The dies/workpiece were divided into three zones where the top and bottom zones accounted for contact area/interface obstacles, while the center zone did not.

Eq.(30) is a simplified approach to the more complicated problem of thermal contact resistance. In reality, Zones 1 and 3 are regions where the current flow between the dies and specimen is constricted to the narrow inter-metallic contacts. A thermal contact resistance calculation should include the resistance of the air pockets and the resistance of the asperity peaks of both surfaces in contact. Therefore the real contact area depends on the surface finish of the dies and the workpiece. During a stationary-electrical test, there is no significant change in the asperities aspect, while during the deformation process, the asperities are flattened to some extent, and thus the real contact area increases. The increase in contact area results in a decrease of the resistance of the zone, thus a decrease in voltage drop across the junction point. A more in-depth calculation of the real contact area and its influence can be done in future research.

The change in the real contact area can have an effect on the workpiece temperature profile throughout the EAF tests. Figure 58 displays representative temperature profiles along the longitudinal axis of the workpiece at the beginning and towards the end of an EAF test. Of note is that, at the beginning, where the real contact area is lower, the die/workpiece interfaces will be hottest, since the electrical power will be greatest at these points. Conversely, the center portion of the workpiece will be hottest at the end of the test, since the real contact area will be larger at the interfaces than at the beginning, thus lowering the electrical power. Figure 58 helps to illustrate this phenomenon. In this figure, there are two EAF tests: 1.) a test with sufficient contact (*i.e.* a large real contact area) and 2.) a test with partial contact (*i.e.* a small real contact area). The test with partial contact at a pre-load of about 670N shows a spike at the beginning of the test where the power at the die/workpiece interfaces is extremely high until sufficient pressure is applied to the part. The other thermal profile, where a much larger pre-load of about 1780N was used, did not show this thermal spiking phenomenon at the start of the electricity application.

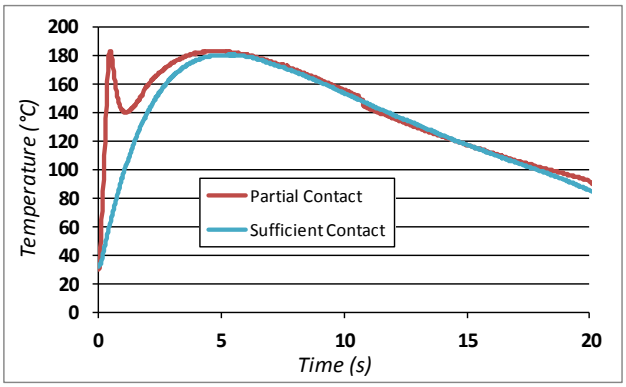

Figure 58. Thermal profiles for partial contact and sufficient contact between the dies and workpiece [83]. If there is not sufficient contact between the dies and the workpiece, then sparking could occur and generate steep spikes at the beginning of the thermal profile for that test.

5.1.4. Experimental Setup and Procedure

The experimental objectives of this portion of the research are to: 1.) compare and validate the thermo-mechanical model via comparing experimental results to modeling results, and 2.) discuss the efficiency of the EAF tests performed in relation to applied electrical power vs. stress reductions. This is approached through Design of Experiments testing using current density and die speed as the input variables, with flow stress per strain as the response. All specimens in this research were made from the same 4.61mm-diameter rod of 304 Stainless Steel. An EDM process was used to cut the specimens to a height of 7.154mm, and to maintain surface finish consistency.

Deformation and stationary-electrical tests were run as part of this work. The deformation tests were run at speeds of 12.7 and 25.4mm/min, coupled with starting current densities of 10, 15, 20, and 25A/mm^2. Further, stationary-electrical tests, where a small static load is applied to the specimen while an electrical current is applied, were also run at the same starting current densities as deformation tests. Three repetitions were run on all test configurations. Of note, is that all of these tests were consistent with each other, therefore only a

single test will be plotted which is representative of the three tests for each test combination. All experimental test combinations can be seen in Table 6.

Table 6. Test combinations [83].

Deformed/Stationary	Conv./EAF	Current Density (A/mm^2)	Die Speed (mm/min)
Deformed	Conv.	-	12.7
Deformed	EAF	10	12.7
Deformed	EAF	15	12.7
Deformed	EAF	20	12.7
Deformed	EAF	25	12.7
Deformed	Conv.	-	25.4
Deformed	EAF	15	25.4
Deformed	EAF	25	25.4
Stationary	EAF	10	-
Stationary	EAF	15	-
Stationary	EAF	20	-
Stationary	EAF	25	-

Figure 59 displays the experimental setup for both the deformation and stationary-electrical testing (specimen area is magnified in the upper-left corner of figure). An Instron Model 1332 hydraulic testing machine was used to compress the specimens at the desired die speeds. Machined, hardened, and insulated dies, made from A2 tool steel, were fitted to the Instron machine (insulation was used to isolate the electricity from the test machine). For thermal measurements, a FLIR A40M thermal camera, with a temperature capacity of 550°C and a resolution of 0.1°C, was utilized. All force and position data was gathered using an Instron on-board data acquisition system.

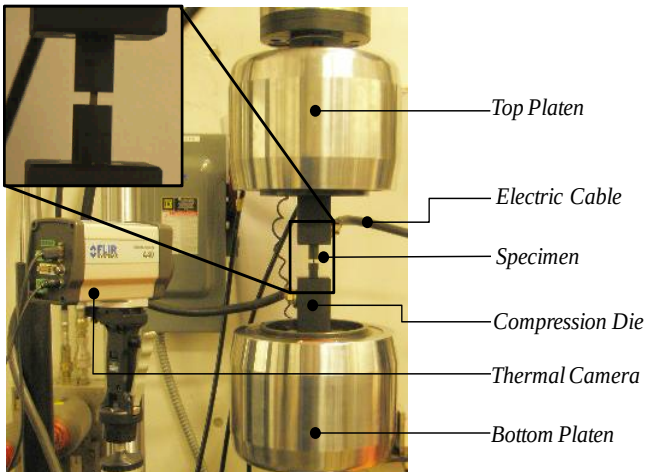

Figure 59. Experimental test setup [83]-[84]. The close-up view of the dies and specimen are shown in the top left-hand corner.

5.1.5. Experimental and Modeling Results

This section contains two sub-sections. First, several stress-strain profiles will be shown (conventional and EAF) to illustrate that the various test parameters are indeed in the electroplastic region, where formability improvements are apparent. Second, the EEC profiles, obtained using both methodologies, will be compared to each other.

Force Reduction due to EAF

Figure 60 and Figure 61 display the stress-strain profiles of baseline and EAF tests run at die speeds of 12.7mm/min and 25.4mm/min, respectively. In both figures, when a higher current density is applied, the reduction in material flow stress becomes greater. Of note is that, irrespective of the die speed, the 25A/mm^2 EAF test reduced the overall flow stress compared to the baseline test by approximately 30% in both cases. This significant reduction in flow stress signifies that the electrical parameters which were run were well within the "electroplastic region" with respect to this particular material. Additionally, when comparing these results with results from [40], where the same metal composition was tested with EAF, the same general

trends were witnessed. Additionally, from both figures, it can be seen that the baseline tests for 12.7 and 25.4mm/min die speeds are very similar, with the 25.4mm/min die speed producing only a slightly higher stress-strain profile. To this end, the strain rate sensitivity of this material was minimal when conventionally formed at the two die speeds tested. However, the behavior is unknown at higher die speeds.

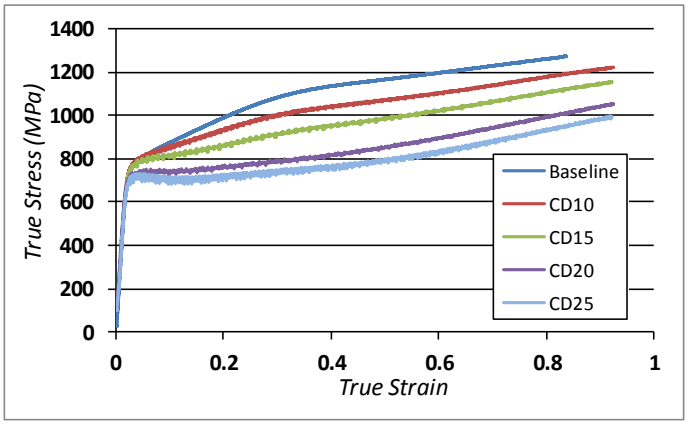

Figure 60. EAF flow stress reduction (12.7mm/min) [83]. The reduction in flow stress is proportional the magnitude of the applied electricity, as is also the case for the slower die speed in Figure 60.

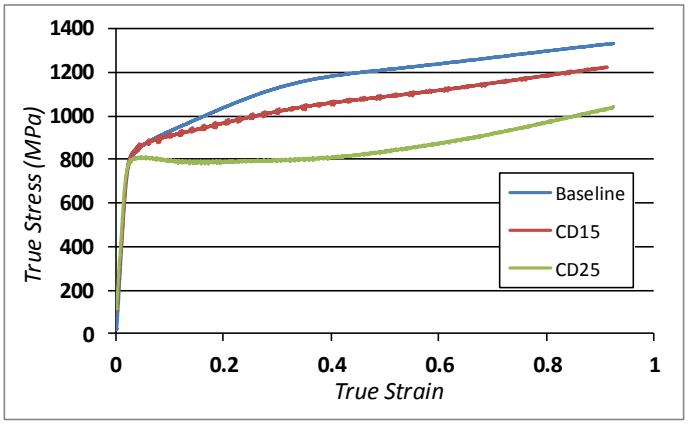

Figure 61. EAF flow stress reduction (25.4mm/min) [83]. The flow stress reductions are still related to the amount of applied electricity.

Experimental vs. Modeling Stress-Strain Results

The EEC profiles that were determined are fed into eqns.(28) and (29) to generate a corresponding stress-strain profile. This predicted stress-strain profile can then be compared to the experimental stress-strain profile for each current density/die speed combination. Of note is that the EEC profiles determined from the thermal method will be used to generate the EAF stress-strain profiles (since they are very similar for all tests, the thermally-derived EEC profiles can be used to represent both profiles).

Figure 62 displays the experimental and analytical stress-strain profiles for the baseline test and EAF tests ($10A/mm^2$ and $20A/mm^2$) for a die speed of 12.7mm/min. The modeled profiles (shown with dashed lines) predict a slightly lower overall stress-strain profile, when compared to the experimental profiles. However, the predicted profiles are within 10% of the experimental results. Additionally, the model at a current density of $20A/mm^2$ was even able to predict some strain-weakening at strains between 0.2 and 0.4.

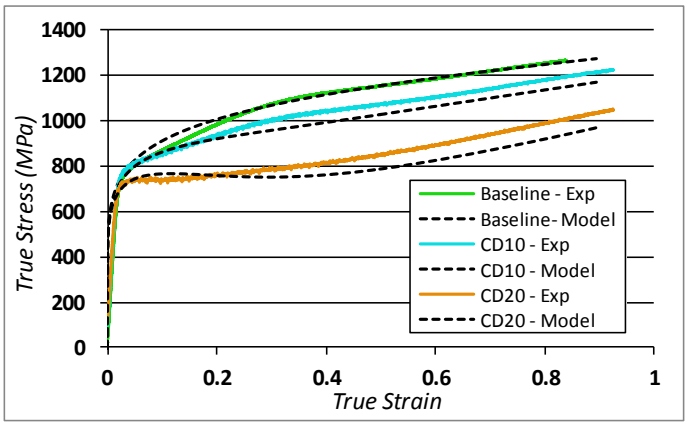

Figure 62. Flow stress model (12.7 mm/min) [83]. The model and experiments generally agree for all of the tests, with a percent error of less than 10%.

Predicted and experimental stress-strain profiles for a baseline test and an EAF test at $25A/mm^2$, for a die speed of 25.4mm/min, are shown in Figure 63. From the figure, the model is

able to predict the general stress-strain profile of the EAF test, but not to the degree of accuracy as with the slower die speed tests in Figure 62. Additionally, the predicted profile shows an overall higher stress-strain profile compared to experiments. Also, the model did not predict as much strain-weakening as the experimental test at 25A/mm^2. Nevertheless, the model is still within 20% accuracy compared to experimental results throughout the entire strain range.

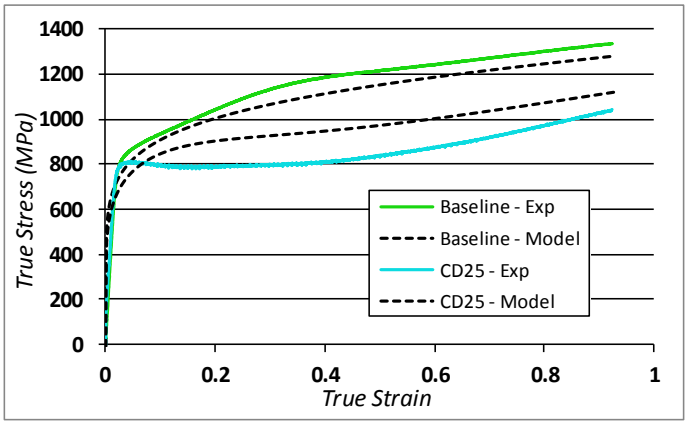

Figure 63. Flow stress model (25.4mm/min) [83]. The model is not able to predict the strain weakening to the same extent as the experiments, but to within a percent error of about 20%.

5.1.6. Electrical Efficiency Analysis

Within this sub-section, the efficiency of the EAM tests run and how the EEC can be interpreted, are discussed [83]-[84]. As previously mentioned, the EEC represents the efficiency of the applied electrical power on the manufacturing process. To this end, the magnitude of the EEC profile is determined on the effect that the applied electrical power has, and not just on the amount of applied electrical power. More specifically, if excess electrical power is added to the process and it cannot be utilized for plastic deformation assistance, it will contribute only to resistive heating, and will result in a lower EEC.

Figure 64 displays EEC-values at 50% and 100% of the total compressive stroke for both die speeds of 12.7 and 25.4mm/min, at the current densities tested for each die speed. The percent of the total compressive stroke was used instead of time such that the two different die speeds could be compared to each other. From the figure, for both die speeds, the EEC's were higher at 100% stroke compared to 50% stroke. This signifies that the efficiency of the applied electrical power (which is represented by the EEC) increases throughout the test and it increased at a higher rate with the slower die speed. With the EAM technique being strain rate sensitive, in this case the slower die speed may have allowed for the applied electricity to continue improving the formability, whereas the faster die speed did not allow for that.

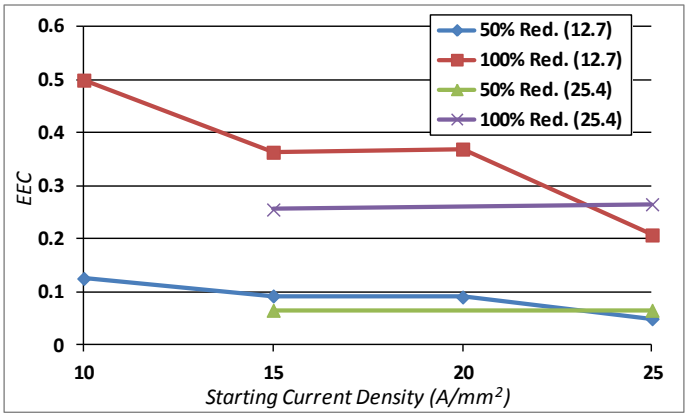

Figure 64. EEC efficiency comparison [83]. The EEC values associated to the lower die speed are the greatest, except when coupled with the highest current density value.

Another notable factor is that the EEC-values for the 12.7mm/min die speed were consistently above the EEC-values for the 25.4mm/min die speed, except for the current density of 25A/mm^2. This supports the time-dependency of the EEC and signifies that a current density as high as 25A/mm^2 is not efficient with a slower die speed of 12.7mm/min because it provides excess electrical power to the system that cannot be utilized, and it results in more wasted electricity by way of heating. It is more efficient when coupled with a faster die speed of

25.4mm/min where a greater amount of the applied electrical power can be utilized, as shown by the higher EEC values in the figure at a current density of 25A/mm^2. A similar finding was determined from uniaxial EAF tension testing of Mg sheet metal specimens [43]. In previous EAF works, a threshold effect, by which significant formability improvements were witnessed above a particular current density, was discovered. This threshold appeared to be a function of die speed and current density magnitude. For the other three lower current densities (10, 15, and 20A/mm^2), the slower die speed allowed for more of the electrical power generated to be utilized compared to the faster die speed, hence the slower die speed produced greater EEC values than the faster die speeds for these current densities.

5.1.7. EAF Forging Model Conclusions

This section utilized EEC profiles, which were determined from mechanical power profiles and thermal profiles, and utilized them to construct stress-strain profiles of the EA-Forging process. The conclusions are as follows:

- The thermo-mechanical model predicted the stress-strain profiles to within 20% of experimental results.
- The model was more accurate with the slower die speed.
- The contribution that thermal softening had on reducing the mechanical profile of the process was dependent on the specific material (since each metal has a different strength vs. temperature relationship) and the specific temperatures reached during the EAF process.
- Factors such as die speed and current density significantly affect the efficiency of the EAM technique. The concept was highlighted in the previous experimental work for

tensile processes. This particular section shows that the current density and die speeds also need to be "balanced" in order to optimize results in compression as well.

5.2. EA-Bending Model

The EAM modeling strategy employed in *Chapters 3 and 4* can be applied to other EAM-applicable processes than just forging. The following work presents how the same modeling approach was instituted to predict forming loads in an electrically-assisted bending (EA-Bending) process [89]-[90]. Within this section, an analysis of how to model an EA-Bending process will be explained, assumptions of the model will be provided, a classical bending process will be described, an analytical piece-wise model for EA-Bending will be presented, the solution schematic will be described, the experimental setup and procedure will be explained, thermal measurements for an EA-Bending process will be illustrated, the EA-Bending model will be validated using experiments, the effects of electricity on a bending process will be given, and conclusions will be summarized.

The overall objective of this section is to establish a closed-form solution that describes the bending force specific to a certain deformation while pulsed current (not continuously applied) is applied through the dies to the workpiece. Since air bending is stretching the metal, the pulse electrical application technique will be used where the electricity is applied in pulses with a set duration and spaced over a given period of time. The model may be used for determination of the state of stress and strain during the deformation and its dependence on different parameters of the applied current (*e.g.* current density, pulse duration, and pulse period). The derivation begins by establishing equations for the effective stresses and strains acting on a plastically deformed sheet metal part in classical bending based on the first principle of mechanics. The material is assumed to follow the power law, $\bar{\sigma} = C\bar{\varepsilon}^{n}$ where $\bar{\sigma}$ is the flow

stress, C is the strength coefficient, $\bar{\varepsilon}$ is the effective strain, and n is the strain hardening exponent. The bending is assumed to be under plane strain conditions (no strain in the width direction), and a transverse force acts on the flat strip of sheet metal through the punch. The forces acting on the material are shown in Figure 66 and Figure 67. Using equilibrium of force and moments, the equations for bending force are established for the classical process, and the deformation energy can be computed.

Using this model as a starting point, the next step is to include the effects of the electrical current applied to the workpiece during the process: energy effect, expressed by the EEC, and temperature rise effect. The analytical model is validated via experiments for classical (non-electrical) and electrically-assisted (EA) bending tests run on 304 Stainless Steel sheet specimens. The effects of the electric current applied on the bending forces and springback reduction achieved are also investigated experimentally for different electrical parameters (*i.e.* current density, pulse frequency, and pulse duration). It is expected that both, model predictions and experiments, will bring a better understanding of the electroplastic deformation mechanism in general, and of EA-Bending in particular.

5.2.1. Analysis of an EA-Bending Process

Due to the punch motion, the geometry, the bending moments, and force directions change continuously; thus the bending is a non-steady state process and the stresses and strains on the material change. At the beginning of the process, the deformation is elastic. As the punch advances, the stresses in the outer fiber at mid-span increase and exceed the elastic limit, thus the plastic deformation starts and propagates toward the inner fiber and into the rest of the material. The punch motion and the amount of material springback will dictate the final bending angle.

In an electrically-assisted test, a power source provides electricity and the current flows through the dies. Figure 65 shows an experimental schematic of an EA bending test. Insulation is placed between the dies and machinery to restrict the flow of the electricity to the workpiece to assist in deformation.

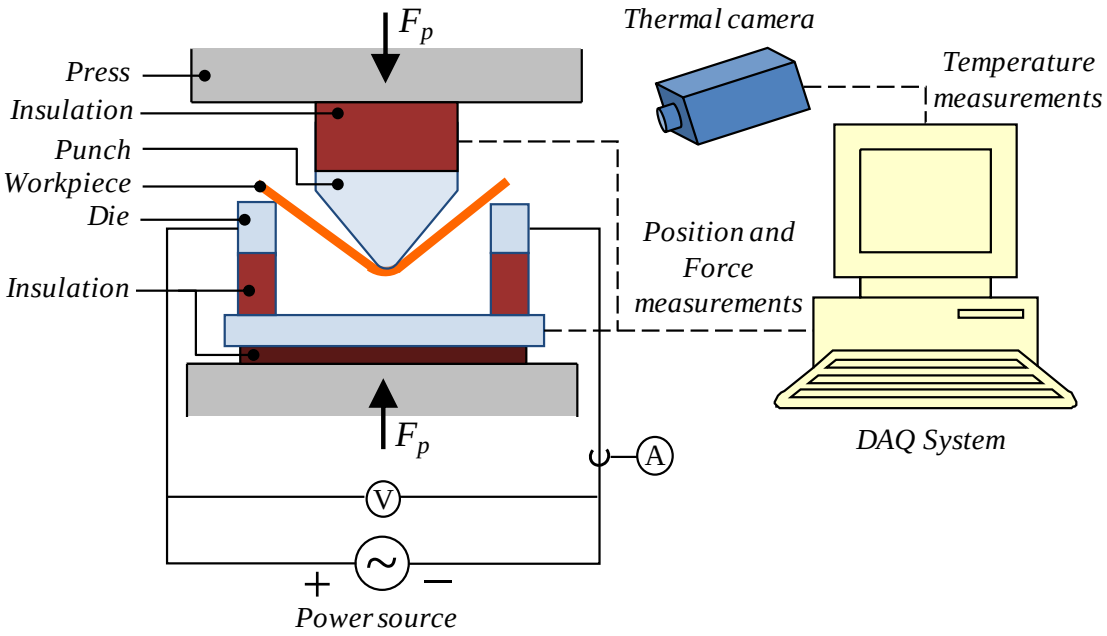

Figure 65. Schematic of an EA-Bending test [89]-[90]. The setup consists of an insulated and adjustable bending die, along with insulation to protect the machinery from the electricity.

5.2.2. Assumptions of the EA-Bending Model

The following major simplifications and assumptions are used throughout the derivations in this study:

- The workpiece material is homogeneous and isotropic, and the thickness and width of the sheet are uniform. This is due to the fact that the sheet metal used for this research was in the annealed state.

- The width of the specimens is at least 10 times larger relative to the thickness, thus plane strain conditions exist.
- In the moment that plastic deformation starts, the elastic deformation is negligible and the power law is used for determining the flow stress of the material.
- The strip is subdivided into three sections: two linear and a circular section. The bending line is a circular arc with the same radius as the punch itself. The sections normal to the sheet surface are assumed to remain plane at all times.
- The friction at the workpiece/die interfaces follows Coulomb's friction law. The lubrication regime is assumed unaffected by the presence of electricity.
- The specific heat and resistivity of the material are assumed independent of temperature.
- The strain rate sensitivity is neglected since previous experimental investigations found that the temperature rise is not high enough for the process to be considered as hot forming.
- Volume constancy is valid throughout the deformation process, thus the change in sheet thickness during the bending process can be neglected.

5.2.3. Classical Bending Process (Force and Springback)

The geometry of the bending tooling and the coordinate system are shown in Figure 66. The model development starts with an analysis of the state of strain and stress in the bending zone under plane strain conditions, using the volume constancy assumption and flow rules. The width of the workpiece is assumed to not change, thus the strain in the *y*-direction is 0. The strains and stresses are given by eq.(31).

$$\varepsilon_x;\ \varepsilon_y = 0;\ \varepsilon_z = -\varepsilon_x,$$
$$\sigma_x;\ \sigma_y = \frac{\sigma_x}{2};\ \sigma_z = 0. \tag{31}$$

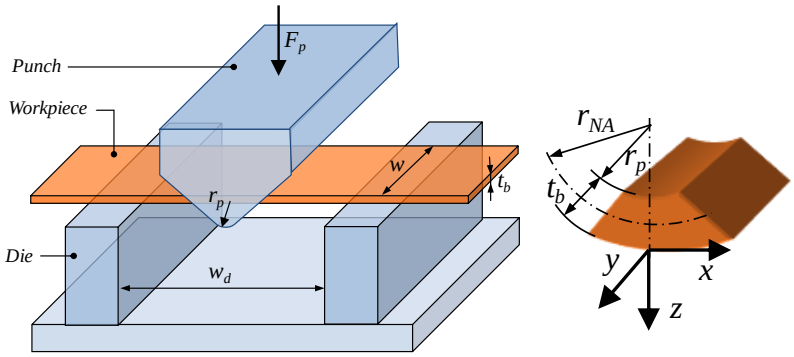

Figure 66. Geometry of an air bending test [89]-[90]. All of the notations that will be used in the following bending equations is provided in the figure.

The effective strain and stress are determined using von Misses yield criterion as given by eq.(32).

$$\bar{\varepsilon} = \frac{2}{\sqrt{3}}\varepsilon_x;\ \bar{\sigma} = \frac{\sqrt{3}}{2}\sigma_x. \tag{32}$$

The strain in the *x*-direction is solved by assuming the exact position of the neutral axis given by Hill et al., $r_{NA} = \sqrt{r_p\left(r_p + t_b\right)}$. Thus the strain can be computed using the engineering strain, given by the change in length of the outer fiber as compared to the neutral fiber [91]. Eqns.(33) and (34) give the strain in the outer fiber, where α is the bending angle.

$$e_x = \frac{(r_p + t_b)\alpha - r_{NA}\alpha}{r_{NA}\alpha} = \sqrt{1 + \frac{t_b}{r_p}} - 1;\ \varepsilon_x = \ln(1 + e_x). \tag{33}$$

$$\varepsilon_x = \ln\left(\sqrt{1+\frac{t_b}{r_p}}\right). \tag{34}$$

The entire section will be stressed, except for an elastic core near mid-plane, which will shrink in thickness as the deformation progresses. For this analysis, the elastic core is neglected after plastic deformation starts. Note that at the beginning of the deformation, elastic deformation based on Hooke's Law is considered. To calculate the bending moment needed to produce this bend, *M*, it is assumed that there is no net external force in the *x*-direction ($\sum F_x = 0$). However, the internal force, dF_x, acting on any incremental element of cross section, *wdz*, is $dF_x = \sigma_x w dz$. The contribution of this element to the bending moment is $dM = z dF_x = \sigma_x w z dz$. The total bending moment can be obtained by integrating from –*t*/2 to *t*/2, as shown in eq.(35). To facilitate the mathematical development, the material is assumed perfectly plastic $\left(\sigma_x = \pm\bar{\sigma}\right)$, and the flow stress is evaluated for the highest stress achieved in the bending process, which is the stress in the outer fiber [92]-[94].

$$M = \int_{-t/2}^{t/2} w\sigma_x z dz = \frac{1}{4}\bar{\sigma} w t_b^2 = \frac{1}{4} K w t_b^2 \left(\ln\left(\sqrt{1+\frac{t_b}{r_p}}\right)\right)^n . \tag{35}$$

The bending moment will be used further to determine the punch force, by employing equilibrium of moment and forces. Figure 67 presents the simplified model used in punch force analysis. The reaction force in the die shoulders and the friction force at the die/workpiece

interfaces are shown. The free body diagram summarizes the bending moment and forces acting on the linear zone. For simplification, it is assumed that the neutral axis does not change during the process, but it stays at the middle of the section.

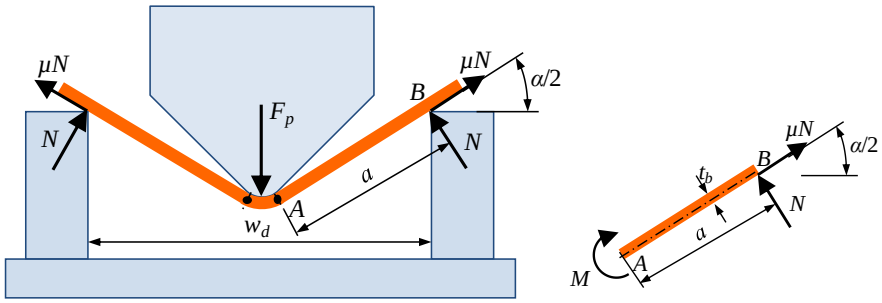

Figure 67. Simplified model for bending force analysis [89]-[90]. This simplified model figure displays the notations that will be used throughout the work.

The following eqns.(36)-(41) are derived from [93]. The equilibrium of forces in the vertical direction results in an expression of the normal force as a function of the punch force F_p, bending angle, α, and friction coefficient, μ (eq.(36)).

$$N = \frac{F_p}{2\left(\cos\frac{\alpha}{2} + \mu\sin\frac{\alpha}{2}\right)}. \tag{36}$$

The equilibrium of moments about point *A* leads to eq.(37).

$$N = \frac{M}{\mu\frac{t_b}{2} + a}. \tag{37}$$

The length of the arm, *a*, is determined geometrically using eq.(38).

$$a = \frac{w_d - 2(r_p + t_b)\sin\frac{\alpha}{2}}{2\cos\frac{\alpha}{2}} \tag{38}$$

After substituting eq.(38) into eq.(37), the resultant equation is combined with eq.(36), and the punch force is resolved as follows

$$F_p = \frac{4\cos\frac{\alpha}{2}\left(\cos\frac{\alpha}{2} + \mu\sin\frac{\alpha}{2}\right)}{\mu t_b \cos\frac{\alpha}{2} + w_d - 2(r_p + t_b)\sin\frac{\alpha}{2}} \cdot M. \tag{39}$$

Then eq.(34) is substituted into eq.(39). Thus, the bending force needed to deform the material to the bending angle α, and to overcome the friction at die/workpiece interfaces can be obtained from eq.(40).

$$F_p = K \cdot \frac{w t_b^2 \cos\frac{\alpha}{2}\left(\cos\frac{\alpha}{2} + \mu\sin\frac{\alpha}{2}\right)}{\mu t_b \cos\frac{\alpha}{2} + w_d - 2(r_p + t_b)\sin\frac{\alpha}{2}} \cdot \left(\ln\left(\sqrt{1 + \frac{t_b}{r_p}}\right)\right)^n. \tag{40}$$

Total power for plastic bending is derived mechanically as eq.(41):

$$J_m^* = F_p \dot{u} \tag{41}$$

where $\dot{u}$ is the velocity of the die/punch.

5.2.4. *Analytical Modeling of EA-Bending*

Previous research indicated that the application of electricity through a deforming workpiece results in reduced required flow stress to reach the same deformation as in the classical process. When analyzing an EAF process, two aspects have to be considered: (*i*) the applied electrical energy, and (*ii*) the electroplastic effect on the material behavior and on the energy efficiency of the process.

For this research, the electricity was applied in pulses, since constantly applied electricity would lead to negative effects because the cross-section of the specimen is decreasing over the test and therefore the current density is increasing. This phenomenon was discussed in *Ch.2: Previous EAM Experimental Work*. The pulse parameters that were varied during the tests are: current density, C_d, pulse duration, Δt, and pulse period, p (Figure 68).

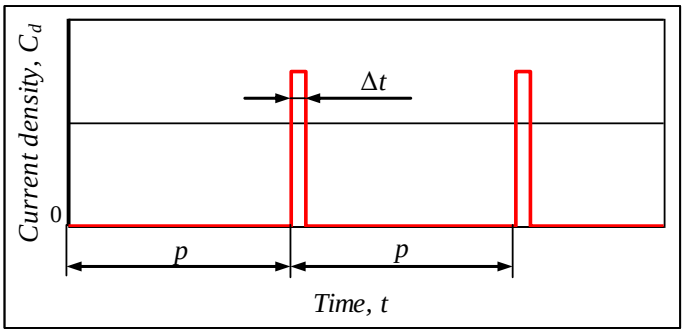

Figure 68. Electrical parameters varied [89]-[90]. The electrical parameters that can be varied are the current magnitude, the pulse duration, and the period between electrical pulses.

Energy Effect

When electricity is applied during plastic deformation, a part of the electrical energy is imparted into the mechanical deformation process. The total power consumed by the deformation process is given by eq.(42):

$$J_{total}^{*} = J_m^* + J_e^* = J_m^* + \xi P_e \qquad (42)$$

where J_m^* is the mechanical component related to the applied forming load applied and die velocity, J_e^* is the effective electric power that aids deformation, P_e is the electrical power ($I \bullet V$) passing through the workpiece, and ξ is the Electroplastic Effect Coefficient. The EEC depends on the material, applied current density, time and strain rate, and can be determined through tests. The remaining electric energy, $(1-\xi)P_e$, is converted into heat through resistive heating.

Temperature Rise Effect

The global heating from the electricity will result in some degree of thermal softening, thereby lowering the flow stress of the material and contributing to the decreased required work. At room temperature, the flow stress is given by the power law presented earlier, but as the temperature rises, the flow curve depends strongly on the temperature. The investigations conducted by previous researchers indicated that the temperature is lower than the temperature at which recovery and recrystallization take place, thus the strain rate dependency may be neglected, but the influence of the temperature on the strength of the material, given by the temperature-dependent coefficient function, *C(T)*, is still significant. The flow stress is given by equation in

eq.(43). The relationship between the strength of several lightweight metals (used in this thesis) and temperature is shown in Figure 56. As the strength coefficient is reduced as temperature is increased for all the metals, each metal has a specific strength-temperature relationship and has a specific temperature range where this relationship is most prevalent.

$$\bar{\sigma} = C(T)\bar{\varepsilon}^{n} \tag{43}$$

The temperature rise is obtained from the energy balance in eq.(44).

$$\frac{\partial \rho U}{\partial t} + \frac{\partial}{\partial x_j}\left(\dot{Q}_{conv} + \dot{Q}_{cond}\right) = Q_{rad} + Q_e \tag{44}$$

where $\frac{\partial \rho U}{\partial t}$ is the rate of change of the internal energy of the part, $\frac{\partial}{\partial x_j}\left(\dot{Q}_{conv} + \dot{Q}_{cond}\right)$ are the convective and conduction components of the heat flux, Q_{rad} is the radiative heat, and Q_e is heat generated in the part from the electric energy dissipated. Using constitutive equations for each component, the heat equation to be solved to determine the temperature rise for particular electric parameters is shown in eq.(45):

$$\rho V_v C_p \frac{\partial T}{\partial t} = -A_s[h(T - T_\infty)] - k(2A_d + A_p)\frac{\partial^2 T}{\partial x_j^2} - A_s \varepsilon \sigma_{SB}\left(T^4 - T_\infty^4\right) + VI, \tag{45}$$

where ρ is the density of the material, V_v is the volume of the part, C_p is the specific heat of the material, T is the temperature, t is time, A_s is the lateral surface of the part, h is the convection

heat transfer coefficient, T_∞ is the surrounding temperature, *k* is thermal conductivity for the die and punch material, A_d and A_p are the cross-sectional area of the dies and punch, x_j are coordinates, ε is radiative emissivity for the part, σ_{SB} is the Stefan-Boltzmann constant, *V* is the electric voltage, and *I* is the intensity of the current, given by the product of the current density and cross-sectional area.

After each pulse, when the current is not applied any longer, the temperature decreases and can be calculated from eq.(46):

$$\rho V_v C_p \frac{\partial T}{\partial t} = -A_s[h(T - T_\infty)] - k(2A_d + A_p)\frac{\partial^2 T}{\partial x_j^2} - A_s \varepsilon \sigma_{SB}\left(T^4 - T_\infty^4\right), \qquad (46)$$

which is obtained from eq.(45) after taking out the heat source.

Summary of Electrical Effects

The analytical model for electrically-assisted bending uses the energy-based approach to incorporate the effects of electricity on the bending force model from the classical bending process. The same punch displacement, *s*, and the same die velocity, $\dot{u}$, are considered for both classical and EA-Bending processes. It is assumed that the same total energy is required for deformation in both cases. Thus the force needed in the EAB process can be determined and compared with the force in the classical process. Using eq.(47) and eq.(48), a relation between the mechanical forces is obtained.

$$J^*_{classical} = J^*_{EAF} \qquad (47)$$

$$F_{p_{classical}}\dot{u} = F_{p_{EAF}}\dot{u} + \xi V C_d w t_b \tag{48}$$

where $F_{p_{classical}}$ is the mechanical load needed in classical bending, $F_{p_{EAF}}$ is the mechanical load required in the EAF process, V is the voltage applied, C_d is the current density, and wt_b is the cross-sectional area of the sheet. The difference in required force, as shown in eq.(49), depends on the material (*i.e.* EEC), dimensions of the workpiece, current density, and die velocity.

$$\Delta F_p = \frac{\xi V C_d w t_b}{\dot{u}} \tag{49}$$

A reduction in force can also be calculated as eq.(50):

$$F_{red} = \frac{\Delta F_p}{F_{p_{classical}}} = \frac{\xi V C_d w t_b}{\dot{u} F_{p_{classical}}} \tag{50}$$

Eqns.(40) and (45)-(50) constitute the analytical model for the forces required for electrically-assisted bending. Since the electricity will be pulsed, the model allowed the user to input the length of the pulses (pulse duration) and the time gap in between each successive pulse (pulse period). These two variables are also experimentally evaluated.

5.2.5. EA-Bending Solution Schematic

The analytical model is solved numerically by implementing a MATLAB program. The solution schematic is given in Figure 69. A stepwise approach is used; the position of the punch moves by an increment, *ds*. Since the velocity is constant, $\dot{u}$, a time increment is also computed,

dt. Because the electricity is pulsated, the model will alternate between classical and EAF bending equations. When the electricity is applied, the contribution of electrical energy to the deformation work is calculated, and the remaining electrical energy is converted to heat. The material workpiece temperature rise and subsequent effect on strength coefficient are derived. This is followed by a period of cooling down. The iteration continues until the desired bending angle is reached, which will correspond with a pre-imposed displacement of the die. The number of pulses is notated by *N*. The forming punch force is determined for each step and then compared to the classical process. Note that the same model can be used for the case when the same mechanical forming load is used, but the punch displacement is different, thus the bending angle differs between the classical and EAF process.

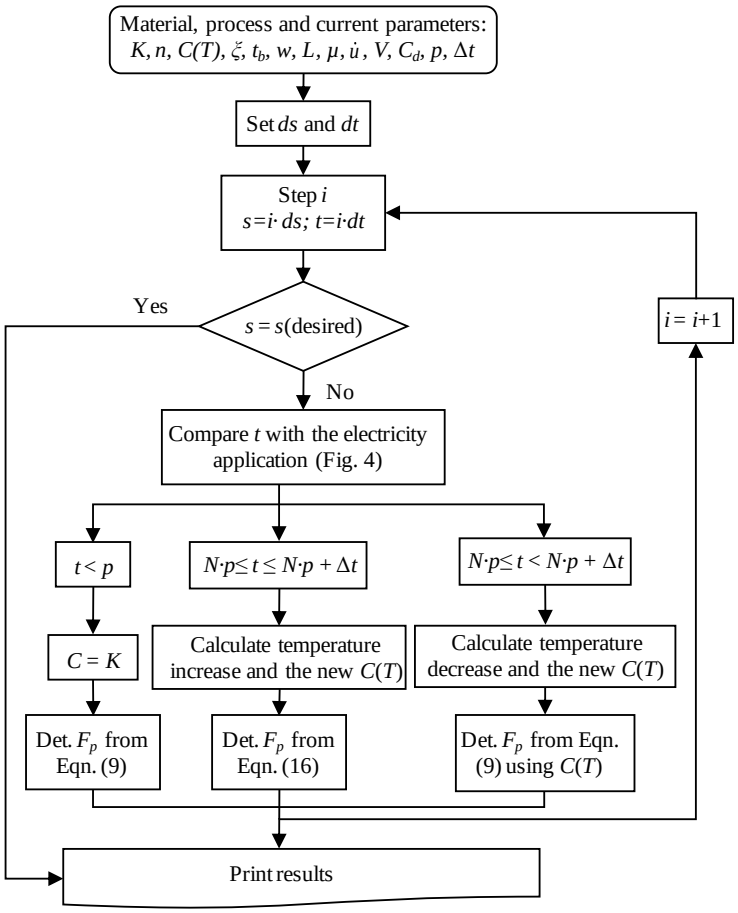

Figure 69. Solution scheme for solving the EA-Bending model [89]-[90]. A piece-wise approach was used to solve the EA-bending model. Specifically, the model switched from conventional bending to EA-bending when electrical pulses were applied.

5.2.6. Experimental Setup and Procedure

The experiments have two aims: (*i*) validate the analytical model, and (*ii*) investigate the effects of electricity in air bending. The aspects considered for evaluation and comparison are related to the bending load and the amount of springback after each test. The specimens used for this portion of the research were fabricated from a single sheet of 304 Stainless Steel. They were sheared into dimensions of 12.38mm wide x 0.864mm thick x 127mm long. All shearing was performed along the roll direction and care was taken when shearing to ensure dimensional repeatability (since any change in the cross-sectional area will affect the current density

(Amps/mm^2 or A/mm^2)). Specifically, a tolerance of +/-0.127mm was held while shearing. Four uni-axial tensile tests were performed and the material parameters were determined as being K = 1275 MPa and n = 0.51.

To fully examine the effects of electricity on an air bending process, many different parameters were explored, while holding others constant (Table 7). For all tests, a single displacement speed of 6.35mm/min and a constant displacement depth of 15mm were used. A variable bending fixture was used to test two different bending diameters (38.1mm and 50.8mm). Additionally, two current densities of 20A/mm^2 and 30A/mm^2 were tested. Preliminary testing resulted in the selections of these current densities since they were above the "electrical threshold" (*i.e*. the current density in which formability enhancement occurs). Pulse durations of 2s and 3s were tested in this work, since preliminary testing revealed that these durations were most beneficial. Pulse period (*i.e*. time in between electrical pulses) was also varied, and pulse periods of 60s, 30s, 20s, and 15s were tested.

Table 7. Testing parameters [89]-[90].

Parameters	Die Width	Current Density	Pulse Duration	Pulse Period
Values	38.1mm	20A/mm^2	2s	15s
				20s
	50.8mm	30A/mm^2	3s	30s
				60s

Experimental Setup

The testing setup can be seen in Figure 70. In the figure, a manually adjustable bending fixture is utilized to produce a variety of die widths. An insulated punch with a diameter of 15.9mm was fabricated. Electrical pulses were supplied to the bending fixture by a Lincoln R3R-500 constant current source welding unit. Beneath the bending fixture, a Sensotec 22,250N

capacity load cell with a signal conditioning box was used to record instantaneous bending force data. The resolution of this system was +/-4.45N, which was able to read the low bending forces as well as help illustrate the flow stress drop-offs due to application of the electricity. This instrument was used because the resolution of the load cell on the testing machine was too low to successfully recognize such low bending forces.

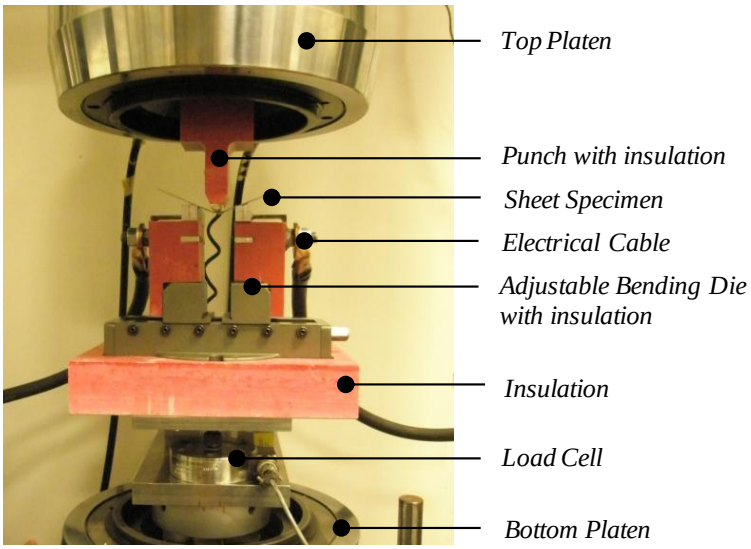

Figure 70. EA-Bending test setup [89]-[90]. The test setup consisted of fiberglass reinforced plastics for insulation.

Insulation was used in the construction of the bending fixture for two main reasons: (*i*) to ensure that all electricity flows through the sheet metal test specimens, and (*ii*) to prevent the high electrical current from harming any sensitive electronic devices. Fiberglass reinforced plastic was used for the insulating material, due to its strong/rigid compressive properties. This material was used in the construction of the punch (to prevent electricity from traveling into the Instron testing machine), was placed between the contact points and the bottom of the bending fixture, and was inserted between the bottom of the bending fixture and the load cell to ensure all components were completely isolated from electricity.

There were two possible configurations for placing the insulation and directing the electrical flow. The chosen configuration was to apply the electricity on one side of the bending fixture and have it travel through the specimen to the other side of the fixture. The top punch was completely insulated except for the tip. Another configuration could have been to apply the electricity through the top punch. In this case, the electricity enters the center of the specimen and then about half of the electricity flows through one side of the bending fixture and the other half flows through the other side. This configuration was not optimum in this case because now the electricity was flowing in parallel and the voltage was reduced by half.

When first testing the bending fixture, some fundamental design flaws were realized in the points of the fixture which contacted the sheet metal specimen and transmitted the electrical current into the specimen. Figure 71(a) shows the initial design of these components. Every time an electrical pulse was applied, the sheet specimen would weld itself to the fixture and this would ultimately increase the bending force after each electric pulse, until the small weld broke. This can be observed in the force/displacement plot. Careful evaluation revealed that the large radii on these contact points caused the line of contact between the fixture and the specimen to constantly move with bending displacement, and the relative velocity between the dies and the part is small. Due to the presence of asperities, until the contact is re-established, it is possible that gaps form, thus allowing for welding to occur. As a solution to this, a second design, with a very small radius, was tested. Because the radii on this design were much smaller, the contact point between the fixture and the specimen did not change as much. This design, coupled with a thin film of dielectric grease placed on the fixture contact points, primarily prevented any welding. The result is force/displacement profiles as seen in Figure 71(b), where the electricity lowers the bending force.

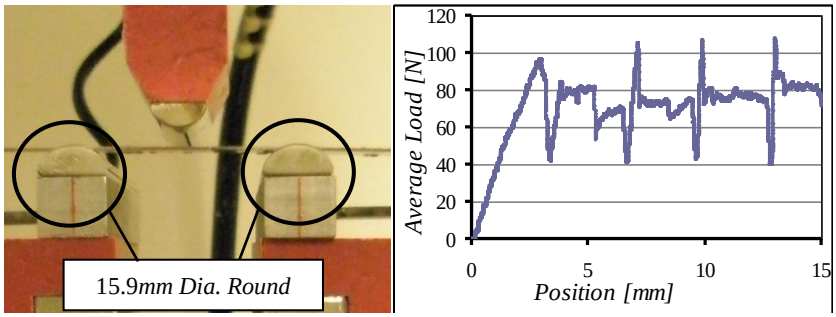

a.) Poor Design – Led to a varying contact point and welding

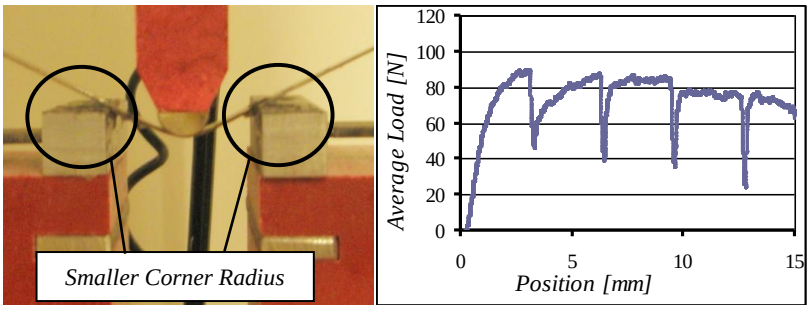

b.) Good Design – Led to a single contact point and no welding

Figure 71. Bending die design variants [89]-[90]. A bending die with rounded edges allowed for tiny micro-welds to form as deformation and electrical application took place. This caused steep spikes in the mechanical load profile. This was alleviated by using sharp edges.

Examples of classical and EA-Bending specimens for both die widths (38.1mm and 50.8mm) can be found in Figure 72. From the figure, one can notice the difference in springback (bend angle) between the classical and EA specimens. This will be quantified later.

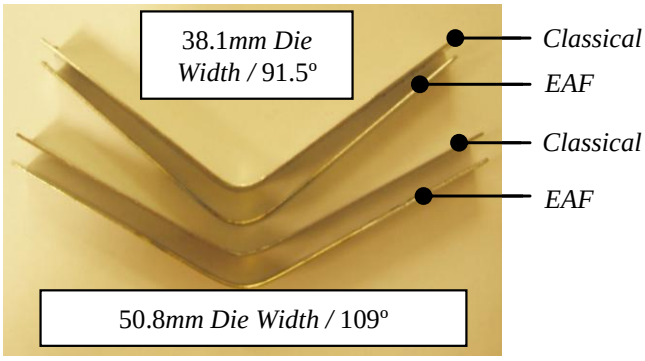

Figure 72. 304 SS Sheet bending specimens [89]-[90]. Sheet metal bending specimens are shown with two different die widths for classical and EA-bending tests.

5.2.7. Thermal Measurements in EA-Bending

An important aspect of modeling EA-Bending is the thermal/heat transfer of the process. To help quantify the magnitude of heating, Figure 73 displays thermal profiles that were recorded using a FLIR infrared camera, from the time when an electrical pulse was applied until the specimen temperature cooled significantly (note the thermal profiles are for a single pulse only). Holding the die width (50.8mm) and pulse duration (2s) constant, thermal profiles for current densities of 20 and 30A/mm^2 were produced. The three specimen locations where temperature was recorded were: (1) the die contact point (where electricity entered/exited the specimen), (2) a point between the punch interface and die contact point, and (3) the punch interface (*i.e.* the bending zone). The die contact point for the 20A/mm^2 test was almost 400°C, and this was due to the minor sparking due to the electricity entering the specimen here. The bending of the part takes place at the top punch/specimen interface, therefore the temperature in this region will be the temperature of the metal as it is being deformed. The most important location to monitor temperature is at the punch interface because this is where the actual bending takes place. The maximum temperatures in this region for the 20 and 30A/mm^2 tests were about 115°C and 335°C, respectively. The temperatures resulting from these different current densities were about 200°C apart. Additionally, for the 20A/mm^2 test, temperature profiles were considerably different for different locations on the specimens. This shows that, with a thin sheet metal part, an increase in applied electrical power could cause a large amount of global heating in the workpiece (as shown here where there was a 200°C difference from a 10A/mm^2 difference in starting current density. This also shows that heat transfer is an important aspect of a bending process, since there is not much contact between the punch/specimen or the bottom bending fixture/specimen.

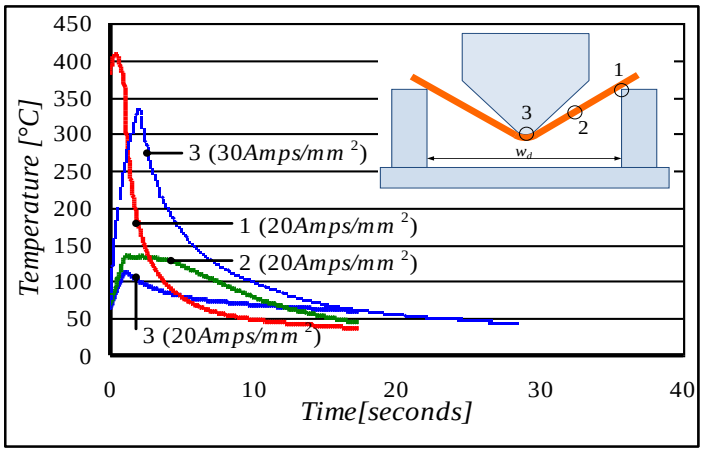

Figure 73. Temperature measurements for EA-Bending [89]-[90]. For a particular EA-bending test, the specimen is the hottest at location 1, and the coolest at location 3.

5.2.8. Validation of the Model via Experiments

The analytical model developed earlier was solved by following the solution scheme from Figure 69, and the bending force needed to reach a desired stroke or bending angle was determined. The model was initially solved for the classical bending case and its predictions were compared with experimental results for two different die widths (Figure 74). A friction coefficient of 0.25 was used, as recommended by previous research [93]. The predictions agree well for the two cases. The differences can be attributed to the simplifications and assumptions of the model.

Next, the model for electrically-assisted bending was solved and compared with experimental results for two current densities, 20 and 30 A/mm^2. The variation of the strength, C, with the temperature was determined by using the data from Figure 56 [88] and this was integrated into the model. The next step is to determine the Electroplastic Effect Coefficient (EEC). Average EEC values are taken from experimental results of previous research specific to the same material, die speed, and current density [40]. The coefficients were approximated as ξ = 0.18 for C_d = 20A/mm^2, and ξ = 0.35 for C_d = 30A/mm^2. For compression tests, the overall EEC profile with respect to time can be used, which is more accurate than an approximated EEC value.

However, in tension, the electricity is only applied for several seconds and an EEC profile as a function time was not able to be determined for this case. These values were included in the numerical solution. Figure 75 and Figure 76 compare the model prediction with experiments for current densities of 20 and 30A/mm^2 respectively, at a pulse duration of 2 sec, and a pulse period of 30 sec, for a die width of 38.1 mm.

It can be observed again that the predictions agreed well with the experimental results for both cases. The differences can be attributed to the simplifications and assumptions done in the model, but also to the approximation of the material strength, C, and Electroplastic Effect Coefficient, ξ. Future work should include refinement of the model to account for the factors that were neglected, *i.e*. the strain rate sensitivity, and also to conduct specific experiments targeting accurate measurements of material properties included in the analytical model.

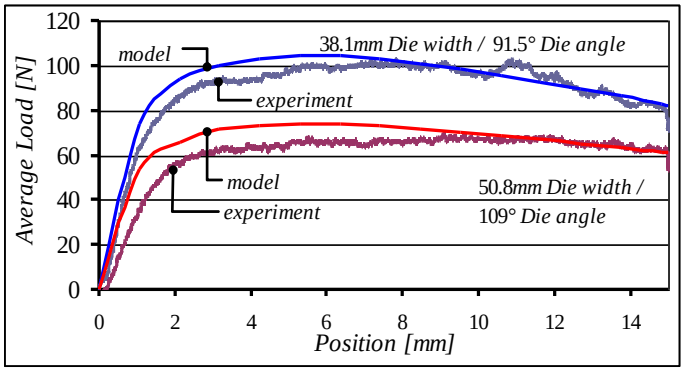

Figure 74. Model verification for the classical case [89]-[90]. The model and experimental profiles are shown for the case of classical bending for the two different die widths.

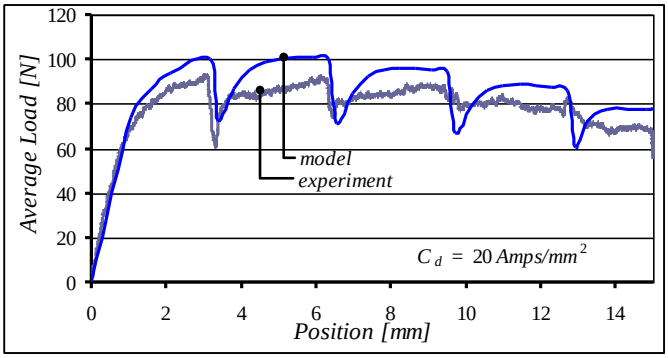

Figure 75. Model verification for EAB at CD=30A/mm^2 [89]-[90]. The piece-wise model for the 38.1mm-die width and a current density of 20A/mm^2.

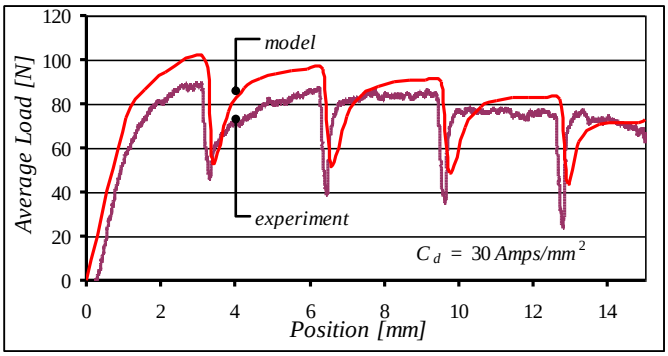

Figure 76. Model verification for EAB at CD=30A/mm^2 [89]-[90]. The piece-wise model for the 38.1mm-die width and a current density of 30A/mm^2.

5.2.9. Effects of Electricity in Bending

The aspects considered for evaluation and comparison were related to the bending load and amount of springback after testing. In the next subsections, bending load vs. position plots will be used to examine the effects of different pulsing parameters (current density, pulse duration, and pulse period), while changes in the bend angle will be used to quantify electricity's effectiveness at reducing springback.

Effect of Current Density

Figure 77 and Figure 78 display experimental EA-Bending tests and modeled load vs. position profiles in which die width, pulse duration, and pulse period are held constant while two different current densities of 20A/mm^2 and 30A/mm^2 are evaluated. Figure 77 is a plot of the specimens tested with a die width of 38.1mm and Figure 78 represents tests performed on a die which is 50.8mm wide. The pulse duration for both plots was 2s, and the pulse period was 30s.

It can be seen in both figures that the electric pulses resulted in instantaneous flow stress "drop-offs", which were proportional to the magnitude of the current density. Specifically, for the 38.1mm die width, the flow stress drop-off of the 30A/mm^2 test were up to four times greater than the 20A/mm^2 drop-offs. For the 50.8mm die width, the 20A/mm^2 drop-offs were more noticeable and the 30A/mm^2 drop-offs were only about twice as large. In Figure 77, the drop-offs for the 30A/mm^2 test were larger than those of the 20A/mm^2 test. However, the average bending load profile throughout the test remained relatively the same between the two current densities (note that the load profile was reduced by about 20N in comparison to the respective non-pulsed classical test). In Figure 78, the drop-offs were again more significant for the higher current density. The bending load profile produced from the 20A/mm^2 test showed no notable reduction compared to the respective classical test, whereas the 30A/mm^2 test posted a bending load profile that was about 15N lower than the conventional load profile. When comparing the two figures, the 38.1mm die width allowed for greater reductions in the load profile, where both current densities lowered the load profile by 20N. However, with the 50.8mm die width, there may be a type of threshold reached since the 20A/mm^2 profile was not reduced compared ot the conventional profile, but the 30A/mm^2 profile was reduced by about 15N.

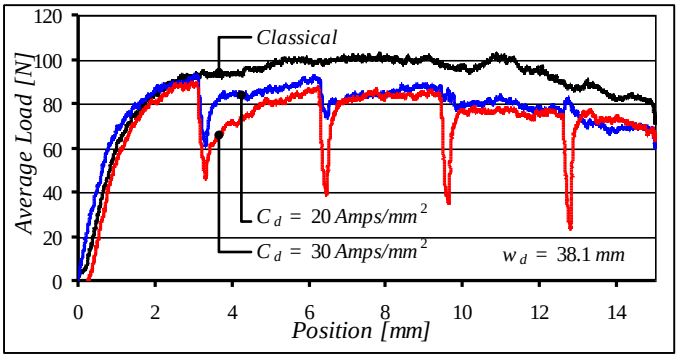

Figure 77. Forming load recorded for w_d=38.1mm [89]-[90]. Displayed are the forming loads for the classical and two EAB tests parameters at a die width of 38.1mm.

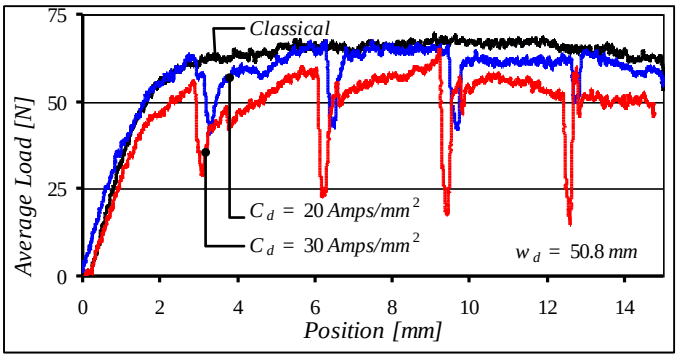

Figure 78. Forming load recorded for w_d=50.8mm [89]-[90]. Displayed are the forming loads for the classical and two EAB tests parameters at a die width of 50.8mm.

The amount of springback after the test, *SB*, was determined from eq.(51).

$$SB = \frac{\beta - \beta_r}{\beta} \cdot 100[\%] \qquad (51)$$

where β is the angle at which the specimen was bent (β = 180° - α), and β_r is the real angle, measured after the test. The application of electricity during the deformation process resulted in lower springback (up to about a 20% overall reduction in springback). However, the springback reduction magnitudes will be far less than those achieved by Green et al. because of

differences in when the electricity was actually applied [45]. Specifically, Green et al. applied the electricity via a single pulse for a specified pulse duration after deformation, but before removal from the die. This method is effective at eliminating a considerable amount of springback effects because deformation has already ceased and there will be no more dislocation pile-ups after the pulse is applied. Conversely, in this research, the electricity was applied during deformation. In this work, the formability increase due to electricity was the main objective to analyze, and the reduction in springback was a beneficial side effect.

Table 8 shows an overview of the EAF springback works by Green et. al. and Salandro et. al. Aside from the fact that Green et. al. applied the electrical pulse after deformation, there are also other differences. Specifically, the materials, the specimen dimensions, the bending diameters, and the electrical pulse parameters were different. The two different materials used have different thresholds, where the electricity begins to improve the formability ($60A/mm^2$ – Green, $18A/mm^2$ – Salandro) [40]. The specific goal of Green et. al.'s research was to determine parameters by which springback could be eliminated, however, the research by Salandro et. al. examined springback as a side effect to the applied electricity that reduced the bending forces. When applying the electricity during deformation, the electrical application parameters (current density, duration, and period) become important, since deformation will continue. For example, if a pulse period is spaced such that the last pulse is right at the end of deformation, then it will have a greater impact on springback than a pulse period that allowed for a given amount of deformation after the last pulse. To this end, it is hard to directly compare both of the works. However, both works show that applied electricity has an effect on reducing the springback in formed parts.

Table 8. EAF application parameters and resulting springback effects [45], [89]-[90].

Researcher	Matl.	Specimen Dims. (mm)	Bending Dia. (mm)	Electrical Application Descriptions	Results
Green et al.	Al 6111	250 x 3750 x 0.91	101.6	• A single electrical pulse was applied after deformation • Single pulse duration of 1.5s • Current densities of 70A/mm^2 - 135A/mm^2	• Springback completely eliminated with a 1.5s pulse at 120A/mm^2
Salandro et al.	304 SS	12.38 x 127 x 0.864	38.1 and 50.8	• multiple electrical pulses applied over distinct periods during deformation	• 27% springback red. (see CD sub-section)
				• Two current densities (20A/mm^2 and 30A/mm^2)	• 80% springback red. (see pulse duration sub-section)
				• Two pulse durations (2s and 3s)	• 50% springback red. (see pulse period sub-section)
				• Four pulse periods (15s, 20s, 30s, 60s)	

In order to have a better evaluation of the effect of electricity, a springback reduction was computed by comparing the EAB tests with the classical test (or C_d = 0A/mm^2), as shown in eq.(52).

$$Red_{SB} = \frac{SB_{classical} - SB_{EAF}}{SB_{classical}} \cdot 100[\%] \qquad (52)$$

Figure 79 displays the percent of springback that is still in the sheet specimens after bending, for both die widths, pulse duration of 2s, a pulse period of 30s, and current densities from 0 to 30A/mm^2. From this, it can be seen that the percent of springback in the specimens is reduced from application of current during deformation. Also, when just focusing on the tests run at 0A/mm^2 (classical tests), the die width plays a notable role in the amount of springback in the part. Specifically, a die width of 38.1mm results in about 14% of springback in the part, while a die width of 50.8mm results in about 12% springback. Figure 80 still represents the same tests as in Figure 79, but now presents them in terms of the percent of springback reduction (or how much springback was removed from the parts compared to the springback in the respective classical tests). This figure also confirms that, as current density is increased, the percent reduction of

springback will also increase. Further, a smaller die width will help to amplify the springback reduction.

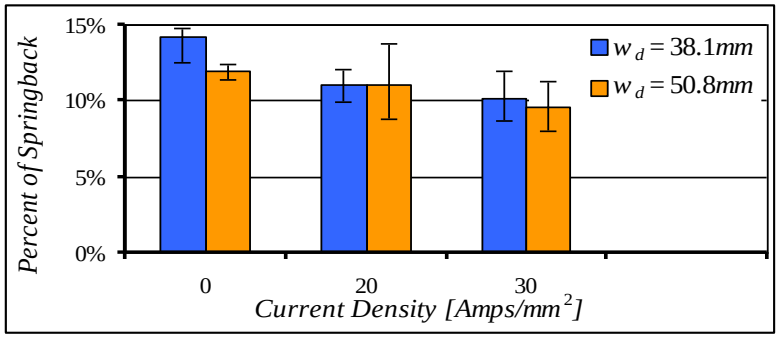

Figure 79. Recorded springback [89]-[90]. Percent of springback recorded for a classical bending test and for the different EAB tests.

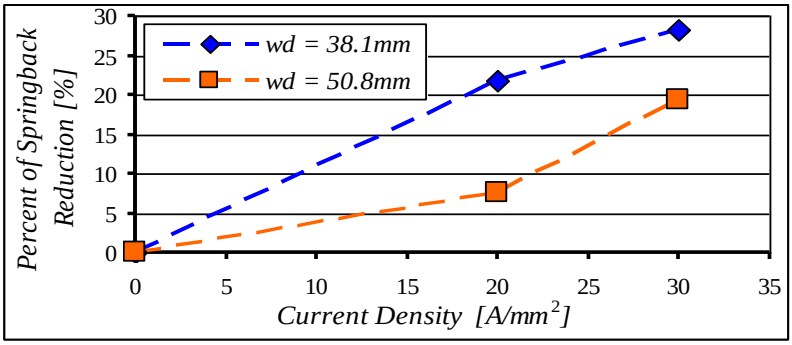

Figure 80. Springback reduction due to electricity [89]-[90]. Percent of springback reduction in relation to the amount of electrical current applied.

Effect of Pulse Duration

This subsection evaluates the isolated effects of pulse duration on the bending load and springback of the 304 Stainless Steel sheet specimens. Figure 81 presents bending load vs. position profiles for tests with a constant die width (38.1mm), current density (30A/mm^2), and pulse period (60s), while having pulse durations of 2s and 3s. From the graph, the bending load was slightly lowered in both electrical tests. Also, there was only about a 5-10N difference in

flow stress drop-offs between the 20 and 30A/mm^2 tests, with the 30A/mm^2 test producing the larger drop-offs.

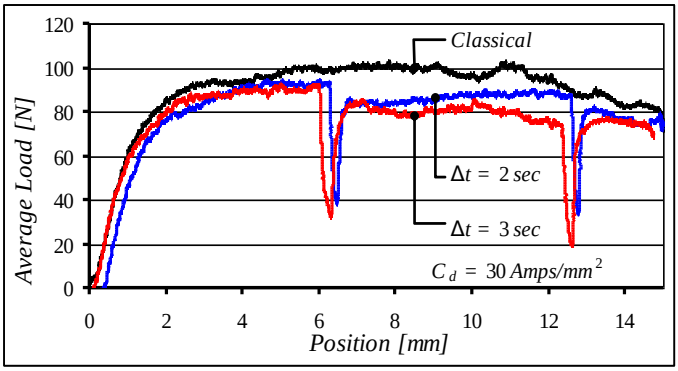

Figure 81. EAB Forming loads for different pulse durations [89]-[90]. Forming load profiles with 2s and 3s electrical pulse durations are shown.

The percent of springback reduction as a function of pulse duration can be seen in Figure 82. For this graph, a constant current density of 30A/mm^2, die width of 38.1mm, and pulse period of 30s were used. The percent reduction in springback is significantly dependent on the length of the pulse duration. Of note is that, using a pulse duration of 3s, and pulsing every 30s during deformation, about 77% of the total springback can be removed from the specimens.

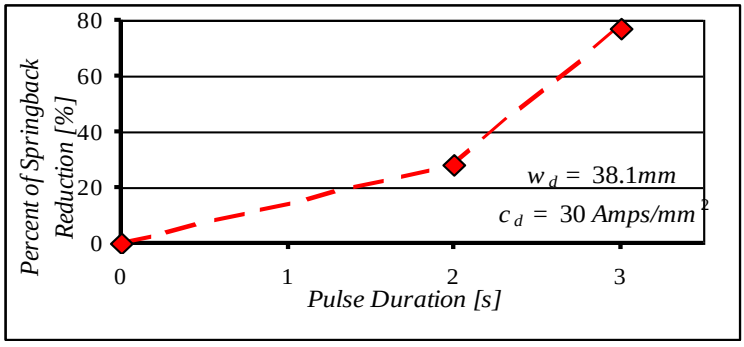

Figure 82. Springback reduction for various pulse duration [89]-[90]. Percent of springback reduction in relation to the duration of each electrical pulse.

Effect of Pulse Period

The following figures help to illustrate how different pulse periods (time in between successive electrical pulses) can influence bending load and springback. Figure 83 displays plots of load vs. position data where a constant current density of 30A/mm^2, a constant pulse duration of 2s, and constant die width of 38.1mm were maintained while pulse periods of 20s and 30s were utilized. The flow stress was reduced by about 5-10N for the 30s pulse period test and by about 15-20N for the 20s pulse period test, when compared to the classical test. The more frequent pulses of the 20s-period test provided for a slightly lower flow stress profile compared to the 30s-period test. Additionally, the drop-off magnitudes of each electrical test were very similar, leading to the fact that pulse period has little effect on drop-offs and more of an effect on the overall flow stress profile.

Figure 84 displays the amount of springback reduction as a function of pulse periods of 20s, 30s, and 60s, while holding constant the die width (38.1mm), current density (30A/mm^2), and pulse duration (2s). The shortest pulse period, allowing for the most electric pulses, reduced the springback the greatest, by about 50%. There was no notable difference between the percent of springback reduction between the 30s-period and 60s-period tests. For the given current density, die width, and pulse duration combination, a pulse period of 20s appears to be optimal, however this will change as the other pulse parameters are changed.

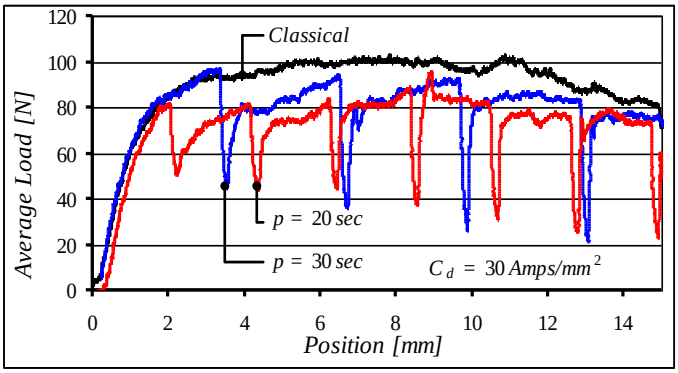

Figure 83. EAB Forming loads for different pulse periods [89]-[90]. Forming load profiles are presented which represent a 20s and 30s pulse period in between successive electrical pulses.

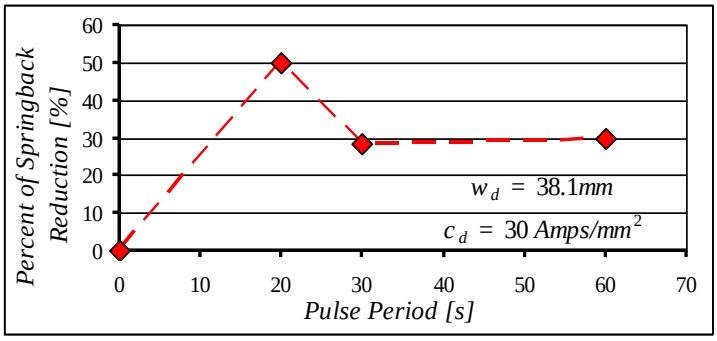

Figure 84. Springback reduction for various pulse periods [89]-[90]. The percent of springback reduction in relation to the period of time in between each successive pulse, is presented.

5.2.10. EA-Bending Model Conclusions

This chapter presented a preliminary approach to the analysis of electrically-assisted air bending by employing equilibrium of forces and moments, and also utilizing the same EEC-based methodology as was used for an EA-forging operation. Two effects of the applied electrical energy were taken into consideration: (*i*) the electroplastic effect of the electricity helping the deformation by assisting the dislocations, and (*ii*) thermal softening as a result of resistive heating.

The bending force needed for a certain deformation can be determined for both classical and electrically-assisted tests. For the second case, the pulse parameters can be varied, and the effect on the deformation process can be estimated, in terms of force reduction. The following conclusions were drawn from this study:

- The experimental results indicated that the electricity can assist the deformation process due to beneficial effects in reducing the flow stress, thus the forming force and mechanical energy required for reaching the same level of deformation as in classical forming are reduced.
- Another benefit of using the electricity during bending was observed in the notable reduction in springback, up to 77%, depending on the electric parameters and pulse characteristics.
- The analytical model was in good agreement with the experiments, and it was able to predict the bending forces within a difference of 10-15% (in most cases).
- The analytical model coupled with the experimental observations can be used to estimate the pulse parameters required for certain reductions in the forming load.
- A model was created for reduction of springback effect in EAF bending as a function of process parameters.

6. Contact Area and Tribological Effect on EAF (Task #5)

Because the electricity in EAM must flow from the dies and though the workpiece, the interfaces between the dies/workpiece are critical. Specifically, the contact area effect and the tribological effects will be examined in this chapter. The contact area will vary depending on the surface roughness of the specimen contact faces and force, which will then vary the resistance of the system, hence the heat of the system [95]-[99]. Even at high forming loads, there will still be some level of differences between the apparent contact area and the actual contact area [100] and it must be determined at which point the differences in the contact areas have a noticeable effect on the effectiveness of the EAF technique. In addition, the tribological effects study investigates several common metal forming lubricants and compare how well they perform when coupled with the EAM technique.

6.1. Contact Area Effect on EAM Effectiveness

The following is a compilation of the findings from the candidate's work on the effects of contact area and surface roughness on the effectiveness of EAM. Within this work, the examination of contact area's effect on EAM effectiveness explores several aspects. The sub-sections include: an explanation of how the surface ground specimens and enhanced asperity specimens were produced, a post-forming EAF roughness profile examination, a description of the experimental setup and procedures, a thermal analysis, an explanation of the voltage-contact resistance contact area model, a mechanical analysis of EAF based on contact area, and finally conclusions on contact area effects.

6.1.1. Specimen Preparation (Surface Ground)

Specimens were prepared in two different ways throughout this research work. Stainless Steel 304 specimens were cut from 6.35mm- and 4.76mm-diameter rods. Then, the overall lengths of the specimens were sized using different surface grinding wheels for different specimens to create specimens with varying surface roughnesses on their contact faces. The following grinding wheels were used: 320 grit, 600 grit, and 800 grit. Upon receiving the specimens back from the machine shop, a Zygo New View 7200 was used to quantify the different surface roughnesses produced by the grinding wheels, as shown in Figure 85. To accomplish this, roughnesses were measured on both sides of each specimen, and on each side, two locations were measured. Further, at each location one horizontal and two diagonal measurements were taken to remove any directional bias from the measurements. Figure 86 shows an example of this measurement strategy. Table 9 below shows the different roughness profiles which were determined.

Figure 85. Surface roughness measuring equipment. A Zygo New View 7200 optical surface profilometer equipped with MetroPro analysis software was used to determine the surface roughness of the specimens.

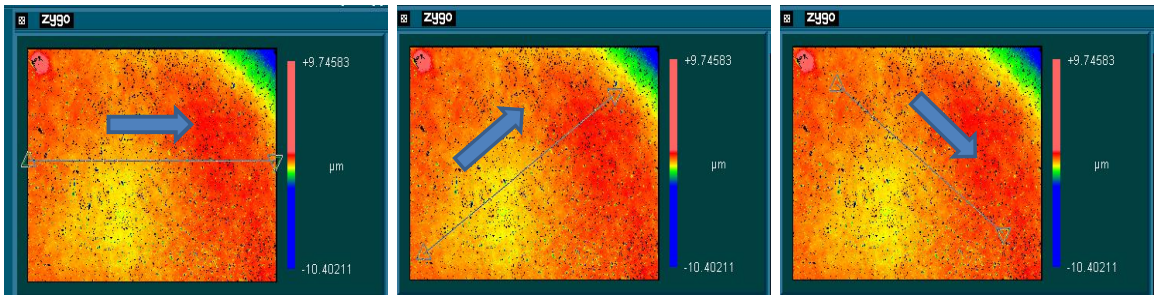

0° measurement 45° measurement 135° measurement

Figure 86. Surface roughness measurement strategy. Measurements were taken at two locations on each side of the specimen. At each location, several roughness profiles were determined along imaginary lines drawn at various angles (0°, 45°, and 135°).

Magnified pictures of the surface ground specimens from the profilometer can be seen in Figure 87. Additionally, surface roughness profiles of the same specimens are shown in Figure 88.

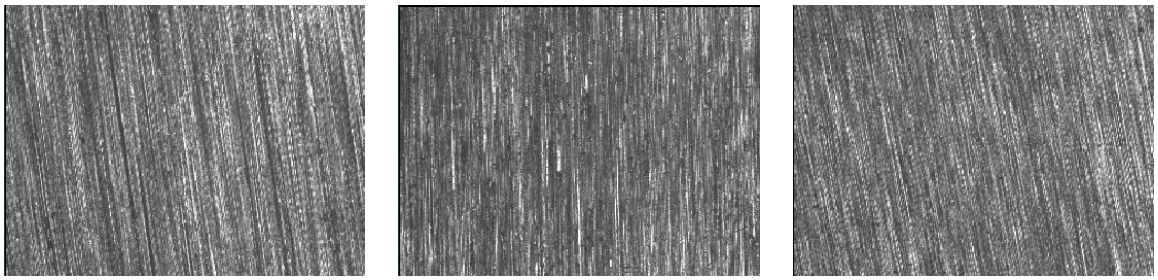

320 Grit 600 Grit 800 Grit

Figure 87. Initial Zygo surface profiles. Shown are magnified images of the contact surfaces of the Stainless Steel 304 test specimens when they were surface ground using different grit grinding wheels.

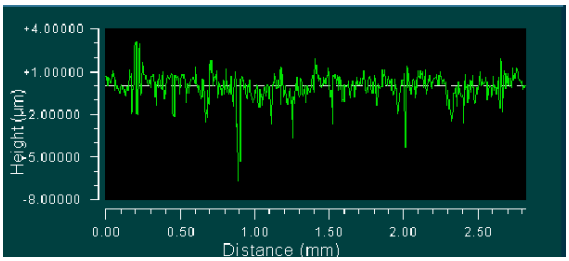

320 Grit

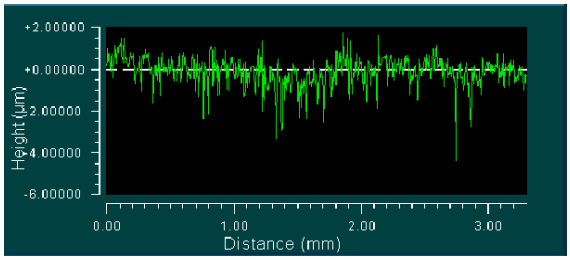

600 Grit

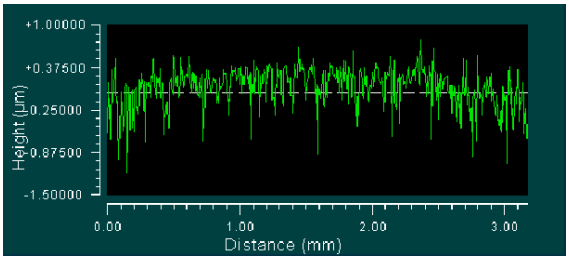

800 Grit

Figure 88. Zygo surface roughness measurements. Shown are the height vs. distance plots of a particular area on the contact surface of each specimen prepared using a different grit grinding wheel.

Table 9. Wheel grit vs. surface roughness relationship.

Wheel Grit	Avg Ra (µm)	Avg RMS (µm)	Size - x (mm)	Size - y (mm)
320	0.668	0.909	2.83	2.12
600	0.539	0.729	2.83	2.12
800	0.217	0.288	2.83	2.12

6.1.2. Specimen Preparation (Enhanced Asperities)

In addition to using the different surface grinding wheels to produce different surface roughness, it was quickly determined that the different in surface roughness was not large enough to witness any trends in the experimental thermal data. To assist with this issue, an EDM was used to machine "enhanced asperity" profiles on the faces of the specimens, as shown below in Figure 89. These "enhanced asperities" provide a significant difference in contact area, so that experimental trends can be easily recognized. Let it be known there were three different

enhanced asperity specimens which were made (*i.e.* Large CA, Med. CA, and Small CA), however, the Large CA specimens were the only ones used in this research.

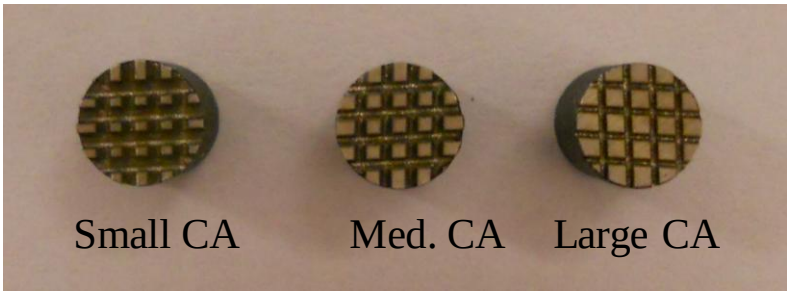

Figure 89. Enhanced asperity specimens. The profiles for the enhanced asperities were cut using an EDM. There are three types of enhanced asperities (small, medium, and large contact area).

Eq.(53) and Figure 90 below show the equation used to determine the apparent contact area of a specimen with exaggerated asperities:

$$CA_{apparent} = \frac{\pi}{4} D^2 - \left[2 \cdot (L_1 \cdot w) + 2 \cdot (L_2 \cdot w) + 2 \cdot (L_3 \cdot w) + 2 \cdot (L_4 \cdot w) - 16 \cdot (w^2) \right] \quad (53)$$

where D is the outer diameter of the specimen, L_1 is the length of the first cut, L_2 is the length of the second cut, L_3 is the length of the third cut, L_4 is the length of the fourth cut, and w is the width of each cut.

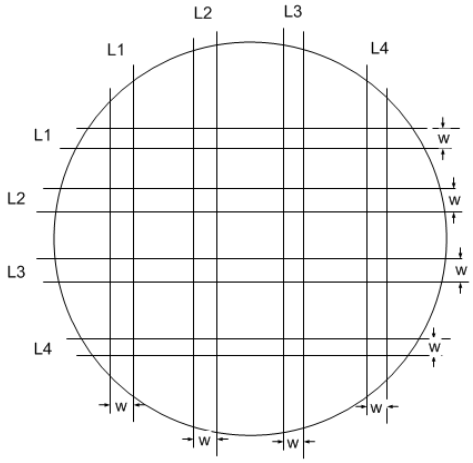

Figure 90. Determination of apparent contact area for enhanced asperity specimens. This scheme presents the approach used to determine the apparent contact area of the enhanced asperity specimens.

Table 10 shows the designations (surface ground, Large CA, Med CA, and Small CA) and the corresponding contact areas.

Table 10. Surface designations and contact areas.

Surface description	Specimen OD (in)	Specimen OD (mm)	Contact area (mm^2)	Area removed (mm^2)	Apparent contact area (mm^2)	Contact area ratio
surface ground	0.1875	4.76	17.81	0.00	17.81	100%
Large CA	0.1875	4.76	17.81	8.65	9.16	51%
Med CA	0.1875	4.76	17.81	10.86	6.96	39%
Small CA	0.1875	4.76	17.81	12.76	5.06	28%
surface ground	0.25	6.35	31.67	0.00	31.67	100%
Large CA	0.25	6.35	31.67	12.04	19.63	62%
Med CA	0.25	6.35	31.67	18.41	13.26	42%
Small CA	0.25	6.35	31.67	25.49	6.18	20%

6.1.3. Post-Forming EAF Roughness Examination

In this sub-section, post-formed surface roughness values were determined for 4.76mm-diameter specimens from conventional compression and EAF tests (at current densities of 20 and

30A/mm^2). The same measuring strategy as discussed in the previous sub-section was used. The total displacement stroke was divided into five different levels of displacement (L_0 to L_4), with L_0 being no deformation. The surface roughness values were determined at each step. Descriptions of each deformation level is

- L_0: No deformation
- L_1: 0.95mm of deformation
- L_2: 1.91mm of deformation
- L_3: 2.86mm of deformation
- L_4: 3.81mm of deformation

Please note that all of the specimens used in this sub-section were sandblasted to an average Ra-value of 2µm prior to machining the enhanced asperities and testing. Table 11 displays the average Ra-values for the conventional compression test and the two EAF tests at each deformation level.

Table 11. Average Ra-values for post-formed compression tests (conventional and EAF).

Deformation Level	Ra Values		
	Conv	CD20	CD30
L_0	2.000	2.000	2.000
L_1	0.782	0.858	0.903
L_2	0.603	0.714	0.838
L_3	0.318	0.421	0.658
L_4	0.205	0.358	0.400

This same data is shown in Figure 91. From the figure and the table, one can see that the post-formed roughness is consistently higher for the EAF tests compared to the conventional

compression tests. Additionally, the EAF tests with the greater current density ($30A/mm^2$) consistently produced a rougher post-formed surface. This helps to prove that the EAF technique can have detrimental impacts on the tribological conditions compared to cold forging. The effect that EAF has on tribological conditions will be further discussed, beginning in section *6.2: Tribological Effect.*

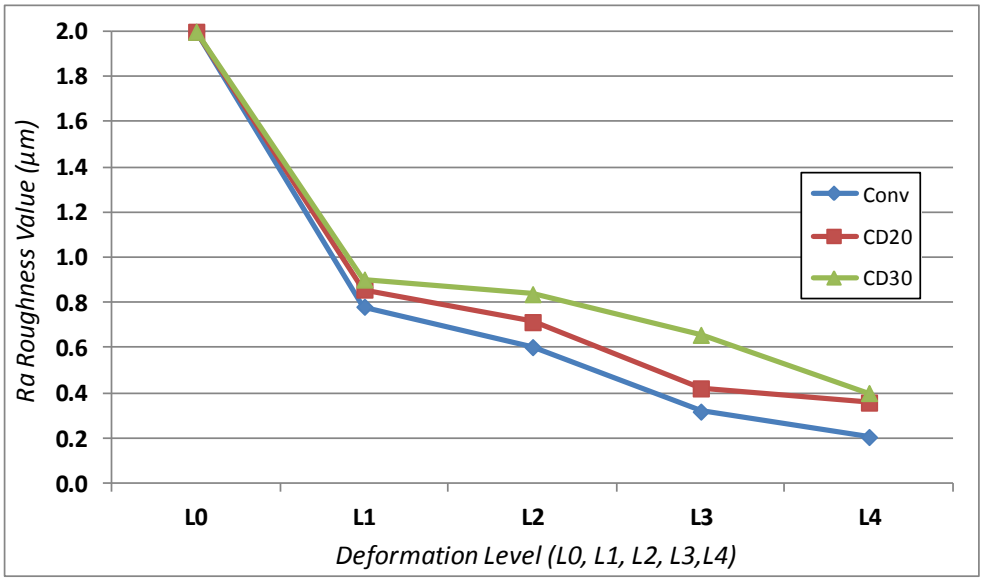

Figure 91. Post-forming surface roughnesses at different deformation levels. The post-forming roughness value is increased as the magnitude of applied electrical power is increased for each respective deformation level**.**

6.1.4. Experimental Setup and Procedure

Figure 92 shows the experimental setup used for this investigation. The Instron testing machine ran stationary-electrical, conventional compression, and EAF tests on surface ground parts and enhanced asperity parts (4.76mm diameter specimens). The part temperature, the voltage across the height of the specimen, the load/position data (when deforming), and Zygo images were recorded.

Figure 92. Experimental test setup for contact area effect investigation. This testing setup includes a multi-meter that reads the voltage drop across the top and bottom dies at the locations where they contact the test specimen.

6.1.5. Thermal Analysis of EAF Based on Contact Area

As part of the thermal analysis sub-section, the method of obtaining thermal data, along with the comparisons of that thermal data will be presented. The thermal measuring strategy consisted of using a FLIR A40M infra-red thermal imaging camera to record the specimen temperature profile for each test. Then, ThermaCAM software was used to generate thermal data for specific locations on the part. In this work, thermal data was generated for three locations on the workpiece:

1. A single point measurement at the top die/specimen interface (the top die is stationary on the Instron machine).
2. A single-point measurement in the middle of the specimen.
3. A maximum of the whole specimen/die area (this is to catch any instantaneous sparking phenomenon during the first initiation of the electricity)

Figure 93 displays the locations of the three areas of thermal data gathering for this work. It was decided that the thermal data used for comparison in the work should be taken from the center of the specimen, since the hottest area of the specimen quickly and consistently becomes the center through testing, which will be shown in the following few figures. This is due to the fact that the center of the specimen consistently and quickly becomes the hottest area during the EAF and stationary-electrical tests.

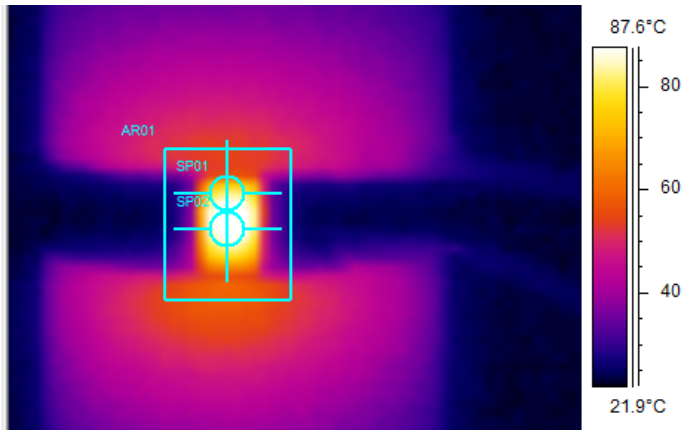

Figure 93. Locations of thermal data gathering at the specimen and die interfaces. The thermal data was taken at points in the center of the specimen, and at the top of the specimen. Also, the maximum temperature was recorded for the whole area surrounding the specimen and the dies.

Shown below in Figure 94, Figure 95, and Figure 96 are heating and cooling sequences during an EAF compression test for specimens with enhanced asperities in particular locations. Figure 94 has the enhanced asperities on the top face, and from the thermal profiles, this is the hottest area at the beginning of the test (notice the white color signifying the hottest temperature). Figure 95 has the enhanced asperities at the bottom face, and this area is the hottest at the beginning of the test. Figure 96 has the enhanced asperities at the top and bottom faces and both of these areas are approximately equally the hottest locations at the beginning of the test. These three experiments show that, where there is a significant change in the contact area (larger than

the micro-level), the temperature will be affected. However, this change in temperature is only noticed briefly at the beginning of the test, and then the center of the specimen becomes the hottest location for all three tests. Let it be known that the heat transfer during EAF can be affected by many different variables (*i.e.* different forms of heat transfer, die volume, etc.) and the specific effects of these variables will be discussed in a later chapter.

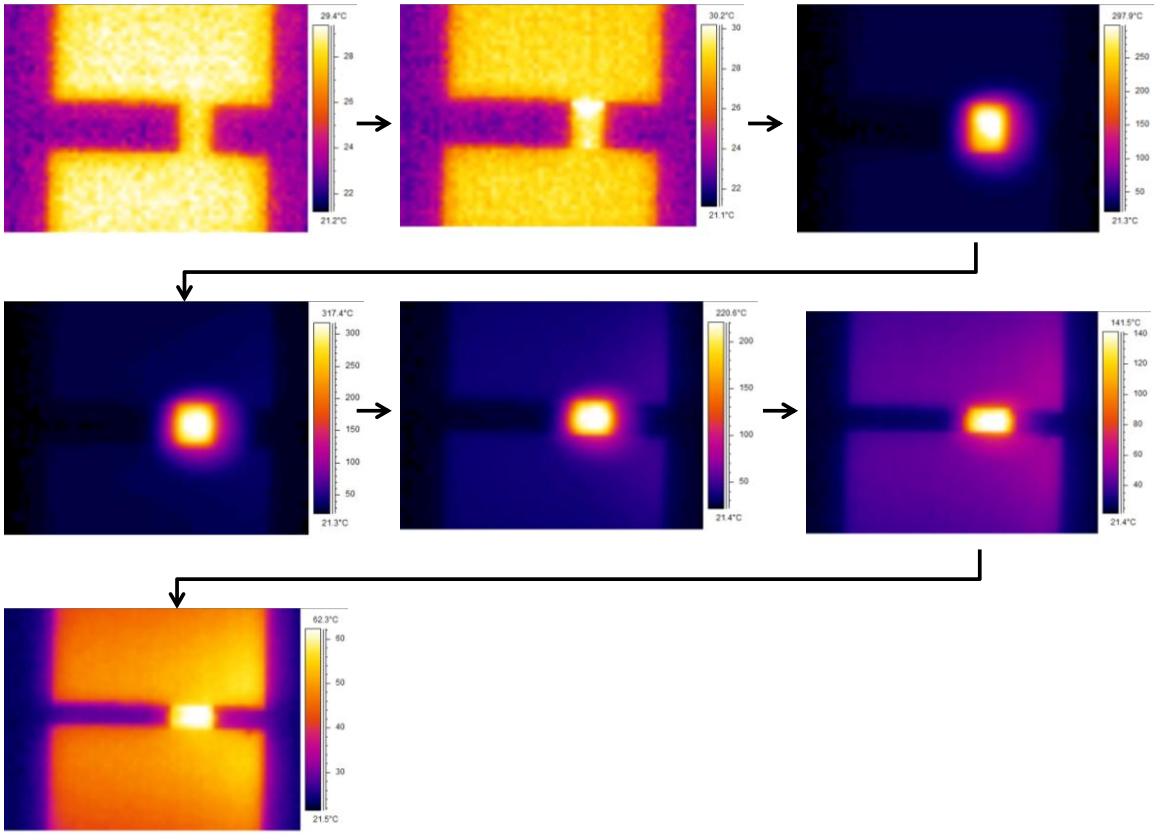

Figure 94. Heating and cooling sequence for enhanced asperities at the top of the specimen. In the case of the enhanced asperities being at the top of the specimen, the most heat is generated at the top of the specimen very briefly, and then this heat moves to the center of the specimen, ultimately making this location the hottest.

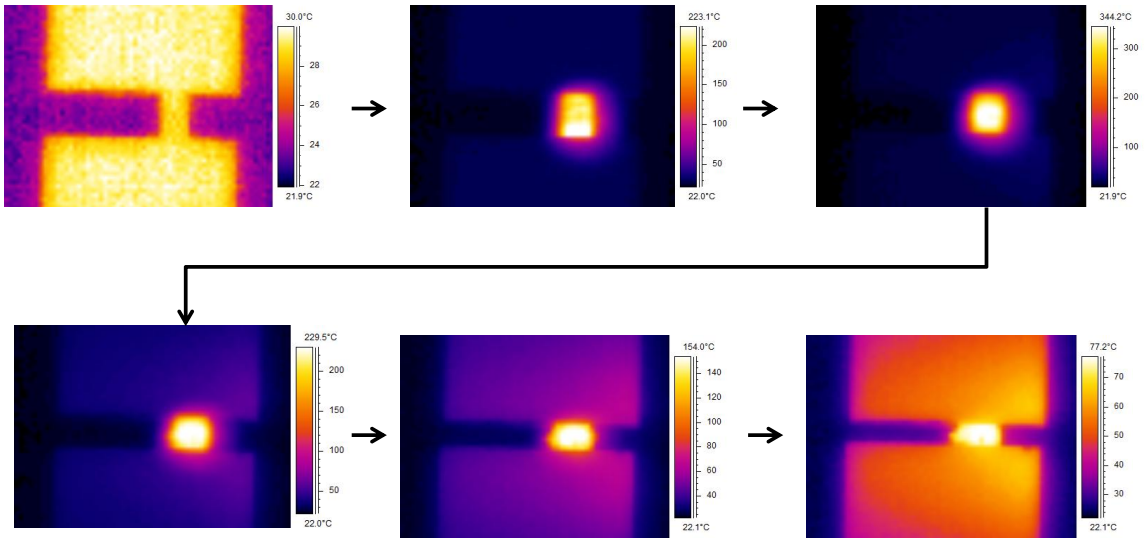

Figure 95. Heating and cooling sequence for enhanced asperities at the bottom of the specimen. In the case of the enhanced asperities being at the bottom of the specimen, the most heat is generated at the bottom of the specimen very briefly, and then this heat moves to the center of the specimen, ultimately making this location the hottest.

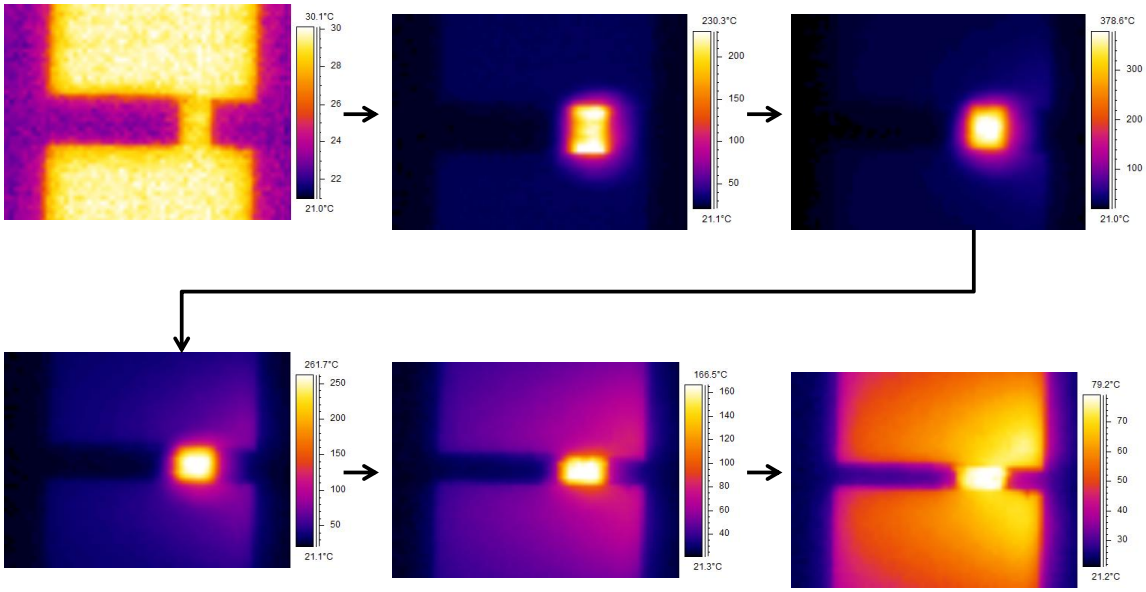

Figure 96. Heating and cooling sequence for enhanced asperities at the top and bottom of the specimens. In the case of the enhanced asperities being at the top and bottom of the specimen, the heat is generated at the top and bottom of the specimen very briefly, and then this heat moves to the center of the specimen, ultimately making this location the hottest.

Figure 97 shows stationary-electrical thermal profiles for specimens which were surface ground using a 320-grit wheel to an average roughness value of 0.539µm. It can be seen that, as the static load is increased, the temperature also decreases to a small extent. Please note that all of these static loads were within the elastic region of the specimens.

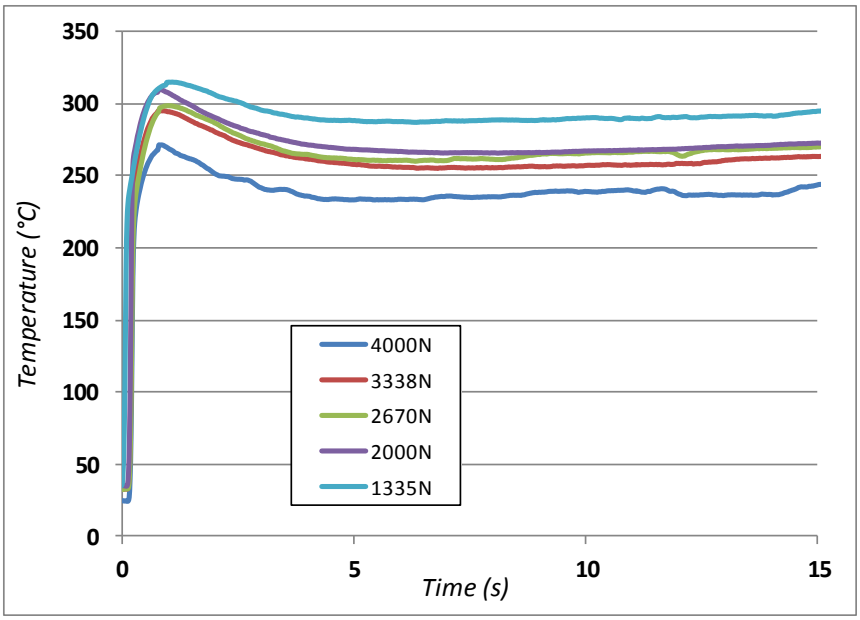

Figure 97. Temperature vs. time plots for stationary-electrical tests at various static loads (320 grit). The temperatures for each of the stationary-electrical tests decreases as the static loads applied to the part while the test is underway increase.

Figure 98 displays the thermal profiles for stationary-electrical tests run on specimens with a "Large CA" surface roughness. From the figure, the temperatures at static loads of 1335N and 2000N are much higher than the temperatures at the other, heavier loads, which were into the plastic regime of the asperity portion of the specimens. Of note, is that the 1335N and 2000N loads are still within the elastic region of the "Large CA" region, but the other three loads are towards the plastic regime. With this said, a clear difference between the elastic and plastic regimes can be noticed. Specifically, when the parts are still in the elastic regime, the

temperature and applied static load have an inverse relationship. However, when the parts are within the plastic regime, the specimen temperature is relatively unaffected due to the increase or decrease in the static load.

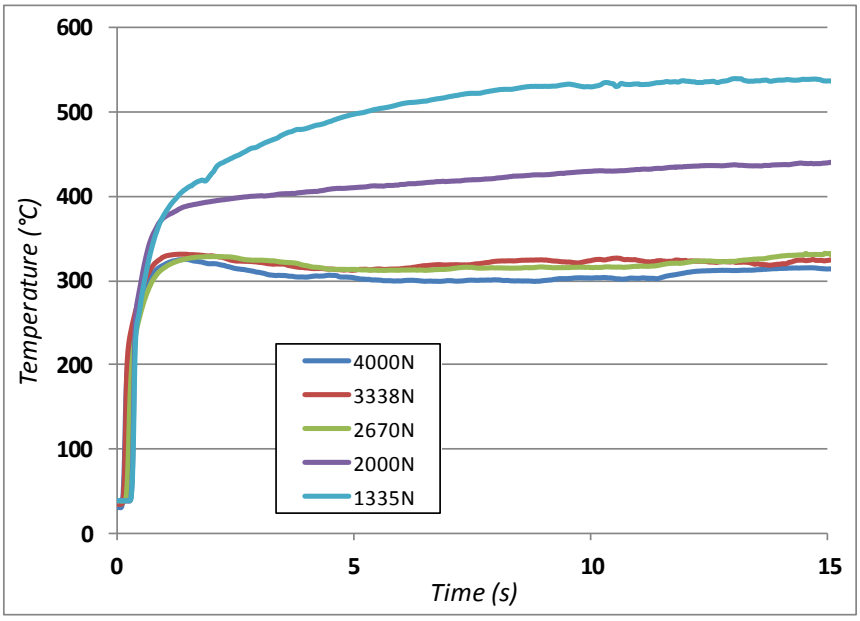

Figure 98. Temperature vs. time plots for stationary-electrical tests at various static loads (Large CA-enhanced asperity parts). The temperatures of the stationary-electrical tests decreased as the static load increased. Additionally, once the static load had surpassed the elastic-plastic threshold, the difference in temperature between the tests was unaffected by the different loads.

Now data will be taken from Figure 97 and Figure 98 to be able to compare temperatures of the 4.76mm-diameter specimens at different discrete times over the different static loads. Table 12 shows the specimen temperatures at 5-second intervals, as well as the percent of the baseline temperature for all of the static loads run on the specimens with a 320-grit surface ground roughness. Additionally, Figure 99 shows this data plotted as "percent of the baseline temperature at 1335N" vs. the static load after 5, 10, and 15 seconds of testing. The figure

illustrates a clear declining trend in the percent of the baseline temperature as the static load is increased.

Table 12. Stationary-electrical test temperatures (4.76mm diameter surface ground specimens).

Force (N)	Time (s)	Temperature (°C)	ΔT (% of baseline Temp at 1335N)
1335	5	288.1	100.0
	10	290.0	100.0
	15	294.6	100.0
2000	5	268.4	93.2
	10	267.3	92.2
	15	272.8	92.6
2670	5	261.3	90.7
	10	265.9	91.7
	15	270.0	91.7
3338	5	257.4	89.4
	10	256.6	88.5
	15	262.8	89.2
4000	5	233.7	81.1
	10	239.5	82.6
	15	244.1	82.9

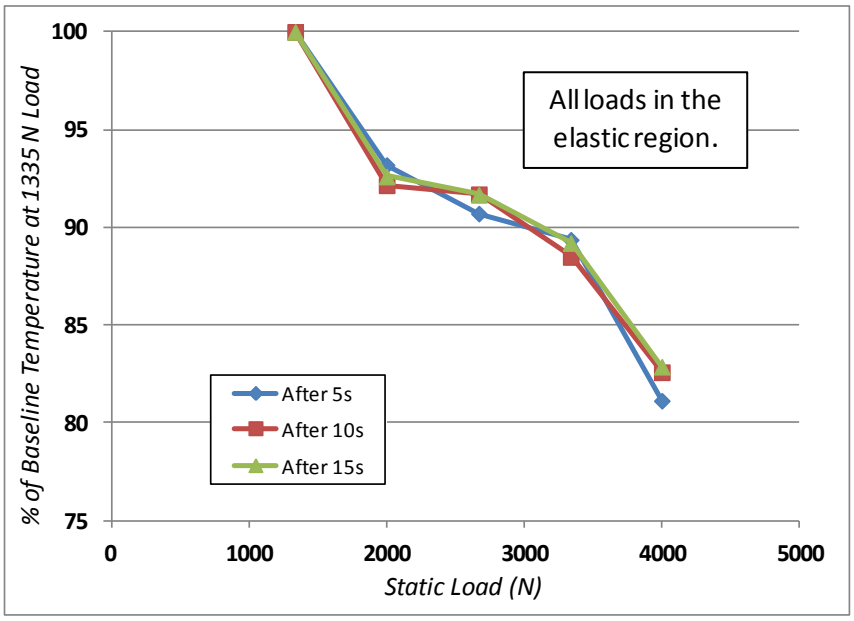

Figure 99. Stationary-electric temperatures (4.76mm diameter surface ground specimens). There is a clear linear decreasing trend for the percent of the baseline temperature and static load because the static loads tested did not surpass the elastic-plastic threshold for these particular specimens.

Table 13 shows the specimen temperatures at 5-second intervals, as well as the percent of the baseline temperature for all of the static loads run on the 4.76mm-diameter specimens with a "Large CA" roughness profile. Additionally, Figure 100 shows this data plotted as "percent of the baseline temperature at 1335N" vs. the static load after 5, 10, and 15 seconds of testing. Unlike the previous figure, this figure shows a very steep declining trend in the percent of the baseline temperature with increased static load for only the first two static loads (note these two loads were in the elastic regime). Then, there is a level relationship between the percent of the baseline temperature and the load for the remaining three static loads. The three loads which show a leveling relationship are within the plastic regime of the "Large CA" region of the specimens.

Table 13. Stationary-electrical test temperatures (4.76mm diameter Large CA specimens).

Force (N)	Time (s)	Temperature (°C)	ΔT (% of baseline Temp at 1335 N)
1335	5	496.7	100.0
	10	529.0	100.0
	15	536.0	100.0
2000	5	410.8	82.7
	10	430.2	81.3
	15	440.3	82.1
2670	5	312.5	62.9
	10	314.6	59.5
	15	331.3	61.8
3338	5	313.3	63.1
	10	324.9	61.4
	15	325.0	60.6
4000	5	303.4	61.1
	10	303.3	57.3
	15	314.1	58.6

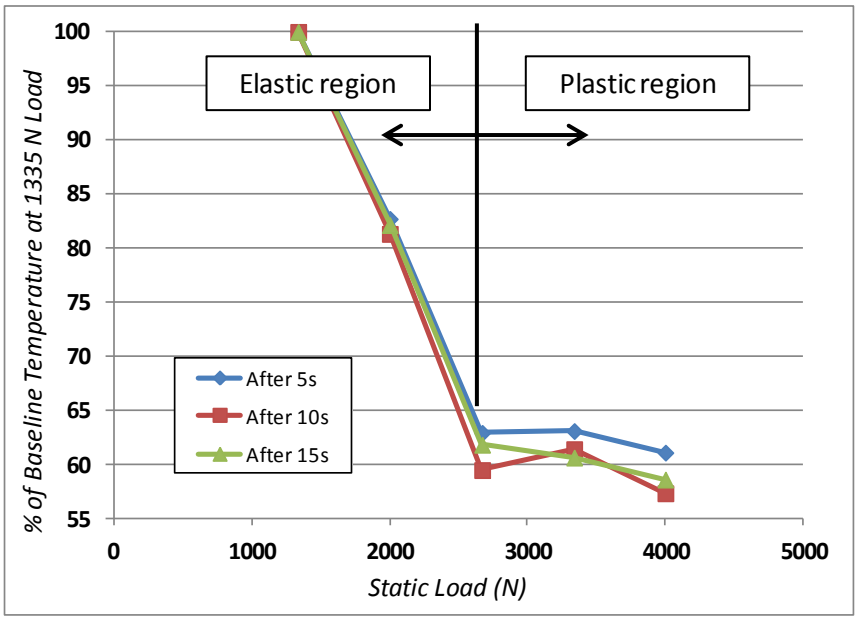

Figure 100. Stationary-electrical temperatures (4.76mm diameter Large CA specimens). There is a clear decreasing trend between the temperature and the static load, until the elastic-plastic threshold is reached. Then, the temperature does not change with an increase in static load.

Table 14 shows the specimen temperatures at 5-second intervals, as well as the percent of the baseline temperature for all of the static loads run on the 6.35mm-diameter specimens with a roughness profile created using a 320-grit grinding wheel. Additionally, Figure 101 shows this data plotted as "percent of the baseline temperature at 1335N" vs. the static load after 5, 10, and 15 seconds of testing. Like the 4.76mm-diameter specimens with the same surface roughness, there is a clear declining trend in the percent of the baseline temperature as the static load increases. This trend is apparent at all static loads, and all of the static loads are within the elastic region of the part.

Table 14. Stationary-electrical test temperatures (6.35mm diameter surface ground specimens).

Force (N)	Time (s)	Temperature (°C)	ΔT (% of baseline Temp at 2376 N)
2376	5	418.7	100.0
	10	507.7	100.0
	15	541.8	100.0
3564	5	393.0	93.9
	10	472.5	93.1
	15	505.2	93.2
4753	5	386.6	92.3
	10	464.2	91.4
	15	496.7	91.7
5941	5	350.6	83.7
	10	427.7	84.3
	15	463.1	85.5
7129	5	331.9	79.3
	10	405.1	79.8
	15	438.3	80.9

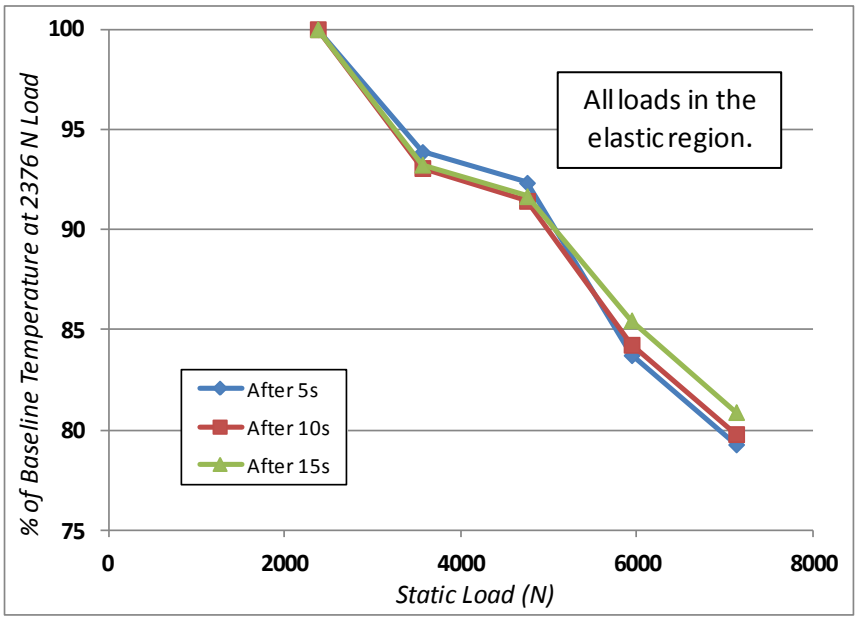

Figure 101. Stationary-electrical temperatures (6.35mm diameter surface ground specimens). The linear-inverse relation between temperature and static load is also apparent for the larger specimens due to all of the static loads only being in the elastic region.

6.1.6. Voltage-Resistance Contact Area Model

The voltage (in mV) was recorded for each of the stationary-electrical tests using a digital multi-meter, as shown in sub-section *6.1.4: Experimental Setup and Procedure*. Since the voltage is related to the actual contact area, the voltage measurements can provide a dynamic confirmation of the asperity crushing due to an increase in the static load. Figure 102 below depicts the voltage measurements obtained during stationary-electrical tests under various static loads for 4.76mm-diameter surface ground specimens and for 4.76mm-diameter "Large CA" specimens. The "Large CA" specimens show a notable decrease in the measured voltage at the first two static loads, and then show the same level effect as the surface ground specimens (although the "Large CA" specimens still have a higher voltage value). The higher voltage value

is to be expected since there is less contact area (because the EDM profiled it out) and there is the same electrical current running through these parts as is with the surface ground parts.

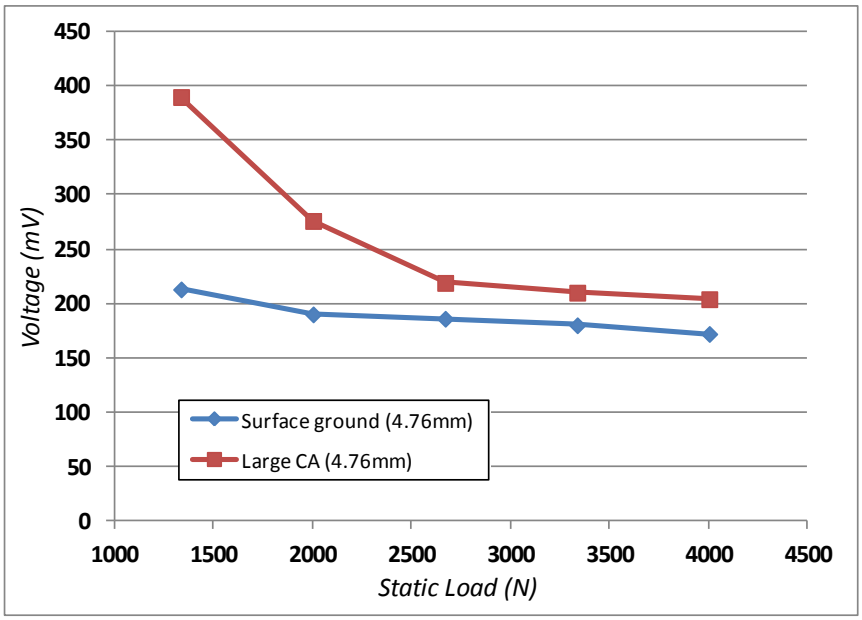

Figure 102. Voltage vs. static load stationary-electrical tests (Large CA and surface ground 4.76mm diameter specimens). There is more of a change in the voltage of the Large CA specimens at the lower static loads in comparison to the surface ground specimens.

Figure 103 displays the voltage vs. static load relationship for the 6.35mm-diameter specimens. There is a very steep decrease in the voltage as the static load is increased, which correlates to the same decrease in specimen temperature as the static load was increased, in Figure 101 above.

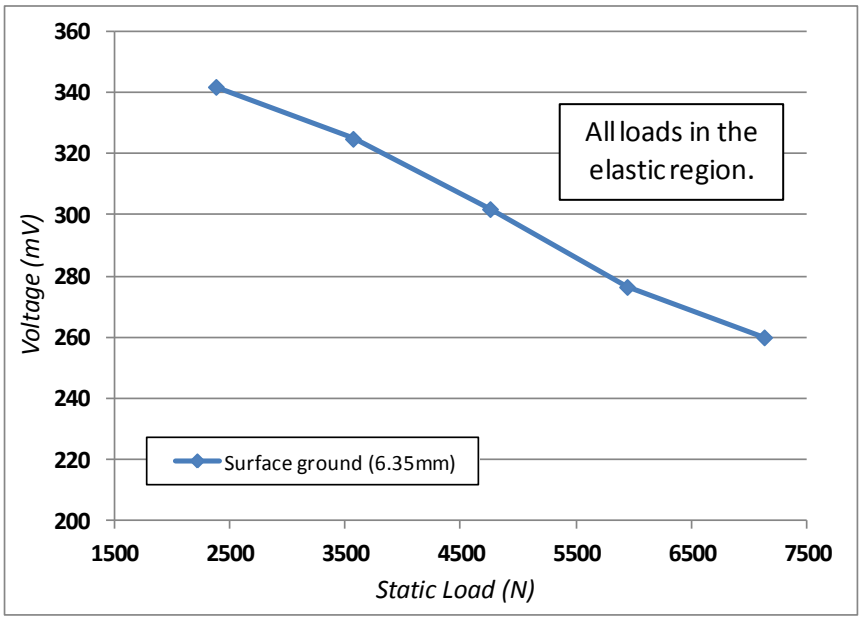

Figure 103. Voltage vs. stationary-electrical tests (surface ground 6.35mm diameter specimens). The voltage in the 6.35mm diameter surface ground specimens shows a decreasing linear trend with the increase in static load.

Now, utilizing the voltage measurements, the actual contact area can be predicted. The basic relation for electrical power can be described as eq.(54):

$$P = IV = I^2 R \tag{54}$$

where P is electrical power, I is current, V is voltage, and R is the resistance. Then, the voltage can be written as eq.(55):

$$V = IR = I \cdot \frac{r \cdot L_{part}}{A_{contact}} \tag{55}$$

where r is the electrical resistivity, L_{part} is the length of the workpiece, and $A_{contact}$ is the actual contact area at the specimen and die interface. The relation for the actual contact area can be re-written as eq.(56):

$$A_{contact} = \left[\frac{r_{part} \cdot L_{part}}{\frac{V}{I}} \right] \tag{56}$$

This relation describes electrical resistance, but it does so assuming that the workpiece and the top and bottom dies are essentially all one piece. However, there is also some type of contact resistance between the specimen and dies since there is a difference in the parts and in the die/workpiece materials. The total resistance in the system (including electrical resistance and contact resistance) is shown as eq.(57):

$$R_{total} = R_{electrical} + R_{contact} \tag{57}$$

The electrical contact resistance was described above, but the contact resistance can be written as eq.(58):

$$R_{contact} = \frac{r_{part} + r_{die}}{4 \cdot n_{asp} \cdot a_{asp}} + \frac{r_{part} + r_{die}}{D} \tag{58}$$

where r_{part} is the resistivity of the part, r_{die} is the resistivity of the die, n is the number of asperities, a is the radius of the contact points, and D is the diameter of the region where the asperities are located. When including both the electrical resistance and the contact resistance, the equation for the total resistance can be written as eq.(59):

$$R_{total} = R_{electrical} + R_{contact} = \frac{r_{part} \cdot L}{A_{contact}} + \frac{r_{part} + r_{die}}{4 \cdot n_{asp} \cdot a_{asp}} + \frac{r_{part} + r_{die}}{D} \tag{59}$$

The final equation to be used to back-solve for the contact area, based on the measured voltage, is eq.(60):

$$A_{contact} = \left[\frac{r_{part} \cdot L_{part}}{\frac{V}{I} - \frac{r_{part} + r_{die}}{4 \cdot n_{asp} \cdot a_{asp}} - \frac{r_{part} + r_{die}}{D_{part}}} \right] \tag{60}$$

For 4.76mm-diameter "Large CA" specimens in which stationary-electrical tests were run, Table 15 summarizes the recorded voltages, the apparent contact area (*i.e.* the area calculated using eq.(53)), the contact areas calculated using eq.(56) (without the contact resistance) and the contact area calculated using eq.(60) (with the contact resistance). Figure 104 displays the contact areas with and without the contact resistance accounted at the various static loads, along with a dashed line representing the apparent contact area created from the EDM process during the fabrication of the specimens. Please note that the area calculated with the contact resistance is higher than the actual apparent area. This is possibly due to the fact that the loads are in the

plastic region and the total specimen height and asperity height/width (*i.e.* cross-sectional area) has changed in this region. Let it be known, that of all the research papers the candidate has reviewed in which the actual contact area is predicted, all of the loadings were localized and were within the elastic regime, not the plastic regime. As the material enters the plastic regime, the overall dimensions of the potential contact areas are continuously changing with the deformation and new contact surfaces are continuously forming with differing roughness profiles, thus making the prediction of actual contact areas under plastic loadings much more difficult.

Table 15. Actual contact area values based on voltage measurements from stationary-electrical tests.

Test #	Specimen Condition	Pre-load (N)	Voltage (mv)	Area (w/o contact resistance) mm^2	A (w/ contact resistance) mm^2	Apparent area (mm^2)
11	Large CA (4.76mm) at 356 Amps	4005	204	9.03	15.51	9.150
12		3338	210	8.77	14.77	9.150
13		3338	215	8.57	14.20	9.150
14		2670	219	8.41	13.77	9.150
15		2003	290	6.35	9.00	9.150
16		2003	276	6.68	9.66	9.150
17		1335	390	4.72	6.05	9.150

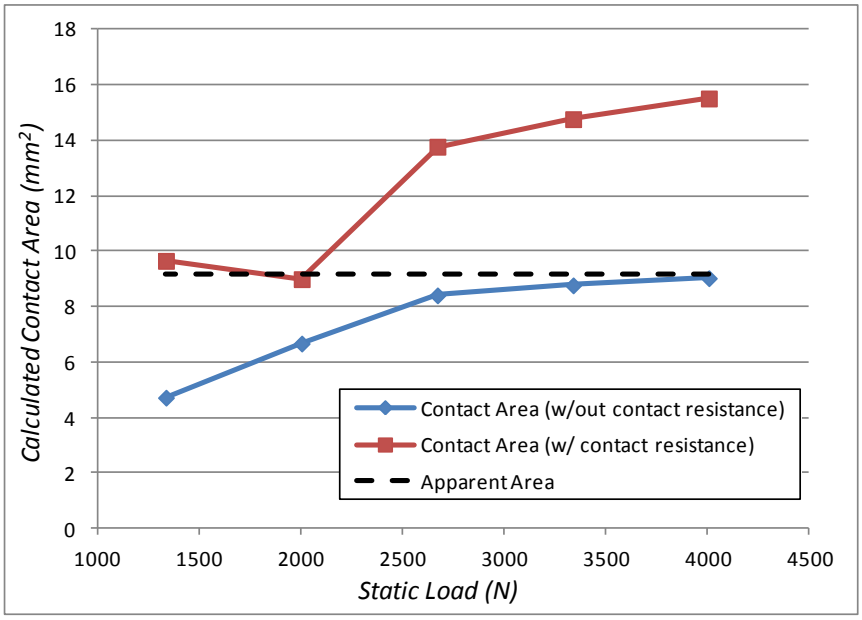

Figure 104. Contact areas calculated from the voltage measurements (4.76mm diameter Large CA specimens). The calculated contact area without the contact resistance is much closer to the actual contact area than the calculated contact area which considered contact resistance. However, the plastic deformation was unaccounted for in the model and could affect the results.

6.1.7. Mechanical Analysis of EAF Based on Contact Area

Within this sub-section, stress-strain plots are shown for 4.76mm-diameter specimens with surface ground and "Large CA" roughnesses, as well as for 6.35mm-diameter specimens with surface ground and "Large CA" roughnesses. In addition to the stress-strain profiles, mechanical power profiles are also plotted, and these will then be used to calculate the EEC

profiles for each of the specimens described above. Finally, the EEC profiles can be compared and analyzed.

Figure 105 and Figure 106 show the stress strain profiles and mechanical power profiles for conventional compression and EAF tests at CD=20A/mm^2 on 4.76mm-diameter specimens with a surface ground roughness. Two stress-strain profiles for each condition were shown in Figure 105 to prove the repeatability of the experiments. The EAF stress-strain profile is lower than the conventional compression profile, thus signifying that the electrical parameters which were chosen are in the electroplastic region for this material.

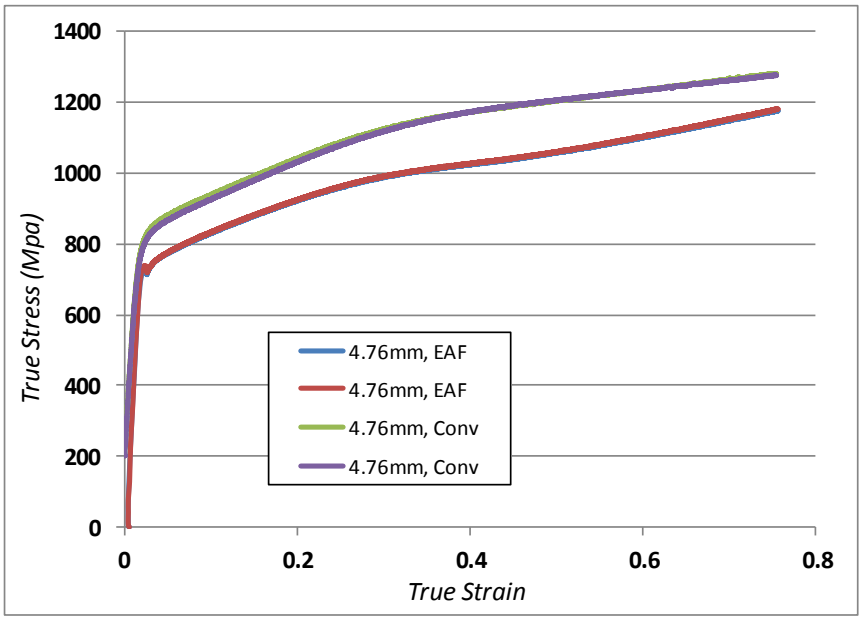

Figure 105. Stress-strain profiles (4.76mm diameter surface ground specimens). The stress-strain profiles show that the EAF tests produced a lower overall stress-strain profile.

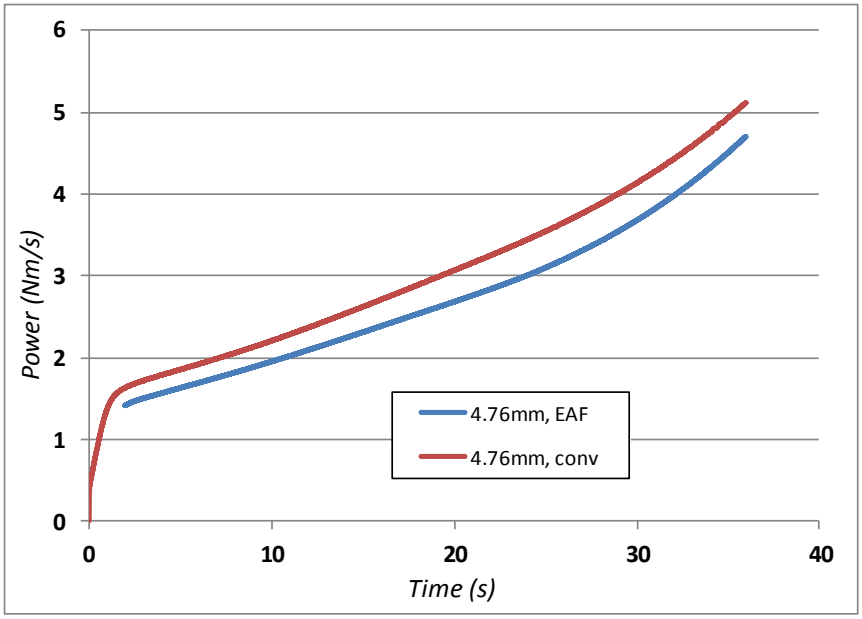

Figure 106. Mechanical power profiles (4.76mm diameter surface ground specimens). The mechanical power profile for the EAF test is lower than the power profile for the conventional test.

Figure 107 and Figure 108 show the stress strain profiles and mechanical power profiles for conventional compression and EAF tests at 20A/mm^2 on the 6.35mm-diameter specimens with a surface ground roughness. Again, duplicates were shown for the stress-strain profiles to signify the repeatability. The EAF stress-strain profile is much lower than the conventional compression profile, when compared to the 4.76mm-diameter specimen stress-strain profiles above.

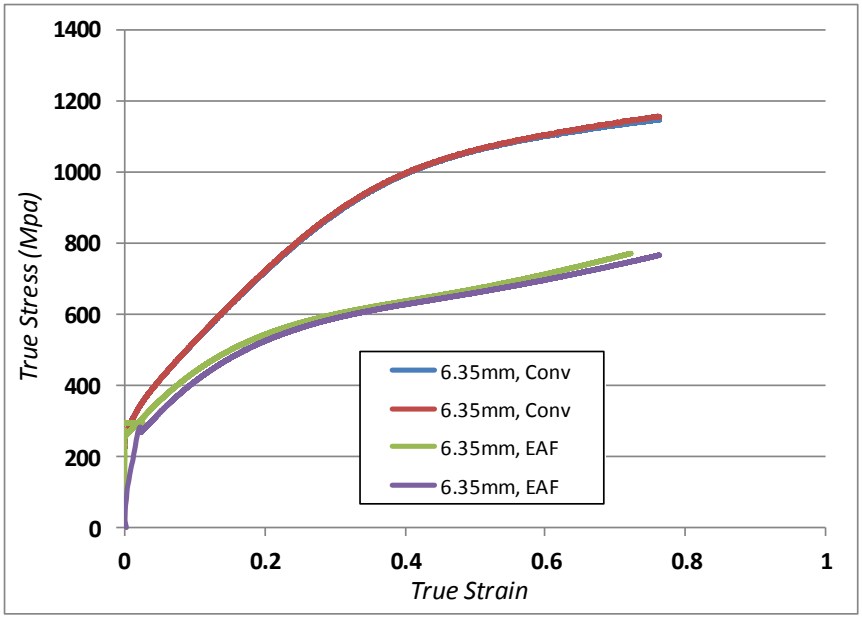

Figure 107. Stress-strain profiles (6.35mm diameter surface ground specimens). The stress-strain profiles for the EAF tests are much lower than the conventional tests. Additionally, the difference between the conventional and EAF tests increases as the strain is increased.

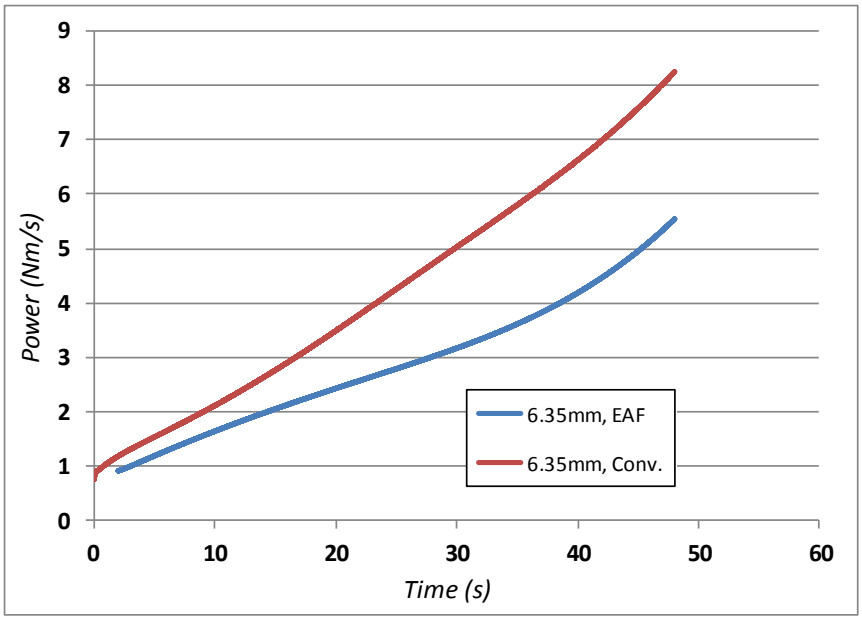

Figure 108. Mechanical power profiles (6.35mm diameter surface ground specimens). The difference in the mechanical power profiles of the conventional and EAF tests increases as the tests progress.

Figure 109 and Figure 110 show the stress strain profiles and mechanical power profiles for conventional compression and EAF tests at 20A/mm^2 run on the 4.76mm-diameter specimens with a "Large CA" surface roughness.

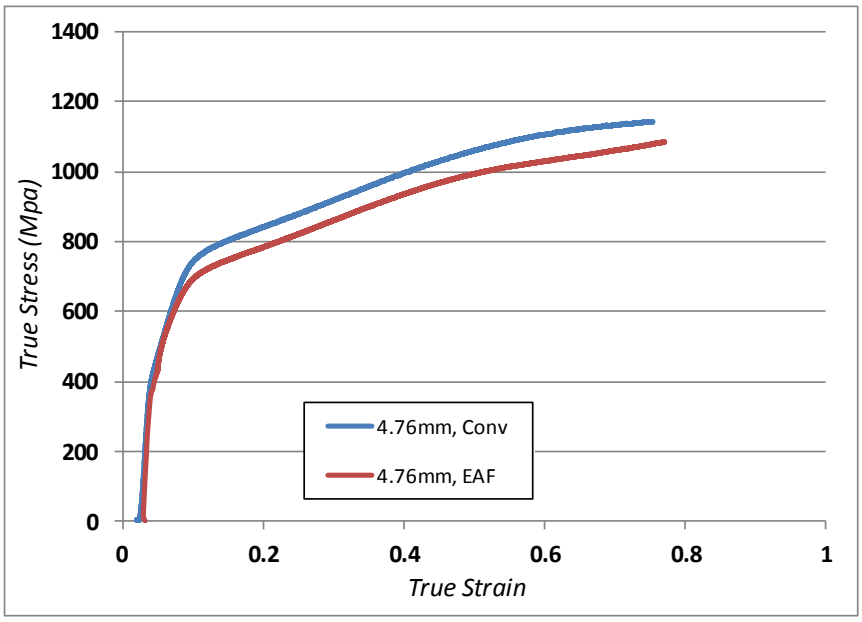

Figure 109. Stress-strain profiles (4.76mm diameter Large CA specimens). The stress-strain profile for the EAF test is slightly lower than the conventional stress-strain profile.

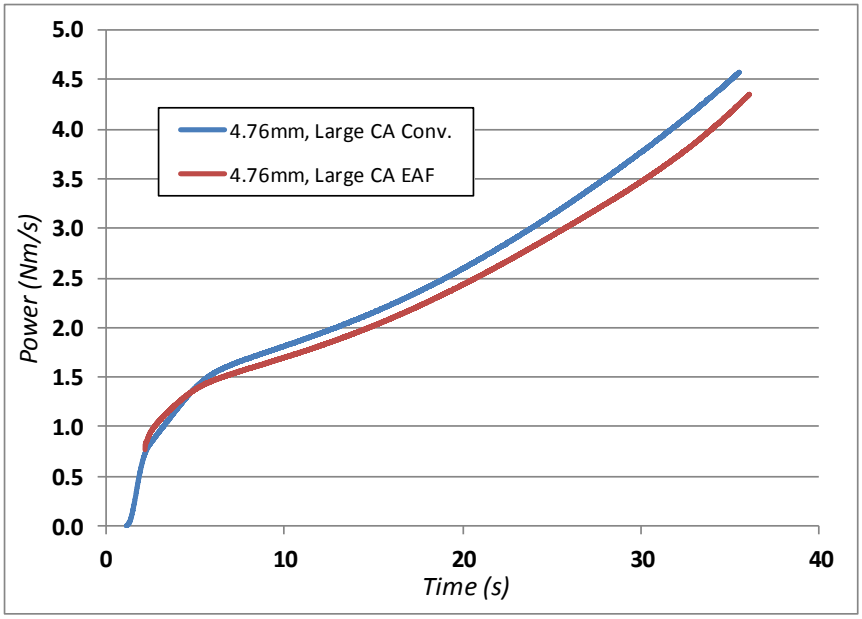

Figure 110. Mechanical power profiles (4.76mm diameter Large CA specimens). The mechanical power profile for the EAF test, is slightly lower than the conventional test, which is consistent with the surface ground specimens in Figure 106.

Figure 111 and Figure 112 show the stress strain profiles and mechanical power profiles for conventional compression and EAF tests at 20A/mm^2 run on the 6.35mm-diameter specimens with a "Large CA" surface roughness.

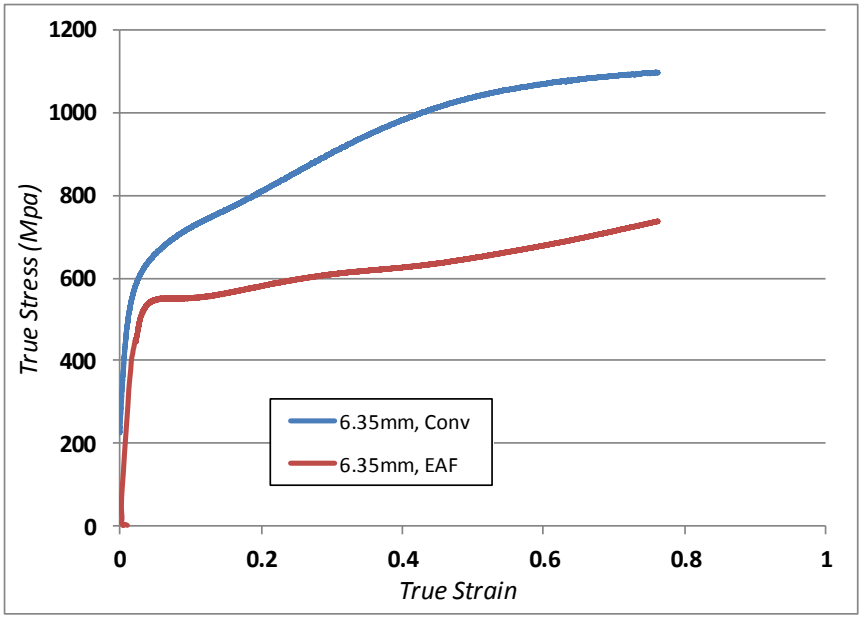

Figure 111. Stress-strain profiles (6.35mm diameter Large CA specimens). The difference in the stress-strain profiles of the conventional and EAF tests increases, as it did with the surface ground specimens.

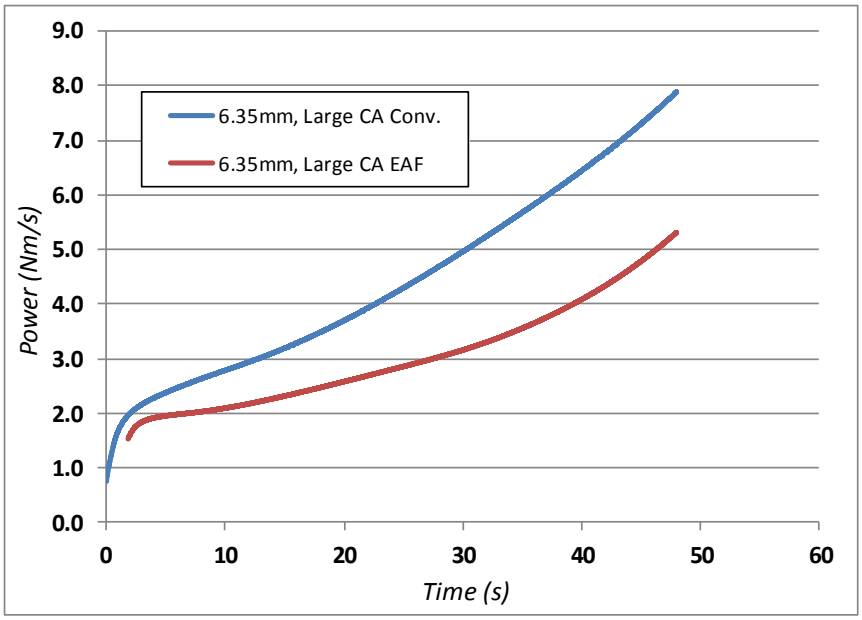

Figure 112. Mechanical power profiles (6.35mm diameter Large CA specimens). The difference in the mechanical power profiles is the same as the difference in the stress-strain profiles for these particular specimens.

Figure 113 and Figure 114 display the EEC profiles for 4.76mm- and 6.35mm-diameter specimens that have been prepared by surface grinding and by enhanced asperities, respectively. Of note is that the general EEC profiles for the surface ground and enhanced asperities surface conditions are very similar for both specimen sizes (when comparing the top and bottom EEC profile in one figure to the same profile in the second figure). With this being said, it can be concluded that that the overall starting contact area is insignificant to the effectiveness of the EAF technique, unless only the elastic region is considered. Furthermore, when considering the contact area for modeling EAF in manufacturing processes, it could be neglected since the part will primarily be in the plastic region (since it will be deformed).

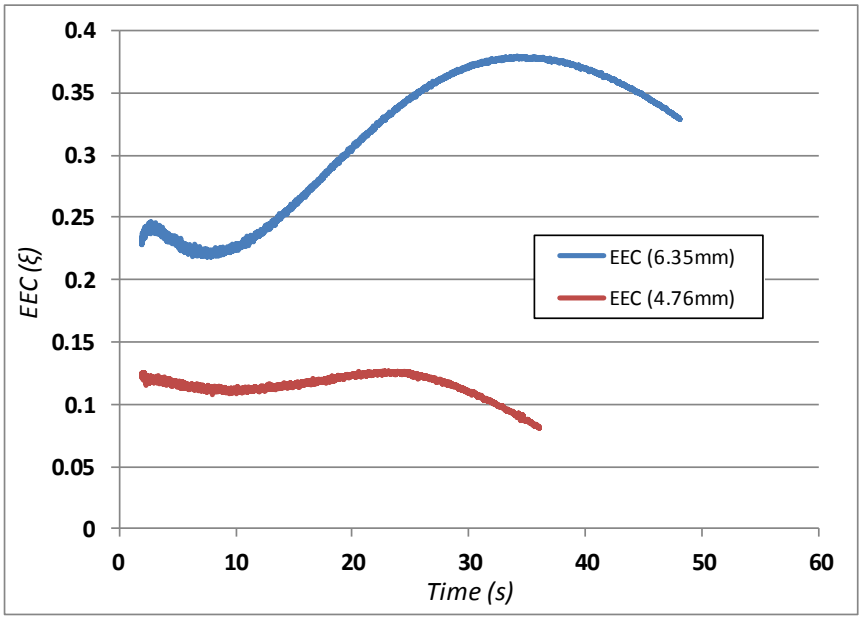

Figure 113. EEC profiles (4.76mm and 6.35mm diameter surface ground specimens). The EEC profiles for both specimen sizes show an increase and then a decrease towards the bottom of the test. These profiles are not consistent with other material EEC profiles because the compression speed used to generate these profiles was much slower.

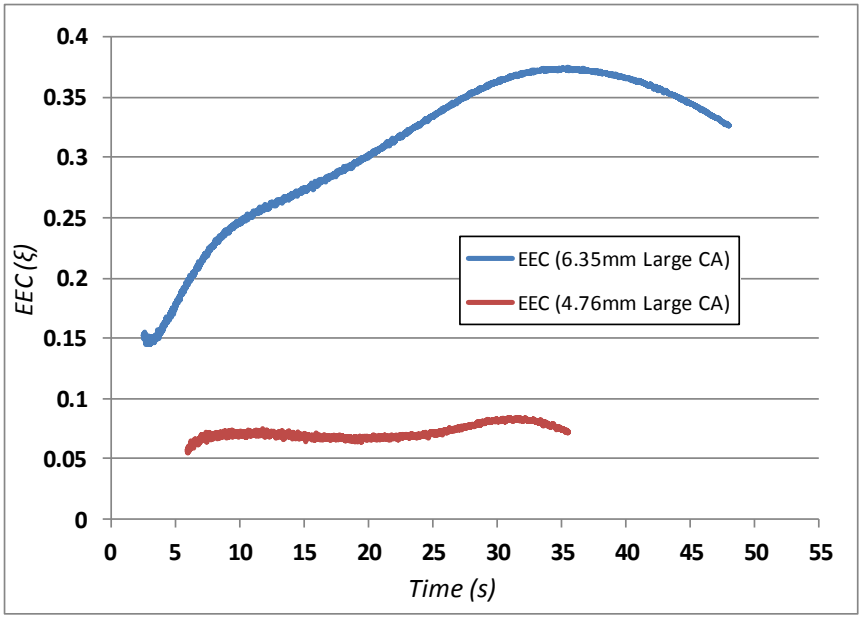

Figure 114. EEC profiles (4.76mm and 6.35mm diameter Large CA specimens). The EEC profile for the larger specimen was much higher compared to the smaller specimen.

6.1.8. EAF/Contact Area Conclusions

Several of the contact area references found, focused on trying to predict the roughness or bearing area of the material [101]-[106]. Of note is that all of these papers concentrated on elastic deformation regime of the material, under low localized loads. The examination in this thesis examined surface roughness under both elastic and plastic loadings, over the entire apparent area of the specimen. The following are a list of conclusions about the EAF/Contact Area research:

- The post-formed surface roughnesses at the die/workpiece interfaces become worse as a higher magnitude of applied electricity is used.
- There is a clear trend in that, as the applied static load is increased for a given amount of current, the overall temperature of the specimen will decrease. However, this was found to only be valid within the elastic regime on the specimen. For the enhanced asperity specimens, where the plastic regime was reached in the asperity region, the temperature from the stationary-electrical tests did not change.

- The EEC profiles from the same EAF tests run on surface ground specimens and specimens with enhanced asperities were very similar, thus indicating that the contact area does not have much of an effect on effectiveness of EAF outside of the elastic region. Hence, this is possibly why there is such a focus on contact area for electrical connectors, where all components are in the elastic region.
- When attempting to model the EAF technique for a forging process, the contact area is insignificant because the manufactured part will always be in the plastic region since it is being deformed.

6.2. Tribological Effect

This section will contain an exploration into the effects of applied electricity on the tribology within an EA-Forging process [107]-[108]. Specifically, within this chapter, the general effects of the electricity on tribological conditions will be explained, the experimental setup and procedure for this section will be described, the method by which the friction calibration curves were determined will be given, test procedures will be stated, candidate metal forming lubricants will be introduced, experimental results and discussion will be detailed, an evaluation of the lubricants based on the reduction in the forming load will be noted, temperature measurements will be provided, and the section will be summarized with conclusions.

Because most metal forming operations incorporate some type of lubricant, it is necessary to generally understand how different lubricant compositions/types react while used in an EAM compression test. Although there is no true record that traces lubricant use to a particular time period, it can be assumed that lubricants were being used to assist metal deformation as early as 5th century B.C. Until the mid-1940's, lubricants remained relatively unrefined, consisting of seed or animal oils/greases. Around the later part of the 19th century,

increasing demands from the aerospace, chemical, and electronic industries led to the development of new exotic metals with which ordinary lubricants were not sufficient. These new metals, along with increased production and heavier material reductions, significantly increased the severity of the conditions on the lubricant. Hence, much effort has supported tribology research in the last half century [109]. One of the directions in lubricant research is to replace the widely used zinc-phosphate-based lubricant which, despite its excellent qualities, presents the disadvantage of being polluting.

Depending on the type of lubricant, type of manufacturing process, and the severity of the forming, metal forming lubricants can serve different purposes. Overall, the main functions of any metal forming lubricant are to reduce or control the friction at the workpiece/die interfaces and control the temperature of the workpiece. Different lubricant compositions use various lubrication regimes to accomplish this feat. By controlling friction, a manufacturer can achieve reduced tool/die wear and improved surface finish. Additionally, by controlling the temperature of the workpiece, the lubricant can produce an overall cooler or hotter part (*i.e.* the lubricant can insulate heat to keep the part hot during forming, or it can help to keep the part cool by transferring the heat rapidly). Some form of lubrication is used in almost every metal deformation process, and the continuous effort to produce better state-of-the-art lubricants confirm the critical nature of their role in the metal deformation process.

Lubricants are used in almost all metal forming operations and, before EAF can be used to potentially replace a widely-used forming technique such as hot working, IF, or TWB's, its impact and effect on metalworking lubricants must first be evaluated. The objective of this work was to investigate the influence of the presence of electricity on the tribological conditions at the die/workpiece interface. Ring compression tribo-tests are conducted and the performance of several lubricants is studied. By combining the experiments and finite element simulation results,

friction coefficients and field effects on friction can be estimated, and possible lubricant candidates to be used in EAF processes identified.

6.2.1. Effects of Electricity on Tribological Conditions

Friction is present at the workpiece/die interfaces, thus lubricants play an important role in forming. They reduce the frictional forces, thus the power consumption, and also improve the formability of the material and surface finish of the final part. In conventional forming, an effective lubricant exhibits a high level of adhesive strength in order to follow the surface expansion without breaking down. In addition, the lubricant must withstand high pressures (up to 2500 MPa in conventional forming), and the interface temperature may reach 200ºC [94] and [110]. But when electricity is applied through the dies and workpiece, it may influence the tribological conditions. Careful attention to the effects of the electricity is needed when selecting the lubricants for EAF due to their complex interaction (Figure 115).

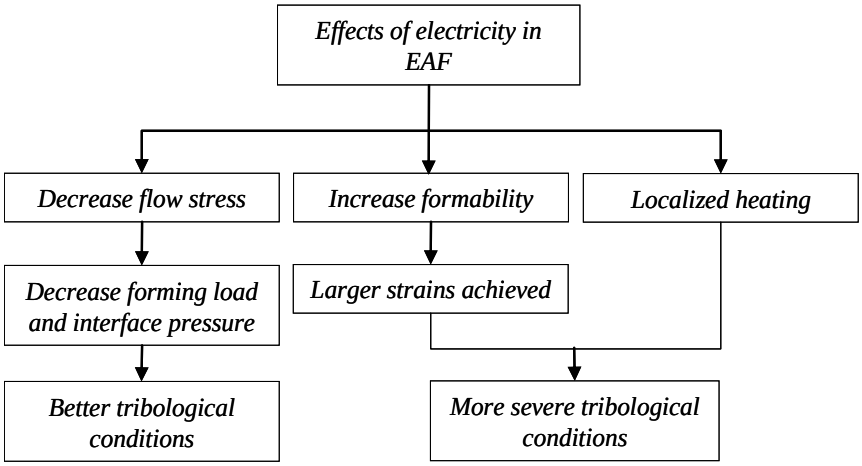

Figure 115. Tribological effects of EAF [107]-[108]. As the electricity is applied to the manufacturing process, it increases the formability of the part, however, it can also have negative effects on the tribological effects at the die/workpiece interfaces.

One effect of the electricity is the decrease in forming load, thus the decrease of the interface pressure, resulting in a better lubrication regime. At the same time, a higher temperature at the workpiece/interface decreases the lubricant viscosity and favors evaporation and chemical decomposition of the lubricant. Thus, the reduced quantity of lubricant and possible modified chemical attributes are not able to continue providing sufficient separation. Metal-to-metal contact between the asperities of the dies and workpiece occurs, resulting in higher friction, die wear, and poor surface quality. In conclusion, one requirement for a good metal forming lubricant for EAF is the capacity of retaining its lubricity at elevated temperatures and in the presence of electric current fields. The objective of this paper is to present the challenges brought by this process, and to screen the performance of a few selected lubricants through electrically-assisted ring compression tests.

6.2.2. Experimental Setup and Procedure (Ring Tribo-Tests)

To evaluate the performance of the three selected lubricants, the ring compression tribo-test was used. This is a relatively simple test that can mimic the medium-to-severe deformation occurring in an actual forming operation. The testing setup for these experiments is shown in Figure 116. The insulated dies, consisting of a combination of A2 steel and reinforced plastics, are securely gripped by the top/bottom platens of the 250 kN-capacity Instron hydraulic testing machine. Electrical cables are fastened to the top and bottom dies, and the insulation ensures electricity flows through the dies/workpiece in a closed loop. The electricity is applied continuously from the beginning to the end of each test.

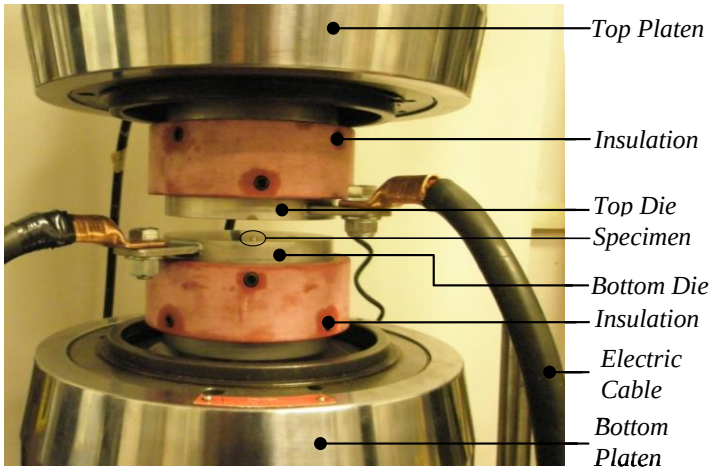

Figure 116. Test setup for EAF tribological evaluation [107]-[108]. This test setup included insulated top and bottom dies that compressed ring compression samples, while thermal and mechanical data were collected.

The ring compression specimens used in this work were manufactured from a rod of 304 Stainless Steel. The rod was received as precision ground to a diameter of 4.763 mm, and cut to a height of 2.10 mm using a wire EDM. Then, a drilling operation was performed using a CNC lathe to create the 2.38 mm inside diameter. Careful measures were taken to ensure the repeatability and flatness of all specimen surfaces in contact with the dies.

The purpose of the ring compression test is to establish a correlation between the friction conditions at the workpiece/die interfaces and the ratio of the reduction of the inner diameter, and use it to quantify the existing friction conditions. The internal diameter of the ring is very sensitive to the friction conditions. If the friction is low, than the internal diameter increases, but if the friction is high, the inner diameter reduces (Figure 117). The shear friction for the lubricant can be estimated when the inner diameter reduction corresponding to a certain height reduction is measured. This value is superimposed on friction calibration curves determined using finite element analysis (FEA) [111]-[112].

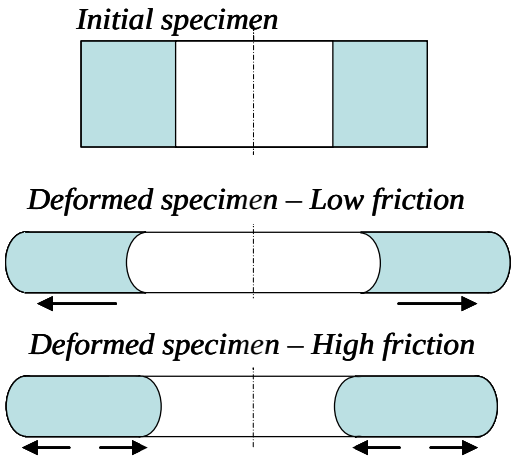

Figure 117. Effect of friction on the deformation pattern [107]-[108]. If there is low friction, the inside diameter of the ring compression specimen will increase throughout the test. Conversely, if there is high friction, the inside diameter will decrease over the duration of the test.

6.2.3. Determining Friction Calibration Curves

For this study, the shear friction is considered, which is more applicable for bulk forming than Coulomb's Law, which uses the coefficient of friction. The friction shear law is written as eq.(61):

$$\tau = m\bar{\sigma}/\sqrt{3} = mk_{shear} \tag{61}$$

where τ is the shear stress, $\bar{\sigma}$ is the flow stress, k_{shear} is the shear strength, and m is the friction factor, which ranges between 0 and 1. Friction calibration curves, determined through FEA are used to estimate the friction factor of the tested lubricant. The simulations were run for 304 Stainless Steel with initial dimensions as specified earlier, for different friction factors, m.

The electric energy applied does not go exclusively into resistive heating, but also into aiding deformation trough various mechanisms. The existing finite element software cannot take into consideration the complex effect of the electricity on the deformation process or on the

lubricant, but it can implement the thermal effect, which results mainly in lowering the flow stress. The electrical current applied contributes to a temperature rise in the billet proportional to the current density and application time. Since the temperature distribution in the workpiece and dies cannot be accurately predicted analytically yet, preliminary electrically-assisted tests were carried out and temperatures were measured. In order to replicate the conditions of the real test, non-isothermal finite element simulations were carried out by considering heated dies and workpiece at a temperature observed in the EAF test. Two types of tests were simulated for different friction coefficients: (*i*) compression at room temperature, and (*ii*) compression at elevated temperature, specifically 200°C and 300°C for the dies and ring specimen, respectively. All the other experimental conditions, such as the material, dimensions, and compression speed were incorporated into the simulations. Although the temperature was observed to have a significant influence on the forming load, due to decreasing the material flow stress, the effect on the inner diameter reduction was insignificant. The comparison between the two conditions is shown in Figure 118. In conclusion, for ease of comparison, the calibration curves used further for superimposing the experimental data will be the set determined at 20ºC.

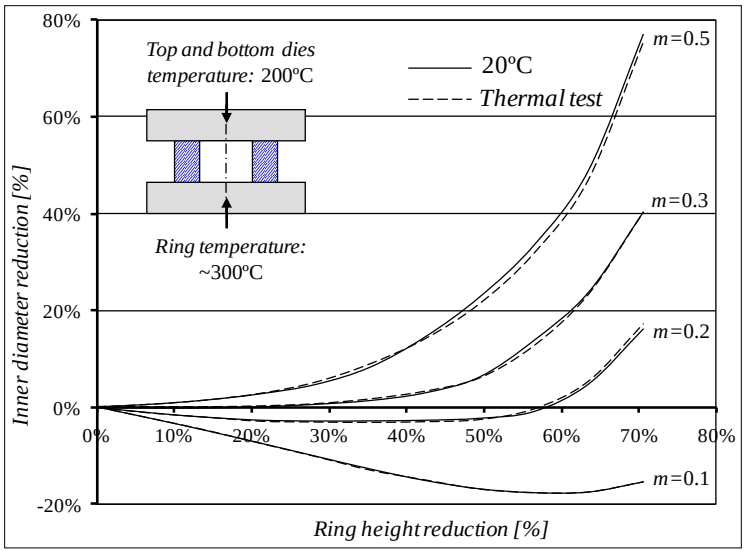

Figure 118. Friction calibration curves for tests at room temperature and at an elevated temperature [107]-[108]. The friction calibration curves were tested at room temperature (20°C) and at an elevated temperature that was respective of what would be reached during an EAF test (300°C).

6.2.4. Testing Procedures

For this work, the effectiveness and compatibility of three metal forming lubricants with EAM is assessed using tribo-tests. Prior to testing, specific measures were taken to ensure consistency. The ring compression specimen was submerged into the lubricant. After excess lubricant was allowed to drip off, the evenly-coated specimen was placed between the dies. Before deformation began, a preload of 300N was placed on the specimen to ensure contact between workpiece/dies, thus providing a path for the electricity to travel and avoid generation of electrical sparks. After this, the ring specimens were compressed at a rate of 6.35mm/min to strokes of 1mm and 1.3mm. Figure 119 displays a ring specimen prior to deformation, deformed to a stroke of 1mm (Stroke 1), and deformed to a stroke of 1.3mm (Stroke 2).

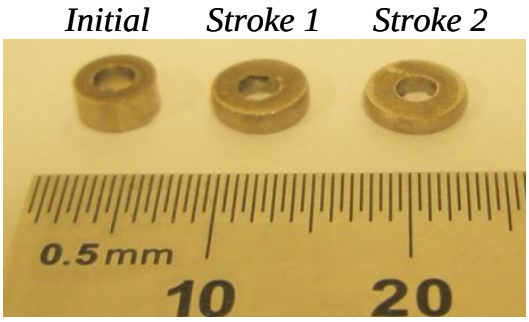

Figure 119. Initial and deformed ring compression samples [107]-[108]. Shown is the initial undeformed ring compression sample, as well a sample that has been deformed to the two different strokes used for testing.

For each stroke, three electrical conditions were evaluated: (*i*) conventional forming (no electricity), (*ii*) a current density of 25A/mm^2 (333Amps), and (*iii*) a current density of 35A/mm^2 (467Amps). The voltage across the specimens was measured at the beginning of the tests. Specifically, the voltage for a current density of 25A/mm^2 was 110mV and the voltage for a current density of 35A/mm^2 was 160mV. From Perkins et al. where the same stainless steel alloy was tested under electrical conditions, the "electrical threshold" (*i.e.*, minimum current density where enhanced formability effects are first observed) was determined to be around 18A/mm^2 [40]. Hence, with the current densities and deformation speeds used in this work, the threshold will be met and exceeded.

For the tests where electricity is present, current is applied at the start of deformation and is ceased when the desired stroke is displaced. Note that the current densities mentioned here are initial values. A constant current (variable voltage) power supply was used to produce the electricity and maintain a constant current throughout the duration of each test. Specifically, as the specimen deformed, the resistance decreased and therefore the voltage was decreased to maintain the specified current. However, while the current is constant, the specimen area increases, thus the current density decreases during a test. For each combination of lubricant, stroke and current density, a number of three-to-five replicates were run to ensure repeatability.

6.2.5. Candidate Metal Forming Lubricants

There are four groups of lubricants used in metal forming processes: water based, oil based, synthetic, and solid film. The choice of the lubricant for one specific process takes into consideration a multitude of process variables that may influence the effectiveness of the lubricant, such as: interface pressure and temperature, sliding velocity, surface expansion, tool and workpiece material properties and geometries, and surface topography [110]. For EAF, there are two more aspects to consider: dielectric permittivity, and higher temperatures at the interface, which may require the presence of pressure additives (EP). For this study, three lubricants were selected: (*i*) Renoform OL569NE (oil-based lubricant), (*ii*) TufDraw 1919 (water-based lubricant), and (*iii*) SynDraw 1310D (synthetic lubricant). Table 16 summarizes some characteristics of the lubricants.

Table 16. Metal forming lubricants analyzed with EAF [107]-[108].

Lubricant	Lubricant characteristics
Renoform OL569NE	• Petroleum-based • Light duty • Exhibits high lubricity from a lard oil additive • Viscosity at 40ºC: 11.5 cSt
TufDraw 1919	• Water dilutable petroleum-based • Heavy duty • Has chlorinated paraffin extreme pressure additives and a proprietary binder/lubricity additive, used 1:1 with water • Viscosity at 40ºC: 400 cSt
SynDraw 1310D	• Water-based synthetic, non-petroleum • Medium duty • Has phosphate ester extreme pressure agent and fatty ester lubricity additives • Viscosity at 40ºC: 110 cSt

6.2.6. Experimental Results and Discussion

Lubricant Evaluation Based on Shear Friction Factor

The reduction of the inner diameter was determined for all the specimens, and the values were superimposed on the friction calibration curves determined earlier for the corresponding ring height reduction. The friction factor was quantified for each lubricant for conventional forming and EAF. Figure 120 shows in (*a*), (*b*) and (*c*) the measurements used to interpolate *m*.

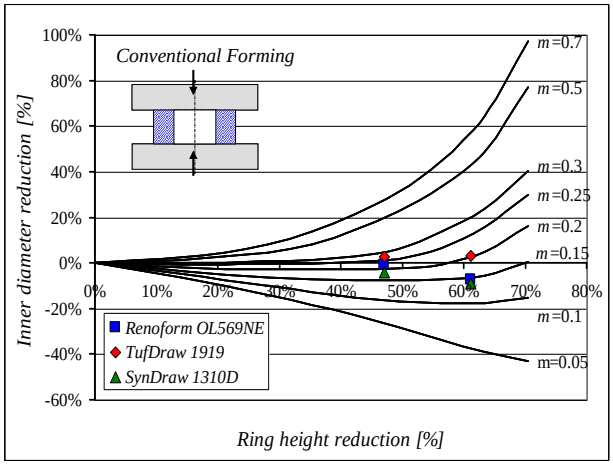

(a)

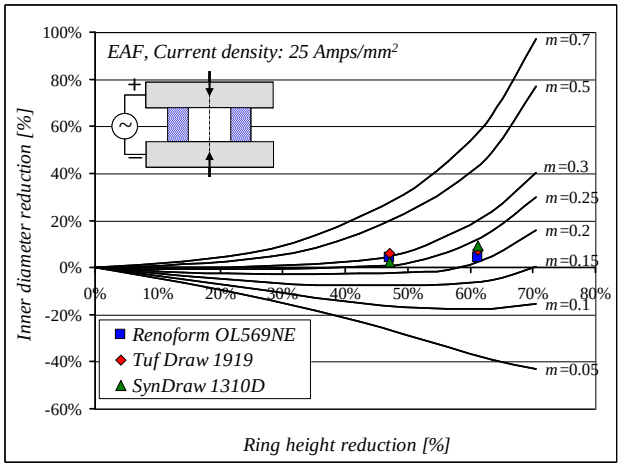

(b)

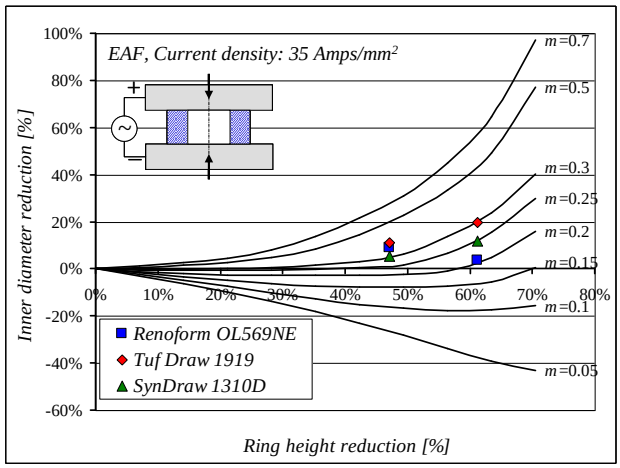

(c)

Figure 120. Friction calibration curves and friction factors for the three lubricants tested [107]-[108]. The friction factors were calibrated for several different applied current densities: (a) Conventional forming, (b) EAF at 25A/mm^2, (c) EAF at 35A/mm^2.

Figure 121 shows the evolution of an average current density-dependent friction factor for each lubricant. Conventional forming was represented by a current density of 0 A/mm^2. The oil-based lubricant exhibited an average friction factor of m = 0.18 in conventional forming. However, when the electricity was applied, the friction factor went to 0.25 and 0.28, respectively. The synthetic lubricant initially exhibited a slightly lower friction factor, but it reached the same values when the electricity was applied. The poorest performance was exhibited by the water-based lubricant, which in conventional forming had the highest average friction factor (m = 0.24), and increased up to m = 0.34 for a current density of 35 A/mm^2. This evolution observed with the current density suggests that the dielectric permittivity of the lubricant has less effect on the lubricant performance under electricity, than the temperature rise. The heat generated will result in more severe evaporation for a water-based lubricant.

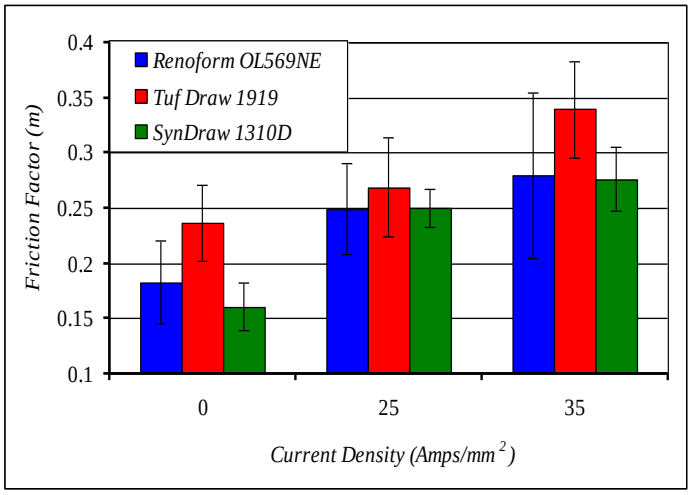

Figure 121. Average friction factors [107]-[108]. The average friction factors in relation to the applied current densities are shown. TuffDraw 1919 consistently had the highest average friction factor.

Note that the error bars depicted in the figure indicate some scattering, which is to be expected when forming micro-scale specimens. At this scale, small differences in material structure, specimen dimensions or applied current may result in variation of the results.

The effective increase in friction with current density can be observed in the flow pattern of the material and increase in the barrel shape. Figure 122 shows magnified images taken on a section of the ring, for a deformed specimen at 0, 25 and 35 A/mm^2. The lubricant used was TufDraw 1919. The specimens were carefully cut on a CNC milling machine. Then, sectioned rings were mounted in resin for the metallographic preparation. Grinding, polishing and etching were performed on the specimen, in order to have a clear delimitation of the grains. Thus the specific 'x' shape of the higher localized strain could be observed with an increase in current density.

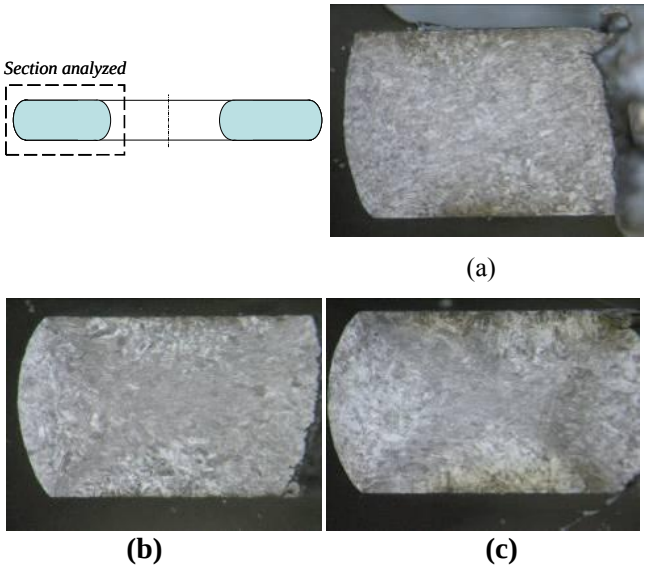

Figure 122. Sections of deformed ring compression samples [107]-[108]. The deformation patterns are different for the different applied current densities: (a) Conventional forming, (b) 25A/mm^2, and (c) 35A/mm^2 (Mag 50X). Lubricant: TufDraw 1919.

To re-emphasize the results discussed in Figure 91, an increase in friction can also be observed from the increased surface roughness of the ring specimens. Preliminary measurements

indicated that the roughness increased from 0.89µm in conventional forming, to 1.24µm at 25A/mm^2, and 1.4µm at 35A/mm^2.

6.2.7. Lubricant Evaluation (Reduction in Forming Load)

When electric current is superimposed on the deformation, the forming load is reduced. Figure 123 shows the compressive force vs. stroke displacement plots for Renoform OL569NE. The plot contains the load profile for a conventional test, a test at 25A/mm^2, and a test at 35A/mm^2.

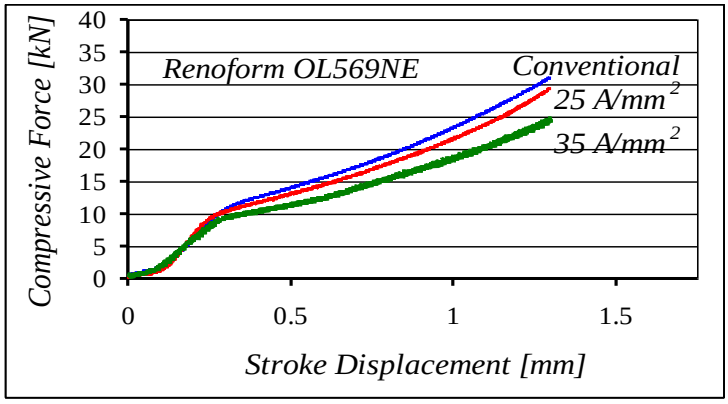

Figure 123. Forming load profiles for Renoform OL569NE [107]-[108]. As the applied electrical power is increased, the overall forming load profiles decreases.

A comparison between the reductions in forming load recorded for all three lubricants is shown in Figure 124. The reduction was calculated using eq.(62):

$$Reduction = \frac{F_{conv} - F_{EAF}}{F_{conv}} \qquad (62)$$

where F_{conv} is the average forming load recorded in the conventional test, represented in the figure by 0 A/mm^2, and F_{EAF} is the forming load recorded in the EAF test.

For Renoform OL569NE, the current densities of 25A/mm^2 and 35A/mm^2 were able to reduce the final forming force by about 8% and 22% compared to the conventional test. Tuf Draw 1919 further decreased the compressive loads to about 16% and 29%, compared to its respective conventional test. Similarly, SynDraw 1310D was able to show force decreases of 15% and 28%. When coupled with EAF, Tuf Draw 1919 and SynDraw 1310D produced greater force reductions compared to their respective conventional forming test.

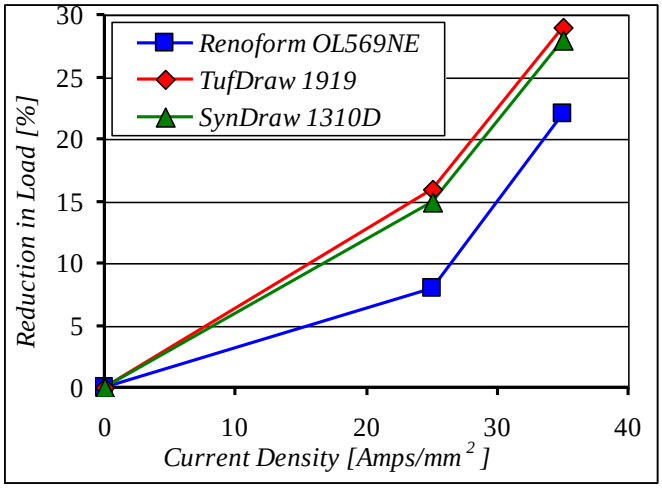

Figure 124. Reduction in the forming load vs. current densities for all lubricants tested [107]-[108]. Renoform OL569NE showed the lowest overall reduction in the forming load, whereas the other two lubricants showed comparable reductions in the forming load.

6.2.8. Temperature Measurements

A thermal camera measured the temperature distribution on specimens as they compressed throughout the test. The thermal measurements were taken using a FLIR Systems ThermoVision A40 camera, calibrated for a temperature range from 0 to 500°C, and checked at room temperature, with an accuracy of ±2°C, and spatial resolution (IFOV) of 1.3 mrad. The

temperature was measured for three tests: (*i*) stationary tests, when electricity is applied through the specimen, but when there is no deformation, just preloading to ensure contact and no electrical spark, (*ii*) an EAF compression test, and (*iii*) a conventional compression test. In order to measure the temperature rise during the tests, no lubricant was used during these tests. The specimens were cylindrical, with the same diameter as the outer diameter of the ring samples, and a height of 4 mm. The same material and same test conditions as for rings were used. For a higher emissivity factor and more accurate readings, the specimens were painted black. The thermal profiles were calculated using ThermaCAM software. Specifically, the software allowed for the selection of an area on the specimen. Then the maximum value in the area was recorded at a frequency of 1/250 seconds until the user ended the recording.

For the stationary test and a current density of 25A/mm^2, the temperature increased rapidly up to approximately 310ºC (Figure 125). The second test, which was an EAF compression test, exhibited a different behavior. The temperature increased initially up to 105ºC, and then it started to decrease, before turning off the electricity. During the conventional compression test an increase of maximum 10°C was recorded. A few conclusions are reached from these tests:

The temperature measurements during the EAF test agreed with other studies that indicated a temperature between 100-200ºC [40]. The low temperature rise during the conventional compression test suggests that the increase in temperature in the electrical tests is due to the resistive heating. The large difference in temperature rise between stationary and EAF tests can be partially attributed to the change in specimen surface area during the deformation, which affects the heat-transfer through convection and conduction. Note though that the change in total area of the specimen was less than 1.5%, which cannot explain the drastic drop in temperature between the two tests. This leads to the conclusion that a significant part of the electric energy is actually imparted by the flow of electrons to the material and this aids the

deformation by various mechanisms, as described earlier, and the remaining energy is converted into heat [66]. Thus the higher temperatures recorded at the beginning of the test may result in rapid evaporation of the lubricant, and potentially change in a less favorable lubrication regime.

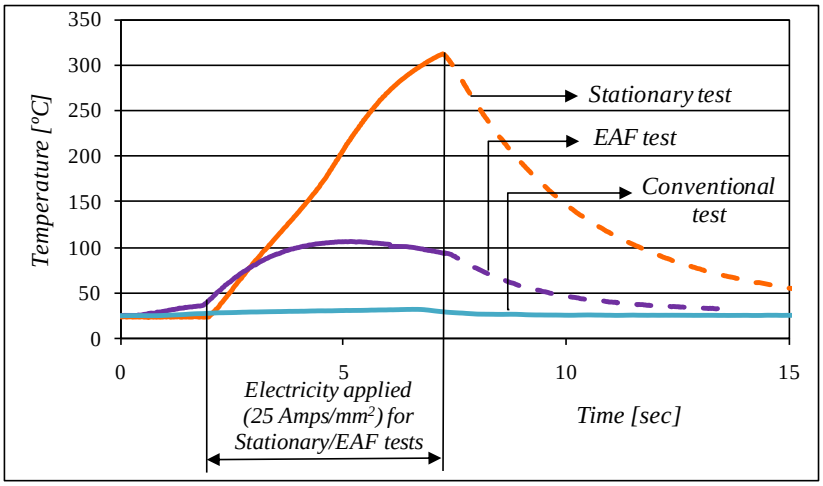

Figure 125. Temperature profiles of stationary-electrical and EAF tests [107]-[108]. The stationary-electrical test at the same current density is much hotter than the EAF test. This supports the idea that the electrons aiding with the plastic deformation of the material.

6.2.9. EAF/Tribology Conclusions

The advance of EAF for larger-scale applications depends on identifying a well-performing lubricant. Three lubricants chosen from three different groups were tested under different current densities and their performance was evaluated. The ring compression tribo-test was used and a friction factor was determined from the friction calibration curves generated through finite element analysis. The following conclusions were drawn from this study:

- The use of electricity during deformation processes has beneficial effects in reducing flow stress, thus the energy required to reach the same level of deformation as in conventional forming is lower. Also, larger strains are reached for the same mechanical load.

- The lubricants analyzed indicated more severe tribological conditions with the application of electricity and with the increase of current density. The higher temperatures resulted in rapid evaporation of the lubricant and chemical decomposition, thus the lubrication mechanism changed to a less favorable regime.
- Although the forming load, thus the interface pressure, decreased in all cases when the electricity was applied, there is potential for even more reduction if the lubricant withstands the effects of electricity. The higher temperatures suggest that pressure additives are needed in order to maximize the efficiency of the process.
- The oil-based/synthetic lubricants performed better than water-based lubricants. Thus it is recommended that the development of the lubricants for EAF should take into consideration the temperature rise, rather than just dielectric permittivity.

7. Grain Size Effect on EAF (Task #6)

The grain size of a metal has a large impact on formability parameters of the material, such as yield and ultimate strength, and percent elongation prior to fracture. Previous researchers have noted these relationships between the grain size and forming characteristics of various metals [113]-[115]. Since it is speculated that the flowing electrons and dislocations will become held up at the grain boundaries, the effect of grain size on the effectiveness of EAF is explored in this section. Specifically, 6.35mm-diameter 304 Stainless Steel specimens were heat treated, using three different temperature and time combinations, to create three different size grain structures. Conventional compression, stationary-electrical, and EAF tests were run on the different specimens in an attempt to quantify the effects of the different grain sizes. This chapter will consist of: 1.) an explanation of the heat treating and resulting grain sizes, 2.) a description of the microstructure specimen preparation grain size measurement procedure, and 3.) an experimental grain size EAM investigation through the types of tests referenced above.

7.1. Importance of Grain Size on EAF Effectiveness

In the theory explaining how electricity affects a metal, there are published theories about how the electrons can provide the dislocations the 'push' they need to surpass lattice obstacles [51]. One main lattice obstacle is a grain boundary. Grain boundaries are areas of dislocation build-up, which reduces the ductility of the metal before failure, and increases with increasing number of dislocations (strain hardening effect). It is already known that different grain size materials produce different flow stress profiles. Consequently, samples of the same material with different grain sizes should react differently to the same electrical power characteristics. In this chapter, conventional compression, stationary-electrical, and EAF compression tests will be run

on the same material with several different grain sizes to determine the grain size-EAF effectiveness relationship.

7.1.1. Specimen Preparation and Resulting Grain Sizes

All specimens were produced from the same initial rod of annealed 304 Stainless Steel, and once the compression slugs were cut to size, they had to be heat treated to produce different grain sizes. Figure 126, Figure 127, and Figure 128 display the temperature and time curves, which are respective of the different heat treatments performed to produce different grain sizes. Specifically, the cycle of 1950°F at 0.5hr produced the nominal grain size, the cycle of 1850°F for 1hr produced the smallest grain size, and the cycle of 1650°F for 1.5 hrs produced the largest grain size. In the figures, the red line represents the thermocouple on the part, the black/blue lines represent the furnace temperature, and the purple line represents the vacuum constancy. Table 17 summarizes the time and temperature of each heat treatment, and the actual resulting grain size.

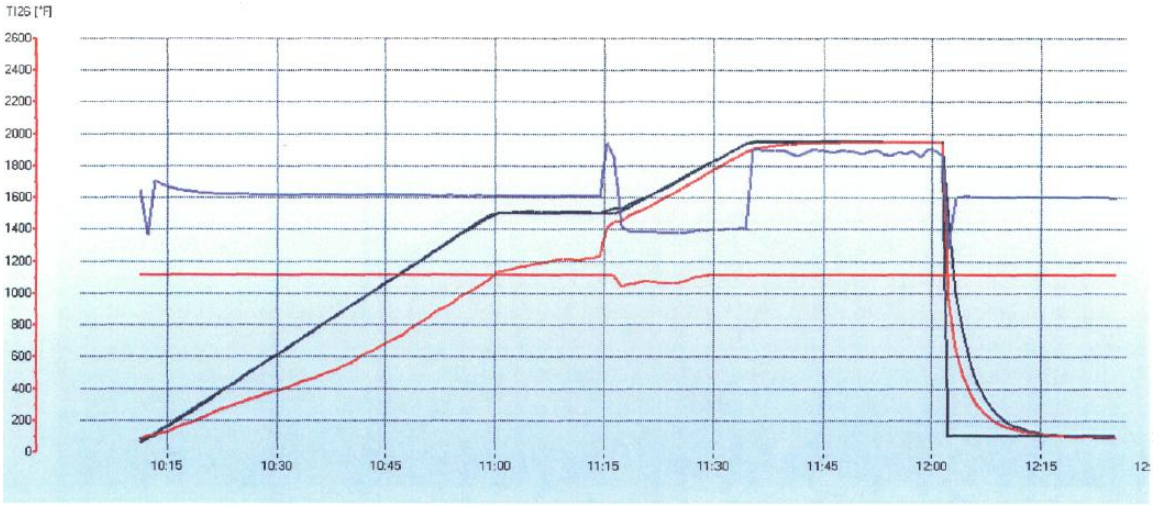

Figure 126. Temperature vs. time profile (1950°F for 0.5 hrs). The supplied chart shows the specimens in this batch were treated at 1950°F for 0.5 hours.

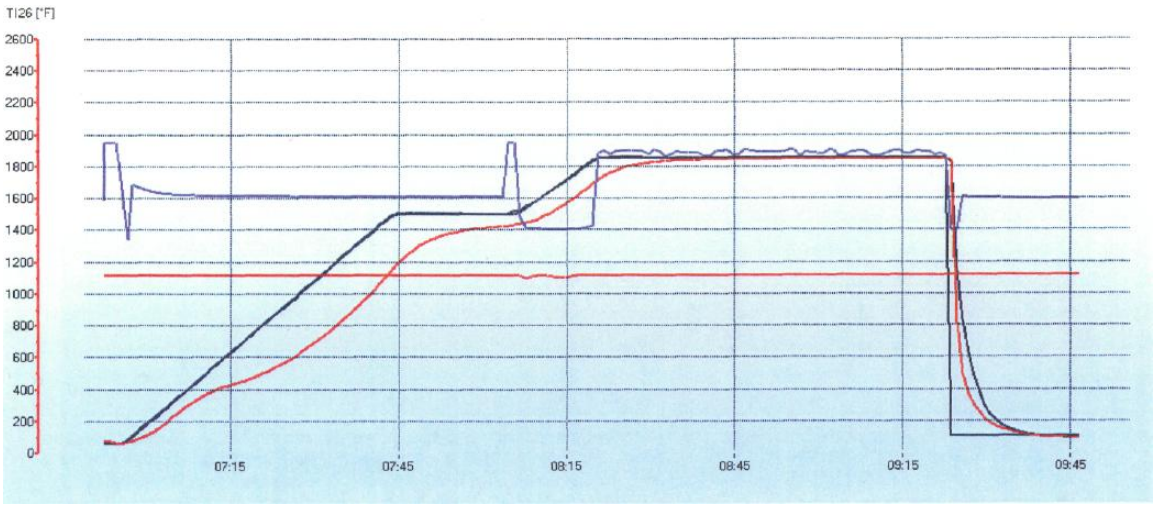

Figure 127. Temperature vs. time profile (1850°F for 1 hr). The supplied chart denotes that the specimens in this batch were heat treated at 1850°F for 1 hour.

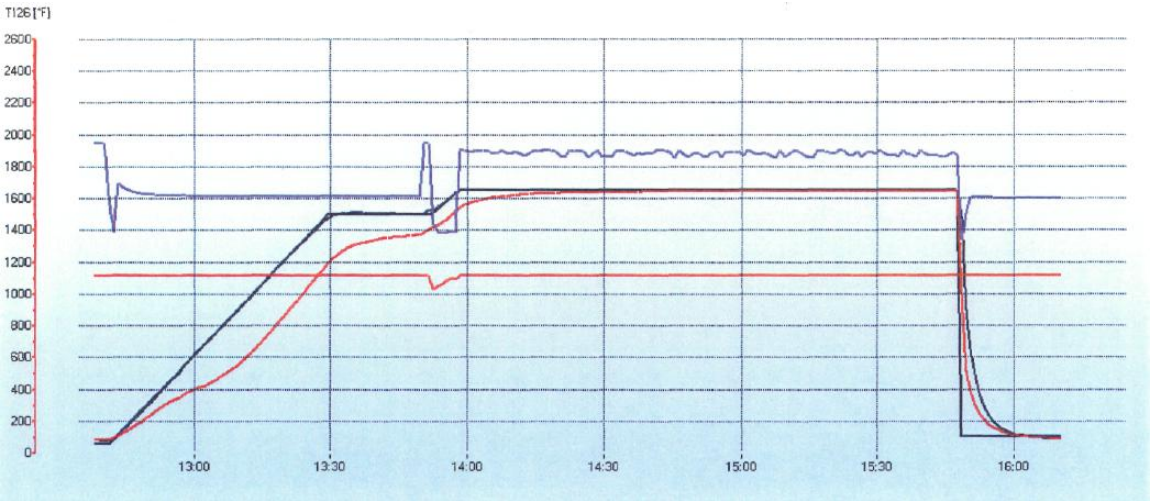

Figure 128. Temperature vs. time profile (1650°F for 1.75 hrs). The supplied chart shows the specimens in this batch were treated at 1650°F for 1.75 hours.

Table 17. Summary of the average starting grain sizes.

Part #	**Temperture** (°F)	**Time** (hrs)	**Avg Grain Size** (μm)
1	1950	0.5	21.99
2	1850	1	15.08
3	1650	1.5	27.2

7.1.2. Microstructure Preparation/Grain Size Measurement

In order to determine the average grain size for each respective heat treatment, a Zeiss Axiovert 25 inverted optical microscope, equipped with a uEye camera, and Buehler OmniMet software were used to generate microstructure pictures and then measure them. The microscope and the computer equipped with the software can be seen below in Figure 129.

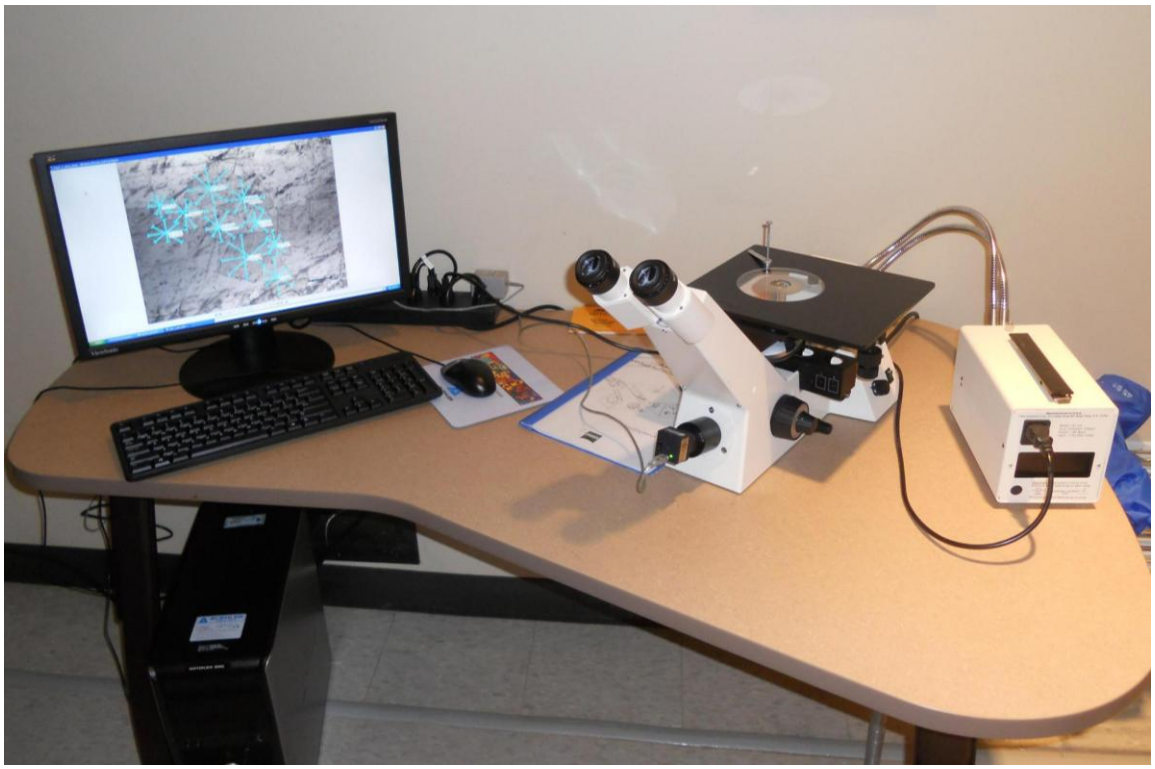

Figure 129. Grain size measuring equipment at Clemson-AMRL. The measuring equipment included a Zeiss Axiovert 25 inverted optical microscope, a uEye Camera, and Buehler OmniMet software.

Upon obtaining grain size measurements, the specimens were cut parallel to and perpendicular to the longitudinal axis, and then cold-mounted, as shown in Figure 130. Figure 131 shows a screenshot of the grain size measurement strategy. A clearly defined polishing and etching procedure for SS304 was followed, as explained below [116]:

- Polish the specimens using grit wheels of 1 micron (Polycrystalline Diamond Suspension) for several minutes.
- Polish the specimens using grit wheels of 0.05 microns (Alumina Polish) for several minutes. Well polished specimens should have no visible scratches on the measurement surface.
- Clean the surface using flowing water.

- Pick up a small amount of Marble's reagent using a cotton swab, brush the specimen along its direction, and avoid too much pressure.
- Clean the surface with ethanol or water, and dry it under big air movement.

Several cautions should be kept in mind to obtain successful images under the scope [116]:

- Before changing grit wheels, the specimens must be cleaned, as remaining diamond particles will leave scratches on the surface during 0.05 micron grit polishing.
- When cleaning the surface, use soap and rub it in one direction.
- Before polishing another mounted sample when using 0.05 micron grit wheel, clean the surface of it and add Alumina Polish again.
- If the images under scope show no clear grain boundaries, re-polish the sample using 0.05 micron grit wheels and etch it again.
- When etching the specimen, brush a specified number of smooth strokes repeatedly, and wash the etchant immediately.

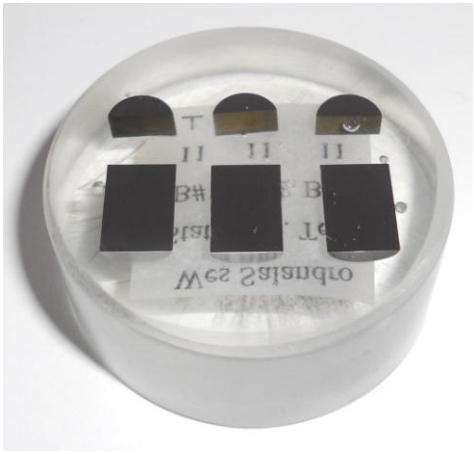

Figure 130. Polished SS304 specimens before etching. The SS304 specimens were cut using an EDM operation, and then cold-mounted using an epoxy-hardener resin mixture. Polishing was performed as explained in this section of the dissertation.

The grain size measurement method consisted of measuring as many full grains as possible in within each micrograph. Additionally, each grain was measured using a four-measurement method, where the grain is measured horizontally (0°), vertically (90°), and on both diagonals (45° and 135°). An example of this grain size measurement strategy on numerous grains can be seen in Figure 131.

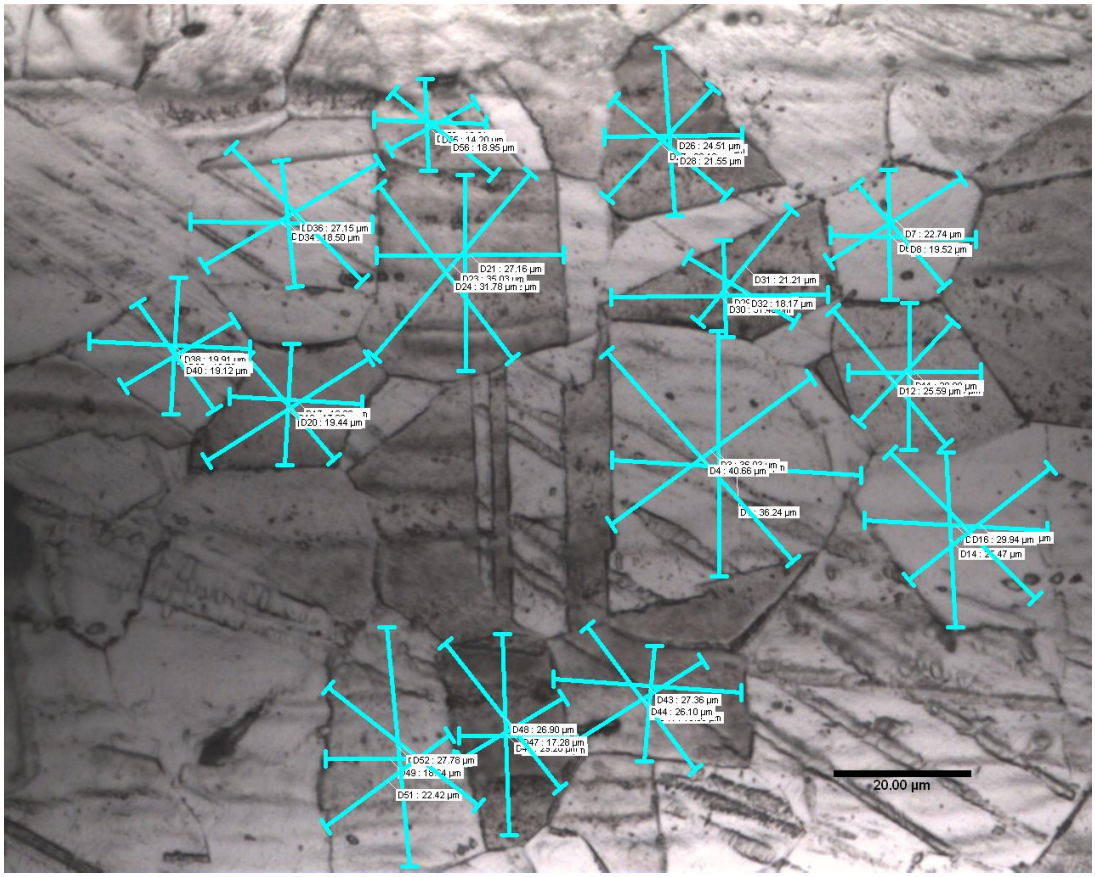

Figure 131. Example of the four-measurement method for determining the average grain size. Each complete grain in the micrograph was measured at four different angles (0°, 45°, 90°, and 135°) to account for any differences in each grain's circular structure.

7.1.3. Experimental Grain Size Investigation

Now that the grain sizes have been quantified, it must be determined if there is a big enough difference in grain sizes between parts to show a difference in the experimental results. To evaluate various thermal and mechanical profiles were collected from all three of the parts to determine this. Figure 132 shows the thermal profiles of stationary-electrical tests run at a current density of 15A/mm^2 at a static load of 2,700N for the three parts. Two replicates were run for each grain size, and the replicates were consistent for each respective grain size. The figure shows that the largest grain size has a thermal profile consistently higher than the other two grain sizes (about 15°C hotter at the end of the test). This is uncharacteristic, because it was expected that the specimen with the smallest grain size would have the hottest temperature profile because there would be more grain boundaries to surpass. However, the difference between the three grain sizes is minimal.

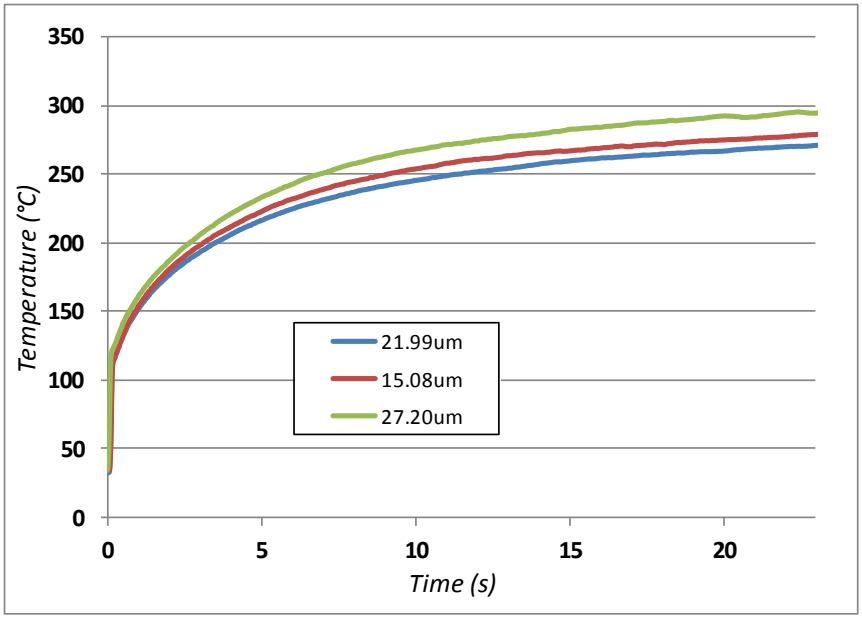

Figure 132. Thermal profiles of stationary-electrical tests run at CD=15A/mm^2. There was no notable difference in the thermal profiles of the stationary-electrical tests run on the different heat treatments.

Figure 133 shows the thermal profiles for EAF tests run at a starting current density of 15A/mm^2 and a deformation speed of 0.5in/min. As was the case with the stationary-electrical tests in the prior figure, the specimens with the largest grain size were the hottest (again, about 15°C hotter at its maximum temperature).

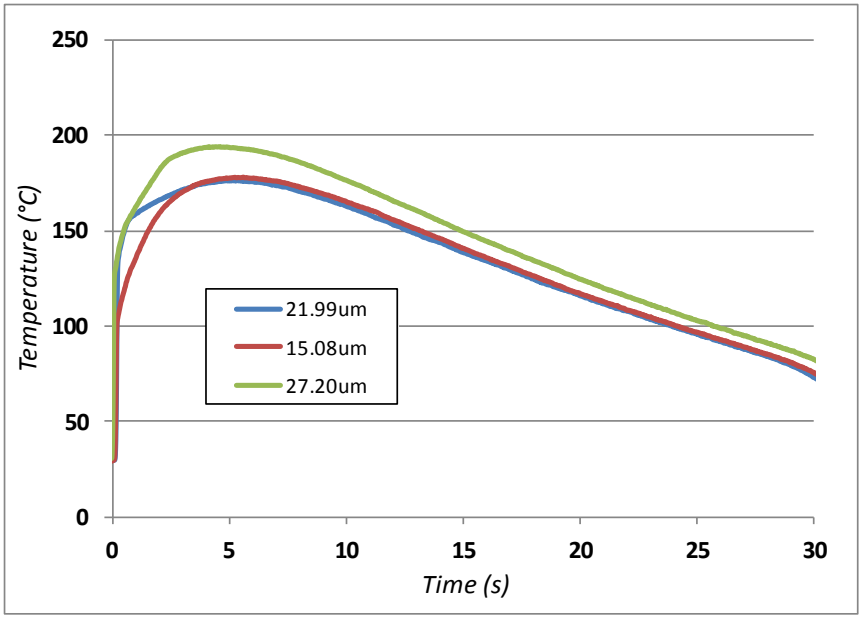

Figure 133. Thermal profiles of EAF tests run at CD=15A/mm^2. As was the case with the stationary-electrical thermal profiles, there is no significant difference in the EAF thermal profiles as well.

Figure 134 displays the true stress-strain profiles of all the parts during a conventional compression test at a deformation speed of 0.5in/min. The stress-strain curves are identical, regardless of the grain size.

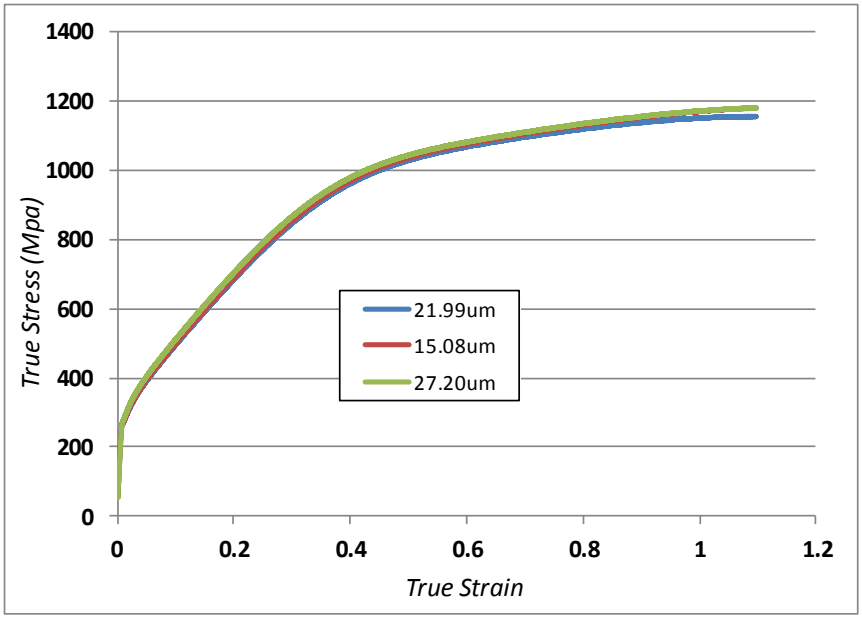

Figure 134. True stress-strain profiles for conventional compression tests. When testing the different heat treated specimens under conventional compression, there was no difference in the conventional compression stress-strain profiles.

Figure 135 depicts true stress-strain profiles for EAF tests with a starting current density of 15A/mm^2. All of the profiles were the same, thus signifying no relation with the different grain sizes tested.

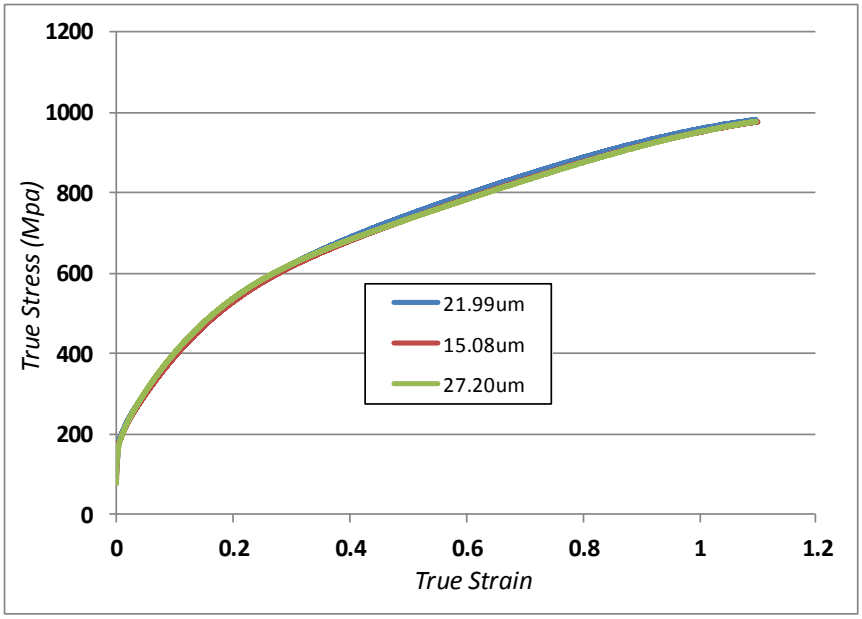

Figure 135. True stress-strain profiles for EAF tests at CD=15A/mm^2. As was the case with the conventional compression stress-strain profiles, the stress-strain profiles for the EAF test also showed no difference.

7.1.4. EAF/Grain Size Conclusions

The differences between the grain sizes did not have an effect on the stress-strain profiles of the conventional compression and the EAF compression tests. Additionally, there was only about a 15°C difference in the thermal profiles (stationary-electrical and EAF compression) between the largest grain size and the other two grain sizes, however this was a very minor difference and this did not have any effect on the mechanical performance during the EAF tests. Work by Siopis et al. examined the effect of different grain sizes on EAF compression at the micro-level [48]. In this work, specimens with a diameter of up to 2mm, with grain sizes of 9µm up to 276µm were compressed while electrical power was applied. This work showed that the difference grain, at the micro-level, did affect the EAF technique, in that as the grain size increased, the electrical threshold current density increased. However, this chapter in this thesis shows that there is not such a relationship between the tested grain sizes and electrical effects at

the macro-level. With the limitations on being able to easily generate new grain sizes, and with the resources available to the candidate, it was decided that efforts would be shifted from exploring effects of the starting grain size to examining the effect of prior cold work on the effectiveness of EAM, as explained in *Ch. 8: Percent Cold Work Effect on EAF*.

8. Prior Cold Work Effect on EAF (Task #7)

Within this chapter, the relationship between dislocation density and efficiency of EAF are explored. Since the starting grain sizes in the previous chapter were not different enough to produce experimental trends, the focus was shifted towards examining the effect of prior cold work in the specimens. As the cold work is increased in a metal, the dislocation density within that metal will increase, thus leading to a greater amount of obstacles which moving dislocations will have to surpass in order to continue plastic deformation. With this being said, this investigation should be able to provide the same type of information as the grain size research was intended to provide, such as how the different dislocation densities affect the EAF technique. The specimen preparation, the experimental setup and procedure, and the results and discussion of thermal profiles and stress-strain profiles of worked/non-worked specimens are described.

8.1. Importance of Percent Cold Work on EAF Effectiveness

As was shown in the previous chapter, the interactions between electrons and dislocations within a metal are responsible for the electroplastic effect. The percent cold work, or prior plastic deformation performed on a metal before forming it again, has a correlation to the dislocation density within a material. Depending on the material, as it is pre-worked to a greater degree, the dislocation density within the metal increases potentially up to 10^{12}mm/mm^3 [117]. More specifically, as the percent cold work within a metal is increased, the dislocation density within that metal is also increased. Since the flowing electrons interact with dislocations, different amounts of dislocations within a metal should have an effect on the efficiency of the EAF technique. Specifically, as the electricity is applied, the electrons interact with the dislocations, thus providing them the "push" needed to continue plastic deformation. Depending on the number of pre-existing dislocations, the flowing electrons will have more or less of an effect on

reducing the flow stress and extending elongation of the workpiece. For example, if the metal is an annealed polycrystalline, the dislocation density may be around 10^7mm/mm^3 [117], and the applied electricity may impact all of the dislocations and thus there will be great effects from the applied electricity. Conversely, if there is a large number of pre-existing dislocations already in the workpiece from a highly worked metal (10^{11}-10^{12}mm/mm^3 [117], the flowing electricity may not be able to impact all of the dislocations and the benefits of EAF would be less compared to the same workpiece with fewer dislocations.

8.1.1. Specimen Preparation

To begin, the specimen preparation for this work will be explained. All of the specimens used in this research work were derived from the same 9.5mm-diameter rod of 304 Stainless Steel. This rod was sectioned off into approximately 125mm-long increments. These increments were then centerless ground to 6.35mm-diameter, along with five other larger diameters which are representative of the diameters which would be reached at various levels of cold work (10% to 50% in increments of 10% - see Table 18). Now, having all the different diameter rods, two types of specimens could be made: one without any cold-work (*i.e.* in the annealed state) and one with cold-work (*i.e.* in the worked state). The worked specimens were fabricated by simply taking a 6.35mm-diameter specimen and physically compressing it to 10%, 20%, 30%, 40%, and 50% cold-work using the Instron machine. The non-worked specimens were created using the other rods which were centerless ground to the same diameters as the cold-worked specimens at each cold work percent (neglecting the barreling effect). The length of these specimens was sized using an EDM operation. In the end, cold-worked and non-worked specimens were fabricated from the same rod to the same dimensions and were ready for testing and evaluation. A flow chat

describing the specimen fabrication procedure can be seen in Figure 136. Table 18 displays the length and diameter changes required to produce each level of cold work.

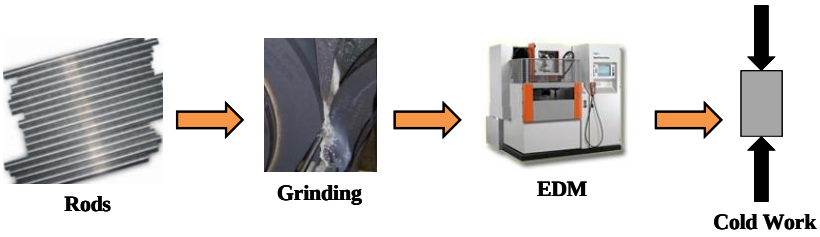

Figure 136. Worked and non-worked specimen preparation procedure. The procedure to produce specimens of the same dimensions with and without cold work required rods to be centerless ground to post-formed diameters and then an EDM was used to size the lengths. The worked specimens were deformed prior to testing, using the Instron machine.

Table 18. Initial percent cold work specimen dimensions.

h (mm)	**Δl** (mm)	**% CW**	$\mathbf{D_{final}}$ (mm)	**ΔD** (mm)	**Exp. Verif. Dia** (mm)
9.525	0.000	0	6.350	0.000	6.350
8.573	0.952	0.1	6.693	0.343	6.706
7.620	1.905	0.2	7.100	0.750	7.163
6.668	2.858	0.3	7.590	1.240	7.696
5.715	3.810	0.4	8.198	1.848	8.230
4.763	4.763	0.5	8.980	2.630	8.915

8.1.2. Experimental Setup and Procedure

To truly determine the effect that cold work has on the EAF technique three different experimental tests were run. Conventional compression tests were performed to quantify the differences in the thermal and stress-strain profiles of the different amounts of cold work without applying any electricity. Then, stationary-electrical tests were performed to determine the differences in the heating profiles of specimens at a static load of 2225N, with different levels of cold work where no deformation was taking place. Finally, EAF compression tests were run,

with an electrical input of 800A, to identify the differences in the thermal profiles and stress-strain profiles of the different cold worked specimens during deformation and during the application of the EAF technique. Table 19 below shows the different test type/cold worked specimen combinations performed for this work.

Table 19. Test type/specimen combinations for %CW research.

Specimen Type	Test Type	Pre-load (N)	Current (A)	Amount of def. (mm)
CW10% Annealed, Worked	Stationary-Electrical	2225	354, 531	0
CW20% Annealed, Worked	Stationary-Electrical	2225	403	0
CW30% Annealed, Worked	Stationary-Electrical	2225	466	0
CW40% Annealed, Worked	Stationary-Electrical	2225	532, 1064	0
CW50% Annealed, Worked	Stationary-Electrical	2225, 62300	400	0
CW30% Annealed, Worked	Stationary-Electrical	42275	466	0
CW40% Annealed, Worked	Stationary-Electrical	50062.5	532	0
CW50% Annealed, Worked	Stationary-Electrical	62300	625	0
CW20% Annealed, Worked	Conv. Comp	2225	0	4.445
CW20% Annealed, Worked	EAF Comp.	2225	806	4.445
CW40% Annealed, Worked	Conv. Comp	2225	0	2.54
CW40% Annealed, Worked	EAF Comp.	2225	806	2.54

8.1.3. Results and Discussion

Figure 137 and Figure 138 display the thermal profiles of stationary-electrical tests performed on 10% CW/Annealed specimens at starting current densities of $10A/mm^2$ and $20A/mm^2$, respectively. One can see that the thermal profile of the cold-worked specimen in each figure is higher, possibly due to the fact that there are a greater number of dislocations, or lattice obstacles that work to resist the flow of electrons and produce heat. Specifically, the maximum temperatures for the $10A/mm^2$ tests are 160°C (annealed) and 200°C (worked), and the maximum temperatures for the $20A/mm^2$ tests are 330°C (annealed) and 425°C (worked). Also of note is that the $10A/mm^2$ specimens reached a saturation temperature during the duration of the test, whereas the $20A/mm^2$ specimens did not reach thermal saturation in the short duration of the test.

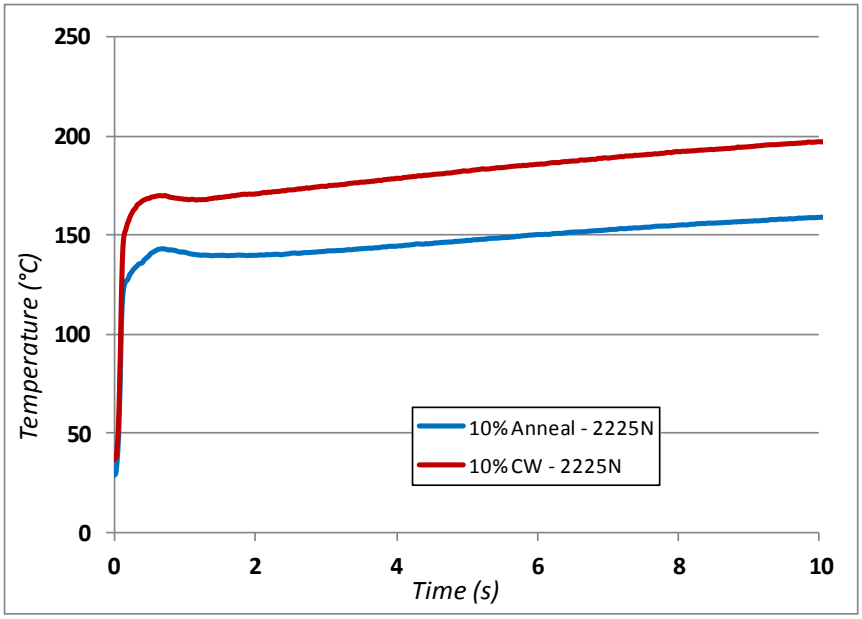

Figure 137. 10% CW/Annealed thermal profiles (stationary-electrical tests at CD=10A/mm^2). The thermal profile for the cold-worked specimens was consistently about 40 degrees higher than the annealed specimens.

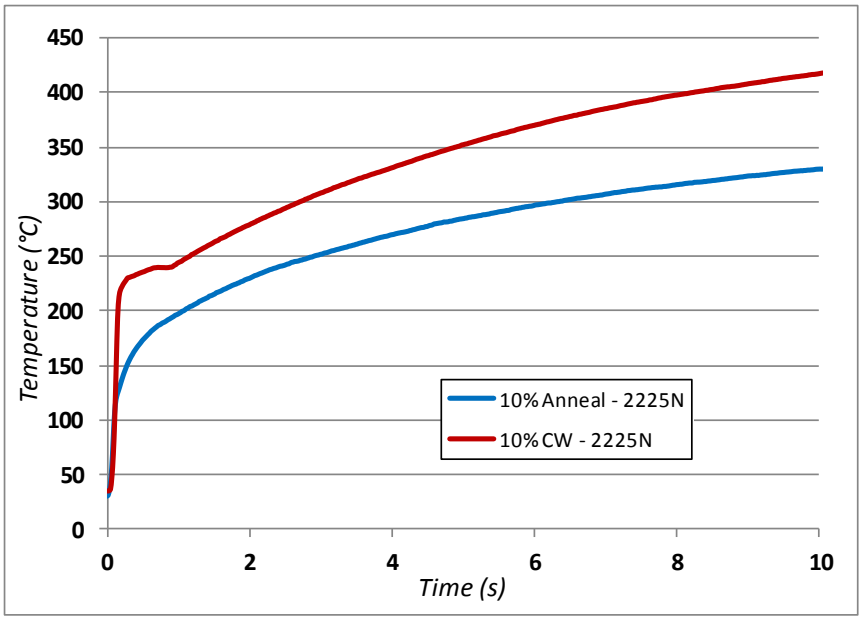

Figure 138. 10% CW/Annealed thermal profiles (stationary-electrical tests at CD=20A/mm^2). The difference in the thermal profiles increases slightly towards the end of the stationary-electrical test to about 80°C.

Figure 139 displays the thermal profile of a stationary-electrical test performed on 20% CW/Annealed specimens at a starting current density of 10A/mm^2. The maximum temperature of the annealed specimen was 200°C, while the maximum temperature of the worked specimen was 230°C. Again, the cold-worked specimen temperature profile was significantly higher than the non-worked specimen profile, and the temperature profiles did not level-off during the tests, but kept increasing toward a steady-state value that would have been reached over a given time period.

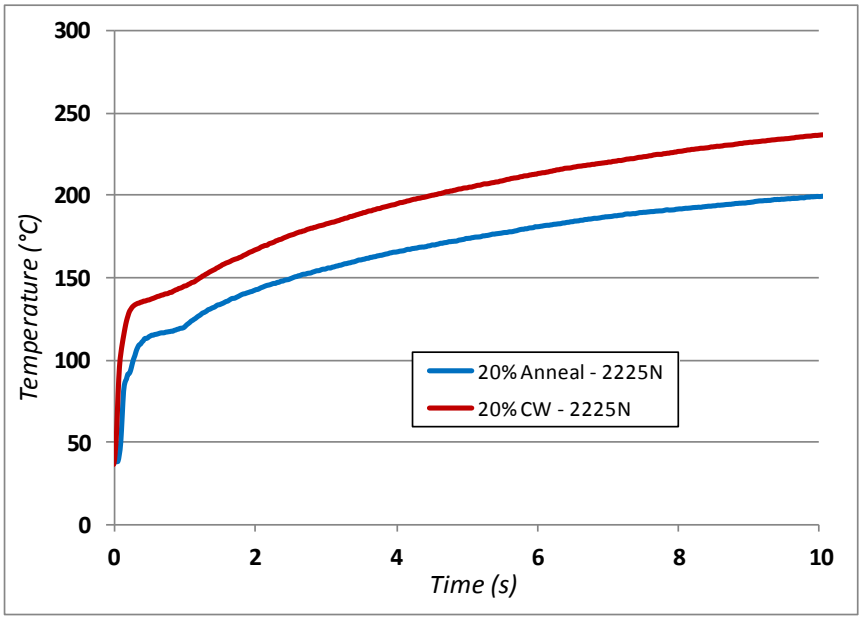

Figure 139. 20% CW/Annealed thermal profiles (stationary-electrical tests at CD=10A/mm^2). The difference in the thermal profiles (40°C) stays fairly consistent throughout the duration of the stationary-electrical test, as was the case with the 10%CW/Anneal tests at the same current density.

Figure 140 displays the thermal profile of a stationary-electrical test performed on 30% CW/Annealed specimens at a starting current density of 10A/mm^2. Specifically, the maximum temperature of the anneal specimens was 200°C (which was the same as the annealed specimens at 20%CW) and the maximum temperature of the worked specimens was 300°C. There was a

very large difference in the thermal profiles of the worked and non-worked specimens, with the woked specimen still producing the hotter profile by about 100°C compared to the annealed specimens.

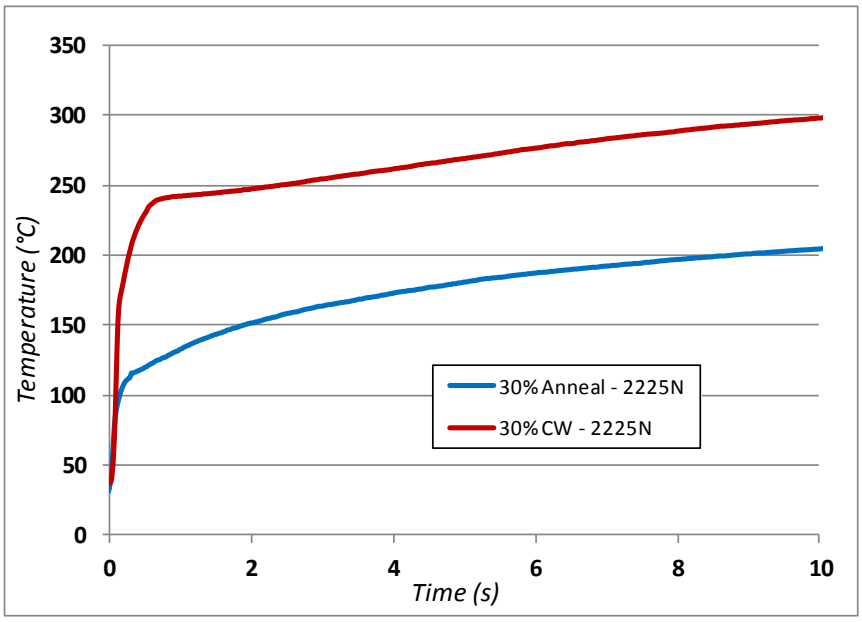

Figure 140. 30% CW/Annealed thermal profiles (stationary-electrical tests at CD=10A/mm^2). There is a consistent difference in the thermal profiles (100°C), however, the magnitude of the difference is much greater than the 10% and 20%CW/Anneal tests.

Figure 141 displays the thermal profile of a stationary-electrical test performed on 40% CW/Annealed specimens at a starting current density of 10A/mm^2. Again, this was a large difference in the thermal profiles of the worked and non-worked specimens, where the worked specimens reached a maximum temperature of about 365°C and the annealed specimens peaked at about 200°C.

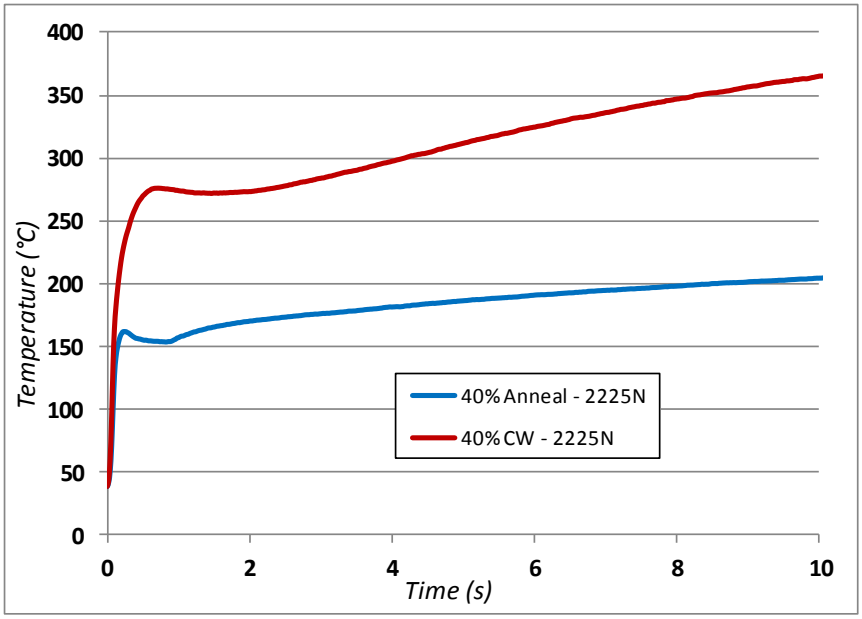

Figure 141. 40% CW/Annealed thermal profiles (stationary-electrical tests at CD=10A/mm^2). The difference in the thermal profile marginally increases over the duration of the test to a difference of about 160°C.

Figure 142 displays the thermal profile of a stationary-electrical test performed on 50% CW/Annealed specimens at a starting current density of 10A/mm^2. Additionally, two contact load trials are shown in this figure. The annealed specimen temperature profile with the contact load of 2,225N was significantly higher than the other two profiles, which had a contact load of 62,300N. This helps to prove that the lower contact load has an effect on the specimen temperature, especially when it is still in the elastic region as shown in *Chapter 6*.

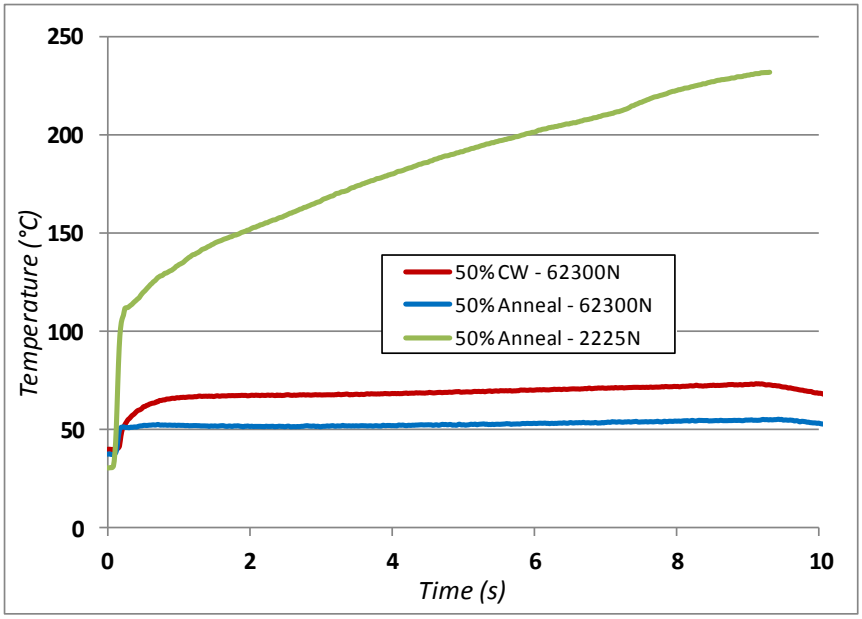

Figure 142. 50% CW/Annealed thermal profiles (stationary-electrical tests at CD=10A/mm^2 with different static loads). This figure shows the difference that the static load can have on the temperature of the part. The load of 2,225N and the annealed part, which is still in the elastic region, produced a much higher thermal profiles compared to another annealed specimen with a static load of 62,300N, which was well into the plastic region.

Figure 143 shows the thermal profiles of stationary-electrical compression tests at a starting current density of 30A/mm^2, and a static load of 42,275N. The 42,275N represents the final load put on the specimens in order to work them to 30% of their original height. The cold worked specimen temperature profile is still higher than the non-worked profile. The maximum worked specimen temperature is 110°C and the maximum annealed specimen temperature is 85°C. Also of note, is that the temperature difference between the %CW and Annealed thermal profiles increase throughout the test duration. When comparing this figure to Figure 140 (where there was only a load of 2,225N on the parts, the temperatures are much lower in this figure with the much higher load. This corresponds to what was discussed in the previous chapter focused on contact area, where the static load has a large effect on the resistive heating of the workpiece in the elastic region.

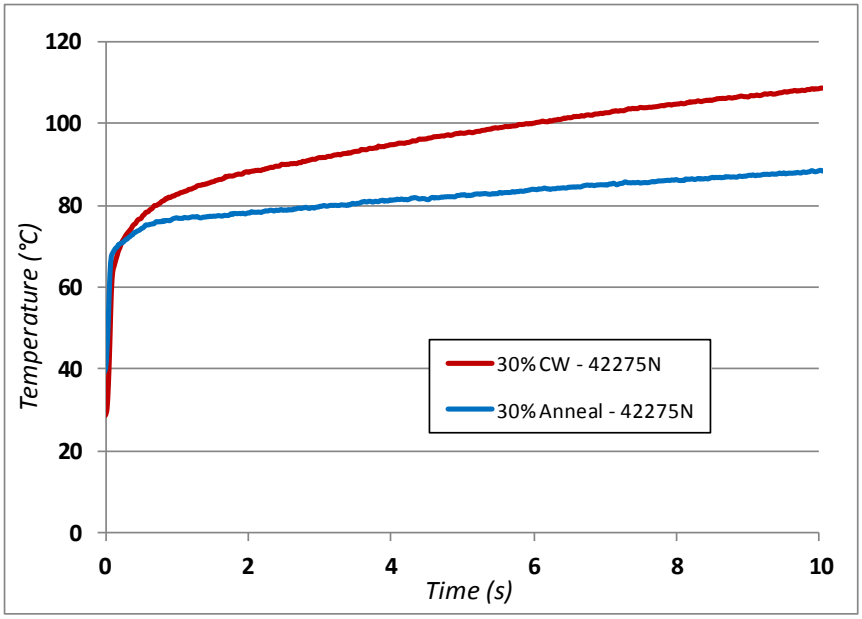

Figure 143. 30% CW/Annealed thermal profiles (stationary-electrical tests at CD=10A/mm^2 at 42,275N). The difference in the thermal profiles of the worked and annealed specimens at 42,275N is comparable to the differences previously discussed in Figure 140.

The thermal profiles in Figure 144 are for worked and non-worked specimens at 40% of the original height, and under a static load of 50,063N (which was the final load required to deform the worked slugs to 40%). The same trend follows, where the worked specimen is much hotter than the non-worked specimen. The worked specimen reached a maximum temperature of 117°C and the annealed specimen reached 82°C. The same linear increasing trend as is shown in the previous figure is also apparent in this figure. Compared to Figure 141, where the static load was only 2,225N, the difference between the worked and non-worked temperature profiles increased only very slightly as the test progressed, whereas the profiles in Figure 141 increased significantly as the tests progressed.

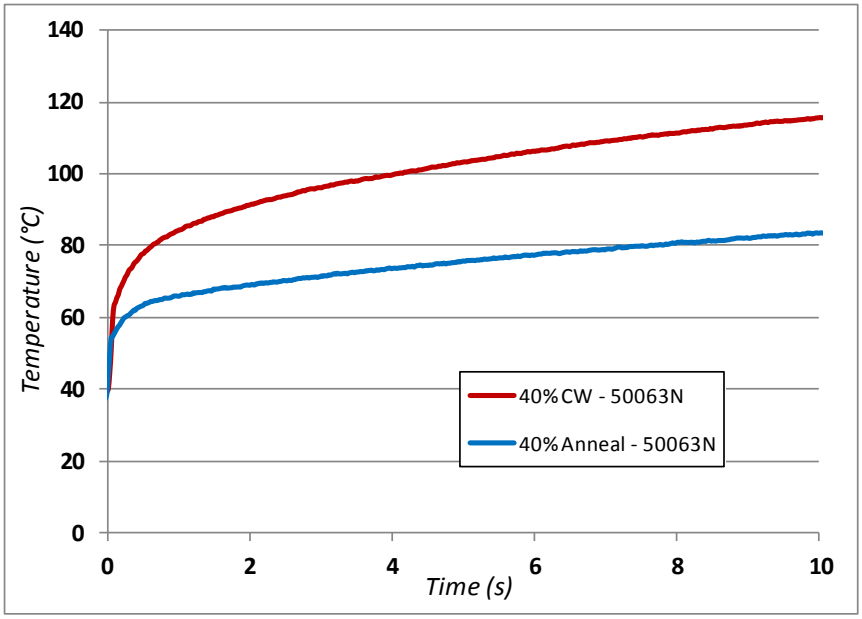

Figure 144. 40% CW/Annealed thermal profiles (stationary-electrical tests at CD=10A/mm^2 at 50,063N). The difference in the thermal profiles of the worked and annealed specimens at 50,063N is not as great as compared to the temperature differences previously discussed in Figure 141.

Figure 145 displays the thermal profiles for stationary-electrical tests at a starting current density of 50A/mm^2 for worked and non-worked specimens under a static load of 62,300N. The thermal profiles follow the same trend as the several figures before it, in that the worked specimen temperature profile was hotter than the non-worked profile, and the overall temperatures were much lower than where the same worked and non-worked specimens were tests under a static load of 2,225N. Specifically, the worked specimen reached 120°C, while the annealed specimen reached 80°C.

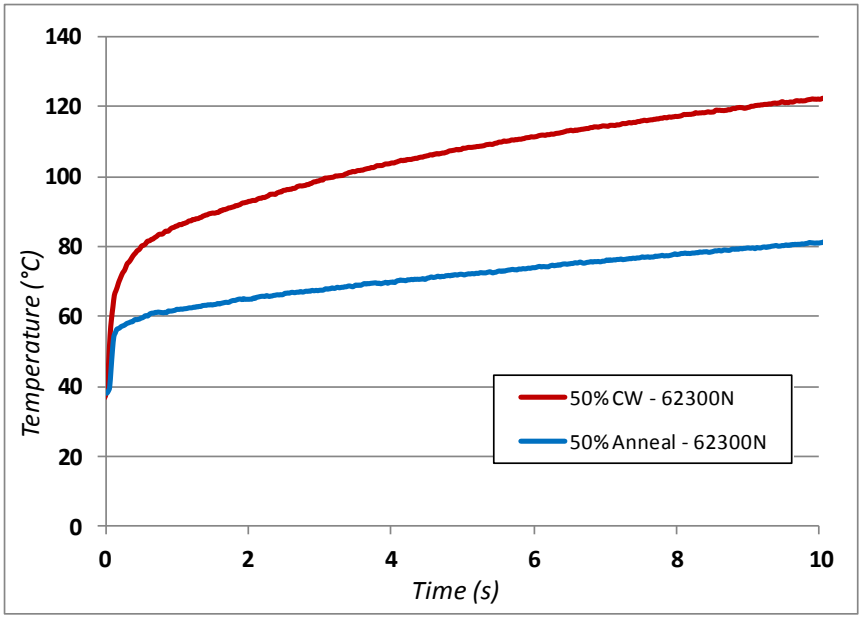

Figure 145. 50% CW/Annealed thermal profiles (stationary-electrical tests at CD=10A/mm^2 at 62,300N load). The temperature difference in the specimens loaded to 62,300N was large, but did not follow the trend of increasing temperature differences as discussed in Figure 143 to Figure 144.

Table 20 summarizes the results of the thermal results of the stationary-electrical tests discussed above. For the same respective current density (10A/mm^2), the temperature increased as the %CW increased (to an overall temperature difference of 165°C). For the annealed specimens, there was only a 40°C difference in the 10% annealed specimen temperature compared to the 40% annealed thermal profile.

Table 20. Summary of %CW and annealed stationary-electrical test results.

Stat.-Elec. Test Description	Maximum Temp. (°C)	Thermal Profile Description
10% CW (CD=10), 2225N	200	Thermal profiles are almost flat, signifying thermal saturation was almost reached.
10% Ann (CD=10), 2225N	160	
10% CW (CD=20), 2225N	425	Thermal profiles very curved, signifying that the specimens did not reach thermal saturation.
10% Ann (CD=20), 2225N	330	
20% CW (CD=10), 2225N	230	Curved thermal profiles with a constant temperature difference over the test duration.
20% Ann (CD=10), 2225N	200	
30% CW (CD=10), 2225N	300	Linear-type thermal curvature with a constant 100°C difference over the test.
30% Ann (CD=10), 2225N	200	
40% CW (CD=10), 2225N	365	Temperature difference increased from 75°C to 165°C.
40% Ann (CD=10), 2225N	200	
30% CW (CD=10), 42275N	110	Linear-shaped thermal profiles with increasing temperature difference to 25°C.
30% Ann (CD=10), 42275N	85	
40% CW (CD=10), 50063N	117	Linear-shaped thermal profile with a small temperature difference (20°C to 35°C).
40% Ann (CD=10), 50063N	82	
50% CW (CD=10), 62300N	120	Linear-shaped thermal profile with a small temperature difference (25°C to 40°C).
50% Ann (CD=10), 62300N	80	

From the data in Table 20, Figure 146 could be created with shows the relationship between the maximum temperature of the stationary-electrical tests and the initial percent cold-work. In this figure, the maximum temperature (which consistently occurred at the end of the tests) increased as the initial percent cold-work was increased. This was due to the fact that the greater amount of cold-work had a larger number of interfacial defects within the lattice, mostly in the form of a greater dislocation density. With the greater number of dislocations, the flowing electrons had more obstacles to scatter off of and thus the heating of the workpiece was increased.

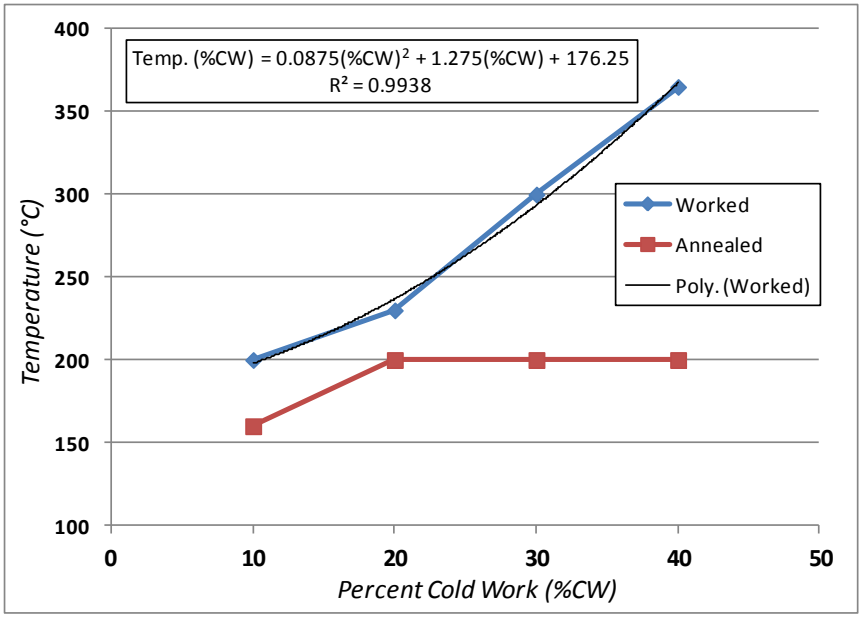

Figure 146. Temperature vs. percent cold-work relationship for SS304. The temperatures of stationary-electrical tests at the same current density increased as the initial percent cold-work was increased.

In addition to analyzing the thermal profiles of stationary-electrical tests, the thermal profiles of worked and non-worked specimens undergoing conventional compression and EAF tests were also evaluated. In the thermal plots for EAF compression tests, the temperature will decrease at some point in the test, where the maximum temperature will not be at the end of the test, as was the case with the stationary-electrical tests. This is due to the increasing cross-sectional area on the specimens as they are compressed. Specifically, the current used to make the starting current density is held constant, and therefore, the current density decreases over the duration of the test. This causes the specimen temperature to peak at some point in the test, and then reduce for the remainder of the test.

Figure 147 and Figure 148 show the thermal profiles of 20% worked/non-worked specimens undergoing conventional compression and EAF compression, respectively. In the conventional compression tests in Figure 147, the worked specimen was about 10°C hotter than

the non-worked specimen. From the profile, the temperatures were identical at the beginning of the test. Then the largest difference between tests was near the middle of the tests. Towards the end of the tests, the temperatures of the worked and non-worked specimens became close to one another. The same trend was followed for the EAF tests in Figure 148, where the worked and non-worked specimen temperature profiles were the same at the beginning, they reached their maximum difference near the middle of the test, and then the difference between the temperatures reduced slightly as the tests came to an end. This divergent then convergent thermal behavior is a result of the initial dislocation densities in the parts. With the higher starting dislocation density, the %CW thermal profile increases at a greater rate in the beginning of the test, whereas the annealed specimen (with a lower dislocation density) showed a linear increase in temperature. In the middle of the test, where the %CW specimens were the hottest, conduction heat transfer could be responsible for the convergence of the %CW and annealed thermal profiles.

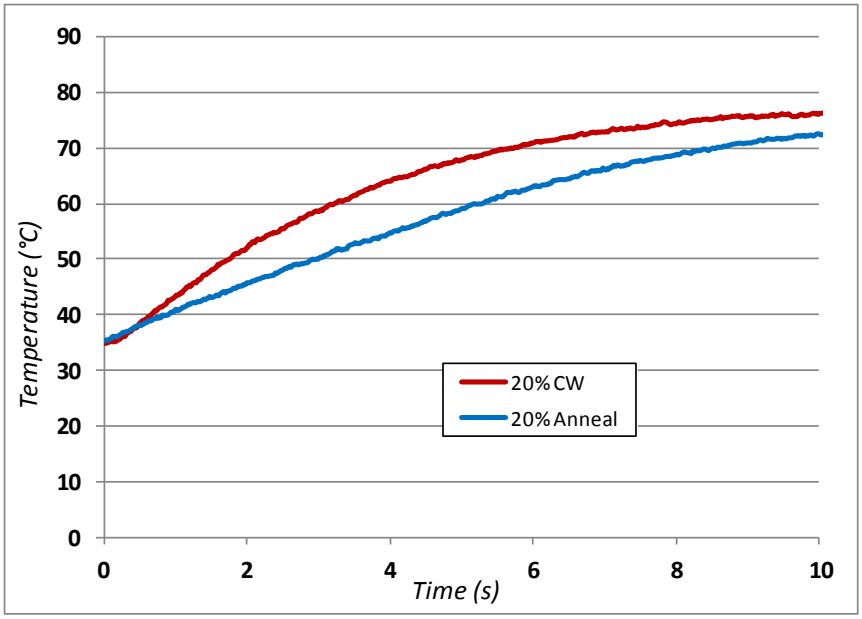

Figure 147. 20% CW/Annealed thermal profiles (conventional compression). The cold worked conventional compression thermal profile was no greater than 10°C higher than the thermal profile of the annealed specimen.

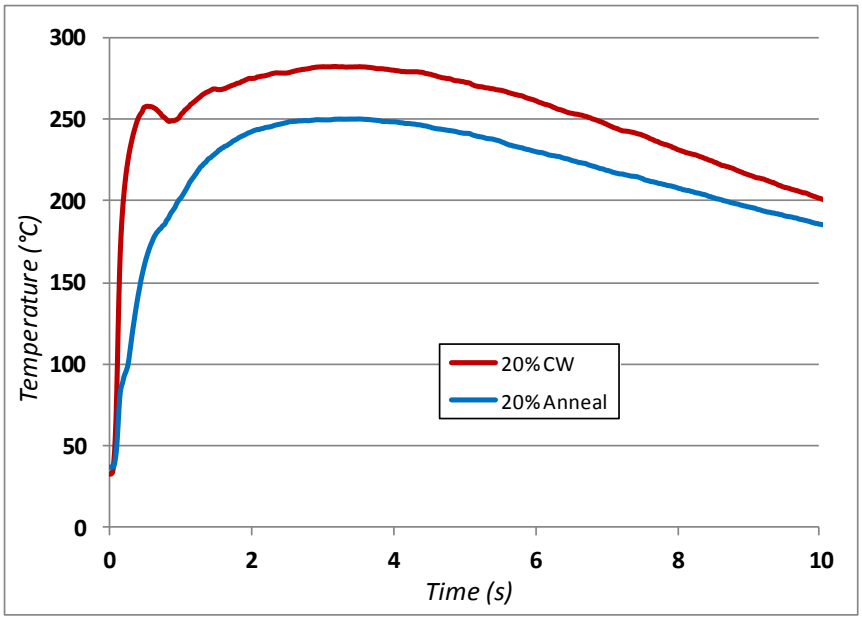

Figure 148. 20% CW/Annealed thermal profiles (EAF tests at 800Amps). As was the case with the stationary-electrical tests, the cold worked specimen temperature profile for the EAF tests was higher than the annealed specimen's temperature profile. The largest recorded difference throughout the tests was about 30°C.

Figure 149 and Figure 150 display the thermal profiles of 40% worked/non-worked specimens undergoing conventional compression and EAF compression, respectively. The conventional compression tests in Figure 149 show a steadily increasing difference in the temperature profiles between the worked and non-worked specimens over the duration of the test. The worked specimen reached about 73°C and the annealed specimen reached about 60°C. The EAF tests in Figure 150 show a fairly consistent difference in the thermal profiles throughout the tests, as was the case with the 20% worked/non-worked EAF tests. In this case, the maximum temperature is reached at about the halfway through the testing, where the worked specimen is 195°C and the annealed specimen is 155°C.

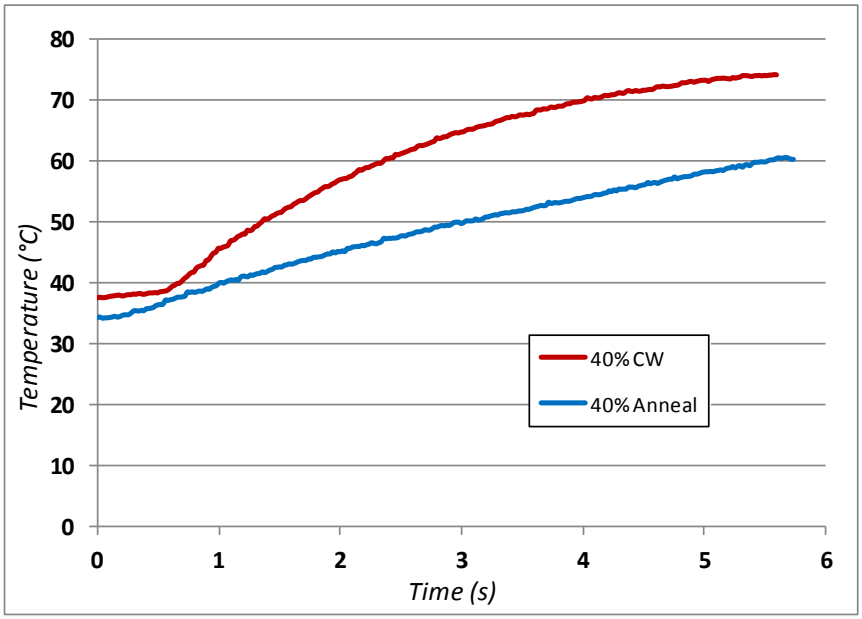

Figure 149. 40% CW/Annealed thermal profiles (conventional compression). There was a greater difference between the annealed and worked thermal profiles at 40% (about 25°C) compared to 30%.

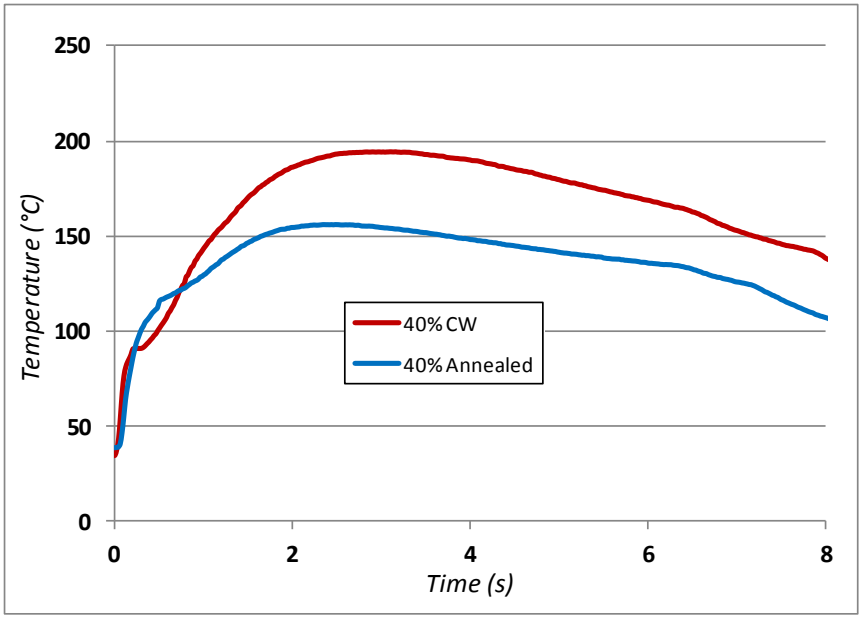

Figure 150. 40% CW/Annealed thermal profiles (EAF tests at 800 Amps). The difference in the temperatures of the profiles is about 40°C, which is slightly lower than the differences for the 20% CW/Anneal specimens.

The engineering stress-strain plots for the 20% worked/non-worked tests are shown below. Specifically, the conventional compression tests are in Figure 151 and the EAF compression tests are in Figure 152. Looking at the conventional compression tests in Figure 151, one can see that the worked specimens can be distinguished from the annealed specimens due to the large difference in the flow stress yield point. However, this difference in flow stress is depleted about halfway through the testing and the ending stress for both specimen types is the same. The EAF compression tests in Figure 152 show the same starting difference in stress at the beginning. The difference decreases through the tests, but there is still a recognizable difference between the stresses of the worked and annealed specimens undergoing these tests. This signifies that the difference in dislocation densities due to the 20% cold-working was enough to minimally affect the effectiveness of the EAF technique.

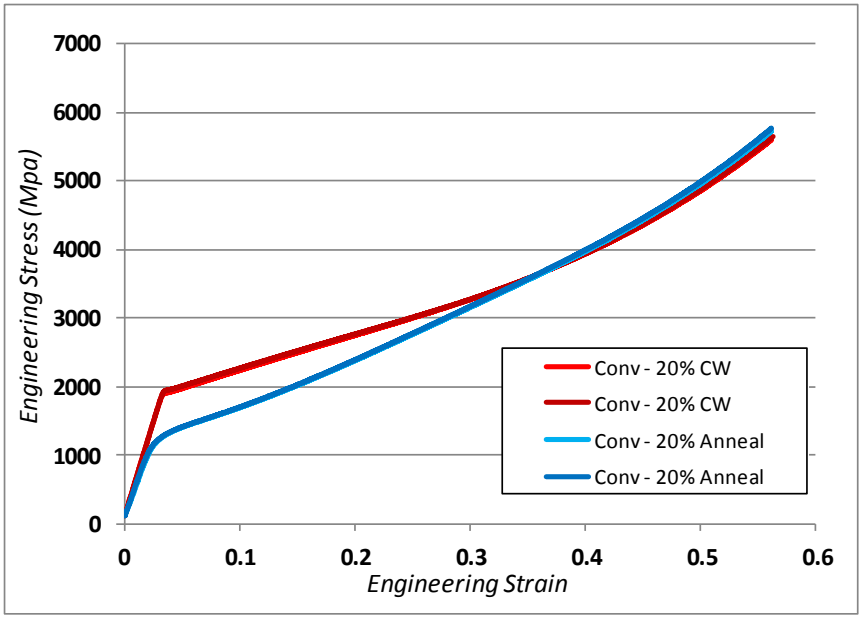

Figure 151. Stress-strain profiles (20% CW/Annealed, conventional compression). The stress-strain profiles of the worked specimens are higher at the beginning of the test, and by the end of the tests, both stress-strain profiles are at the same level.

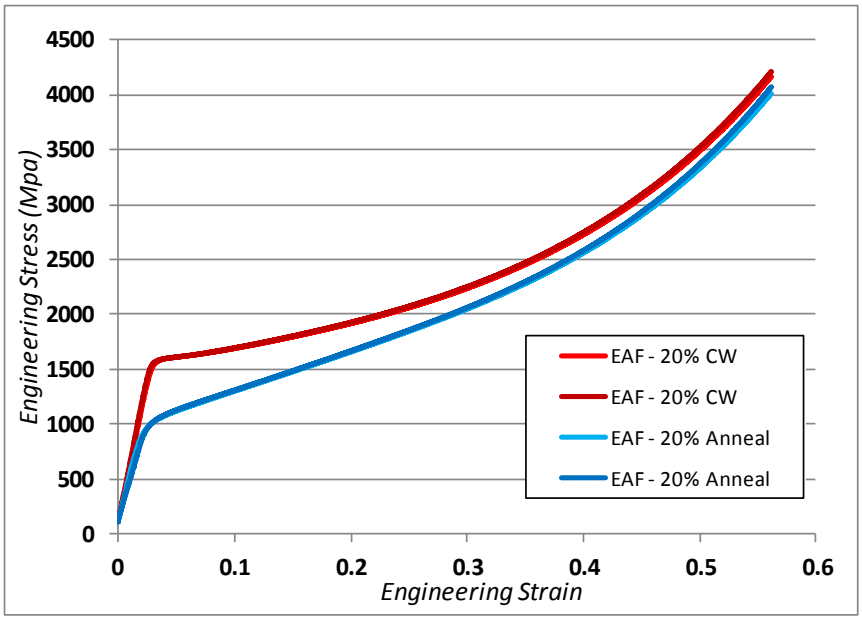

Figure 152. Stress-strain profiles (20% CW/Annealed, EAF at 800 Amps). The EAF stress-strain profiles show the same differences as the conventional compression tests, however, the stress-strain profile of the worked specimens is still slightly higher than the annealed profile at the end of the tests.

The 40% worked/non-worked tests are shown in Figure 153 and Figure 154 below. The conventional compression tests in Figure 153 show a much larger difference in the yield stress, due to the larger amount of cold-working. This stress difference decreases throughout the tests, but there is still a small difference in the ending stresses of the worked/annealed specimens (note that there was not a difference between the 20% worked/non-worked conventional compression specimens). The convergence of the conventional compression and the EAF compression tests could be due to the applied electricity assisting the deformation by "pushing" the dislocations. Even though there is a higher dislocation density in the worked specimens, the magnitude of the applied electrical power is able to overcome this difference in dislocation density. With the 20% cold-worked specimens, the applied electrical power was able to overcome this dislocation density difference completely, whereas the applied electrical power was not able to fully overcome the dislocation density difference for the 40% cold-worked specimens, and that is why there is still a small difference between the stress-strain profiles of the conventional and EAF compression tests. The EAF compression tests are depicted in Figure 154, where there is an ending stress difference of about 350MPa between the worked/annealed specimens. There is still about the same stress difference of approximately 700MPa at the elastic-plastic transition region. Additionally, the reduction in flow stress at the end of the tests is different for conventional/EAF compression of each respective specimen condition. Specifically, the reduction in stress between the conventional 40%CW and the EAF 40%CW tests is about 500MPa (3000MPa – 2500MPa). Further, the difference between the conventional 40% annealed and the EAF 40% annealed tests is about 750MPa (3000MPa – 2250MPa). This signifies that the high dislocation density in the %CW specimens affected EAF, such that the applied electrical power did not have as great of an effect at reducing stress as it had with the annealed specimens. To this end, the larger difference

in dislocation density (due to the level of cold work) affected EAF's effectiveness to an even greater extent than the 20% worked/non-worked specimens.

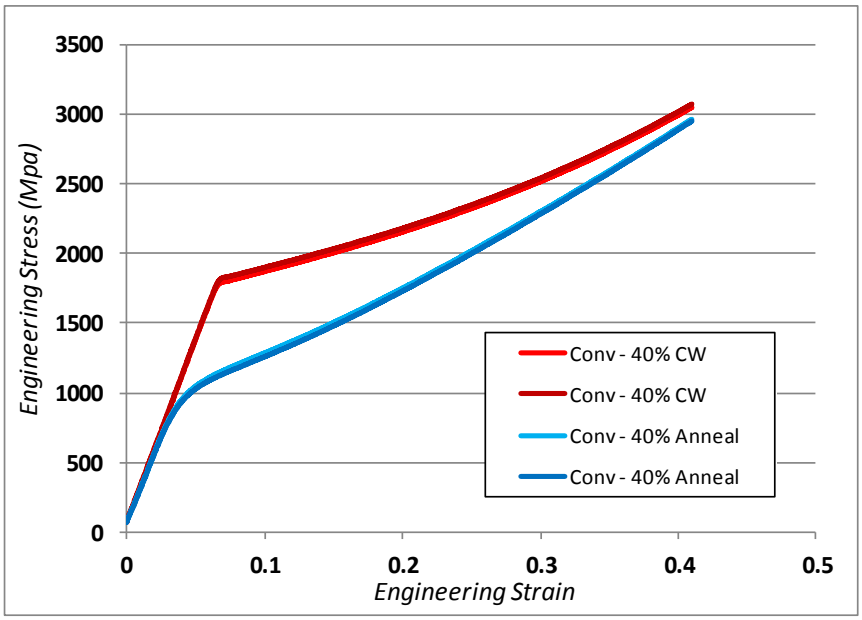

Figure 153. Stress-strain profiles (40% CW/Annealed, conventional compression). The stress-strain profiles of the worked specimen were much greater than the profiles of the annealed specimens at the beginning of the tests, and by the end of the tests, they were only marginally higher.

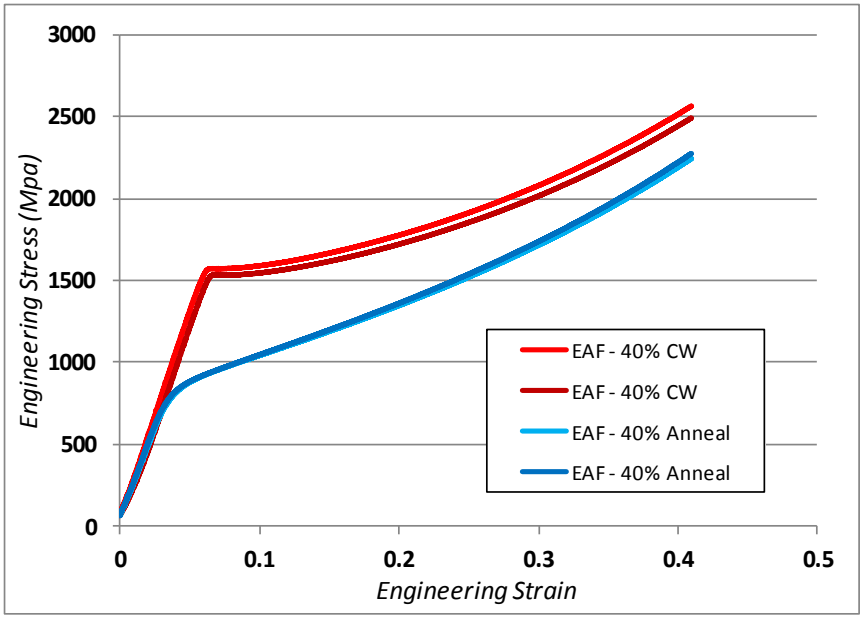

Figure 154. Stress-strain profiles (40% CW/Annealed, EAF at 800 Amps). As was the case with the 20% CW/Anneal specimens, the stress-strain profile difference at the end of the tests was greater than the respective conventional compression tests.

From the thermal figures above, it can be seen that the worked specimens consistently produced higher thermal profiles compared to the annealed specimens of the same dimensions. As the percent cold-work is increased, the metal has a higher dislocation density (*i.e.* a greater number of dislocations per area of lattice). With more lattice obstacles, it is understandable that the worked specimens would be hotter because there are more lattice obstructions for the flowing electrons.

In an attempt to correlate the different levels of cold work to different dislocation densities, the following was performed. First, a static load of the magnitude that it took to deform the specimens to the desired height, was applied to each specimen, while 300 Amps of electrical current was run through the specimen. A value of 300A was chosen such that there was sufficient current to cause a heating effect, but not so much current to resistively heat the specimen to temperatures about the maximum temperature of the thermal camera. While the current was

applied, the voltage between the top and bottom dies was recorded using a multimeter. This procedure was performed for each level of cold work and the resulting voltages are shown below in Table 21. In addition, Figure 155 provides a way to compare the voltages of the annealed and worked specimens at the same height reduction levels. From the figure, it can be seen that the annealed specimen voltages were consistently lower than the voltages of the worked specimens. This supports the belief that the worked specimens had much higher dislocation densities compared to the annealed specimens, which lead to more resistive heating and overall higher temperature profiles for the worked specimens.

Table 21. Stationary-electrical voltage measurements of worked and annealed specimens.

Height	Designation	Static Load (N)	Voltage (mV)
10%	Worked	22,250	70
	Annealed		57
20%	Worked	32,040	58
	Annealed		30
30%	Worked	42,275	31
	Annealed		17
40%	Worked	50,063	24
	Annealed		15
50%	Worked	62,300	15
	Annealed		8

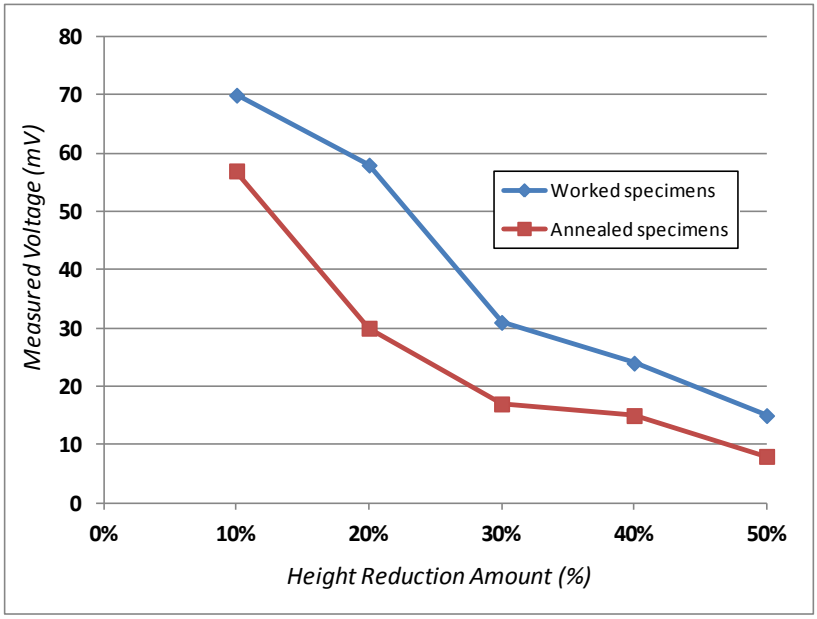

Figure 155. Voltage vs. percent cold work. The voltages resulting from running a small amount of electricity through the specimens worked to different levels is shown.

8.1.4. EAF/Percent Cold Work Conclusions

The amount of percent cold-work in a material designates the dislocation density within the material. Within this chapter, stationary-electrical tests were run and temperature was recorded, and EAF tests were run where temperature and stress-strain profiles were recorded. The conclusions from this section are as follows:

- For stationary-electrical tests, the temperature profile will increase as the starting percent cold-work in the specimen is increased.
- The recorded voltages in the stationary-electrical tests increased as the percent cold-work increased and the higher resulting dislocation densities caused the resistance of the specimen to increase. The measured voltages of the %CW and annealed specimens decreased at the same rate, but the annealed voltage values were consistently below the %CW voltage values.

- The amount of induced percent cold-work within a specimen has an effect on the ability of the applied electricity to reduce the overall flow stress. The overall reduction of the flow stress between conventional and EAF testing of annealed specimens may be greater than the difference between cold-worked specimens.
- The stationary-electrical test thermal profile curvatures are dependent on the electrical application parameters (current density) and the material parameters (%CW or annealed). Sometimes this profile is curved and still increasing, and sometimes it can flatten out, thus representing that thermal saturation has taken place.

9. Sensitivities and Simplifications to the EAF Modeling Strategy

The proposed EAF modeling strategy in this thesis is based in augmenting conventional metal forming and heat transfer equations with hypotheses of electrical influence on their behavior. This chapter serves to analyze the effects of several different model variables on the overall accuracy of the model. In addition, this chapter also explores potential ways to simplify the EAF modeling strategy and not lose desired accuracy. Specifically, the effects of the specific heat variability with temperature, the impacts of neglecting certain heat transfer modes, the observed differences in the EEC profiles of different materials (notably Ti-G2 and SS304), and frequency analysis of stress variation for an EAF compression test are explored. The objective of this investigation is to explain the sensitivities and relationships of the material and process inputs in the current and the resulting EEC profile, which designates the direct electrical effects of EAF [85].

9.1. Specific Heat Sensitivity

Although the heating effects from EAF are not a major contributor to the formability enhancements (as highlighted from the work by Ross et. al in Figure 14), these effects are utilized in the thermal-based EEC-determination method, where differences in temperatures between stationary-electrical and EAF tests were used to quantify the EEC profile. Therefore, it is important to understand the effect that the temperature has on the specific heat of the material, and ultimately on the EEC profile (*i.e.* the efficiency of the applied electrical power). In this analysis, specific heat sensitivities for both SS304 and Ti-G5 are evaluated at three different temperatures respective of the temperatures reached during three different tests (conventional forming, EAF tests, and stationary tests). Figure 156 displays the relationship between the specific heat values and the temperatures for each metal (note that the maximum temperature

which was reached during stationary testing at 25A/mm^2 for each material is denoted by a black dot). Additionally, Table 22 lists the exact specific heat values used for each test description in the model per material [118]. The maximum temperature observed in each type of tests was considered, in order to observe the maximum variability in the results due to variation of C_p with temperature.

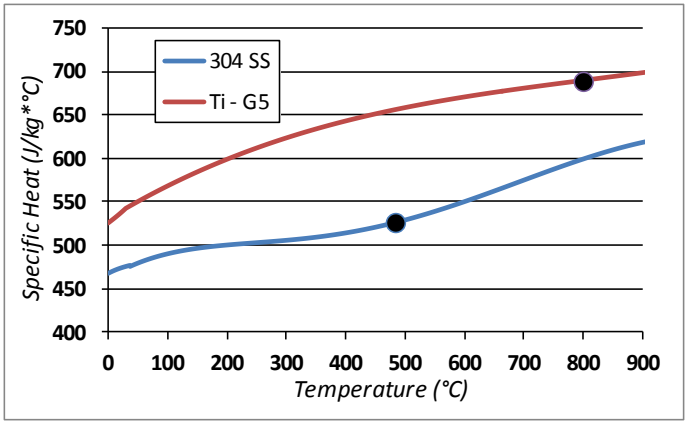

Figure 156. Specific heat vs. temperature profiles (304SS and Ti-G5) [118]. Relationships between the specific heat values and temperatures for 304SS and Ti-G5.

Table 22. Specific heat values used for analysis (SS304 and Ti-G5) [118].

Material	Description	Temperature (°C)	C_p (J/kg°C)
304 SS	Conv.	30	475
	EAF	250	503
	Stationary	500	530
Ti	Conv.	30	544
	EAF	450	650
	Stationary	800	690

To analyze the sensitivities of the specific heat value, stationary electrical tests, where a non-deforming static load is applied to the workpiece and a constant electrical power is applied, were simulated using the previously-developed thermo-mechanical predictive model [66] and [82]. Figure 157 displays the thermal profiles for stationary electrical tests with specific heat

values representative of maximum temperatures witnessed during conventional, EAF, and stationary electrical tests for Ti-G5. Additionally, Figure 158 displays the same information for Stainless Steel 304.

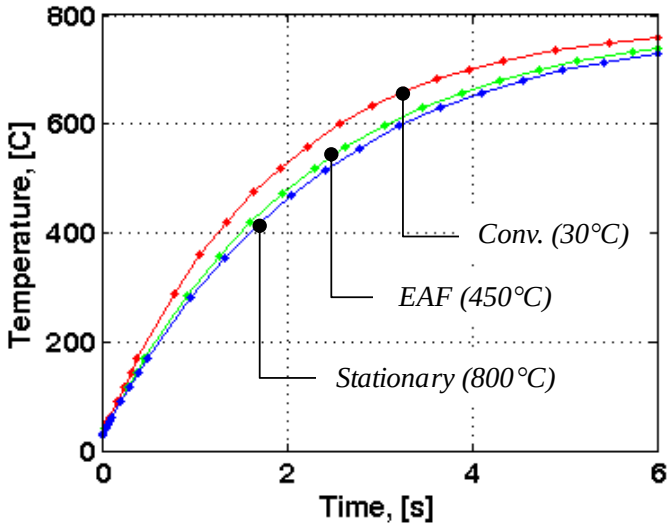

Figure 157. Specific heat sensitivity (Ti-G5) [85]. Thermal profiles of stationary-electrical tests with specific heat values for particular temperatures.

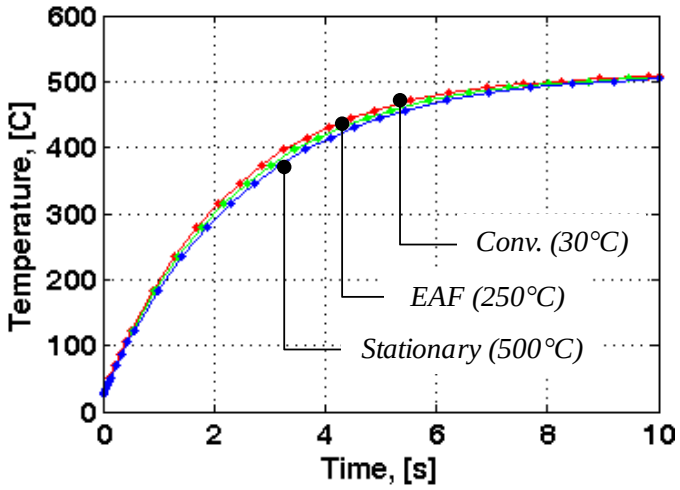

Figure 158. Specific heat sensitivity (SS304) [85]. Thermal profiles of stationary-electrical tests with specific heat values for particular temperatures.

When comparing the two figures, one can see that the specific heat of the Ti-G5 material was more dramatically affected, and this resulted in a larger variation in the specimen thermal profiles when using the three different specific heat values. At one point, the difference in the temperature profiles of the three tests for Ti-G5 was about 50°C, whereas the maximum difference between the three tests for 304SS was about 15°C. One possible reason for this is the intrinsic specific heat property of the material and its relationship with temperature (Figure 156), coupled with the temperatures reached during testing. The black dots in the figure represent the maximum temperature reached for each material. The temperature range reached for the Ti-G5 (0°C to 800°C) produced a 30% increase in the metal's specific heat value as the temperature was increased. In comparison, the temperature range reached for the SS304 (0°C to 500°C) produced a 12% increase in the specific heat value as the temperature increased. In this case, the Ti-G5 material had a slightly steeper specific heat vs. temperature relationship, and the maximum temperature reached during the Ti-G5 testing was about twice the temperature reached during the SS304 testing. In summary, the specific heat of the material needs to be considered when modeling EAF. It is highly dependent on the temperature range reached during forming (between room temperature and the hottest electrical temperature). As the specific heat increases, the energy required to increase the temperature of the workpiece also increases, and this can lead to an overall lower thermal profile. This is shown in Figure 157 and Figure 158, where the thermal profiles using the highest specific heat values are the lowest.

9.2. Heat Transfer Modes Analysis

As electrical power is input into a system, as in the EAM technique, some level of heating will take place. To this extent, heat will be lost by way of the three heat transfer modes

(conduction, convection, and radiation). The temperature increase of the workpiece can be represented by eq.(63):

$$\begin{aligned} \dot{E}_{part} &= \dot{E}_g - \dot{E}_{out}, \\ \dot{Q} &= \dot{Q}_e - \dot{Q}_{cond} - \dot{Q}_{conv} - \dot{Q}_{rad}, \end{aligned} \tag{63}$$

where $\dot{E}_{part}$ is the rate of change of the energy content in the part analyzed ($\dot{Q}$), $\dot{E}_g$ is the rate of heat generation due to the electric resistive heating ($\dot{Q}_e$), and $\dot{E}_{out}$ is the rate of energy leaving the part due to the sum of conduction into the dies in the contact zone ($\dot{Q}_{cond}$), convection ($\dot{Q}_{conv}$) and radiation from the surface ($\dot{Q}_{rad}$). To clarify, $\dot{E}_g$ has only one contributor ($\dot{Q}_e$), whereas $\dot{E}_{out}$ has three contributors ($\dot{Q}_{cond}, \dot{Q}_{conv}, \dot{Q}_{rad}$) which are the three forms of heat transfer. The energy is the total amount of heat lost or gained, and the power is the rate of heat lost or gained over time. Using constitutive equations for each component, the heat equation that determines the temperature rise for particular electric parameters is shown in eq.(64):

$$\rho V_v C_p \frac{\partial T}{\partial t} = -A_s[h(T - T_\infty)] - 2kA_c \frac{\partial^2 T}{\partial x_j^2} - A_s \varepsilon_r \sigma_{SB}\left(T^4 - T_\infty^4\right) + (1-\xi)VI \tag{64}$$

where ρ is the density of the material, V_v is the volume of the part, C_p is the specific heat of the material, T is the temperature, t is time, A_s is the exposed surface of the part, h is the convection heat transfer coefficient, T_∞ is the surrounding temperature, k is thermal conductivity of the die material, A_c is the cross-sectional area, x_j are coordinates, ε_r is

radiative emissivity for the part, σ_{SB} is the Stefan-Boltzmann constant, V is the electric voltage, and I is the intensity of the current, given by the product of the current density and cross-sectional area.

The goal of this sub-section is to determine the significance of each of the three heat transfer modes. To determine this, eq.(64) was modified in the model to represent the following heat transfer mode combinations and then compared to experimental results:

- All heat transfer modes except radiation (eq.(65))
- All heat transfer modes except radiation and convection (eq.(66))
- All heat transfer modes except conduction (eq.(67))

$$\rho V_v C_p \frac{\partial T}{\partial t} = -A_s[h(T - T_\infty)] - 2kA_c \frac{\partial^2 T}{\partial x_j^2} + (1-\xi)VI \quad (65)$$

$$\rho V_v C_p \frac{\partial T}{\partial t} = -2kA_c \frac{\partial^2 T}{\partial x_j^2} + (1-\xi)VI \quad (66)$$

$$\rho V_v C_p \frac{\partial T}{\partial t} = -A_s[h(T - T_\infty)] - A_s \varepsilon_r \sigma_{SB}\left(T^4 - T_\infty^4\right) + (1-\xi)VI \quad (67)$$

The resulting thermal profiles for all of the combinations are displayed in Figure 159. From the figure, the experimental temperature profile and the profiles neglecting both convection and radiation are nearly identical. Conversely, the thermal profile neglecting conduction heat transfer is nearly three times hotter at the maximum temperature than the experimental thermal profile. The fact that there is a large discrepancy between the experimental thermal profile and that without conduction signifies that conduction heat transfer is a major contributor to the

magnitude and overall shape of the thermal profile of an EAF test. Furthermore, the fact that the profiles neglecting radiation and convection are very similar to the experimental profile signifies that the effect of these two heat transfer modes is minor. Overall, when modeling EA-Forging, the all-inclusive heat transfer model could be simplified by neglecting both the radiation and convection heat transfer (in eq.(66)). Note that this simplification is only valid for EA-Forging. Alternative EA-processes, such as EA-stretch forming or EA-bending, may require including the other forms of heat transfer since the exposed surfaced area is typically greater in comparison to the total volume of the workpiece. An accurate thermal profile can be generated by assuming only conduction heat transfer is present. For the results presented here, C_p was assumed constant. As presented in an earlier section, the variability of C_p with temperature may results in a difference, more significant for Ti.

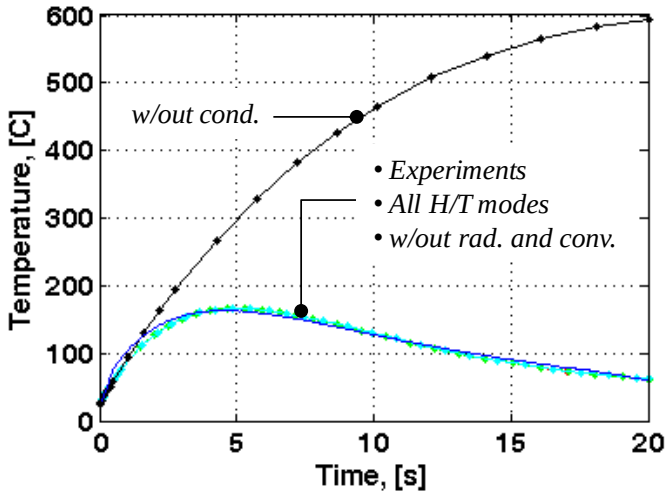

Figure 159. EAF heat transfer modes analysis [85]. Thermal profiles for stationary-electrical tests were calculated without particular heat transfer modes to identify the most significant mode (conduction).

Figure 160 displays a thermal image of the workpiece and the upper/lower dies after electricity has been applied during an EAF test. The figure helps to highlight the notable amount

of heat that is transferred from the workpiece into the die by way of conduction, as the dies act as thermal sinks in the system. The fact that conduction is the primary heat transfer mode is important in manufacturing process design because the size of the contact area between the dies and the workpiece will dictate the magnitude of heat transfer into and out of your system.

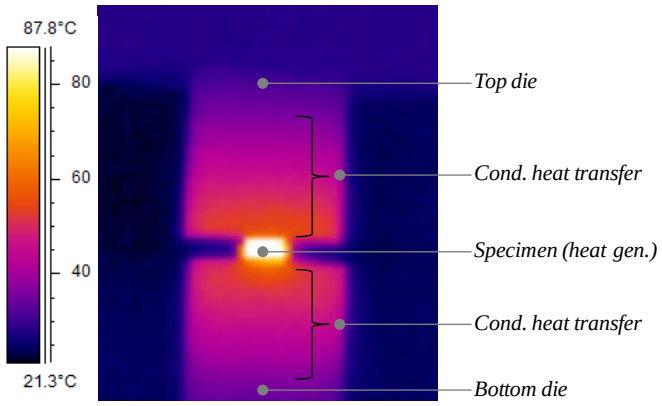

Figure 160. EAF thermal camera conduction heat transfer image [85]. This image depicts how the heat generated at the specimen center is conducted though the dies.

Now that conduction was determined to be the primary heat transfer mode for EAF compression, it is critical to verify any specific sensitivity. One variable that can change the thermal profile of the workpiece is the die conduction length, or the length of the die that contributes towards drawing heat from the workpiece (L_{dc}). Figure 161 displays workpiece thermal profiles for several different die lengths, along with the actual experimental data for EAF tests run at a starting current density of 20A/mm^2 and a die speed of 12.7mm/min. Currently, the authors use the thermal images to estimate the die conduction lengths, where the excessive heating was apparent when electricity was applied. The die conduction length used for the model in this case was 0.0085m. This was determined visually from the thermal camera profiles of the EAF tests. From the figure, where the conduction lengths are moved in increments of 2mm, the overall thermal profile is extremely sensitive to the die conduction length value. By varying the

conduction length by about 0.004m, there is about a 40°C difference in the maximum temperatures within the thermal plots. Overall, when modeling the electroplastic effect, it is critical to devise a consistent and accurate method of approximating the conduction length.

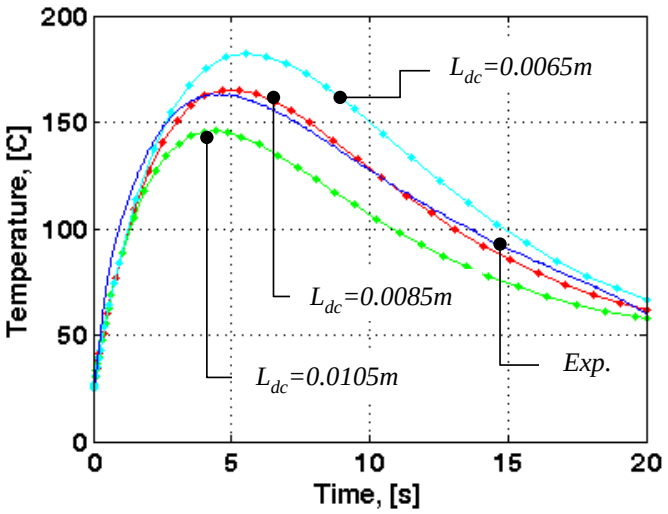

Figure 161. Stainless Steel 304 die conduction length sensitivity [85]. Different die conduction lengths were used in the model to determine the significance and sensitivity of the die conduction length value.

9.3. EEC Profile Material Sensitivity Comparison

In this sub-section, the general shape of the EEC profiles for the Stainless Steel 304 and Ti-G5 specimens will be discussed. Figure 162 and Figure 163 display the EEC profiles for Ti-G2 and SS304, respectively (both tests run at a starting current density of 25A/mm^2 with a die speed of 12.7mm/min) [85]. The EEC's are plotted here as a function of stroke. Other parameters could be used as well, *e.g.* strain or displacement, but the overall observations are still valid. From the two figures, it can be seen that the percent of "usable" electricity increases throughout the test, however, the increase is different for each material. Specifically, the majority of the EEC-profile increase for the Ti-G2 material occurs in the initial part of the stroke (about 50% of the maximum EEC value occurs over about the first 5% of the compressive stroke), whereas the

majority of the EEC-profile increase for the SS304 material occurs at the end of the stroke (about 50% of the maximum EEC value occurred in the final 25% of the stroke). Both of these EEC profiles were approximated using the power law, and the value of the exponential term is what determines the overall shape of the profile. Specifically, if the exponential term is less than one, the profile will be convex-shaped, and if the exponential term is greater than one, the profile will be concave-shaped.

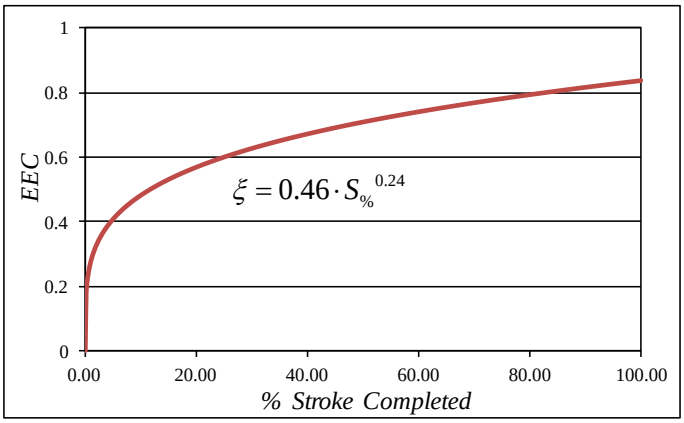

Figure 162. Ti-G2 example EEC profile (v=12.7mm/min) [85]. Depicted is a general shape of an EEC profile for Ti-G2 at this particular speed.

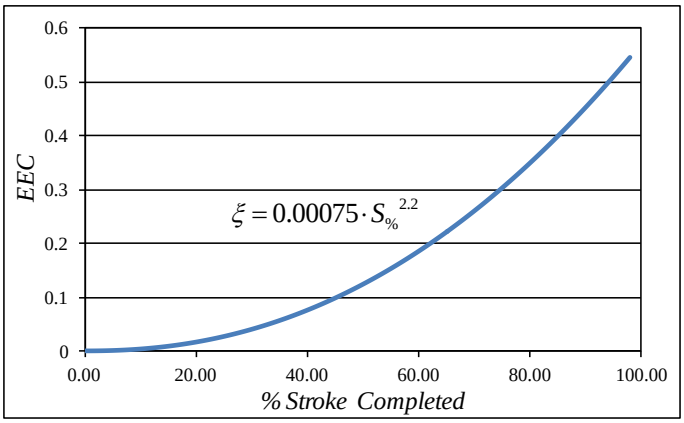

Figure 163. Stainless Steel 304 example EEC profile (v=12.7mm/min) [85]. Depicted is a general shape of an EEC profile for SS304 at this particular speed.

The concave/convex shapes of the profiles can also be explained visually by examining the mechanical power profiles of the EAF tests run on each of the materials. Figure 164 shows the mechanical power profiles of a conventional compression test and an EAF compression test for the Ti-G2 material. The difference between the baseline and EAF power profiles, at discrete points, becomes slightly smaller or remains the same as the test progresses. This explains the profile in Figure 162, where minimal increase is seen towards the end of the test, when compared to the increases at the beginning. Figure 165 displays the mechanical power profiles for EAF tests on the SS304 material. Contrary to the Ti-G2 material, the difference in the baseline and EAF power profiles increases as the tests progress. This leads to the profile in Figure 163, where the largest EEC increase is witnessed towards the end of the tests. The same differences between the conventional compression and EAF compression tests for each material were apparent in the stress-strain plots in Perkins et al. [40], as Figure 15 and Figure 211.

Two properties of the metals can be responsible for the difference in the shapes of the EEC profiles: the effect of temperature increase on the strength of the metal, and the effect of alloying. The strength of the titanium begins to immediate decrease as temperature is increased, whereas the strength of the stainless steel does not show much of sensitivity to temperature until higher temperatures are reached [87], [88]. The thermal softening could take place at a faster rate for the titanium due to the temperatures reached during the EAF tests coupled with the sensitivities of this metal's strength with temperature. The amount by which each metal was alloyed could also have an effect on the EEC profile. The 304SS had up to 20% chromium alloyed into the base iron metal. The chromium was weaker than the iron base metal and this allows for high ductility of the stainless steels. Also, the titanium was more than twice as resistive as the stainless steel, which contributed to the faster heating profile and higher EAF temperatures.

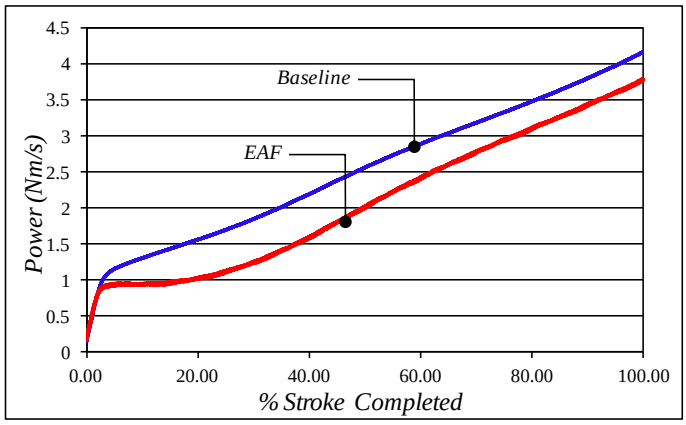

Figure 164. Ti-G2 example mechanical power profiles [85]. Depicted are example mechanical power profiles for EAF tests on Ti-G2.

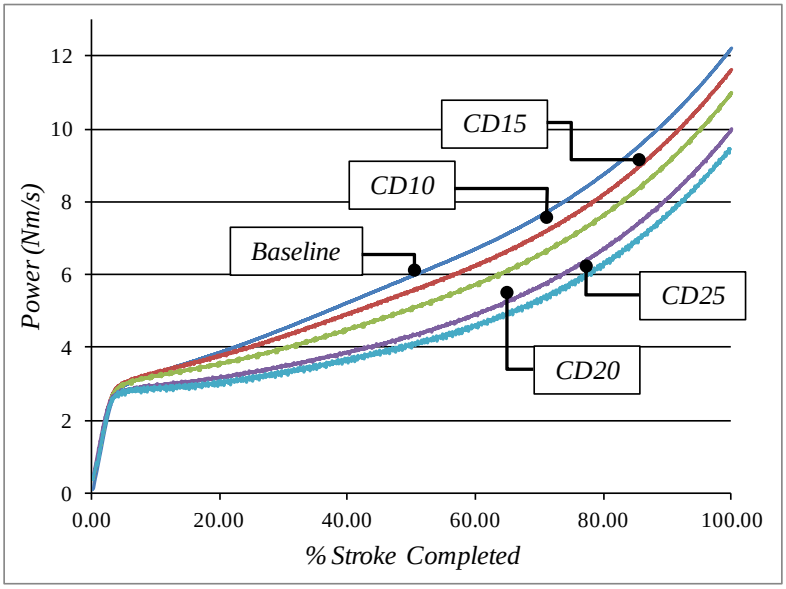

Figure 165. Stainless Steel 304 example mechanical power profiles [85]. Depicted are example mechanical power profiles for EAF tests on SS304.

9.4. EEC Frequency Analysis

During analysis of conventional/EAF tests on 304SS material, it was noticed that the EAF tests consistently produced a "thicker" load vs. time profile compared to the conventional tests (as seen in Figure 166). In the magnified, detailed view in this figure, the EAF test profile

had “spikes” in it. In this sub-section, a frequency analysis of the data is presented to try to investigate a frequency relationships to the “thicker” EAF load vs. time profile [85]. A comparison of the load recorded indicated the presence of a ‘noise’ in the data for the EAF. Figure 166 shows the load for both tests for Ti-G2 at a die speed of 12.7mm/min and an initial current density of 25A/mm^2. A detailed view of the results is included. Oscillation in the data is observed for the EAF test, while the conventional test is clean. The Fast Fourier Transform (FFT) analysis on the data was performed to rule out the influence from the electricity itself. The analysis for this particular test found dominant frequencies in the spectrum of ~23Hz and its multiples (Figure 167).

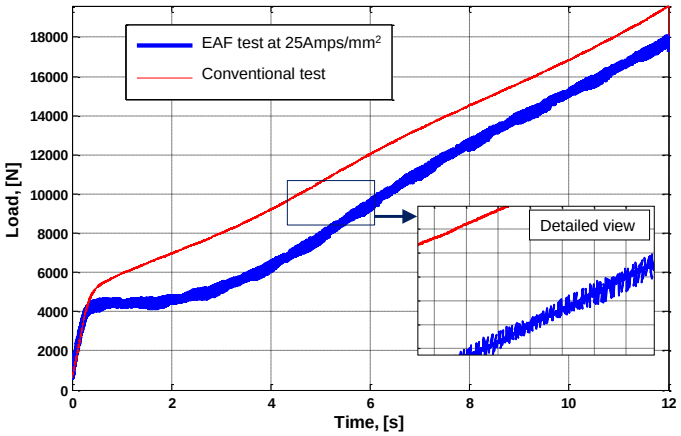

Figure 166. Comparison of the forces for a conventional and EAF test and details on the "noise" (Ti-G2) [85]. The EAF test load vs. time profile shows much more “noise” in the profile than the conventional compression test.

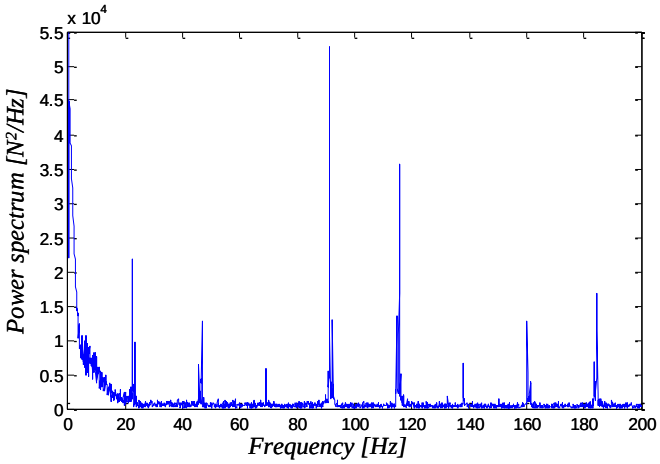

Figure 167. Power spectrum (FFT) for an EAF test (Ti-G2) [85]. The power spectrum shows the key frequencies for this particular set of electrical parameters.

Figure 168 displays the position vs. time profile for the conventional and EAF compression tests in Figure 166. This figure shows a linear displacement profile with a constant die speed. This confirms that the compliance of the testing machine was not responsible for the oscillatory portions of the load vs. time plot above. Figure 169 plots the frequency as a function of initial current density and corresponding current for the tests performed on stainless steel (SS304) at a die speed of 12.7mm/min. As the current density (*i.e.* current intensity/area) is increased, the frequency is increased, which means a decrease in the period or time of one oscillation. More specifically, as more electricity is applied, the oscillations occur at a faster rate. Note that only the first peak frequency was considered here.

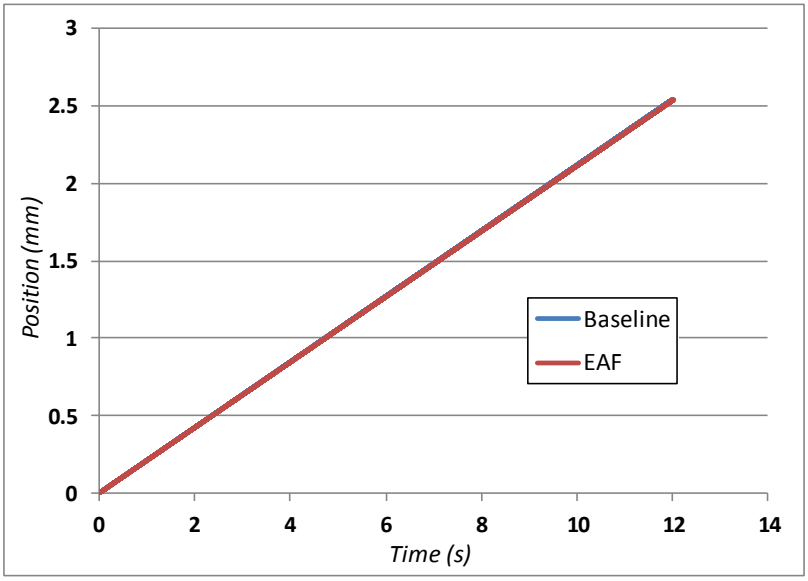

Figure 168. Position vs. time profile for conventional and EAF compression of Ti-G2. The position vs. time profile shows that the displacement is linear with respect to time and that there are no oscillatory portions of the profile. This proves that testing machine compliance was not the cause for the oscillatory profile, as seen in Figure 166.

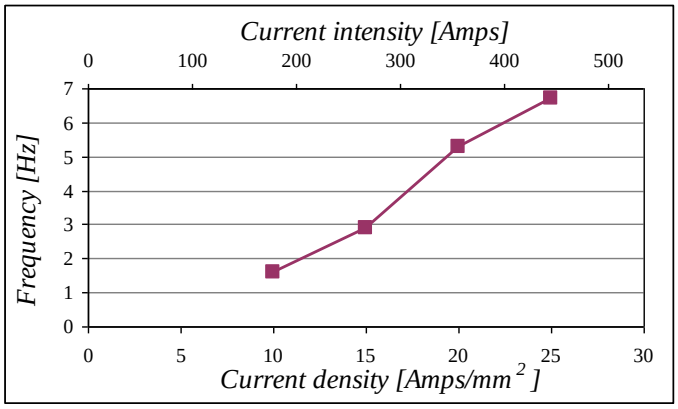

Figure 169. Frequency response for EAF loads for SS304 as a function of current intensity and initial current density [85]. As the current intensity or current density is increased, the frequency is also increased.

A first observation is that these values are lower than for titanium (G2, Figure 167). While it is not exactly known why SS304 frequency values are less than those of Ti-G2, some of the differences may be due to the crystalline structures or the different alloying components in each metal. Also, based on these results, one may speculate that there is a cyclic

softening/hardening phenomenon present during EAF. The input of electric energy results in alternating of electroplastic softening of the material, when the electric energy helps the dislocation to surmount obstacles and move, and hardening of the material due to deformation (schematic of the electrons impacting the dislocations is shown in Figure 170). This is responsible for the oscillations in the "detailed view" portion of Figure 166. The softening results in lowering the forming load, while the work hardening contributes to increase in load, until there is again enough energy for dislocation movement. The larger current density results from more electric power input, thus the oscillation in load happens faster and the frequency is higher. More specifically, as the average electrical input power is increased, the dislocations will be able to be "pushed" across the grain boundaries quicker and more often, thus increasing the frequency of the oscillations.

The amount of electric power contributing towards helping the deformation ($P_{EAF\text{-}def}$) was defined earlier as being a fraction of the total electric energy, where the fraction is the Electroplastic Effect Coefficient. Eq.(68) shows this relation as a product of two terms:

$$P_{EAF-def} = \xi VI = \xi RI^2 = \left(\xi I^2\right) \cdot R \qquad (68)$$

where R is the resistance. Figure 171 plots the variation of the first term, ξI^2 by considering the Electroplastic Effect Coefficient function determined earlier for 304 SS from the EAF tests at a die speed of 12.7mm/min. For current intensities of up to about 333A, the frequency profile and the first term profile are nearly identical. However, at current intensities above 333A, the frequency profile becomes higher than the first term profile. The difference may be due to the change in the resistivity, thus resistance, of the part with the increase in temperature due to the electric field applied. The temperature of the workpiece during EAF tests at a current density of

10A/mm^2 (167A) was 75°C, compared to 250°C at a current density of 25A/mm^2 (417A). The resistivity of the metal increased by 15% between these two temperatures [135].

The cyclic aspect of the load recorded during the electrically-assisted forming test and the apparent proportionality of the frequency with the energy input need to be further investigated. Some similarity is found with the oscillatory flow observed at high-temperature tensile tests, mainly for steels and aluminum, named the Portevin – Le Chatelier (PLC) effect [119]. The oscillation in the load is attributed to an unstable plastic flow, and depends on temperature and strain rate. The commonly accepted explanation for the PLC effect is based on a dynamic strain aging model, and is due to the interaction between the moving dislocations and diffusing solute atoms. In addition to temperature and strain rate, the PLC depends also on alloy composition, crystal lattice, dislocation density and grain size. Since all these are parameters that also influence the electroplastic effect, further tensile tests will be performed and the possible correlation between the PLC and electroplastic effects will be investigated.

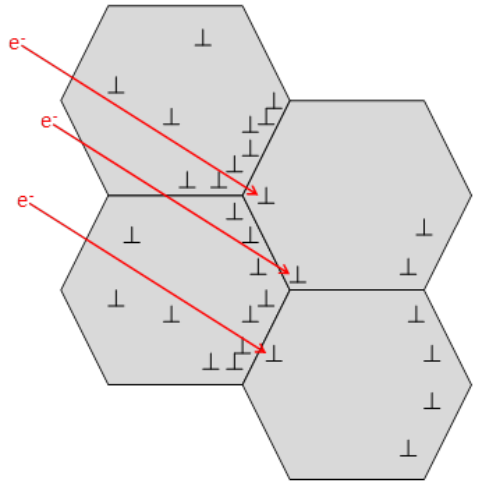

Figure 170. Grain boundaries, dislocations, and applied electricity [85]. This figure depicts how the electrons will interact with the dislocations and aid them in moving past the grain boundaries in the metal.

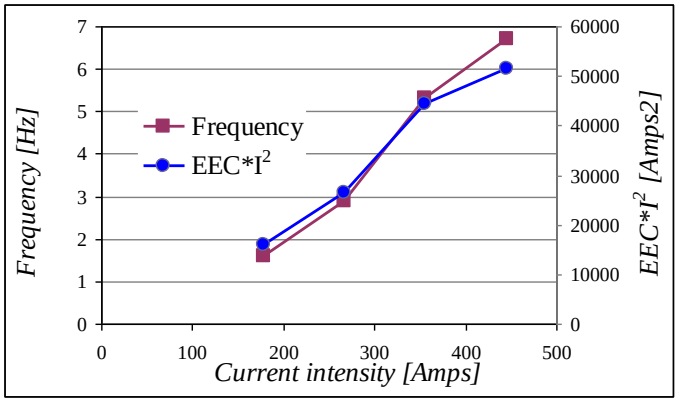

Figure 171. Variation of the frequency response and the electric energy component [85]. There is a direct relationship between frequency/electric energy component and the current density.

9.5. Quality of Electricity Effect on EAF

When analyzing the effect of applied electricity on the formability of metals, it is also important to quantify the quality of the electricity, as it may have an effect on the process. When beginning EAF research at CU-ICAR, a Lincoln R3S DC welder was used to supply the electricity for the metal forming experiments. Recently, a Darrah fully-controllable SCR power supply has been acquired and is capable of supplying much higher currents for much longer durations. Shown below in Figure 172 are the voltage vs. time waveforms of the Lincoln welder and the Darrah power supply, respectively, generated by an oscilloscope (please note that the waveforms are at different magnitudes). For the figure, the Darrah supply was run at a current of 300A. A multimeter was hooked to the positive and negative leads, as well as an oscilloscope. For this amperage, the multimeter read 0.738V, and the waveform amplitude was about 428mV.

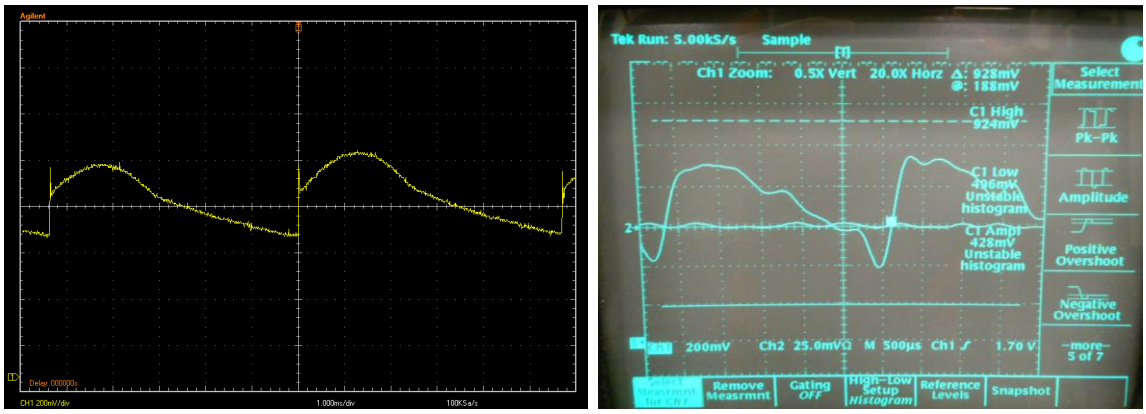

Lincoln R3S welder profile

Darrah SCR power supply profile

Figure 172. Welder and power supply waveform profiles. Voltage vs. time waveforms of the Lincoln welder and the Darrah controllable power supply are shown, with the Darrah supply producing more of a square-like wave as compared to the welder waveform.

Similar tests were run on both the welder and the Darrah power supply, with 3.81mm-diameter Titanium-G2 compression slugs. Figure 173 shows the engineering stress-strain profiles for these EAF compression tests run at a platen speed of 12.7mm/min for 2.54mm of deformation, while 300Amps were applied by each respective power source, as indicated on the figure.

From the figure a few key points can be made. First, the stress-strain profiles of the specimen with electricity supplied by the Darrah supply was higher overall compared to the Lincoln welder. Secondly, the "noise" in the stress-strain profiles was much less for the tests run with the Darrah power supply as compared to the Lincoln welder. One reason for this may be that the Darrah welder is more controllable and that it consistently output power closer to 300A as compared to the Lincoln welder. In comparison, the Darrah unit is self-compensating, whereas the Lincoln welder is manually controlled by potentiometer. Figure 173 shows that there is a small, but noticeable difference in the stress-strain profiles of identical specimens/tests when a different power supply is used.

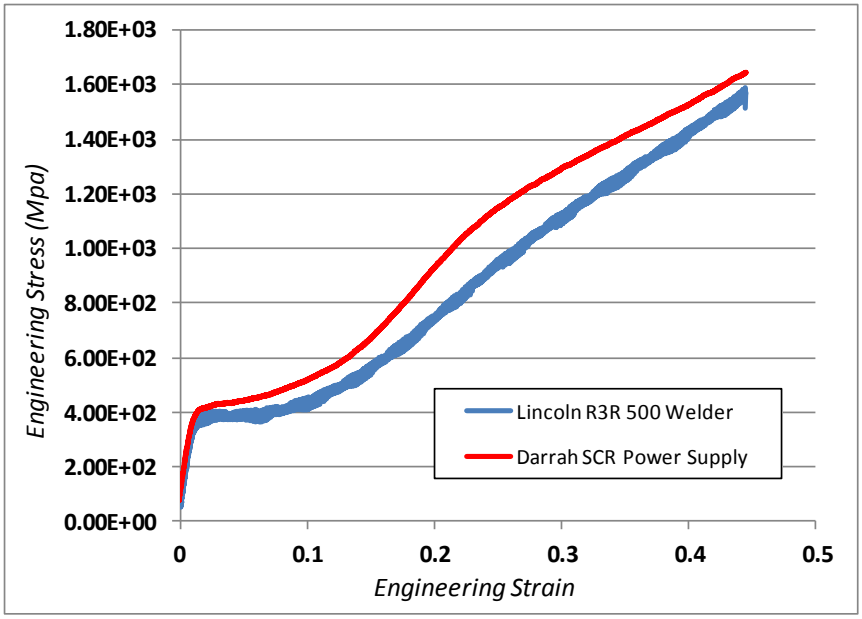

Figure 173. Ti-G2 engineering stress-strain profiles. The engineering stress-strain profiles were generated from running EAF tests at 300Amps, where the electricity was supplied with a Lincoln R3R 500 welder, as well as with a Darrah SCR power supply.

9.6. Power Supply Output Voltage Waveforms

The voltage waveforms produced from the Darrah power supply were further analyzed such to characterize the applied electricity. The purpose of this investigation was to determine how much variation was present in the output voltage profiles, and then to analyze if this magnitude of variation would have an effect on the electroplastic effect. To determine this, output voltage profiles were recorded from the power supply using an oscilloscope for two different current settings. The amount of voltage variation was compared for each current setting, and was also normalized with respect to the average voltage output profile. The work shows that the voltage variation is a constant related to the specifications of the power supply and the percentage of the variation as compared to the average voltage value decreases as the power output increases.

In the experiments, constant currents of 400A and 800A were run and the following attributes were discussed: 1.) the overall shape of the voltage profile, 2.) the peak-to-peak difference, or the variation in the voltage profile, and 3.) a comparison between the variation in the voltage and the average overall voltage profile value. Then, a discussion into the effects of the variations in the voltage waveform on the electroplastic effect will be covered. All of the voltage waveforms were produced by connecting an oscilloscope to the positive and negative leads of the power supply, while the power supply produced the specified current magnitudes in a closed loop.

Figure 174 and Figure 175 show the voltage waveform profiles of the power supply as it is continuously producing 400A, where Figure 175 is a magnification of the same waveform. In each figure, there are three parts, in which the lower peak-to-peak voltage, the higher peak-to-peak voltage, and the zero voltage designation line (in red) are all described. The actual lower and higher voltage values between the magnified and the un-magnified tests may vary slightly, since there was a higher accuracy in defining the true peaks with the magnified waveform pictures. Therefore, the voltage variation values reported in this section will be taken from the magnified figures at each respective current. From Figure 175, it can be seen that there was a difference in the peak-to-peak voltage of 56mV for the 400A tests. When compared to the average voltage value of about 88mV for this respective current, this variation in the voltage profile spanned 64% of the total average voltage value.

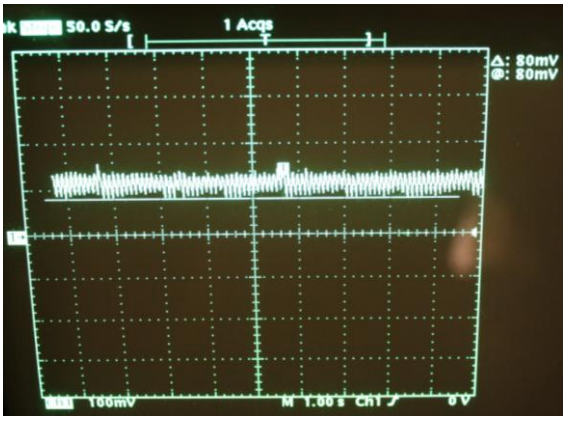

a.) lower voltage measurement (80mV)

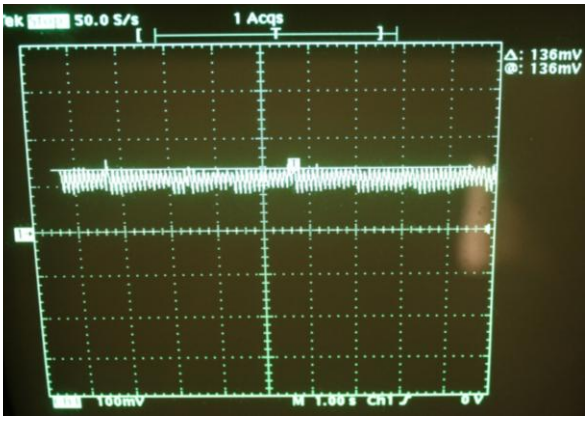

b.) upper voltage measurement (136mV)

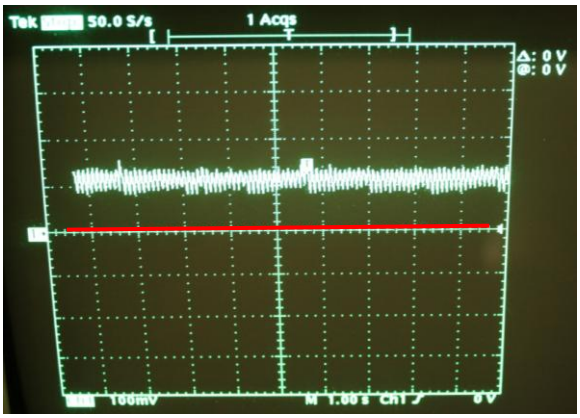

c.) zero voltage level

Figure 174. Power supply voltage waveforms at 400A (1.00s horizontal increments, 100mV vertical increments). The variation in the voltage profile was about 50mV, as compared to the average voltage value of about 100mV.

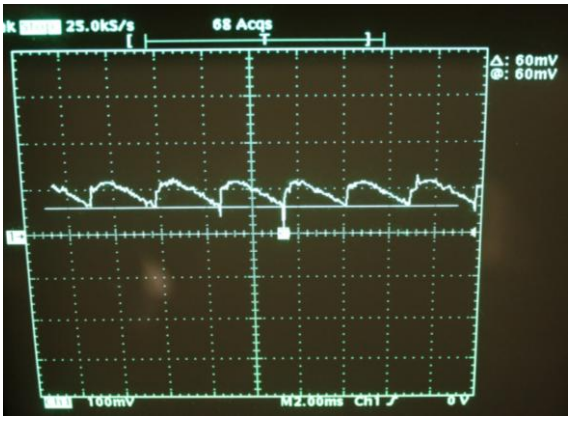

a.) lower voltage measurement (60mV)

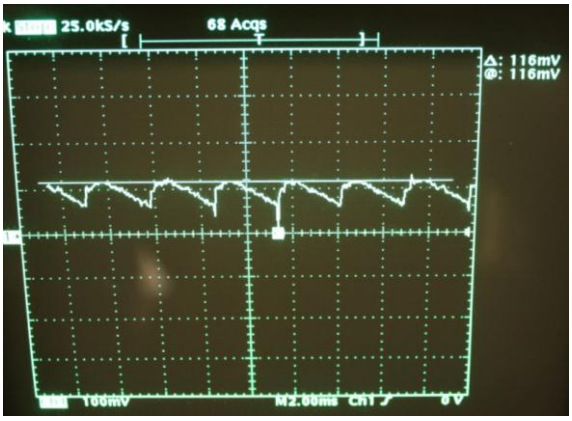

b.) upper voltage measurement (116mV)

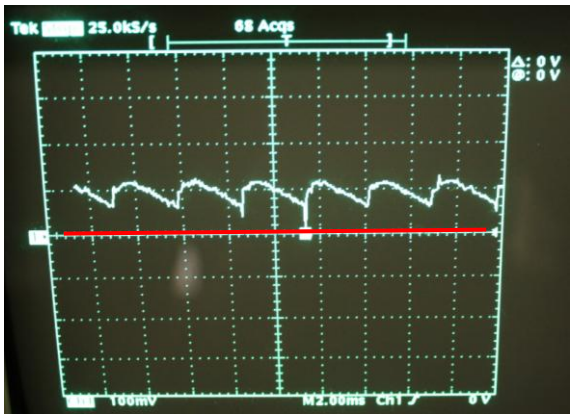

c.) zero voltage level

Figure 175. Magnified power supply voltage waveforms at 400A (2.00ms horizontal increments, 100mV vertical increments). The variation in the voltage profile was about 50mV, as compared to the average voltage value of about 100mV.

Figure 176 and Figure 177 display the un-magnified and magnified voltage waveform profiles from the power supply when outputting 800A, respectively. The difference in the peak-to-peak variation of the voltage profile was 72mV, which was 16mV larger than the voltage variation in the 400A-voltage profile. Additionally, the average voltage profile was 174mV, which increased since the current was also increased. The voltage variation was 41% of the average voltage value.

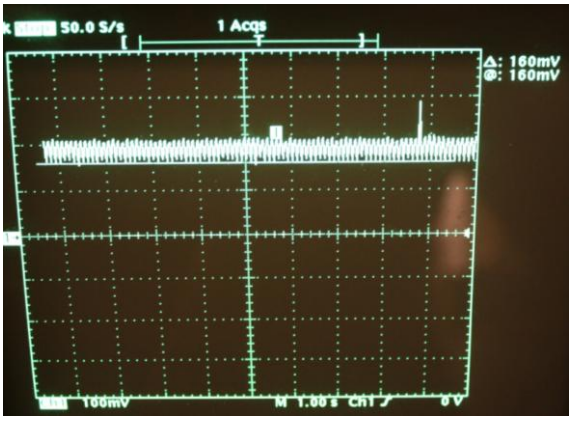

a.) lower voltage measurement (160mV)

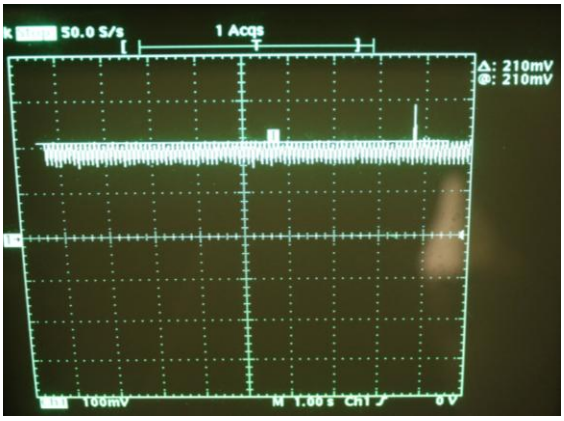

b.) upper voltage measurement (210mV)

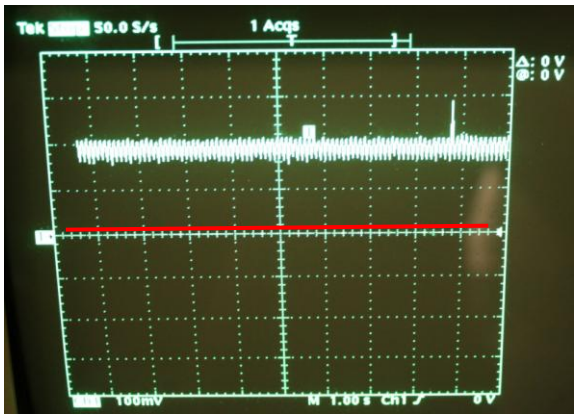

c.) zero voltage level

Figure 176. Power supply waveforms at 800A (1.00s horizontal increments, 100mV vertical increments). The variation in the voltage profile was about 50mV, as compared to the average voltage value of about 180mV.

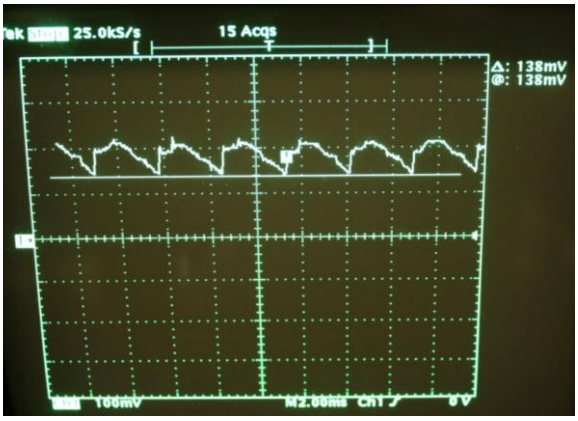

a.) lower voltage measurement (138mV)

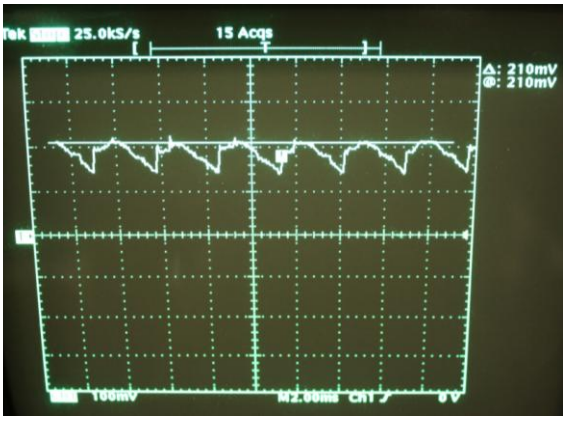

b.) upper voltage measurement (210mV)

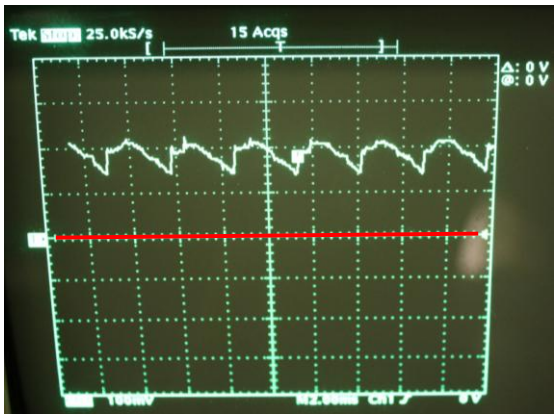

c.) zero voltage level

Figure 177. Magnified power supply waveforms at 800A (2.00ms horizontal increments, 100mV vertical increments). The variation in the voltage profile was about 50mV, as compared to the average voltage value of about 180mV.

The overall shape of the voltage output profiles for the two different currents were consistent with each other. The average voltage value increased as the current increased. Additionally, the variation in the voltage profile only increased slightly (16mV) from 400A to 800A. The variation in the voltage is unrelated to the electrical power output, but rather related to the capabilities of the power supply. The voltage variation spanned a larger portion of the average voltage profile for the lower current (64%) and spanned a lower portion of the average voltage profile for the higher current (41%).

The variation in the output voltage profile was a constant related to the power supply. Regardless of the current value that was chosen to be output, the variation within the voltage profile was a constant between 56-72mV. At lower currents, the voltage variation was a larger percentage of the average voltage value, and this percentage decreased as the current that was output increased. The theories supported by work from this thesis describe that the flowing electrons from the applied electricity impact lattice obstacles and cause resistive heating, and additionally dislocation motion if the impacted obstacles are dislocations. Electricity flows at a constant speed of light (300,000km/s), and when electrical power is increased, the quantity of electrons flowing through the circuit is also increased. The quantity of flowing electrons directly relates to the magnitude of heating effects and the magnitude of dislocation motion because the greater number of electrons will provide for more impacts with lattice obstacles.

The variation in the voltage profile will not have an effect on the EAF technique. With the DC voltage profiles, all of the voltage values are positive. As the average voltage value is what is intended and there are no negative values, the voltage variation will not matter. If the voltage profile is translated into the current profile (*i.e.* same shape) and then into the power profile, there will be times when extra power is supplied and times when less power is supplied. However, overall, the average power supplied will be the value that the power supply was programmed to output. In relating the electrical power to the quantity of flowing electrons, more or less electrons will be applied at high and low points of the voltage peaks, respectively. But as long as the average power is what was requested, the total quantity of electrons that passed through the metal will be the same, regardless of the magnitude of the voltage variation.

To continue this discussion on voltage variation, there may be particular manufacturing processes that may be sensitive to the variation in the output voltage profile. For example, tensile-based processes, where the cross-section of the workpiece decreases throughout the

process, are more sensitive to variations in heating. If the voltage and current profile variations produce higher-than-average and lower-than-average electrical power fluctuations, this could affect heating in the tensile-based processes because the quantity of electrons will be increasing and the cross-section by which they are flowing will be increasing. In forging, where the cross-section of the workpiece increases, the heating due to the electricity is not as sensitive as with the tensile-based processes, because although the quantity of electrons is changing, the cross-section that they are flowing through is increasing.

Future experimentation to further analyze the effects of power supply output variation could be performed. Specifically, the voltage profiles of 400A and 800A from the power supply could be compared to the output at the same currents from different power supplies, and even from a battery. Additionally, electrically-assisted compression and tension tests could be run with the power produced from a power supply and from a battery, and the workpiece temperature and mechanical profiles could be compared.

9.7. EAF Model Sensitivities and Simplifications Conclusions

This paper analyzes the effects of specific heat values, and various heat transfer modes on the effectiveness of EAF. Additionally, observations are provided for the different EEC profiles for certain materials. Also, a frequency analysis was performed on the force position data acquired from the testing machine. The following conclusions can be drawn from the research:

- The specific heat of a material must be considered when modeling EAF. The effect that the specific heat has on the ability to model EAF is proportional to the sensitivity of the specific heat value with respect to temperature.
- When modeling EA-Forging, the all-inclusive heat transfer model could be simplified by neglecting both the radiation and convection heat transfer. This simplification is only

valid for EA-Forging. Alternative EA-processes, such as EA-stretch forming or EA-bending, may require including the other forms of heat transfer since the exposed surfaced area is typically greater in comparison to the total volume of the workpiece.

- Different metals produce different EEC profiles when the EAF technique is used on them during a forging process. The differences include the overall shape of the profile (the profile could be concave, convex, etc.), this shape determines the overall efficiency of the applied electrical power throughout the duration of the process.
- The frequency analysis indicated that there are specific frequencies dependent on the magnitude of the current density applied. The frequency increases with the current density, thus with energy input. This may be an indication of a cyclic softening/hardening phenomenon present during EAF.
- The frequency observed for titanium is higher than that for SS304. This could be due to any differences in the crystalline structure or specific alloying components within the metals.
- The quality of the electrical power output during an EAF process can vary depending on the capabilities of the power source. This can also have an impact on the mechanical profiles of the same parts undergoing the same EAF process.

10. Science of the Electroplastic Effect

This chapter describes the fundamental theorized mechanisms responsible for the electroplastic effect in Electrically-Assisted Manufacturing (EAM). Within this section, plastic deformation of metals is explained, focusing on bonding, dislocations, crystal structures, and lattice defects. In addition, electric current flow is defined and resistive heating is discussed. Then, the effects of electricity coupled with deformation (*i.e.* the electroplastic effect) are explained.

The background information on plastic deformation and electricity is used to describe the three postulated theories on the electroplastic effect from previous EAM research. All three previous theories discuss bond breaking and reformation, but some attribute it to heating effects and others attribute it to momentum transfer effects. The scientific contribution from this thesis is the consolidation of the previous theories into one clear explanation of assisted dislocation motion, which incorporates both heating and momentum transfer effects from the electrons. The basis behind when heat is generated and when momentum is transferred is dependent on the type of lattice obstacle the electron impacts. Impact with a lattice obstacle that does not facilitate deformation or does not travel through the lattice, such as an atom, impurity, and grain boundary, will result in mostly heat, whereas energy released from impact with an obstacle that is moveable and facilitates plastic deformation (*i.e.* a dislocation) will be partitioned into heating and momentum transfer effects, which are quantified by the EEC. To conclude this chapter, experimental data from the thesis is used to support the comprehensive theory.

10.1. Plastic Deformation of Metals

Plastic deformation can be classified as permanent reshaping of a metal. In plastic deformation, dislocations move through the crystal structure of the metal, breaking and reforming

metallic bonds. Dislocation motion (*i.e.* deformation) can be hindered by defects in the crystal structure of the metal. In this section on plastic deformation, the following will be explained:

- Bonding
- Dislocations
- Crystal structure
- Lattice defects

10.1.1. Bonding

Any group of bonded atoms has an energy associated with it. The bonding force for metallic bonds consists of the attraction forces, due to opposing charges of the atoms, and the repulsion forces, that are due to the overlapping of the outer shells of the electrons. The equilibrium spacing is achieved by the attractive forces and the repulsive forces balancing each other. As these forces increase, the energy state of the bonded atoms increases and thus it is more willing to find another atom to bond with that will decrease the energy state. In metals, the ion nuclei (consisting of protons and neutrons) exert a net positive charge. The valence (or free) electrons (with a negative charge) surround these ion cores, creating an attraction. Note that the mass of an electron (9.11×10^{-31} kg) is much smaller than the mass of a proton or neutron (1.67×10^{-27} kg) [140]. Each ion core carries a net positive charge because its valence electrons were given up to create the "electron cloud" or "sea of electrons" that is shared between all the ion cores. The positive charge of a particular ion core and the same positive charge of neighboring ion cores lead to the ion cores having repulsive forces between them. The negatively-charged valence electrons are attracted to the much larger positively-charged ion cores. In doing this, the valence electrons negate these repulsive forces from the neighboring ion cores. The valence electrons create the spacing between the ion cores and absorb the repulsive

forces from the same charges. Depending on the magnitude of the charge of the ion cores, a corresponding amount of valence electrons will be attracted to it.

Of the three main types of bonds (ionic, covalent, and metallic), metallic bonds are the weakest. A bond generally consists of atoms or a core, and electrons. Surrounding each atom are shells of electrons. Each shell has the maximum number of electrons that it can hold in it. The electrons in the outer-most shell are called valence electrons, or free electrons because they have the ability move from one outer shell to another. If a particular atom has open spaces for extra electrons in its outer shell, then that particular atom is at a higher energy level as compared to an atom with all of the open spaces in its outer shell occupied. If the atoms have their outer shells completely full of electrons, then they will be at the lowest energy state and will not be reactive to the other atoms (like the noble gases at the far right column of the periodic table). If there are openings available in the outer shell, the atom is still at a higher energy state than what it could be. In addition to missing valence electrons, the energy of the atoms could also be increased by an applied external stress. As this external stress on the atom increases, it will create an energy state higher than what the atom can withstand and will force the atom to break its bonds and reform new bonds and share valence electrons.

In essence, the classification of the bond type is dependent on how the valence electrons are utilized by the material. In ionic bonds of NaCl, the valence electrons are permanently transferred from a metallic element to the nonmetallic element. In doing so, the two elements now will have equal and opposing charges. This is a strong type of bonding because the valence electrons are not shared, but actually transferred and each atom exclusively owns their electrons. Materials with ionic bonding are ceramics. These materials can also withstand high temperatures, since their bonding strength is high and it would take a lot of heat to increase the energy of the atoms to cause the bonds to break.

In covalent bonds, the valence electrons are shared between multiple atoms. Methane (CH_4) is an example of a covalently bonded material, since electrons are shared between the carbon element and the four hydrogen elements. In this case, each element needs the shared valence electrons to stay bonded. This type of bond is not as strong as the ionic bond because the valence electrons are being shared, rather than actually being transferred from one atom to another, so several atoms own the electrons and each can have an effect on what happens to the total electron count in the bond. In the case of CH_4, if one out-of-the four total hydrogen elements (per CH_4 molecule) breaks and reforms with another set of elements, than the CH_4 molecule is now left at a higher energy state and looking for another hydrogen element to share electrons with.

In metallic bonds, electrons are collectively shared to an even greater extent that with covalent bonds. These bonds consist of positively-charged ion cores (protons and neutrons) and a commonly shared "sea of electrons". Each ion core gives up several of its valence electrons, thus creating the "sea of electrons". The negatively charged electrons are attracted to positively-charged ion cores, and they serve to provide the spacing between the ion cores, which repel each other. The electrons are collectively shared between many ion cores and they can easily move. With all of the valence electrons ("sea of electrons") easily able to move around and not be associated with one particular atom, the breaking and reforming of bonds is easy, making metals much more ductile, as compared to other materials (*e.g.* ionic bonded ceramic). This also contributes to the low melting points of metals as compared to ceramics, because the metallic bond is the weakest primary bond and it requires less energy to excite the atoms enough to break the bonds.

10.1.2. Dislocations

Dislocation motion is required for plastic deformation. A dislocation is simply a misalignment of the atomic structure in the lattice of a metal. There are three types of dislocations (edge, screw, and mixed dislocations). In the edge dislocation in Figure 178, there is an extra set of atoms within the top half of the figure. The location of where the string of atoms is unbonded at its end is the dislocation in the lattice structure and it is at a higher energy state as compared to the bonded atoms. As a force is applied to the metal, the string of atoms that were previously unbonded at its end will now bond with the neighboring string of atoms in the lower half plane. This will then leave the neighboring string of atoms in the top plane, which are one atomic unit in the direction of the force, unbonded. Thus, the dislocation, or the bonding defect in the lattice moved one atomic unit. As the bonds continue to break and reform, which is caused by the external force exerted on the metal leading to the stress exerted on the dislocation, the bonding defect (dislocation) will migrate through the metal's lattice. This overall shifting of the dislocations is termed plastic deformation. To clarify the difference between elastic and plastic deformation, in elastic deformation, the bonds are only stressed, and the lattice goes back to its original spacing once the metal is unloaded. Conversely, bonds must be broken for plastic deformation to take place. Once bonds are broken, the metal cannot go back to its original shape without rebreaking and reforming of the bonds.

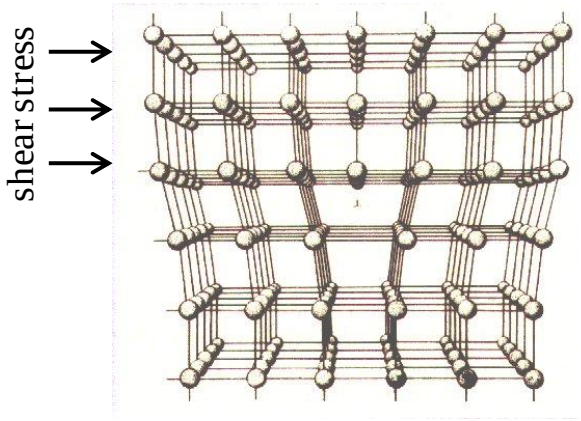

Figure 178. Edge dislocation [136]. The bonding defect in the center of lattice, where there is a string of unbonded atoms, is an edge dislocation.

The second type of dislocation is the screw dislocation, as seen in Figure 179. In this type of dislocation, there is a step, or ramp shape that is created due to the external forces. As seen in the figure, the external forces create a shear stress that moves the front upper region of the lattice one atomic spacing unit past the front bottom region. As you examine the depth of the lattice, a screw-like "ledge" is formed since the front region shifted a complete atomic spacing unit and the rear region did not yet. As a greater amount of shear force is exerted, the neighboring bonds near the front region will become more stressed and will likely break and reform to enable this shift to move its way along the depth of the crystal structure in the figure.

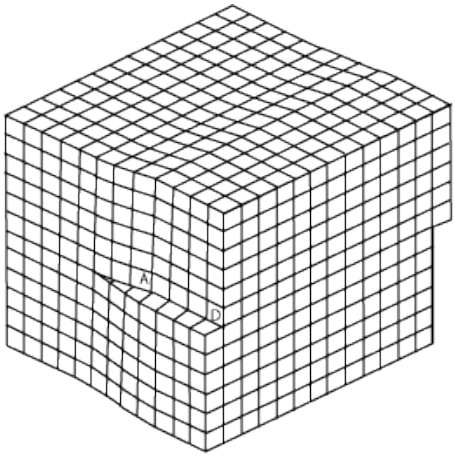

Figure 179. Screw dislocation [137]. The screw dislocation is created by a shear stress that causes the lattice above or below the shear line to advance one atomic spacing unit.

The third type of dislocation is the mixed dislocation, as shown in Figure 180. Most of the dislocations in metals are mixed dislocations, since they may consist of multiple lattice defects that are representative of both edge and screw dislocations. In the figure, as the force is exerted at point A, the bonded atoms at the location of where the force was applied break bonds with the aligned atoms and reform bonds with the atoms one atomic spacing in the direction of the force to cause a screw dislocation. This causes one set of bonded atoms in the top half of the unit cell to now be unbonded, which is shown by the edge dislocation at Point C.

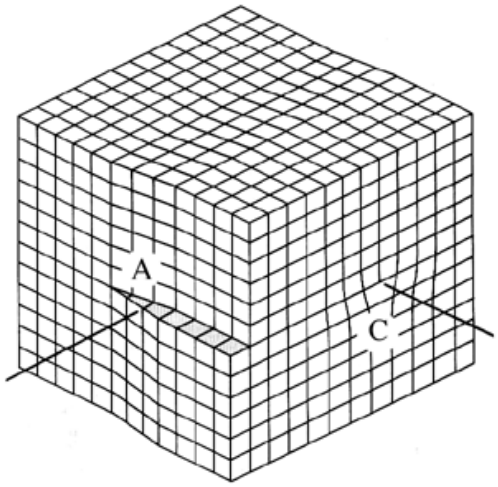

Figure 180. Mixed dislocations [138]. Mixed dislocations are a combination of edge and screw dislocations.

Regardless of the dislocation type, the number of dislocations within a metal increase as the level of plastic deformation increases. This is because the dislocations do not only move through the lattice, but new dislocations are created at lattice defects. A dislocation line can be classified as an unbonded string of atoms. A defect in the lattice disrupts the equilibrium bonding of the lattice. If forces are exerted on the lattice and bonds must consistently break and reform, this disruption by the lattice defect can create bonding inconsistencies in the form of dislocations, because of the extra energy needed to break and reform bonds around this defect.

There are certain "pathways" that dislocations can move throughout a metal's lattice. These pathways are called slip systems. The dislocations travel on slip systems, which are comprised of slip planes and directions, and are specific to the particular crystalline structure of the material. While traveling on these slip systems, the dislocation motion can be hindered by different interfacial defects within the lattice. Such defects include impurities, voids, grain boundaries, faults, and other dislocations. As the dislocation movement is hindered by these obstacles, the dislocations begin to pile-up, thus increasing the forces needed to continue plastic deformation. This phenomenon is known as strain hardening. In order for the dislocations to be

able to surpass the obstacles, additional energy is required to force the dislocation past the defect. In order for the dislocations to continue moving, there must be enough energy to: 1.) Distort the lattice surrounding the dislocation, 2.) Move the dislocation past the lattice defect, and 3.) Break and reform bonds within the lattice [140].

If dislocation motion is not continued, the metal will fracture. In this case, fracture is a result of too many dislocation pile-ups. As the metal deforms more dislocations are created and there is a higher dislocation density within the metal. As the density increases, the separation distance between the dislocations is reduced and the repulsive forces between the dislocations will increase as the dislocation density increases. To this end, if a metal is being deformed and dislocations cannot move, more dislocations are being generated and are being moved until they come across a stuck dislocation, or a pile-up. The addition of dislocations continues until the repulsive forces between dislocations become too high and cause the metal to break. One possible way to eliminate dislocations from a metal before fracture would be to perform an annealing procedure, where the metal is heated to a material-specific time and temperature setting, and a new lattice structure would be created from recrystallization with fewer dislocations in it.

10.1.3. Crystalline Structures

A crystalline material can be any material that has an actual pattern in which atoms are situated over a given atomic level distance. The pattern of atoms is the lattice. There are three main crystal structures for metals, and the separating characteristics of these structures involve spacing, packing, and stacking patterns. For each crystalline structure, several key characteristics will be discussed, including the coordination number, the atomic packing factor, and the number of slip systems. Figure 181 shows the unit cells of the three primary crystalline structures. The

coordination number describes the number of neighboring atoms that a single atom touches within a unit cell of the metal. This can be important for characteristics such as heat transfer, since thermal conductivity would typically be higher in metals where more atoms are contacting each other. The atomic packing factor (APF) shows the ratio of the volume of the atoms to the total volume of a unit cell. This can describe the amount of excess space within a unit cell of a metal. The higher the APF, the less excess space there is for any other atomic level particles to fit through. The number of slip systems that a metal has is important for plastic deformation, because these are the only methods by which dislocations can travel in order to facilitate deformation (ignoring nano-deformation mechanisms).

Face-Centered Cubic (FCC)

The coordination number of a FCC metal is 12, which is the number of atoms a single atom touches within a unit cell. In addition, the atomic packing factor (*i.e.* the volume of the atoms in a unit cell compared to the total volume of the unit cell) is 0.74. FCC metals have 12 slip systems. As stated above, these are like "roadways" for the dislocations to travel on in order to allow for plastic deformation. Examples of some FCC metals are copper, aluminum, and some stainless steels [140], [141].

Body-Centered Cubic (BCC)

The number of neighboring atoms contacting each atom in a BCC metal is 8 (the coordination number). Additionally, the packing factor for BCC metals is 0.68, which is lower than the FCC metal. The BCC metals can have 12 or 24 slip systems, depending on the different slip plane/direction combinations [140], [141].

Hexagonal Close-Packed (HCP)

The coordination number and the atomic packing factor for HCP metals are the same as for FCC metals, which are 12 and 0.74, respectively. The HCP metals have the lowest number of slip systems, with three. This limited number of slip systems makes these metals very brittle. Additionally, these metals often twin to facilitate deformation, due to the lack of active slip systems. Twinning is when a mirror representation of a particular lattice arrangement is created across a given plane (*i.e.* a twin plane). In HCP metals, plastic deformation by way of dislocation motion can be difficult with the limited number of slip systems for the dislocations to travel on. As the shear force within the metal increases, it will generate a mirror representation of a particular lattice structure. This newly generated lattice structure will provide for reoriented slip systems that will provide the dislocations potential pathways for which to travel on and continue deformation. Examples of HCP metals are titanium and magnesium [140], [141].

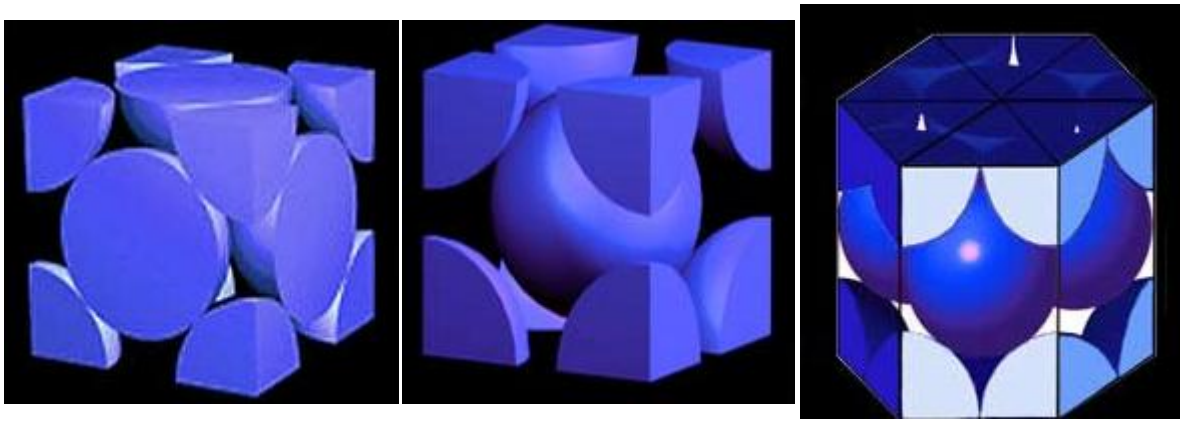

a.) FCC unit cell b.) BCC unit cell c.) HCP unit cell

Figure 181. Unit cells of the primary crystalline structures [139]. a.) FCC, b.) BCC, and c.) HCP.

10.1.4. Lattice Defects

A characteristic of a crystalline material is a repetitive atomic structure or pattern across its lattice. However, there can be several different types of defects throughout the lattice of a crystalline material. The importance of lattice defects are that they can affect dislocations that are traveling through the different slip systems within the lattice. Some examples of lattice defects are voids, impurities or alloying components, grain boundaries, phase boundaries, and other dislocations.

- A void is an empty spot in the lattice structure where an atom should be. Since there is not an atom, the neighboring atoms either cannot fully bond or must bond with further away atoms, both of which will increase the energy state of the bonding.
- An impurity can be any element in the atomic structure that is not normally included in the lattice. Each element has atoms which have a specific atomic radius. To this end, if all the atoms in the lattice were the same size (*i.e.* a pure material), the bond spacing between the atoms would be equal. However, if an original atom is replaced with an atom of a different size atomic radius, the bond spacing at and near this impurity will now be affected. There can be two types of impurities. A substitutional impurity is when the atom of a base metal is replaced with an atom of another material. The difference in atomic size of the new atom will provide for either a state of compression or tension on the bonds surrounding it. The second type of impurity is the interstitial impurity, where an atom from a new element is aligned in the free space between two bonded atoms of the base metal. As is the case with the substitutional impurities, the interstitial impurities also distort the bonds around it.
- Grain boundaries mark the end of one lattice in a crystal structure and the beginning of another. The lattice structure consists of slip planes oriented in particular directions with

respect to the grain that they are in. Once into another grain boundary, the slip planes on either side of the grain boundary will be oriented with respect to the particular grain they are in, which will be different compared to the previous or next grain. In dual-phase materials, the different phases act the same as the grain boundaries, in that they break up the consistency of the lattice pattern.

- Dislocations can also be considered lattice defects because they represent portions of unbonded atoms within a lattice.

Regardless of the type of lattice defect, any flaw in the lattice of the material will have an effect on the dislocations that are moving through the metal. In the case of a perfect lattice, the dislocations will move by way of breaking and reforming bonds due to external forces that are exerted, as was described in the previous sections. However, when there is something in the structure of the lattice that is not normally there (*i.e.* a defect), the dislocations now have a harder time advancing past this point, unless extra energy is provided to do so. The halting or hindering of dislocation motion leads to dislocation pile-ups. If the dislocations cannot move through the metal, the metal cannot continue deforming (since a collection of many dislocation motions result in deformation at the bulk level). Continuing this example, if the metal was being plastically deformed and dislocation pile-ups were beginning to occur, the force required to continue deforming the metal would increase, and this additional force is required to provide the dislocations with the extra force they need to surpass the defects within the lattice. In general, this is the basis for strain hardening. Different types of lattice defects can cause dislocation pile-ups in different ways.

- Impurities can be intentionally added to a material for strengthening purposes (*i.e.* alloying in Aluminum or Stainless Steel alloys). These impurities can be intended to

increase the strain hardening of the metal in order to make it stronger for a particular application. As the number of impurities in a metal increase, the magnitude of strain hardening increases.

- Grain boundaries are the locations where the orientation and direction of the lattice changes, and different grains are spread throughout the microstructure of the metal. Each time a dislocation comes to a grain boundary, it cannot progress through the boundary. The dislocation creates a stress at this boundary such that a new dislocation is created from the stress at the grain boundary inside the new grain, and then this dislocation can begin moving through the new grain's different oriented slip systems. For the same bulk dimensions, a metal with a smaller grain size would have more grain boundaries and a greater grain boundary surface area for the dislocations to travel through so they would need excess energy each time they reached a grain boundary in order to change direction/orientation, or to create stress to produce a new dislocation. Therefore, a metal with a smaller grain size is typically stronger than a metal with a larger grain size. In addition, the number of slip systems also plays a role in the strain hardening because a metal with fewer slip systems will have a less likely chance of the slip planes lining up well at the grain boundaries, and the dislocations will have a higher probability to need to change directions to a larger degree.
- The dislocations are also a defect, but they are not stationary, like the impurities and the grain boundaries. If a moving dislocation comes into contact with another dislocation, they could either cancel each other out or they could repel each other. If the first dislocation cannot move, because it is being held up (repelled) by another dislocation, then the pile-up will continue until enough energy is now supplied such to provide the

dislocation at the front of the pile-up with enough energy to break the bonds in front of it and travel through the lattice.

Aside from alloying, potential lattice defects can also be intentionally created (strengthening mechanisms) or removed (weakening mechanisms). For strengthening mechanisms, heat treating the metal to produce a small grain size could strengthen the metal so there are more grain boundaries for the dislocation to pass through. Also, the metal could be preworked so that the dislocation density within the metal is higher than in the annealed state and these dislocations dispersed through the metal are all additional defects. Dislocation density is presented in terms of the total of all the dislocation lengths within a unit volume [mm/mm^3], or it could be presented as the number of dislocations intersecting a 2-D unit area of a material [$\#/mm^2$]. For a polycrystalline metal, the dislocation density at an annealed state can be about $10^7 mm/mm^3$ and the dislocation density in a worked state can be about $10^{12} mm/mm^3$, which means that the overall dislocation density between annealed and worked conditions could be about 100,000-times different [117]. Heat treating could also be performed to weaken the metal, by way of allowing for recrystallization and grain growth to occur. The larger grains would equate to a fewer number of grain boundaries that a dislocation must pass through and change its direction, hence less external force would be needed.

10.2. Electric Current Flow

Electricity is flowing electrons that travel through a conductor. This section will concentrate on providing a definition for electricity and also on explaining its effects on metals without deformation. The following parts of this section will address:

- Description of electric current flow

- Electrical resistivity
- Heat generation due to electricity

10.2.1. Description of Electric Current Flow

Electricity is defined as electrons flowing through any conductive medium (*e.g.*, a metallic workpiece). Electrons are small particles with a negative charge. In relation, the size of an electron is about 1000-times smaller than the size of a proton or neutron. In addition, the mass of an electron is 9.11×10^{-31}kg, whereas the mass of a proton or neutron is 1.67×10^{-27}kg, providing for a mass difference of about 1830-times [140]. An electron and a proton both have charges of 1.6×10^{-19} Coulombs, however, the electron charge is negative and the proton charge is positive [140].

10.2.2. Electrical Resistivity

Each metal has a set resistance to electron flow which is affected by lattice obstacles such as voids, dislocations, grain boundaries, impurities, stacking faults, and any other interfacial defects within the lattice. This set resistance is known as a material's resistivity, which can be defined in eq.(69):

$$r = r_T + P_v C_v + P_I C_I + P_D C_D + P_s C_s \tag{69}$$

where r_T is the thermal resistivity, C_v and C_I are the concentrations of vacant lattice sites and interstitial ions, C_D is the density of dislocations, C_s is the area of stacking faults, and P_v, P_I, P_D, and P_s are the material specific weightings [31]. As the amount of these lattice obstacles is increased, the electrical resistivity of the respective material is also increased. Continuing the

discussion on the lattice defects, the general crystalline structure can also affect the resistivity of the metal. FCC and HCP metals have an atomic packing factor (APF) of 0.74. Volumetrically, this states that about 74% of the total volume of a unit cell is taken up by the atoms, and about 26% is free space. Since the electrons are very small, they are not restricted to only traveling along slip systems, like dislocations. Instead they can travel through the lattice of a metal in any direction as long as they can fit. In comparing the APF of 0.74 of FCC/HCP to 0.68 of BCC, the electrons have a higher probability of impacting the atoms in the HCP/FCC metals and provide for a greater amount of heating because there is less free space.

10.2.3. Heat Generation due to Electricity

The speed of electrons traveling as part of the electrical current is near the speed of light (300,000km/sec). As the amount of electrical power is increased, the speed of the flowing electrons is unchanged, but rather the flux or flow rate of the electrons is increased because the electron density of the stream is increased. Irrelevant to plastic deformation and when considering pure resistive heating effects, if the current that is applied to a workpiece increases, the resulting temperature of that workpiece will also increase. This is solely because there is a greater quantity of electrons flowing through the part when the electrical power setting is increased, and each of these extra electrons has the opportunity to impact lattice defects as they pass through the workpiece. This is the basis of thermal softening due to Joule heating.

To the take this explanation a step further, there is also an effect that different sizes and quantities of lattice defects have on the heating of a part with electricity. Aside from the actual atoms that make up the crystal structure in the material, there are grain boundaries, impurities, and additional dislocations that can be found throughout the lattice and in different quantities.

- The grain boundaries can act as another potential barrier for which the electrons must move through if electricity is applied to a metal (again, this is not during deformation, but purely heating of a metal by electricity). If a metal has a small average grain size, the number of grains that a flowing electron must pass through will be higher than for the same metal with a larger average grain size. Hence, the part with the smaller grain size will be hotter.
- Depending on the exact impurities and the types of impurities, they can be larger or smaller in size compared to the atoms of the base metal, and their location within the lattice can also change. In the case of substitutional impurities (*i.e.* where a base metal's atom is replaced by an alloying component atom of bigger or smaller size), the APF could increase or decrease depending on the size of the impurity compared to the size of the base metal atom. Additionally, in the case of interstitial impurities (*i.e.* where an impurity becomes aligned in a free space between bonded atoms), the APF would definitely increase because a portion of the free space is now occupied by an impurity and the electrons which would have been able to flow through this free space are now impacting the impurity and causing heating effects.
- Dislocations are another prevalent defect in a metal's lattice structure that can have an effect on electron motion. As previously stated, the overall density of dislocations within a worked vs. annealed metal could be up to 100,000-times greater [117]. The additional unbonded atoms (dislocations) are different from the grain boundaries and grain sizes because the dislocations will move (as bonds break and reform), whereas grain boundaries are primarily stationary and impurities have some movement, but in fact both restrict dislocation movement.

In summary, resistive heating occurs when running electricity through a metal, where the flowing electrons come into contact with any objects within the metal's lattice (atoms, defects). Of note is that dislocations are also lattice defects and they are one of the few obstacles in the lattice that are moveable. In the case of the electrons impacting the dislocations, the energy of the impacts will be partitioned into heating and the transfer of momentum. This effect will be further explained in section *10.3.* The level of resistive heating can be increased by two ways (increasing the number of electrons or increasing the number of obstacles the electrons can impact):

1.) If the electrical power is increased, the there will be a greater number of electrons flowing through the same dimensions of the metal and more of the electrons will impact all of these lattice objects and release heat.

2.) If the number of defects in the lattice is increased, there will be a greater number of obstacles for the flowing electrons to impact and release energy in the form of heat, thus increasing the temperature of the part as the number of lattice obstacles is increased.

10.3. Electrical Effects during Plastic Deformation

This section will encompass a discussion into the effects of electricity when applied to a metal as it is being deformed. Additionally, discussions will be provided on previous electroplastic effect theories and then a collection of these theories will be explained and supported by experimental work. The parts of this section are:

- Definition of the electroplastic effect
- Previous electroplastic effect theories
- Consolidated and comprehensive electroplastic effect explanation

- Supporting experimental work

10.3.1. Electroplastic Effect

The electroplastic effect can be summarized as the general formability improvements in a metallic workpiece as a result of electricity applied to the metal during the manufacturing process. These benefits can be quantified in the form of the following:

- Reduced required deformation forces
- Increased achievable deformation
- Reduction of springback in formed parts

10.3.2. Previous Electroplastic Effect Theories

From previous research on EAM, there are three main theories which help to explain the electroplastic effect, or the effect of improved formability by way of applied electrical power. These theories pertain to localized heating effects, direct electron-dislocation interaction, and the addition of excess electrons. A description showing the three theories is depicted in Figure 12.

The first theory pertains to localized resistive heating. As explained in the previous section, a metal's lattice has various lattice obstacles in it. Also, the amount of Joule heating in a particular metal is related to the size and amount of the lattice defects, and how they affect the flowing electrons. In this first theory, the electrons traveling through the lattice of the metal scatter off of any of these defects within the lattice. In doing so, they release energy in the form of heating due to the reduction in the speed of the electron or the need for the electron to change its direction once impacting a lattice defect. The release of energy results in Joule heating (resistive heating) of the metal and the metal's bulk temperature rises to a value that appears consistent throughout the metal. However, on the atomic scale, there are certain atomic "hot

spots", particularly where there are large densities of lattice defects. The larger densities of lattice defects mean that more electrons (from the electricity) will impact these defects and they will also have a harder time getting around the defects. This leads to more energy being released by the flowing electrons, thus more heating in these areas. The excessive heating around the lattice defects expands and weakens the local lattice in the immediate proximity of the areas of large defect densities.

These areas of high defect densities also restrict dislocation motion and hinder the continuation of plastic deformation by way of dislocation pile-ups. However, if the local lattice in these areas of larger dislocation pile-ups is expanded and weakened from the heat generated as a result of the electrons impacting the obstacles, the dislocations can begin to move more freely, and this will alleviate the pile-up conditions, thus increasing the achievable elongation and reducing the required deformation forces. Overall, the electron and dislocation motion are restricted by the same lattice obstacles (atoms, impurities, grain boundaries). However, the more electron impacts in the high defect density locations concentrates the heating of the lattice to exactly where it is needed the most (*i.e.* where the dislocations are piled-up), and this heat is utilized to weaken the lattice and free some of the stuck dislocations. This effect is similar to hot working, but instead of heating the entire workpiece to a particular temperature, the flowing electrons generate "hot spots" where the defect densities in the lattice are the highest, and these "hot spots" help to free the dislocations that are stuck due to these high defect densities [3]. When applying the electricity, the entire part will heat up on the macro level, but on the atomic level temperatures will be dependent on the amount and size of the defects within particular lattice locations.

While the first theory explained the indirect effects of the electrons on the dislocations by way of heat generated, the second theory explains direct electron-dislocation interactions. All

lattice obstacles have a given amount of mobility. The atoms and grain boundaries are the most stationary. The impurities have the possibility to have some movement by diffusion. Dislocations within the lattice have the most potential to move because of the stress on them from the external forming forces. In addition, the number of dislocations in a metal can exponentially increase with deformation, whereas the other mentioned lattice defects cannot. In this theory, the flowing electrons impact the dislocations in the metal and momentum is transferred from the moving electrons to the dislocations. Please note that the electrons are traveling much faster than the dislocations, but they are also much smaller than the dislocations, so it will take a continuous stream of electrons impacting the dislocation to put it in motion. The extra energy imparted into the dislocations from the momentum transfer will supplement the mechanical stresses on the dislocations and provide them with sufficient energy to surpass lattice defects that they may not have been able to surpass otherwise. As long as the dislocation motion is assisted, plastic deformation can continue, leading to greater achievable amounts of deformation at lower required deformation forces [57].

The third theory is the fact that excess electrons are run through the metal. The metal, being held together by metallic bonds, already contains many electrons that are dispersed around the ion cores within the metallic bonds. The electrons in these metallic bonds are shared between the ion cores and they can easily move around to assist in breaking and reforming bonds [58]. By adding extra electrons into the electron clouds, the movement of the electrons in the electron clouds in amplified and the breaking and reforming of bonds becomes easier because everything is at a higher energy state and there is a greater number of electrons in the lattice of the metal to bond with.

There could also be a counter-argument to this theory, where the electricity could potentially have a negative impact on the metal's formability. Electricity is the concentrated flow

of electrons through a metallic medium, and in this case it is a workpiece. The fact that the electrons are flowing is a specific direction, are highly concentrated, and are moving at a high rate of speed, lead to the possibility of the flowing electrons impacting the existing electrons in the metal. When these electrons impact the existing electrons, the existing electrons could be knocked out of their current bonds with the ion cores from the flowing electron stream (*i.e.* electricity). As more and more electrons are knocked out of their current bonding situations, there will be less bonded electrons to keep the ion cores equally spaced apart, and this could ultimately restrict the formability of the metal. It is difficult to separate the positive or negative effect of the flowing electrons of the third theory with the electron-defect heat generation explained in the first theory. The thermal softening generated by the Joule heating in the third theory could potentially mask the negative effects of the flowing electrons knocking the existing electrons out of their current bonding situations. Beneficial gains are generated due to the applied electricity, so the effects of the first two theories outweigh the possible negative effects of the third theory.

The previous theories provide plausible explanations of the electroplastic effect and effectively explain different reasons that lead to the same electroplastic effect. The localized heating theory around lattice defects is realistic because more defects will restrict more electrons and cause a higher level of heating. The electron-dislocation interactions are realistic because the dislocations have the ability to move when a force is exerted on them by the electrons. The theory of the excess electrons that are added a metal from the electricity is also realistic because the electrons will provide more atomic vibrations that assist in breaking a reforming of neighboring bonds, however, the effect of the flowing electrons could possibly have a detrimental effect. It is estimated that the increase in temperature due to the application of the electricity (as explained in the first theory) overrides the effect of the flowing electrons possibly knocking the

existing electrons out of their bonds and this is why beneficial formability effects are still witnessed from the application of the electricity. With this said, only the first two previous electroplastic theories will be considered when establishing the comprehensive theory. The theories focus on the breaking and reforming of bonds (*i.e.* dislocation motion) as a result of either heating effects or momentum transfer effects from the flowing electrons. Hence, in explaining the same effects of bond breaking and reformation, the first two theories can be consolidated into one collective theory that accounts for all the reasons for bond breaking and reformation, and partitions their contributions towards the overall electroplastic effect. Specifically, no new theory is created, but the realization that the electroplastic effect is a result of both heat and momentum transfer is explained.

10.3.3. Comprehensive Electroplastic Effect Theory

The first two previous theories explain reasons for enhanced dislocation motion, where one theory relates this towards resistive heating effects and other relates this towards electron-dislocation momentum transfer. The scientific contribution from this thesis is the consolidation of two of the previous electroplastic theories into one comprehensive explanation of the electroplastic effect where it is stated that heat and momentum transfer collectively produce this effect. Specifically, the flowing electrons will cause resistive heating at lattice obstacles such as atoms, impurities, and grain boundaries, and momentum transfer at moveable dislocation defects. The two main previous theories are essentially explaining the same things and they can be consolidated into this one comprehensive theory. Additionally, this thesis devises a methodology to partition the effects of the electrons into heating effects and momentum transfer effects by introducing the electroplastic effect coefficient (ξ).

The explanation of the comprehensive electroplastic theory will be provided in two parts. As the electrons flow through the metal, the type of lattice obstacle that they impact will determine what is produced from the interaction. As stated previously, there is not a lattice obstacle that is completely rigid. However, there are particular lattice obstacles that are more prone to move as compared to other obstacles. For example atoms and grain boundaries will not move a considerable amount because the bonded atoms make up the lattice structure and grain boundaries are the divisions between different lattice orientations throughout the metal. On the contrary, dislocations can move through a metal and their continued movement constitutes bulk plastic deformation in metals. When considering a conventional compression test, the dislocations move due to stresses exerted on them from the external forming force applied to the workpiece. In EAF compression tests, these external forces are supplemented by forces from impacts with the flowing electrons. Impurities within the lattice can also be moved through the lattice to an extent by way of diffusion. One difference between impurities and dislocations is that the amount of dislocations in a metal exponentially increases with plastic deformation, whereas the number of impurities (and number of atoms and grain boundaries) stays the same. In addition, impurities work to hinder dislocation motion, and the movement of impurities does not contribute towards plastic deformation.

If the electrons impact a lattice obstacle that generally restricts dislocation motion or is a dislocation-immobilizing defect (*i.e.* atom, impurity, and grain boundary), the majority of the energy transferred from the moving electron to the lattice defect will be in the form of heat and will contribute towards Joule heating. There may be a very small portion of the energy that will contribute towards providing minimal elastic movement to the defects from stretching of the bonds due to the impacts, simply because they are not perfectly rigid. On the other hand, if the electrons impact dislocations, which are intended to move for plastic deformation to occur, the

electrons will transfer a portion of their momentum to the dislocation they impacts, thus causing this dislocation to move. In addition, there will also be some level of heating. However, the level of heating when an electron impacts a dislocation is far less than the level of heating when an electron impacts a lattice defect that normally restricts dislocation motion. Again, the dislocations already have a mechanical stress imparted on them from the forming forces and they are the lattice defects with the motivation to move because of this. In discussing the collective electroplastic theory, the heating effect from electron interactions with dislocation-immobilizing lattice obstacles will be explained first, and then the partitioning of the energy transfer between the electrons and the dislocation will be explained next.

The first portion of the comprehensive explanation of the electroplastic effect is related to heat generation. Regardless of the metal, electricity will generate heat when passed through any conductive medium, and the magnitude of the heat generation is a function of the atomic structure, size/quantity of the lattice defects, and the amount of electrical power (electron density) supplied. The electrons will contact these lattice obstacles and the change in momentum of the electron will result in heating. The magnitude of this heating will be dependent on whether the lattice defects are ones that restrict dislocation motion and are more stationary (atom, impurity, grain boundary) or whether the defects have the motivation to move through the lattice (dislocations). The dislocation defects will generate much less heating from the same impacts with the electrons because a portion of the momentum from each electron will be transferred towards coupling with the mechanical stresses on the dislocation and assisting its motion. On the contrary, with the other lattice obstacles that hinder dislocation motion, a majority of the momentum from each electron will be converted into heat because these lattice defects cannot move through the lattice to the degree that the dislocations can. At the locations of high defect density or the areas of dislocation pile-ups, more heating will take place in this immediate area

because of the greater number of defects for the electrons to impact. The many atomic level generations of heat produce an overall bulk heating of the metal, which increases the bulk temperature. The increase in temperature of the part on the bulk level translates into a greater amount of vibration between the atoms on the atomic level. This increased motion signifies that the atoms are at a higher energy level. Because of this, the metallic bonds can be broken and reformed under lower stresses and therefore dislocations can surpass lattice defects with less stress than what would be required at room temperature. This describes the thermal softening effect that is commonly achieved by hot working a metal, and this effect is active in EAF.

The second portion of the comprehensive electroplastic theory is the direct contact between the flowing electrons and the constantly multiplying dislocations, and the momentum transfer as a result of the impacts. The main atomic level difference between a metal that was not plastically deformed and one that is plastically deformed is the presence of a greater number of dislocations. The number of atoms, impurities, and grain boundaries are constant between the same non-deformed and deformed metal. The number of dislocations within a metal can increase by up to 100,000-times as the metal is worked [117]. When a metal is plastically deformed, the external forming force translates into a stress on the dislocations which provides the reason for the dislocations wanting to move and bond. Since the dislocations have the need to move (due to the stress on them), they do not stay stationary when the flowing electrons impact them (as is primarily the case with the atoms, grain boundaries, and impurities), but the momentum transfer from the electrons to the dislocations will contribute towards moving the dislocations so that they can bond and migrate through the lattice. While all of the other lattice obstacles primarily only heat up as they are impacted by the electrons, because they are not very mobile, the dislocations are able to harness the momentum that the electrons exert on them and use this for motion instead of exclusively for heating. This is why the temperature difference between a stationary-electrical

test (electricity applied to a workpiece with no deformation) and an EAF test is so large. The stationary-electrical test does not provide for a forming force, hence there is no stress applied to the dislocations and they have no motivation to move. Because of this, a larger portion of the energy transferred to the dislocations from the electrons results in heating and the dislocations behave more like the other defects (where they are more stationary) when they do not have motivation to move. Note that there will be some portion of the impact energy on the dislocations that will still cause some level of heating. The motion of the dislocations allows for the unbonded atoms to be moved closer to bonded atoms so that the bonds can break and reform and dislocations can continue traveling through the lattice. Figure 182 illustrates the exclusive heating, and partitioned heating and momentum transfer effects from the flowing electrons impacting with different lattice obstacles.

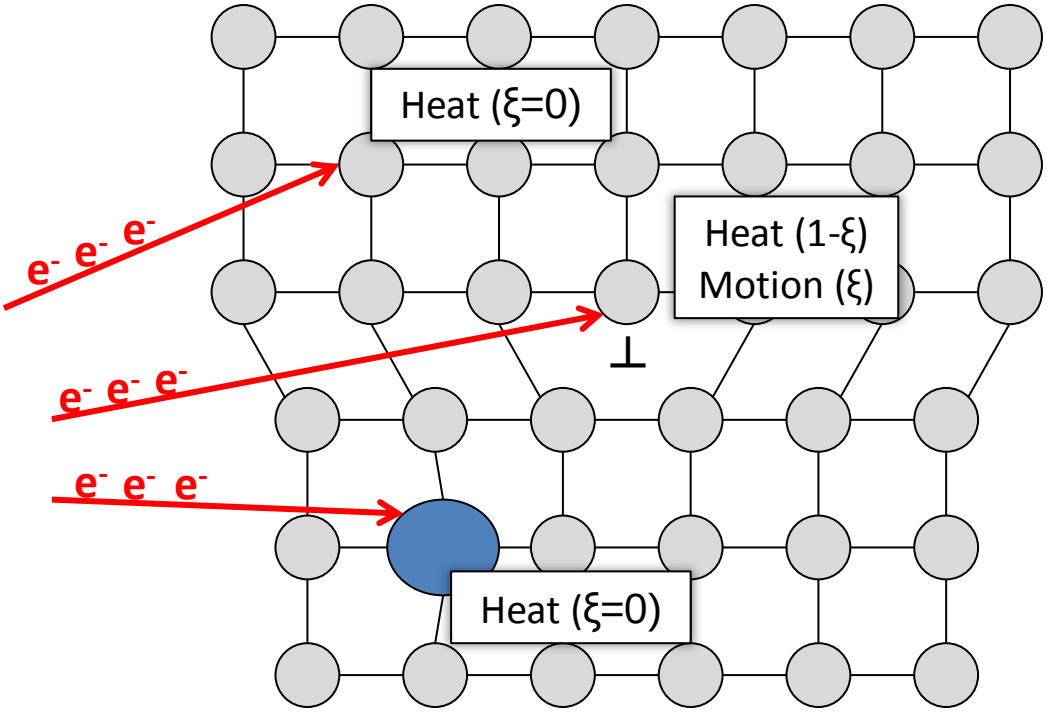

Figure 182. Effects of flowing electrons impacting different lattice obstacles. When the flowing electrons impact dislocation-immobilizing lattice obstacles, like atoms (top) and impurities (bottom), heat is primarily generated. However, when the flowing electrons impact the more moveable dislocations (middle), the momentum from the electrons is partitioned into the motion of the dislocation, along with heating (to a lower temperature than what is seen with stationary lattice obstacles) which is quantified by the EEC.

The dislocation transfer through a metal with EAF can be illustrated by a string of trapeze swingers in a circus. The trapeze swingers in the middle are connected at the start of the stunt. When an additional swinger begins to swing in from the side (receiving the momentum to swing by the applied electricity), one of the middle swingers realizes that, and breaks their connection with the other swinger in the middle, and moves and makes a connection with the new trapeze swinger. As the duo begins swinging towards the second middle trapeze swinger, the new trapeze swinger breaks their bond with the first middle swinger and connects with the second middle swinger. All of the swingers are analogous to atom chains and the swinging motion, leading them to break bonds and reform bonds with other trapeze swingers, is the result of the

applied electricity. Without EAF, the swingers would simply be hanging from the trapeze with no back-and-forth motion to initiate bond breaking and reforming.

The comprehensive electroplastic explanation concludes that the flowing electrons can impact any of the lattice obstacles as they pass through the lattice. Specifically, electron motion can be hindered by the same obstacles that hinder dislocation motion. Electrons exclusively create heat when impacting the lattice objects that normally restrict dislocation motion (atoms, impurities, and grain boundaries), and electron kinetic energy is partitioned into heat and energy transfer when it encounters a dislocation. Both the heating (from impacts with all the lattice objects, including dislocations) and dislocation momentum transfer constitute the electroplastic effect, where the metal is able to be formed at lower forces and to greater elongations as compared to a conventional forming test because of the thermal softening and the assistance to the moving or stuck dislocations. The heating effect can be seen from the 85% increase in temperature of a part when electricity is applied to it, due to it being pre-worked to a level of 40%CW prior to the addition of the electricity. In addition, the EEC (determining the percent of the total applied electricity that assists with dislocation motion) increased as the pre-work was increased and there were more dislocations present in the metal. These examples and others will be provided in detail in the following section on supporting experimental work.

10.3.4. Supporting Experimental Results

There has been various experimental works performed by the candidate and other researchers, which support the new comprehensive electroplastic theory. Specifically, the experimental conclusions will be categorized into heating effects and momentum transfer effects.

Heating Effects

- Threshold vs. resistivity relation [40], [46]
- Dislocation density vs. temperature relation (stationary-electrical tests)
- Springback elimination in sheet bending [45]

Experimental work by the candidate supports the theory of localized resistive heating due to the applied electricity. From work by the candidate and by previous researchers, a threshold current density value has become apparent which is specific to each metal tested [40], [46]. This threshold value is the current density value (for a specific metal/deformation speed combination) whereby significant formability improvements are witnessed, by way of decreased flow stress or increased achievable elongation as compared to conventional testing. Upon further investigation, as the resistivity of metal is increased, the threshold current density, where increased formability effects occur, is decreased (Figure 28). This supports the theory of resistive heating. The metals with a higher resistivity have a greater number of lattice obstacles and there are more sites for the flowing electrons to scatter off of. The increased number of locations of local lattice heating allows for easier dislocation movement through the lattice.

In another work, the candidate examined the thermal profiles of stationary-electrical tests of specimens with different amounts of cold work in them (up to 50%). In these specimens, as the percent cold work was increased, the dislocation density within the metal was increased. After a constant current was applied to each of the specimens, the maximum temperature value increased by 85% as the level of cold work was increased from 10%CW to 40%CW. This can be seen in Figure 146. Additionally, the voltage potential across the top and bottom dies was larger when comparing a worked specimen to an annealed specimen of the same dimensions at different levels of %CW. This indicated that the resistance was higher in the worked specimen.

An interesting note is that although the dislocation density (number of dislocations) was the only variable that changed with the cold work, and the dislocations are the only moveable lattice defect, the temperature of the specimens during a stationary-electrical test still increased significantly with cold work, and the part did not deform just due to the forces from the electrons. When considering deformation without electrical assistance, the dislocations receive the motivation to move due to a stress exerted on them by the external forming force. This proves that the force on the dislocations from the flowing electrons is lower in magnitude than the mechanical stresses. Additionally, the force from the electrons cannot solely cause dislocation motion or plastic deformation, but rather it acts as a supplemental force to the mechanical stresses on the dislocations. When the electricity is applied by itself without being coupled with deformation, the forces from the electrons on the dislocations will assist in stress relaxation by breaking and reforming bonds in the immediate area around the dislocations. This effect is similar to a process anneal, where heat is added to a material to assist in breaking and reforming of bonds to lower their energy states. This will result in elastic relaxation, or springback reduction. The work by Green et al. showed that a short, single pulse of electricity was able to eliminate elastic springback in sheet specimens that were already formed around a die [45]. The electrons were able to accommodate breaking and reforming of the bonds to eliminate the tension in the bonds above the neutral axis and to eliminate the compression in the bonds below the neutral axis.

<u>Momentum Transfer Effects</u>

- Dislocation density vs. EEC (EAF tests)

The second portion of the comprehensive theory is the partitioning of the energy from the direct electron-dislocation interactions as a result of EAF, where momentum is transferred from

moving electrons to moveable dislocations and some level of heating is apparent. As the electrons impact the dislocations, they impart a momentum onto the dislocations and can provide the energy needed to assist the dislocations past the lattice obstacles that are holding them up. Again, this momentum transfer is only applicable between electrons and dislocations, because dislocations are the only lattice obstacles that have the ability to move. Kravchenko, in his explanation of electroplasticity, succinctly stated this effect when he explained that, if there is an electric current flowing, the energy from the electrons is transferred to the dislocations, thus making the plastic flow easier [4].

Work by the candidate supports this theory of direct electron-dislocation interaction. Specifically, the percent cold work research shows that, as the amount of pre-existing dislocations within the metal's lattice increase (by way of cold working), the efficiency of the applied electrical power is increased. This is because the larger number of dislocations within the lattice allow for applied electrons to impact them and exert this impact energy towards dislocation motion instead of exclusively resistive heating and the larger number of dislocations allows for more dislocations to be "pushed" rather than the material simply being heated. This is the reason why the specimen temperature of a stationary-electrical test (where a static load is applied and a constant current is run through the part) is normally several times greater than that of an electrically-assisted test, where the applied electricity also contributes towards dislocation motion. Specifically, in the stationary-electrical tests, the only force acting on the dislocations is from the flowing electrons. However, in an EAF test, the dislocations have the electron force and the mechanical stress from the external forming force. The mechanical stress provides the motivation for the dislocation to bond and the electron force provides the movement of the dislocations to get close enough to the neighboring atoms to initiate the bonding.

In the chapter exploring the effect of percent cold work, as the specimens are pre-worked to a greater degree (and have a higher dislocation density), the efficiency of the electricity increases because there is a greater amount of dislocations to "push" with the electrons. However, there may come a point where there could be too many dislocations within the metal (*i.e.* an oversaturated state) and the applied electricity is not able to withstand the relation of increased efficiency with increased dislocation density. In this case, the EEC-value would not increase any further, heating effects could increase since the electricity cannot be further utilized for assisting deformation, and plastic deformation may not be able to be sustained.

10.3.5. Comprehensive Electroplastic Theory Conclusions

The comprehensive electroplastic theory consolidates the multi part previous theories on electroplasticity and formulates one explanation about the electroplastic effect that incorporates the EEC that was initiated as part of the EAF modeling strategy. Let it be known that this theory is not new, but rather emphasizes that the explanations of the first two previous electroplastic theories are correct, and that the effects from each theory occur simultaneously. This comprehensive theory states that the total effect from applying electricity to a metal during deformation is created from the flowing electrons impacting lattice obstacles. The outcome of the interactions is dependent on the specific type of lattice obstacle. The lattice obstacles that hinder dislocation motion, such as the atoms, impurities, and grain boundaries, will primarily generate heat as a result of the impacts with electrons. When the electrons impact the moveable lattice dislocations, the impact energy is partitioned into the transfer of momentum from the electron to the dislocation, and some level of heating due to the reduction of the speed of the electrons and the change in their direction from the impacts. The momentum transfer supplements the mechanical stresses on the dislocations from the external forming forces and provides for the

dislocations to move easier throughout the lattice. Additionally, the heating at the lattice defects weakens the lattice at these sites and assists in breaking and reforming of bonds to further assist the dislocation motion. Both attributes coupled together produce the electroplastic effect.

11. Conclusions and Discussions

The scientific contributions of this thesis include a methodology and quantification strategy for electroplastic modeling, and a materials-based explanation of the electroplastic effect. This explanation consolidates the aspects from a previous three-part electroplastic theory into one comprehensive justification of the electroplastic effect. The flowing electrons from the electricity can impact all lattice obstacles. Each electron's interaction with stationary lattice obstacles (atoms, grain boundaries, and impurities) results in heat generation, whereas each electron's interaction with moveable dislocation lattice obstacles can result in momentum transfer to the dislocations rather than exclusively heating the lattice. The combination of increased heating, leading to thermal softening of the material, and momentum transfer from electrons to dislocations provides an explanation of the electroplastic effect and encompasses multiple existing electroplastic theories. This explanation is aligned with the proposed EAF modeling methodology via the electroplastic effect coefficient (ξ), which serves as a quantification of the magnitude of the effects of electron-dislocation momentum transfer. The consolidation of the previous three-part electroplastic theory into the comprehensive theory where electron-dislocation interactions are partitioned towards heating and momentum transfer can be seen in Figure 183.

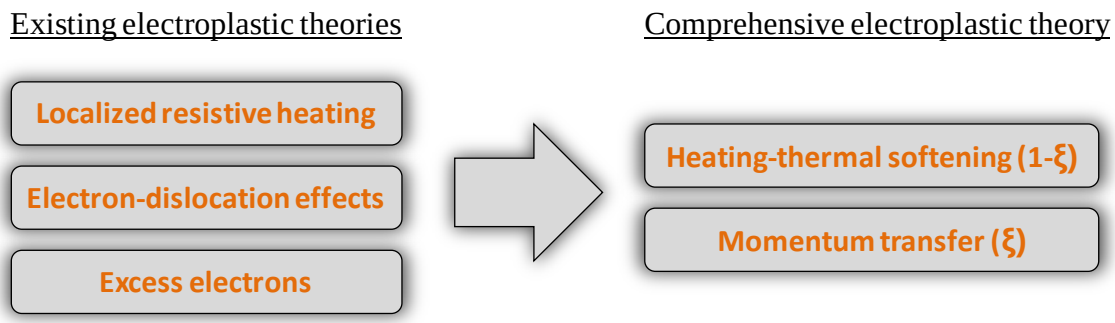

Figure 183. Electroplastic effect theories. The previous three-part electroplastic theory is consolidated into one comprehensive theory that encompassed heating of all lattice obstacles, and momentum transfer to dislocations from the flowing electrons.

Experimentation and previous work is used as a basis to understand material and process sensitivities to EAF, and to confirm the comprehensive electroplastic theory of heating and momentum transfer from the flowing electrons. An inverse relation of a higher material resistivity requiring a lower electrical power to produce the electroplastic effect supports the theory of increased heating due to greater lattice obstacles. The model is used to determine the relevancy of different forms of heat transfer and the sensitivity of variables for the prevalent heat transfer forms. The investigations into percent cold-work provide that dislocation density can increase significantly with deformation, and these dislocations can have an effect on both the heating and momentum transfer aspects of the electroplastic effect. The modeling methodology is based on materials-based interactions, which are confirmed by previous work and experimentation. The EAF model is effective at predicting mechanical forming profiles, and evaluating material and process sensitivities.

Within this chapter, conclusions from each of the main topics discussed in each chapter are provided with explanations. The conclusions are categorized based on functionality, so some sections may cover material from several thesis chapters.

11.1. Modeling Strategy (Ch.3)

A mechanical modeling strategy, derived from Avitzur et al., and a basic heat transfer model, were combined to produce a thermo-mechanical model for EAF forging operations. This modeling work presented an energy-based approach to analyze electrically-assisted forming. Specifically, the energy input into the system (*i.e.* the electrical power with respect to time) was balanced with the energy needed to deform the part. The input electrical energy was separated into the useful energy that assists the mechanical deformation process, while the remaining energy is converted to resistive heat, causing thermal softening by way of resistive heating. The Electroplastic Effect Coefficient (EEC) was created by the candidate to account for the ratio of "useable" electrical power compared to the overall magnitude of applied electrical power.

11.2. EEC Determination and Quantification (Ch.4)

An explanation of the two different methods of obtaining an EEC profile for a particular metal was described. At first, the mechanics-based method was described, where differences in the mechanical power profiles of a conventional compression test and an EAF compression test are normalized over the magnitude of electrical power required to produce those mechanical power differences. The thermal-based approach to determining the EEC profiles requires a conventional compression, stationary-electrical, and an EAF compression test. Thermal profiles are taken for each of the tests. The thermal model is calibrated using the stationary-electrical test, and is offset using the conventional compression test (where the heating due to deformation is taken out). The power law relation of the thermal model is adjusted according to the EAF test and the result is an EEC function in terms of strain, strain rate, and an exponential coefficient which represents the EEC profile curvature. The EEC profiles determined using both methods were consistent to each other throughout the entire strain range for both die speeds. The

mechanical-based approach to determining the EEC required only force vs. position data to generate the EEC's, whereas the thermal-based approach required thermal data, which necessitated the use of a thermal camera.

11.3. Model Validation and Application (Ch.5)

The simplified EAF model, which was outlined in *Chapter 3*, is now integrated with the EEC profiles determined from methods described in *Chapter 4*, to produce stress-strain profiles to be compared to experiments. This research work utilized EEC profiles, which were determined from both mechanical power profiles and thermal profiles, to construct stress-strain profiles of the EA-Forging process. The thermo-mechanical model predicted the stress-strain profiles to within 20% of experimental results. Different die speeds are able to be input into the model, and the model was more accurate with the slower die speed. Furthermore, factors such as die speed and current density significantly affect the efficiency of the EAM technique.

In addition to presenting a model of EA-Forging, the same EAF modeling strategy was employed for EA-Bending. Specifically, the total power to deform the bending specimen consisted of the mechanical power of deformation along with the applied electrical power due to EAF. Two effects of the applied electrical energy were taken into consideration: (*i*) the electroplastic effect of the electricity helping the deformation by assisting the dislocations, and (*ii*) thermal softening as a result of resistive heating. The experimental results indicated that the electricity can assist the deformation process due to beneficial effects in reducing the flow stress, thus the forming force and mechanical energy required for reaching the same level of deformation as in classical forming are reduced. Another benefit of using the electricity during bending was observed in the notable reduction in springback, up to 77%, depending on the electric parameters and pulse characteristics. The analytical model was in good agreement with the experiments, and

it was able to predict the bending forces within 15% (in most cases). The analytical model coupled with the experimental observations can be used to estimate the pulse parameters required for certain reductions in the forming load.

11.4. Contact Effects (Ch.6)

The surface roughness effect on EAF under both elastic and plastic loadings over the entire apparent area of the specimen was investigated. The following are a list of conclusions about the EAF/Contact Area research:

- The post-formed surface roughnesses at the die/workpiece interfaces become worse as a higher magnitude of applied electricity is used. A function of this EA-induced roughness was developed.
- The temperature dependency on the magnitude of the static load applied to a part while electricity is applied is only relevant in the elastic region. Once into the plastic regime, there is no clear relationship between load and temperature, and the temperature does not vary as frequently as in the elastic region.
- The EEC profiles from the same EAF tests run on surface ground specimens and specimens with enhanced asperities were very similar, thus indicating that the contact area does not have much of an effect on EAF performance outside of the elastic region. This helps to explain why the research focus on contact area for electrical connectors is restricted to the elastic region.
- When attempting to model the EAF technique for a forging process, analytical consideration of the contact area is insignificant because the manufactured part will always be in the plastic regime, which is insensitive to contact area effects.

In addition, the effect of EAF on tribological behavior was explored in this chapter. The advancement of EAF for larger-scale applications depends on strategies for identifying a well-performing lubricant. Three lubricants chosen from three different composition groups (oil-based, water-based, and synthetic) were tested under different current densities and their performance was evaluated. The ring compression tribo-test was used and a friction factor was determined from the friction calibration curves generated through finite element analysis. The following conclusions were drawn from this study:

- The lubricants analyzed resulted in more severe tribological conditions with the application of electricity and with the increase of current density. The higher temperatures resulted in rapid evaporation of the lubricant and chemical decomposition; thus the lubrication mechanism changed to a less favorable regime.
- Although the forming load, thus the interface pressure, decreased in all cases when the electricity was applied, there is potential for even more reduction if the lubricant can withstand the effects of electricity. The higher temperatures suggest that pressure additives are needed in order to maximize the efficiency of the process.
- The oil-based/synthetic lubricants performed better than water-based lubricants. Thus it is recommended that the development of the lubricants for EAF should take into consideration the temperature rise, rather than just dielectric permittivity.

11.5. Grain Size Effects (Ch.7)

For *Chapter 7*, the effect of grain size on EAF was explored. The differences between the grain sizes did not have an effect on the stress-strain profiles of the conventional compression and the EAF compression tests. Additionally, there was only a minimal difference in the thermal profiles (both stationary-electrical and EAF compression) between the largest grain size and the

other two grain sizes, however this was a very minor difference and this did not have any effect on the mechanical performance during the EAF tests. With the limitations on being able to easily generate new grain sizes, and with the resources available to the candidate, it was decided that efforts would be shifted from exploring effects of the starting grain size to examining the effect of prior cold work on the effectiveness of EAM. This will be explained in the next chapter.

11.6. Mechanical Work Effects (Ch.8)

Within this chapter, stationary-electrical tests were run and temperature was recorded, and EAF tests were run where temperature and stress-strain profiles were recorded. The differences in temperature, stress-strain, and resistance profiles between the tests were described. The conclusions from this section are as follows:

- For stationary-electrical tests, the temperature profile will increase as the starting percent cold-work in the specimen is increased.
- The recorded voltages in the stationary-electrical tests increased as the percent cold-work increased and the higher resulting dislocation densities caused the resistance of the specimen to increase. The measured voltages of the %CW and annealed specimens decreased at the same rate, but the annealed voltage values were consistently below the %CW voltage values.
- The amount of induced percent cold-work within a specimen has an effect on the ability of the applied electricity to reduce the overall flow stress. The overall reduction of flow stress between conventional and EAF testing of annealed specimens may be greater than the difference between cold-worked specimens.
- The stationary-electrical test thermal profile curvatures are dependent on the electrical application parameters (current density) and the material parameters (%CW

or annealed). Sometimes this profile is curved and still increasing, and sometimes it can flatten out, thus representing that thermal saturation has taken place.

11.7. Sensitivity Analysis (Ch.9)

Any major sensitivities within the model, and any possible simplifications that could be made were analyzed. The following conclusions can be drawn from this chapter:

- The specific heat of a material must be considered when modeling EAF. The effect that the specific heat has on the ability to model EAF is proportional to the sensitivity of the specific heat value with respect to temperature.
- When modeling EA-Forging, the all-inclusive heat transfer model could be simplified by neglecting both the radiation and convection heat transfer. This simplification is only valid for EA-Forging. Alternative EA-processes, such as EA-stretch forming or EA-bending, may require including the other forms of heat transfer since the exposed surfaced area is typically greater in comparison to the total volume of the workpiece.
- The conduction length of the dies has a significant effect on the overall temperature profile of the specimen. The die conduction length is related to the magnitude of applied electrical power (increasing conduction length) and the volume of the die (decreasing conduction length).
- Different metals produce different EEC profiles when the EAF technique is used on them during a forging process. The differences include the overall shape of the profile (the profile could be concave, convex, etc.), and this shape determines the overall efficiency of the applied electrical power throughout the duration of the process.
- The frequency analysis indicated that there are oscillations in the forming load recorded during the EAF tests for all the tests performed. The frequency increases with the current,

thus with energy input. This may be an indication of a cyclic softening/hardening phenomenon present during EAF.

- The frequency observed for titanium is higher than the one for steel, and that may be related to the specific properties of each material, such as the resistivity, the crystal lattice microstructure, and any interfacial defects within the lattice that could obstruct the movement of dislocations.
    - The quality of the electrical power output during an EAF process can vary depending on the capabilities of the power source. The difference in electrical quality still produced the same stress-strain profile, and the maximum difference between the two profiles was 200MPa.

12. Future Work

Within most of the chapters and sections of this thesis, there have been ideas generated to further explore aspects of the EAF technique. This chapter consolidates these potential future work opportunities.

12.1. Reasoning for the Future Work Section

EAM modeling is a complex phenomenon with many different variables and sensitivities. This thesis introduces a simple modeling strategy to be used as a base by which to model an EAF forging process. In addition, the effect of several potential key material- and process-based variables on the EAF technique were also investigated to quantify their impacts on the ability to further model EAM. While the experimental works in *Chapters 6-9*, and *11* highlight key relationships and provide feedback on key questions about EAM, they do not explain all of the EAM theory, and therefore, this future work section was created to highlight different pathways which the candidate feels is important to further explore.

12.2. Thermal-Based EEC Determination Future Work

The relationship of *b* in the power law relation is not clearly understood yet, and more experiments are required to investigate this exponent in more detail. In the power law relation, *b* determines the overall curvature of the profile. From the tests run on Ti-G2 and Ti-G5, both had different curvatures and different *b*-values, however, it is unknown what primarily affects the *b*-value.

12.3. Electrical Forging Efficiency Analysis

In the Electrical Efficiency Analysis sub-section, it was determined that the slower die speed (12.7mm/min) was more efficient than the faster die speed (25.4mm/min), except for the highest current density ($25A/mm^2$). It was hypothesized that, at the lower current densities (10-$20A/mm^2$), the greater efficiency from the slower die speed tests was due to the fact that the slower die speed may have allowed for the applied electricity to continue improving the formability, whereas the faster die speed did not allow for that. For the tests at $25A/mm^2$, the current density was high enough to still improve the formability, even with the faster die speed. This supports the claim that there needs to be a balance between current density and die speed to achieve maximum efficiency of an EAF process.

12.4. EEC Frequency Analysis Future Work

The oscillation in the load is attributed to an unstable plastic flow, and depends on temperature and strain rate. The commonly accepted explanation for the PLC effect is based on a dynamic strain aging model, and is due to the interaction between the moving dislocations and diffusing solute atoms. In addition to temperature and strain rate, the PLC depends also on alloy composition, crystal lattice, dislocation density and grain size. Since all these are parameters that also influence the electroplastic effect, further tensile tests will be performed and the possible correlation between the PLC and electroplastic effects will be investigated.

12.5. Electrical Connections and Transmission Lines

The work from *Chapter 6* shows that the contact area (or surface roughness) of the dies/workpiece does not necessarily affect the EAF technique once deformation takes place outside of the elastic region. There is a focus on the surface roughnesses of electrical contacts,

since the loadings on these are within the elastic region. In some switch applications, the switch connectors can deform under high electrical loads, which can then lead to insufficient contact between the switch contactors and thus cause them to weld together. The EEC-based modeling strategy in this work may be able to be applied towards helping to design electrical switches that will not deform.

It is known that electricity is strain-rate dependent, but the time dependency of extreme amounts of electricity (*i.e.* lightening) is not known. More specifically, the effect of lightening on OHTL's in high tension and under wind loading may be able to be explained using this modeling strategy.

13. Broader Impacts

Although the candidate has been influential in experimentally evaluating the effect of EAM on many different metals and manufacturing processes [42]-[43], [47], and [51], this Ph.D. focuses on the predictive model, which will show the predictability of the EAM technique and act as a gateway for EAM to begin being used in industry. For that reason, the applications (or industries) which could use EAM will be discussed first, followed by potential users of the EAM thermo-mechanical predictive model.

13.1. Automotive and Aircraft Industries

Like other formability-enhancing manufacturing techniques, EAM is not the optimum technique to use for all metals or all part designs. Specifically, during EAM, excess electrical power needs to be supplied to the workpiece, which does not always make it the most efficient process. However, the results from using EAM are significant and it may be one of the very few techniques which allow efficient forming of particular metals. For this reason, EAM should be used to form metals and alloys which are currently not able to be formed to great lengths, or require excessive heating or annealing. The EAM technique would act as a gateway for these metals to be used in industry. Two metals whose formability improves tremendously using EAM are magnesium and titanium, which are targeted by the automotive and aerospace industries, respectively.

With the rising fuel and operational costs, the automotive and aircraft industries are becoming more weight-, performance-, and efficiency-focused. One way to achieve all three variables is by lightweighting. In this technique, lighter and stronger materials are used instead of the heavier carbon steels mainly used today. Magnesium is a desirable material for the automotive industry (Figure 184), where it is currently used in mainly cast components due to its

very low formability. Research in the Previous Work section by the candidate proves that EAM can significantly increase the formability of Mg sheet metal, which would be a tremendous gain for the automotive industry. On the other hand, titanium is popular for use in aerospace applications (Figure 185), but the manufacturers constantly struggle with the poor formability and high required forming forces of this material. Again, previous research has shown that EAM significantly improves the formability of titanium, which will increase the number of potential aerospace applications for the alloy.

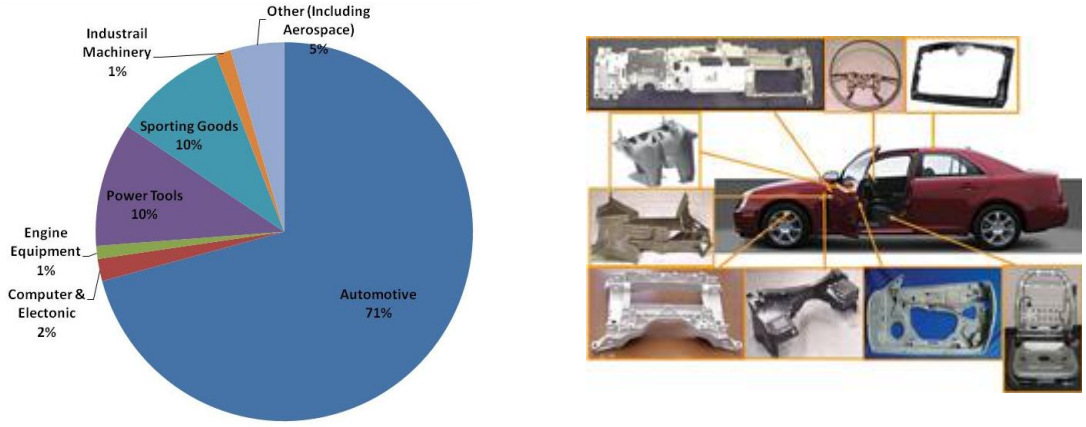

Industries Using Magnesium [120] Magnesium uses in automobiles [121]

Figure 184. Magnesium-dependent industries and applications [120]-[121]. Magnesium is a lightweight alloy that is targeted by many industries, including the automotive industry. (a) A pie chart depicting the industries which use Mg, (b) examples of current Mg uses in automobiles.

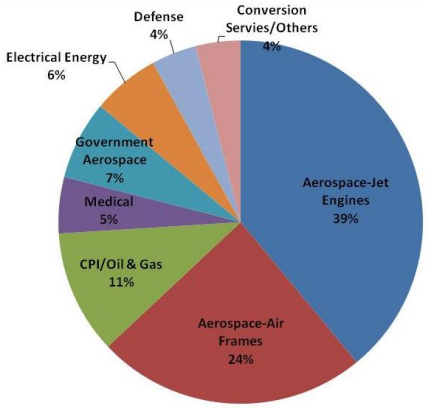

Industries Using Titanium [120]

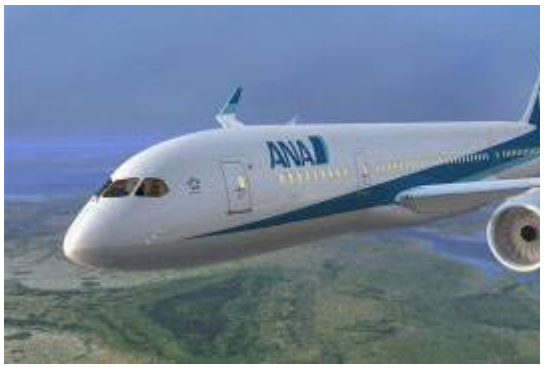

Titanium uses in aircraft [122]

Figure 185. Titanium-dependent industries and applications [120], [122]. Titanium is a strong and durable metal that is frequently used in the aerospace industry. (a) A pie chart depicting the industries which use Ti, (b) Titanium uses in aerospace applications.

13.2. Potential Early Adopters of EAM Modeling

Now that the main industries which could benefit from EAM have been identified, it is also important to explain how the predictive model could be used. Depending on the business model that the candidate would like to pursue, there are two main potential "Early Adopters" for the model

Simulation Software Companies

- These simulation software companies already produce software that is able to predict outcomes of many current manufacturing processes. They already have all of the general algorithms/methodologies needed for conventional forming. By integrating the main algorithms generated by this research into their software package, these companies would be able to sell EAM-predictive software.
- There are different applications of simulation. The main simulation applicability would be for metal forming, however, there is also the potential to simulate, or model, alternative EA processes. Such process could be EA-machining, -bending, or –joining.

Metal Forming Companies

- The predictive model can be used for EAM process design, where the speed, electrical settings, and die design will be optimized. The Tier I and Tier II metal forming suppliers will also be probable early adopters because the EAM technique may be their chosen formability-enhancing technique for forming Mg and Ti, as explained earlier. This is where the "heart" of metal forming is and each metal forming supplier wants to ensure that they are not overtaken by new technology of a competitor. Of note is that the automotive/aircraft OEM's would not be considered early adopters because they want something immediately and that is 100% dependable. It is safer to market to the suppliers because they are more likely to work with some "growing pains" of a new manufacturing process.

13.3. Overhead Transmission Line Design using EAF

Over-Head Transmission Lines (OHTL's) deliver electricity from the generation point (*i.e.* the power plant) to the customer (*i.e.* homes or businesses). In the EAF technique, electricity is applied to a metal while it is mechanically deformed. Overhead electric transmission lines are simply coated metal cables in static tension loading with high power electricity flowing through them. From the statements above, there are some similarities between the EAF technique on a forging process and what goes on within a high-power electric transmission line. This section will include an explanation of the electrical system grid, different transmission line structures and set-ups, commercially available conductors and sizing procedures, conductor sag and what it means, the effect of high temperatures on transmission line longevity, and finally how the EAF technique explained in this thesis could be applied to the analysis of OHTL's.

13.3.1. The Electricity Transmission Grid

Electrical transmission lines are placed throughout the United States, thus forming a transmission "grid" that can transport the electricity to where it is needed. Figure 186 shows the electrical generation and transmission process [123]. From the figure, there are two types of transmission lines (high-voltage and low-voltage). The high-voltage lines are used to transport the electricity over very large distances quickly with little loss. The low-voltage lines are used to deliver the electricity closer to the customers. High-voltage lines can be rated from 100kV up to 1000kV, whereas low-voltage lines can be rated from 4kV to 46kV [124]. Note that the voltage coming directly into a residence is typically 240V; the above values are for distribution.

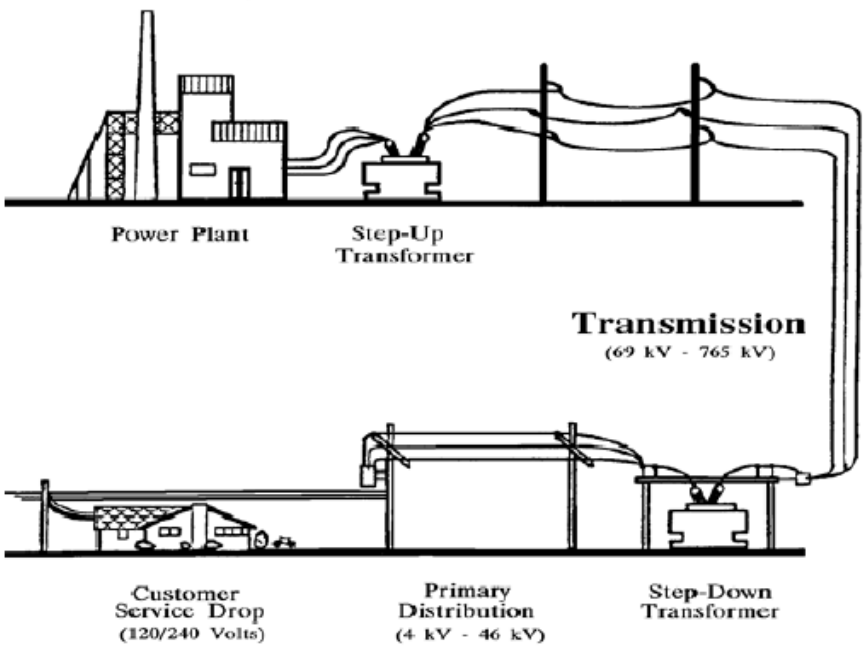

Figure 186. Electrical generation and transmission process [123]. Electricity is generated at the power plants and transmitted large distances through high-voltage lines, where the electricity is filtered through low-voltage lines in order to be brought to the customers.

In general, the size of the conductors is determined from estimating the potential power use of the customers at the end of the lines. Outages can occur if the voltage in the lines is more than that for which the line is rated. If one link in the grid is down, the electricity can reroute itself, thus adding more voltage to the amount which the other line was already carrying. Ultimately, the overloading of several lines within a grid could lead to a blackout.

13.3.2. Transmission Line Structures and Set-ups

There are several different types of transmission line structures, as shown in Figure 187 [123]. For each of these structures, there are clearance limitations and structural compliances. Most recently, the H-frame design structure has been replaced with the various single-frame structures because they require less right-of-way restrictions. When setting up a new transmission line system, there are several main procedures that need to be followed (*e.g.* installing the foundations, erecting the towers, pulling the conductors), which is further explained in [124]. The installation of the conductors is an important step in the transmission structure finalization. After a regulated amount of time has passed since setting the footings for the transmission towers, one can then begin to pull the conductor lines. In most cases, the wires are mounted to vehicles and pulled through the stringing hardware to position the lines and set the sag in the lines.

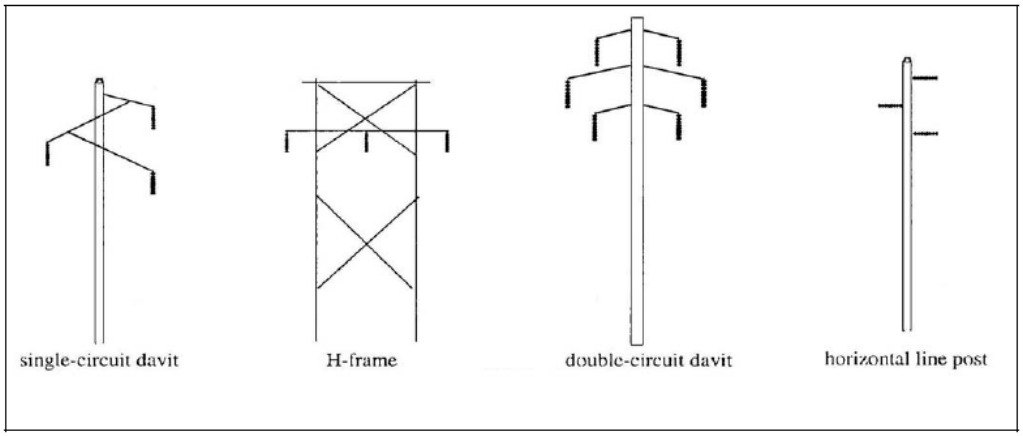

Figure 187. Different transmission structures [123]. There are several different transmission structures. Some have only one circuit with three conductor wires and others have two circuits with a total of six conductor wires.

13.3.3. Commercial Conductors and Sizing

There are several types of conductors that can be used as transmission lines; however, the most-common is the steel-reinforced aluminum conductor (ACSR). This conductor has a relative low cost and high weight-to-strength ratio compared to its competitor conductors. Several other conductor types are an All Aluminum Conductor (AAC) and an All Aluminum Alloy Conductor (AAAC) [125]. The different conductor types are named after different objects. Specifically, the AAAC conductors are named after types of trees, while the ACSR conductors are named after different animals (the ACSR conductor used in the example in the following sub-sections is named "DOG"). According to [126], the ACSR-type conductor can be sized two different ways. First, the most economical method is to use Kelvins Law, which states, "The most economical area of a conductor is that for which the annual cost of energy losses is equal to the interest on that portion of the capital outlay which may be considered as proportional to the weight of the conductor." Second is the more efficient sizing method, in which the conductor is sized based on balancing the I^2R losses and the installation costs. Figure 188 shows how the most efficient

conductor is sized. To put the cost of an OHTL into perspective, a 200-mile single circuit 500kV, 3-conductor line is approximately $700,000 per mile [124]. The main factors impacting the price of a transmission line are: the terrain, the location, the overall distance, the configuration of the conductors, and any relevant environmental regulations. Wires which shield the conductor bundles from lightning and grounding are normally installed above the bundles.

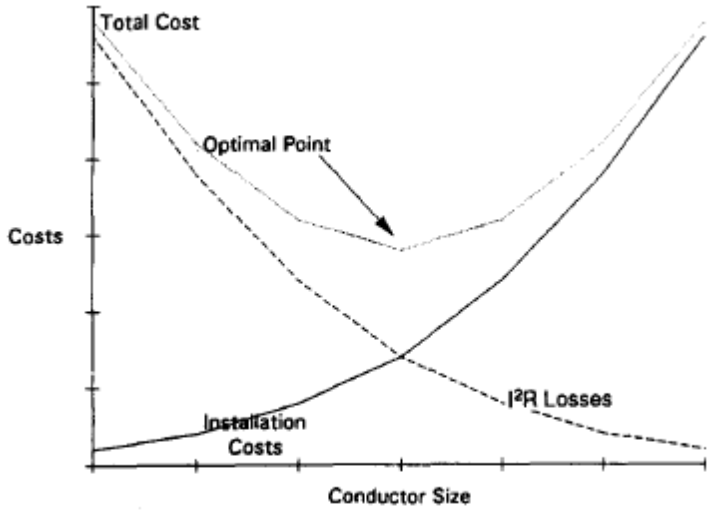

Figure 188. Determination of the most efficient conductor size [126]. The most efficient method of sizing a conductor is to balance the power losses and the installation costs, since these are inversely proportional.

13.3.4. Conductor Sag

Because of all the different weather and loading conditions, one can never eliminate sag in transmission lines and, thus, it must be designed in. The sag is a measurement of the vertical difference between the line connection point on the adjacent tower and the lowest vertical point within a particular span of the conductor. There are regulations as to how low a transmission line can be to the ground. Eq.(70) below shows how to easily calculate the sag of a parabolic shaped line [127].

$$S_{cond} = \frac{wL^2}{8T_{cond}} \tag{70}$$

where S_{cond} is the sag in meters, w is the conductor weight in N/m, L is the horizontal span length in meters, and T_{cond} is the conductor tension in N. In order to use the above equation, the conductor weight must be provided in N/m. Eq.(71) below shows how to convert the weight from kg/km to N/m.

$$w = \frac{w_c \cdot 9.81}{1000} \left[= \right] \frac{N}{m} \tag{71}$$

where w_c is the weight of the conductor in kg/km.

The sag in a transmission line is directly related to the tension in the line, and this can be affected by the following variables [127]:

- An increase in temperature of the line can lead to thermal expansion of the conductor, thus resulting in an increase in its length, as shown in eq.(72) below.

$$\Delta L = \alpha_{\exp} \cdot T \cdot S \tag{72}$$

where α is the coefficient of thermal expansion, T is the temperature increase in °C, and S is the span length in meters.

- An increase in the wind speed can produce an extra force on the conductor, thus increasing the tension in the conductor. This can elongate the conductor by way of elastic stretching, as shown below in eq.(73).

$$\Delta L = \frac{(T - T_o)}{E \cdot A} \tag{73}$$

where T_o is the initial tension in N, T is the final tension in N, E is the coefficient of elasticity, and A is the cross-section of the conductor in meters.

- If ice forms on the conductor, it will increase the overall diameter of the conductor and will also add weight to the line. This will increase the tension and can lead to elastic stretching as was calculated in the equation above.
- As the transmission lines age, they go through countless cycles of loading and unloading and heating and cooling, which can weaken the overall strength of the line.

13.3.5. Effect of Temperature on Transmission Line Longevity

The heating of the transmission lines is currently the most critical attribute responsible for the line sag and the longevity of the lines. The heating effect is due to the large power running through the lines. Initially, the lines are sized for an estimated amount of electricity, but as more is run through, their temperature increases significantly. Standard operating temperatures of OHTL's may be around 30°C -70°C, however, lines have been known to reach up to 175°C or more when overloaded [128]. In the case of aluminum conductors, the degradation in the aluminum strength due to heat is cumulative and irreversible.

In [128], the effect of high temperature cyclic loadings on an ACSR conductor with compression dead-ends and full tension compression splices was examined though evaluation of the tensile strength, hardness, and metallurgical changes. Cyclic tests at 250, 500, 750, and 1000 thermal cycles were run at temperatures of 100°C and 175°C.

The average hardness values of the conductors decreased at both temperatures, however, they significantly decreased for the 175°C tests, so much so that they could not even be read using the Rockwell H scale for the 500- and 100-cycle tests. This is shown in Figure 189.

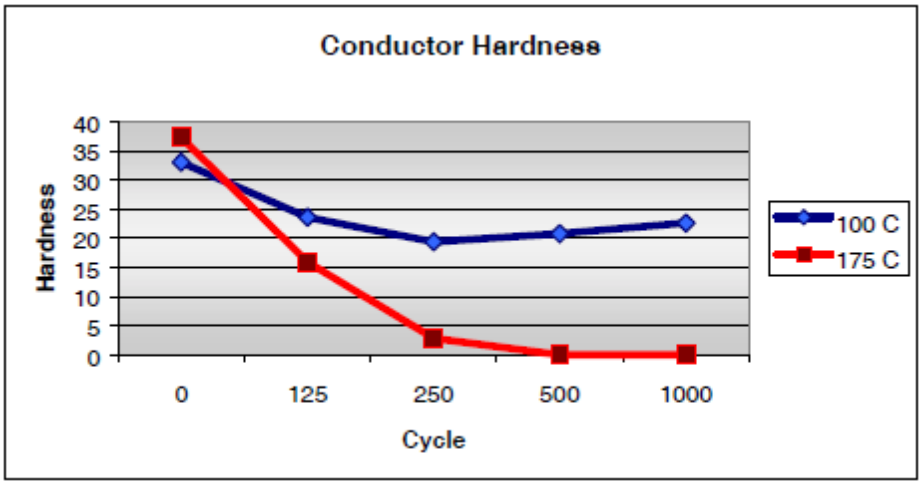

Note: Hardness readings taken on the Rockwell H scale.

Figure 189. Hardness readings of the conductors [128]. After a given number of thermal cyclic loadings at specified temperatures, the conductor at 175°C showed a significant decrease in hardness.

The same conductors were tested in tension in compliance with ANSI C119.4 class 1 full tension. In this case, the conductor is required to withstand 95% of its Rated Breaking Strength (RBS), which was 4066lb in this case. Figure 190 shows the results, along with a notation of where the 95% RBS strength is on the chart. From the figure, the tension force decreased as the number of cycles increased for each respective temperature. For the 100°C tests, the 1000-cycle test produced a tensile strength below the required 95% RSB. For the 175°C tests, the 250, 500, and 1000-cycle tests all produced tensile strengths below the 95% RSB. Hence, this indicates that the cycling of high temperatures has a notable effect on the tensile strength of the conductor.

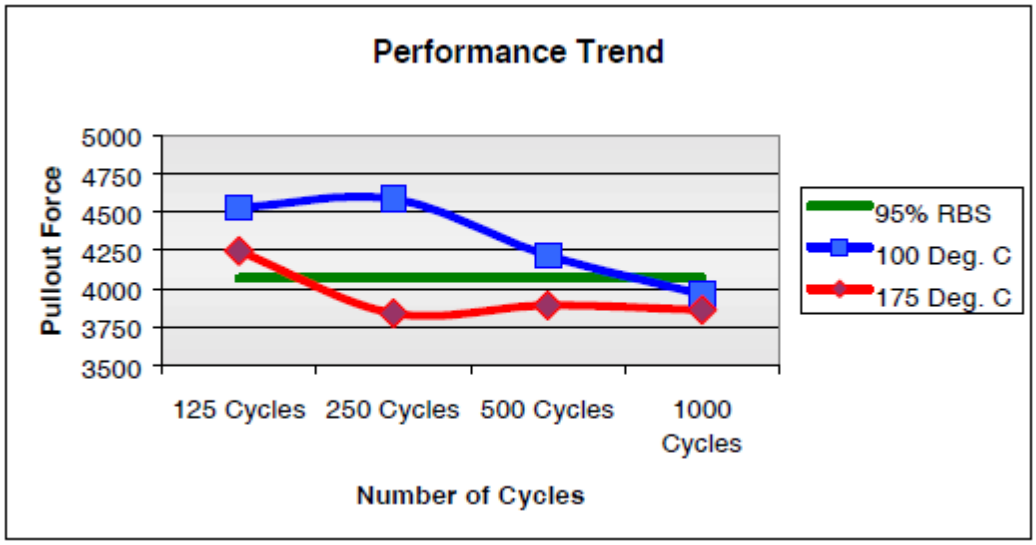

Figure 190. Tensile strength results of the conductors [128]. The tensile strength of the conductors was decreased as the number of cycles increased for both temperatures.

The metallurgical evaluation in this work involved lightly magnifying the conductors to try to evaluate them. No differences could be seen at this level of magnification, however, grain size should be evaluated. It is expected that there will be differences in the pre-test and post-test samples, since there was a significant effect on the hardness and tensile strength.

This specific work supports the statement that the temperature of the conductor can dictate its integrity. Some ideas to improve the conductor life would be to minimize the temperature and duration for which the conductor is at a high temperature. To this end, new technology has produced wireless sensors that can be attached to the conductor and can be used to monitor the temperature in real-time [129].

13.3.6. The EAF Modeling Technique Applied to OHTL Sag Calculations

Of note, from all the research that has been collected on transmission line design and the sag in transmission lines, the main reason for the increase in the sag is due to the temperature increase by way of thermal expansion when excess electricity is supplied through a transmission

line [130]. However, what if there were actual effects due to the electroplastic effect as well? For example, in the EAF modeling strategy of this thesis, the applied electricity is separated into the portion that assists deformation and the portion that assists resistive heating. The resistive heating portion of the applied electricity is all that is accounted for in the thermal expansion calculation.

For example purposes, a "DOG" ACSR conductor will be examined with the following specifications [131]:

- Overall line diameter of 14.15mm
- Line weight of 3.89 N/m
- Calculated breaking load (CBL) = 32.68kN
- Initially set tension in the cable = 20%CBL = 6.536kN
- Tower span = 275m

Using eq.(70) above, the conductor sag can be calculated, as shown below in eq.(74):

$$Sag = \frac{3.89\frac{N}{m}\cdot\left(275m\right)^2}{8\cdot\left(6,536N\right)} = 5.6m \tag{74}$$

The typical amount of sag in an OHTL can be from about 3m to 10m, depending on the electrical conditions. Aside from the sag on the line, it is also important to analyze the tension, and corresponding stress in the line. The stress can be calculated from eq.(75) below:

$$Cable\,Stress = \left(\frac{Tension}{Area}\right) = \frac{\left[N\right]}{\left[m^2\right]} = MPa \tag{75}$$

The stress on this particular OHTL is shown in eq.(76):

$$Cable\,Stress_{Dog\_Conductor} = \frac{6,536N}{\frac{\pi}{4}(.01415m)^2} = 41.56MPa \quad (76)$$

Although the stress in the ACSR is below the yield strength limit for high strength steel [132], it may already be higher than the yield strength limit for 1xxx electrical aluminums depending on the temperature of the conductor [133]. In addition, the lines could potentially be rated for carrying several hundred or even thousands of megawatts (MW) of power through them. Experimental works by the candidate and colleagues has shown that EAF has the ability to significantly reduce the stress needed to plastic deformation in both aluminum and steel metals [3], [38], [40], [42], and [47]. With this being said, the direct electrical effects may lower the plastic deformation strength of the lines even further than what the heating can attribute towards.

The heat balance for overhead conductors can be shown in eq.(77).

$$q_c + q_r + mC_p \frac{dT_c}{dt} = q_s + I^2 R(T_c) \quad (77)$$

where q_c is the convection heat loss, q_r is the radiation heat loss, q_s is the solar heat gain, mC_p is the total conductor heat capacity, and $R(T_c)$ is the resistance of the electrical conductor as a function of temperature [134]. The term in this equation represents the watt losses in the conductor, where all of the power is assumed to contribute towards resistive heating. However, if the stress in the OHTL is close to the yield strength of the conductor and electricity is now flowing, there may be a possibility that some plastic deformation could take place.

In *sub-section 2.6*, Figure 24 depicts the steep drops in the tensile flow stress of Al 5052 each time an electrical pulse is applied (note there was about a 40% reduction in the stress at each pulse). To this end, in *sub-section 2.1*, Figure 15 shows the threshold effect of EAF for Ti-G5, where different metals have different starting current densities where a significant improvement in the formability is witnessed. Overall, applied electrical power has been proven to have the capability to greatly reduce a metal's yield strength above a material-specific, electrical power threshold. Therefore, a portion of the conductor sag, which was originally considered to be due to heating effects, may actually be due to direct electrical effects, and could be represented by an EEC, specific to the conductor material properties, the loading conditions, and the electrical power flowing through the line.

To bring the electroplastic effect on OHTL's into perspective, data from [40] will be used to estimate currents which may be above the electrical threshold of materials similar to the materials in the ACSR-DOG conductor. From this reference, the electrical thresholds for Al6061 and A2 tool steel were found to be $60A/mm^2$ and $45A/mm^2$, respectively (Note that these threshold current densities were for compression and were for specific die speeds. These current densities are just intended to provide an idea of how much current could be needed to potentially have an effect on the conductor strength.). For the given diameter of the conductor (14.15mm), eq.(78) and eq.(79) below calculate the amount of electrical current where effects on conductor strength would be notable, based on the electrical thresholds from [40].

$$Amps_{Al} = C_d \cdot Area = 60\frac{A}{mm^2} \cdot \left(\frac{\pi}{4}(14.15mm)^2 \right) \approx 9400A \tag{78}$$

$$Amps_{Steel} = C_d \cdot Area = 45\frac{A}{mm^2} \cdot \left(\frac{\pi}{4}(14.15mm)^2 \right) \approx 7100A \tag{79}$$

The large OHTL's coming from the electrical generation stations may be able to carry this amount of electrical current. However, the EAF experiments explained throughout this thesis were conducted where the electrical power was supplied as constant current, with varying voltage. The power in OHTL's is supplied in the opposite manner, where the electricity in the lines is described in terms of voltage, since the voltage running through the lines is constant, and the current fluctuates depending on the power usage of the customers. In order to determine the magnitude of the reduction in the strength of the conductor due to direct electrical effects (*i.e.* the EEC), specialized experiments would need to be run, which are explained in the following sub-section.

13.3.7. Future Work to Determine EEC-Values for OHTL's

Although a full relationship between transmission line sag calculations and invented EAF modeling strategy will not be covered in this thesis, the following is an envisioned procedure to follow to begin to do this. It is known that all the sag calculations referenced by the Ph.D. candidate consider the heating effect due to electricity the sole contributor to the sagging. However, the invented EAF modeling strategy indicates that there could also be a direct electrical effect on the deformation of the transmission line.

In order to begin to determine if there is a direct electrical effect and to quantify it, the candidate suggests running an EAF tension test at an electrical power combination comparable to what is seen daily in the transmission lines. Then, compare the power profile of this test to a conventional tension test without EAF. By calculating the difference in the mechanical power profiles, one can determine the EEC using the mechanical approach (as described in *Chapter 3*). This coefficient will describe the percentage of applied electricity that actually contributed to

assisting the deformation and did not just account for heating. If the EEC is very low, then the assumption that only heat contributes to sag, is sufficient. However, if the EEC is quite large, then there are unaccounted affects which could amplify the magnitude of the transmission line sag beyond that of which can be calculated using current transmission line sag calculations.

14. Intellectual Merit

The candidate's ultimate intent for this Ph.D. thesis was to take a potential manufacturing technique, experimentally prove its benefits, analytically model its behavior, explore several potential important material- and process-based parameters that could affect the EAF process, and evaluate EAF's place within industry. The following are intellectual contributions made by the Ph.D. as part of his research:

- A simple model of electrically-assisted forging was created. This model predicts material flow stress to an error of approximately 20% across the following process ranges: die speeds of 12.7mm/min and 25.4mm/min, starting current density ranges from 0-60A/mm^2, for various metals (304SS, Ti, Al) (*Chapter 5*).
- An Electroplastic Effect Coefficient (EEC) was introduced to represent the power contribution of the direct electrical effects during the EAF technique (*Chapter 3*).
- Two methods were developed and can be used to obtain an EEC profile for any metallic workpiece and manufacturing process combination. Each EEC-determination method was consistent in predicting the EEC profiles over a range of conditions (*Chapter 4*).
- The methods were used to model an electrically-assisted bending process with reasonable accuracy (*Chapter 5*). This demonstrates applicability of the model to different processes to which electrical assistance is applied.
- A new comprehensive electroplastic effect theory was developed, which accounts for heating and electron-dislocation momentum transfer effects, both of which are quantified by the EEC (*Chapter 10*).
- Investigation was carried out on the tribology conditions during an EA-Forging process (*Chapter 6*). From this work, a nascent strategy for EA lubricant selection was developed.

- An investigation into the effect of contact area and surface roughness on the thermal and mechanical profiles for an EA-Forging operation was completed (*Chapter 6*). Contact area considerations were shown to be negligible with respect to plastic deformation modeling; however, workpiece roughness increased significantly with increasing current density.
- On the macro-level, starting specimen grain size differences of almost 45% did not have a recognizable effect on the mechanical profiles of an EA-Forging test, and there was only a small thermal difference between the specimens with different grain sizes *(Chapter 7)*.
- Different amounts of initial cold work significantly affected the EAF technique performance (*Chapter 8*). Specifically, as initial dislocation density increases, the resistivity in the part increases, which leads to a workpiece temperature increase once the electricity is applied. The stress-strain profiles of initially worked and non-worked specimens begin to converge as the strain is increased throughout the tests. The amount by which they converge is dependent on the magnitude of initial cold work in the workpiece.
- For an EA-Forging process, the model showed that the only significant form of heat transfer was conduction, and that convection and radiation could be neglected without risking modeling accuracy (*Chapter 9*).
- Varying quality in the supplied electrical power minimally affects the mechanical profiles of workpieces undergoing the EAF technique during deformation (*Chapter 9*).

- The sag of high-voltage overhead transmission lines and specifications for sag may be explainable using EAF modeling methodology (*Chapter 12*). Electrical transmission lines are analogous to an EAF tension process, and a relation to previous EAF experimental work showed that safety factors must be included not only for thermal softening, but also to avoid reduced yield due to direct electrical effects.

APPENDICES

15. Appendices

15.1. Creation of EAM Facilities at CU-ICAR

As a graduate student at CU-ICAR, my first task was to construct a complete EAM testing and analysis setup in the labs. During the first several months, the following achievements that were made, which enabled EAM research to begin at ICAR will be covered in *sub-sections 14.1.1 through 14.1.4.*

15.1.1. Instron EAM Testing Setup

An Instron hydraulic testing machine with onboard programming and data collection software was installed in the lab, as displayed in Figure 191. Additionally, I wrote an all-inclusive training manual explaining safety, capabilities, and data collection procedures specific to the machine.

Figure 191. Instron EAM testing setup at CU-ICAR. The EAM testing setup includes an Instron hydraulic testing machine, a controllable DAQ, and a power supply.

15.1.2. Microstructure Sample Preparation Cell

A complete microstructure mounting and polishing cell was constructed, including a cut-off saw, cold-mounting trays and supplies, and a dual spindle polishing table. Shown in Figure 192, this cell is used to prepare samples for microstructure analysis of EAM.

Figure 192. Microstructure sample preparation cell. The microstructure setup includes a cut-off saw, mounting supplies, and a dual-table grinding/polishing station for preparation of microstructure samples.

15.1.3. EAM Tool Design

Since electricity needs to flow through particular pathways and into the specimens, specialized tooling, which incorporated insulation and conductive materials, had to be designed for each specific EAM manufacturing process of concern. The candidate used his networking skills and received support from local companies for tooling materials *(see Acknowledgements section)*, and also used his CNC experience to construct several specialized EAM-compliant dies to be used with the Instron machine for EAM experiments (Figure 193).

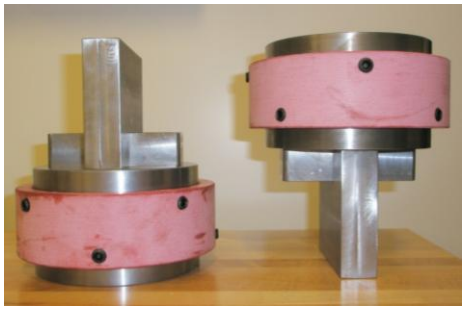

a.) Compression dies

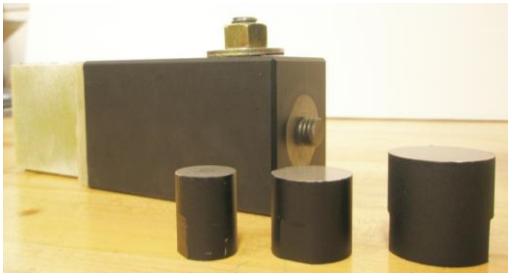

b.) Modular compression dies

c.) Bending setup

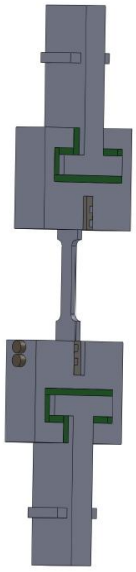

d.) Tensile fixtures

Figure 193. EAM-specific die designs. Due to the fact that electricity must be directed through the workpiece and not the machinery, specialized EAM tooling must be designed. (a) compression dies with fiberglass-reinforced insulation GP-04, (b) insulated compression dies with modular die ends, (c) a fully-adjustable and insulated 3-pt. air bending setup, and (d) insulated EAM-specific tension fixtures.

15.1.4. EAM Power Supplies

As limited funding was received for this project, a larger 4000A Darrah fully-controllable SCR power supply was purchased. With a significantly larger output current capability, this power supply will allow for larger, more realistic compression slugs to be tested in the lab at CU-

ICAR. Additionally, various wave shapes and duty cycles can be dictated and run easily. A comparable power supply to the one purchased can be seen in Figure 194.

Figure 194. Darrah power supply. The Darrah power supply is fully-controllable and capable of outputting up to 4000 Amps.

15.2. 304SS EEC Profiles vs. Time and Strain

The following four figures (Figure 195 to Figure 198) display the EEC profiles for 304SS in as a function of time. The EEC profiles were generated using the mechanical- and thermal-based approaches. These profiles are displayed in terms of stroke in *sub-section 4.3.2*, such to provide for an easier visual way to compare the effects of the different die speeds. However, since the EEC is a function of time, the following figures display this, such that these EEC profiles could be used by other researchers in the future.

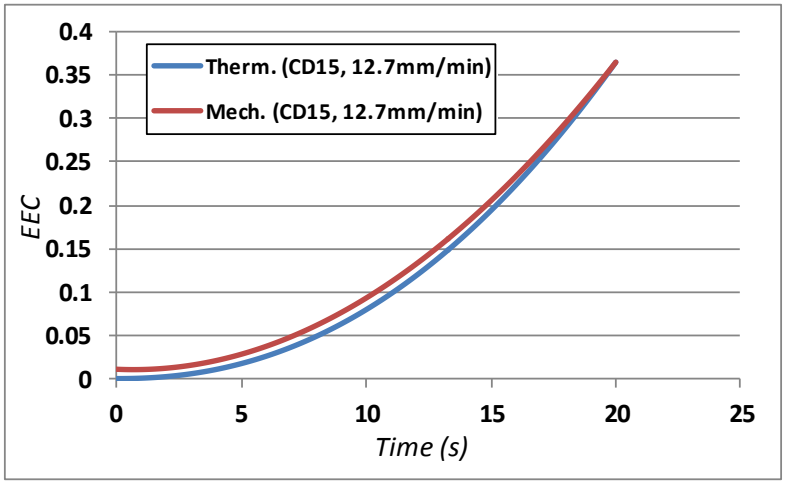

Figure 195. 304SS EEC profiles vs. time (CD15, 12.7mm/min). The EEC profiles, determined using the mechanical and thermal methods, are plotted vs. time.

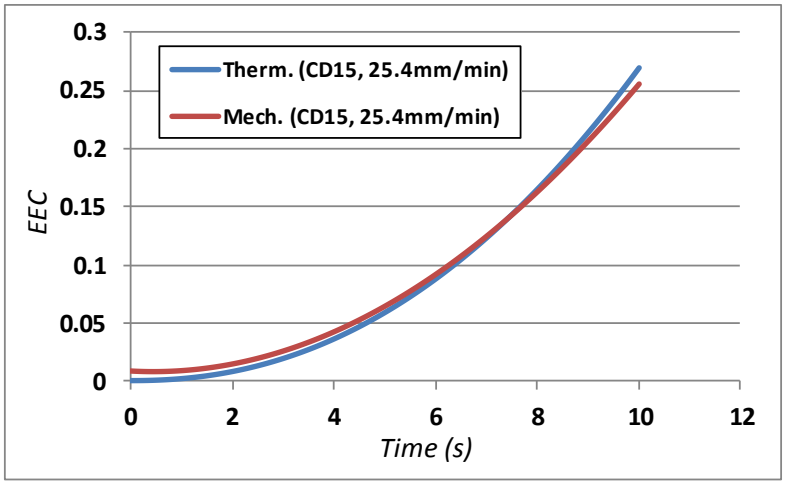

Figure 196. 304SS EEC profiles vs. time (CD15, 25.4mm/min). The EEC profiles, determined using the mechanical and thermal methods, are plotted vs. time.

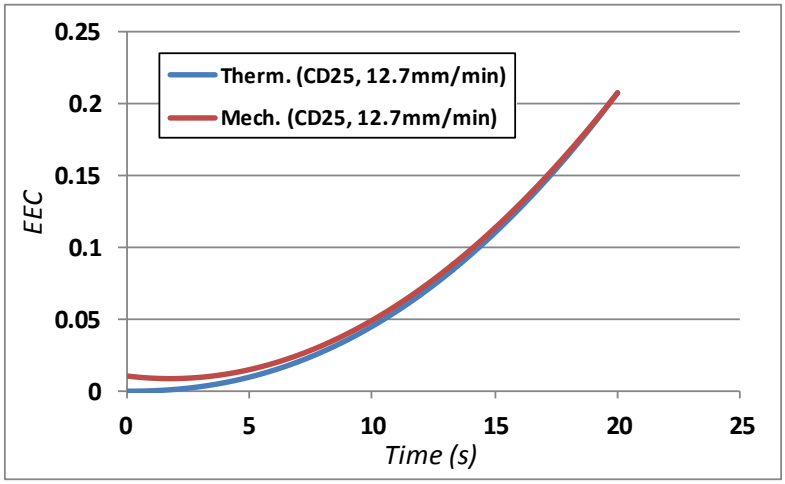

Figure 197. 304SS EEC profiles vs. time (CD25, 12.7mm/min). The EEC profiles, determined using the mechanical and thermal methods, are plotted vs. time.

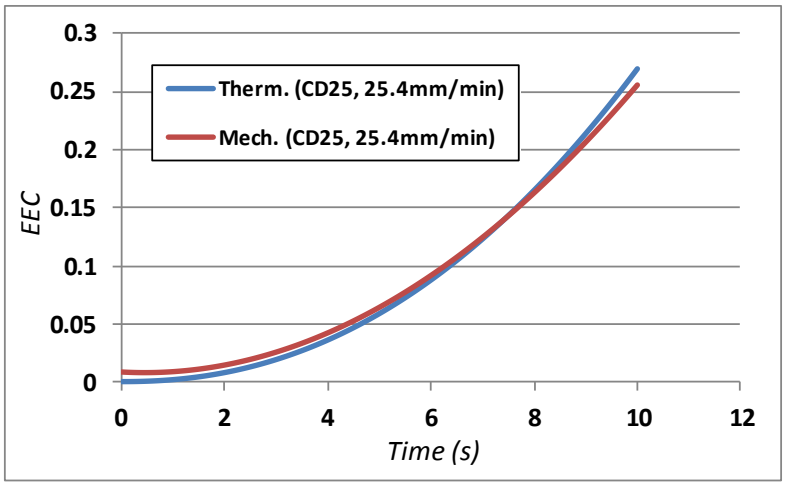

Figure 198. 304SS EEC profiles vs. time (CD25, 25.4mm/min). The EEC profiles, determined using the mechanical and thermal methods, are plotted vs. time.

The following four figures (Figure 199 to Figure 202) display the EEC profiles for 304SS in as a function of time. The EEC profiles were generated using the mechanical- and thermal-based approaches. These profiles are displayed in terms of stroke in *sub-section 4.3.2*, such to provide for an easier visual way to compare the effects of the different die speeds. However, since the EEC is a function of time, the following figures display this such that these EEC profiles could be used by other researchers in the future.

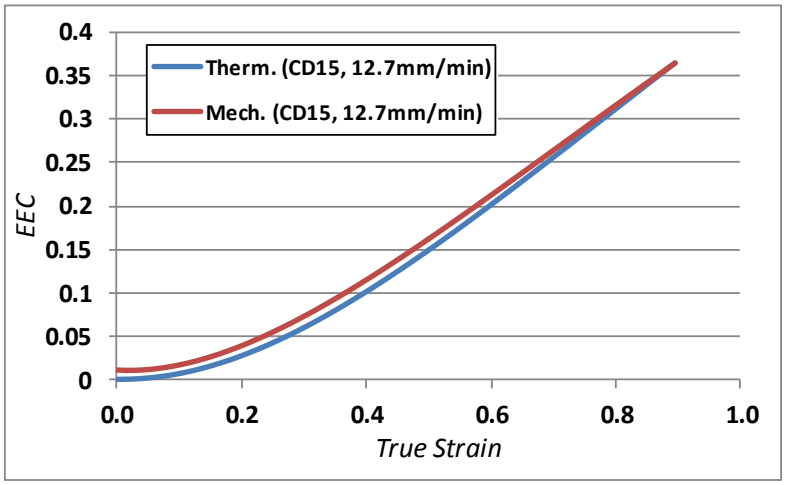

Figure 199. 304SS EEC profiles vs. true strain (CD15, 12.7mm/min). The EEC profiles, determined using the mechanical and thermal methods, are plotted vs. true strain.

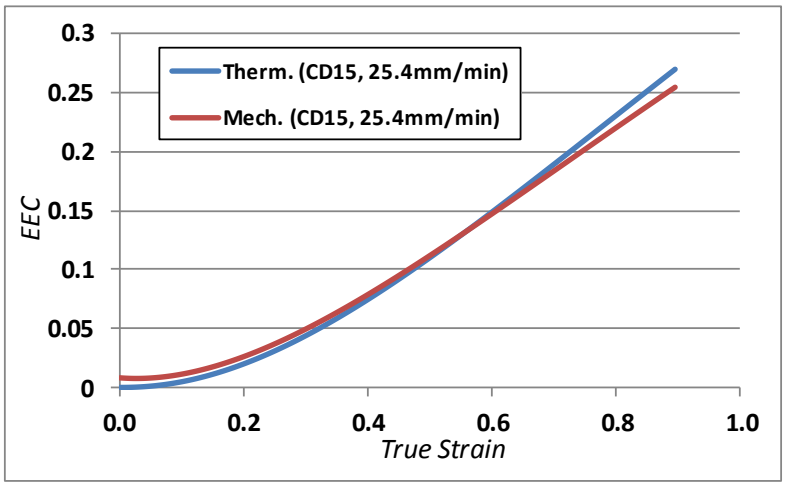

Figure 200. 304SS EEC profiles vs. true strain (CD15, 25.4mm/min). The EEC profiles, determined using the mechanical and thermal methods, are plotted vs. true strain.

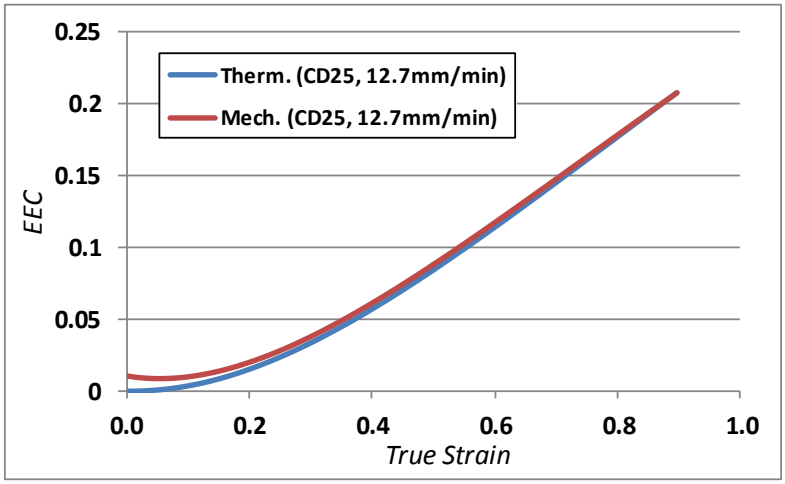

Figure 201. 304SS EEC profiles vs. true strain (CD25, 12.7mm/min). The EEC profiles, determined using the mechanical and thermal methods, are plotted vs. true strain.

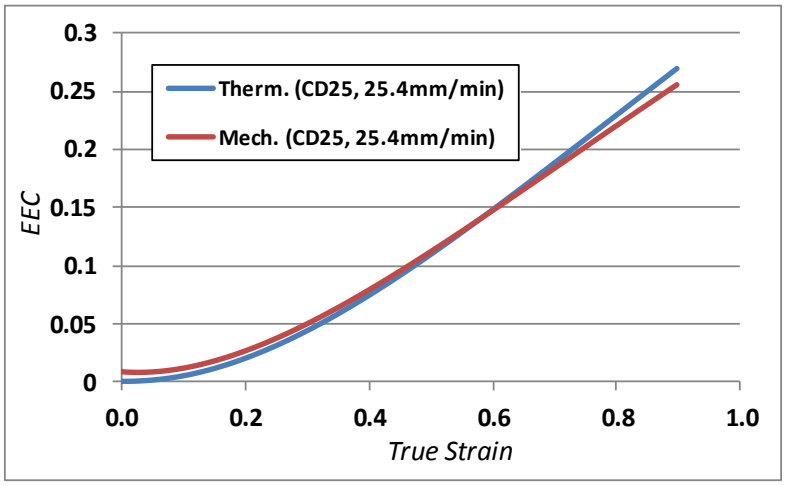

Figure 202. 304SS EEC profiles vs. true strain (CD25, 25.4mm/min). The EEC profiles, determined using the mechanical and thermal methods, are plotted vs. true strain.

15.3. Temperature-Based Relations for EAF Modeling

The following figures show the efforts to incorporate the thermal softening effect into the EAF modeling strategy. Figure 203 shows the relationship between the strength coefficient for Al6061 and temperature of the metal [67]. Figure 204 displays the flow stress modeling by the candidate for Al6061 at different temperatures.

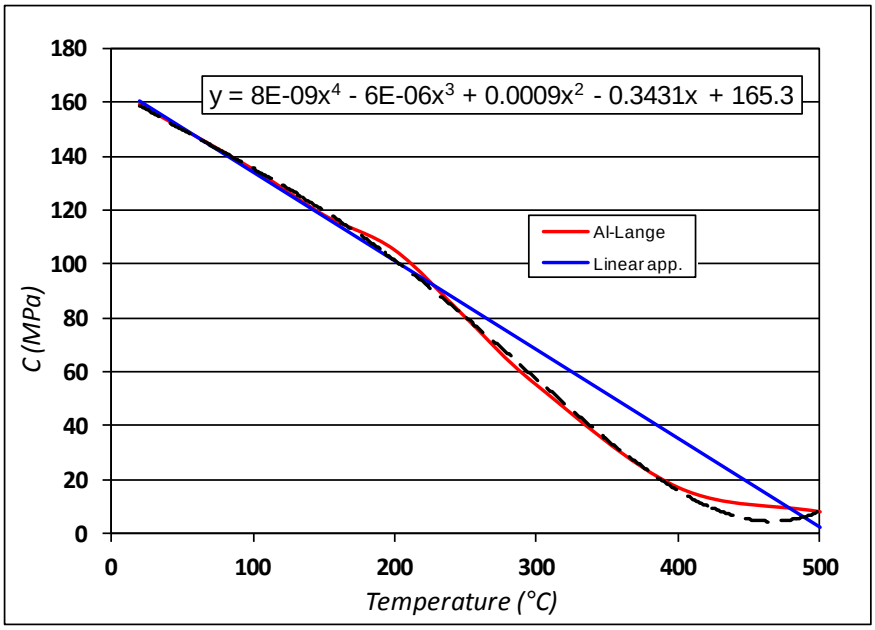

Figure 203. Dependence of Al6061 strength coefficient with respect to temperature [67]. The strength coefficient ofAl6061-T6511reduces as the temperature is increased. A 4th order linear approximation is used to represent this relationship.

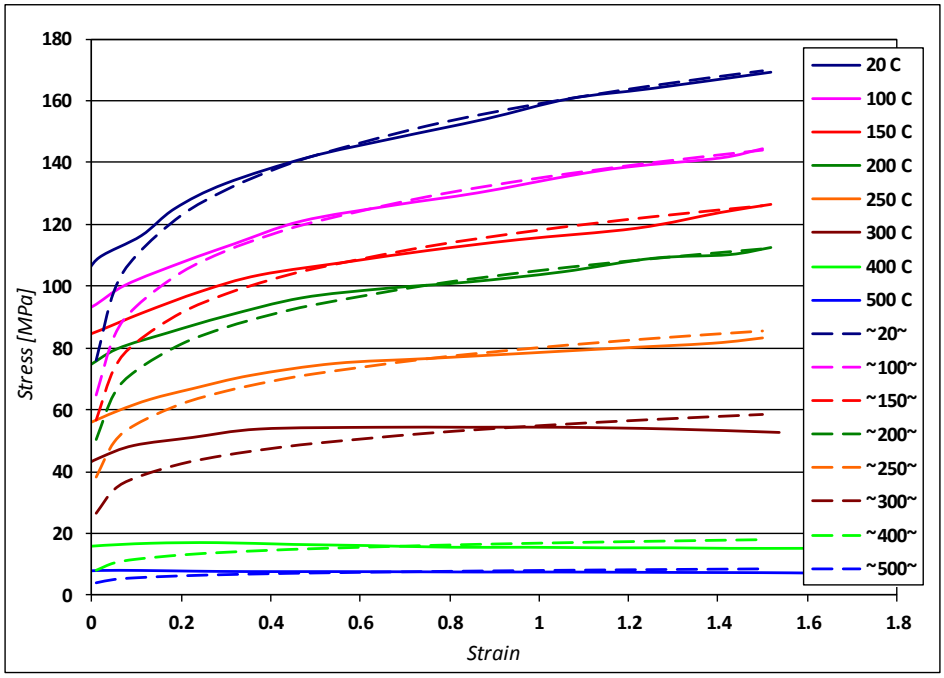

Figure 204. Al6061 flow stress modeling at different temperatures. Flow stresses at different temperatures. Depicted are flow stress model predictions and experimental results of Al6061-T6511 compression at different temperatures.

The following three figures show the temperature-material property relationships of different metals. Figure 205 shows the relationship between tensile strength and temperature for Al 1100 [86]. Figure 206 shows this same relationship for an A36 steel material [132]. Figure 207 displays the relationship between electrical resistivity and temperature for 304SS [135]. Please note that all of these relations were used throughout the thesis.

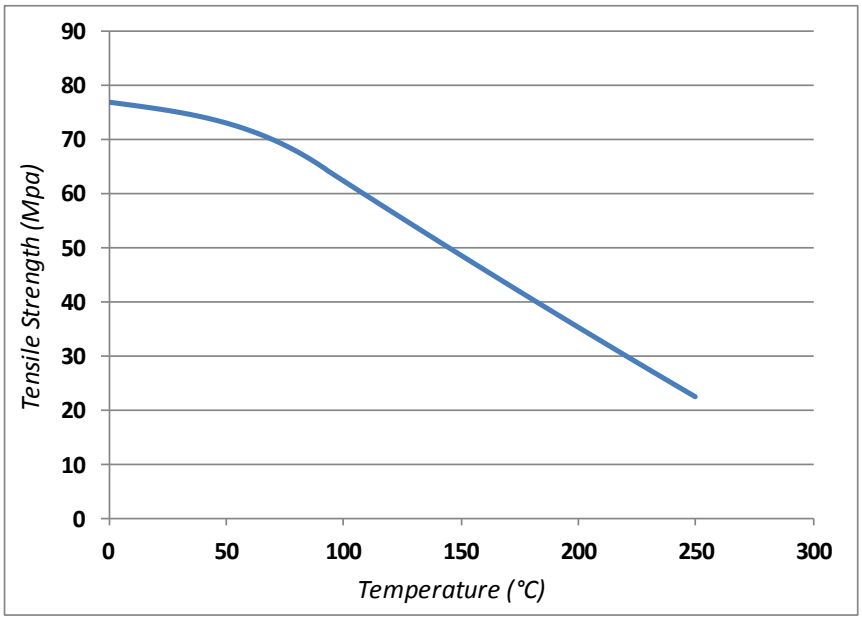

Figure 205. Al 1100 (UNS A91100) tensile strength vs. temperature relationship [86]. The tensile strength of Al 1100 begins to decrease linearly at about 75°C.

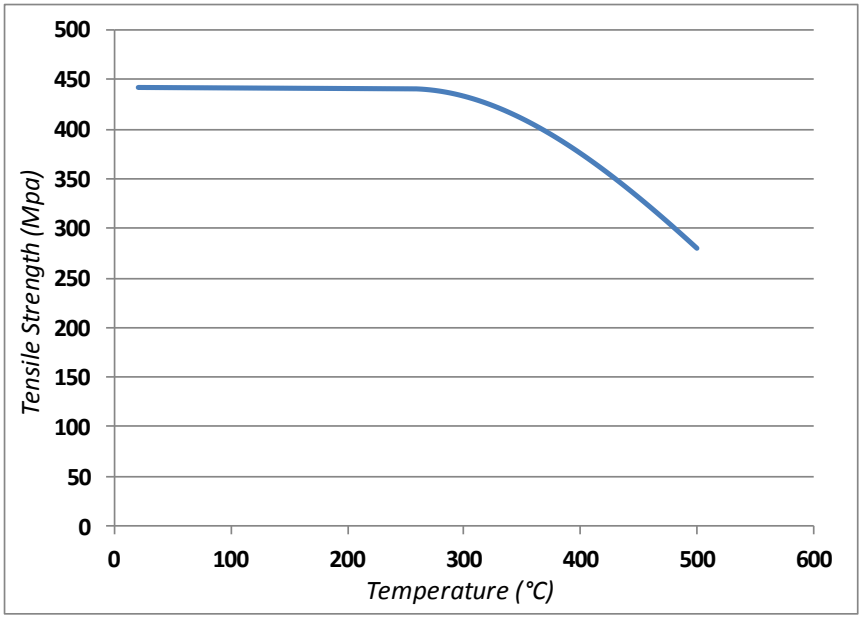

Figure 206. A36 (UNS K02600) tensile strength vs. temperature relationship [132]. The tensile strength of A36 steel remains constant from room temperature until about 275°C.

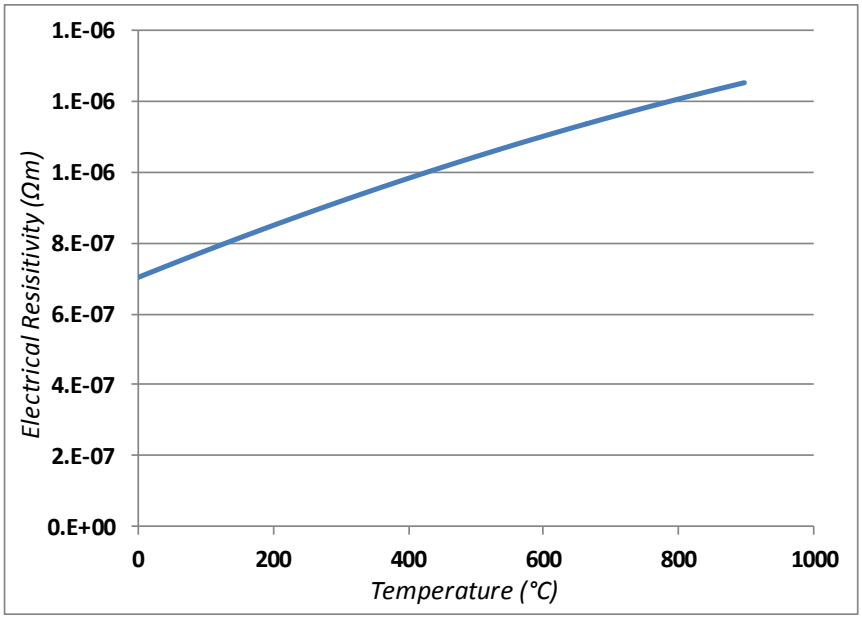

Figure 207. 304SS electrical resistivity vs. temperature relationship [135]. The electrical resistivity of 304SS increases linearly as temperature is increased.

15.4. Post-Deformation EAF Springback Reduction

Green et al. performed work on the reduction of springback in bent sheet metal specimens while applying a single electrical pulse after deformation had taken place but prior to removing the metal from the die [45].

Figure 208 shows the amount of springback reduction that was achieved from this work [45].

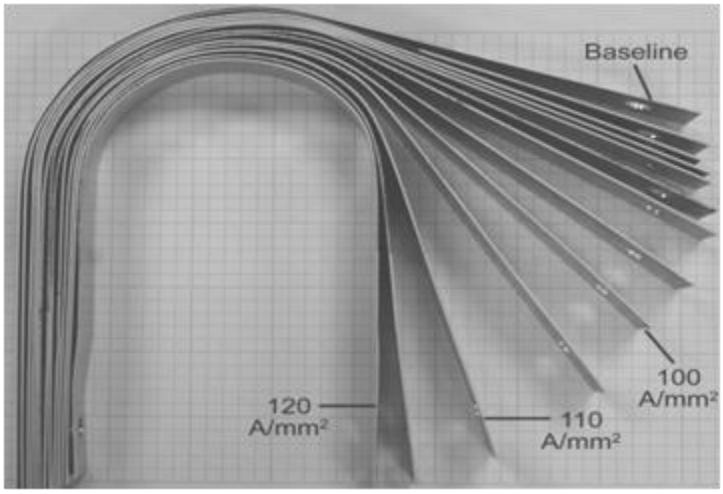

Figure 208. Post-deformation springback reduction using EAM [45]. Springback in Al6111 sheet metal strip specimens was completely eliminated with a single 1.5-second electrical pulse of 120A/mm^2 or greater post-deformation, but prior to removing the material from the die.

15.5. Previous Work EAM Compression Results

The following figures (Figure 209 to Figure 211) are results from work by Perkins et al., which are used for comparison of results in this thesis document [40].

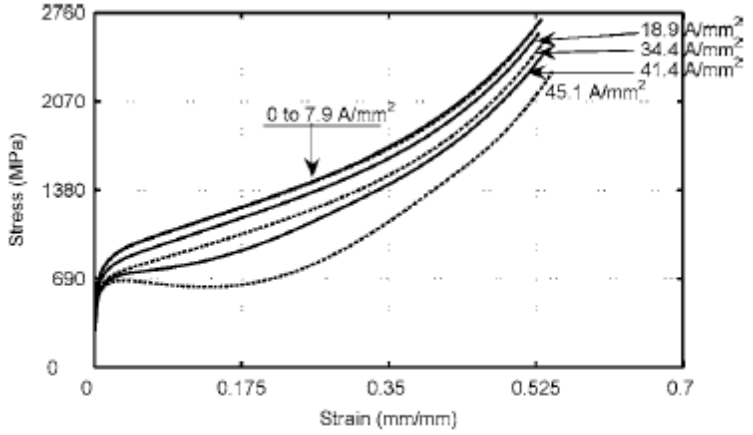

Figure 209. A2 tool steel EAF stress-strain profiles [40]. The A2 tool steel material began to have notably improved formability around a starting current density of 45A/mm^2.

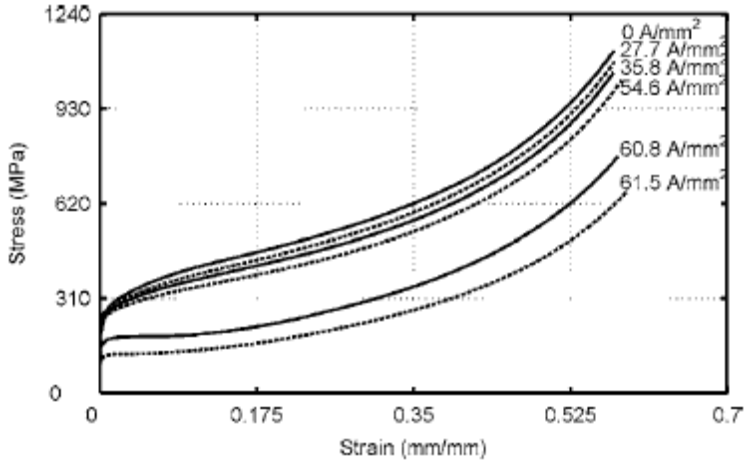

Figure 210. Al6061-T6511 EAF stress-strain profiles [40]. The Al material began to have notably improved formability around a starting current density of 60A/mm^2.

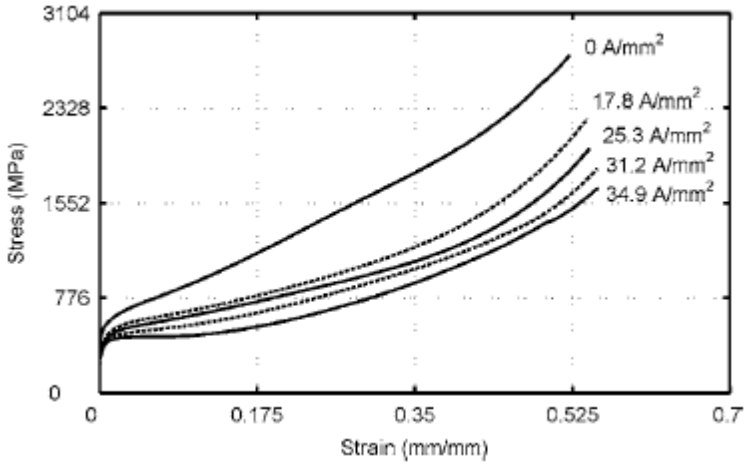

Figure 211. SS304 EAF stress-strain profiles [40]. The difference between the stress of the conventional vs. the EAF test increased as the strain increased.

15.6. EAF Percent Cold Work Micrographs

Figure 212 shows the polished percent cold-worked and annealed compression specimens before and after etching. Figure 213 displays the post-formed microstructure of 20% CW/Annealed specimens that were compressed 4.445mm at a die speed of 12.7mm/min conventionally or using the EAF technique, where a constant 800A was applied. Each horizontal row shows the microstructure at 20x and 50x magnification. The pictures of the microstructure were taken in approximately the same location from specimen-to-specimen.

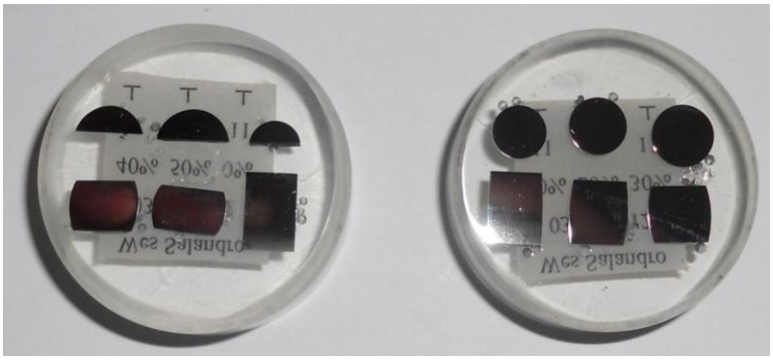

a.) Polished specimens

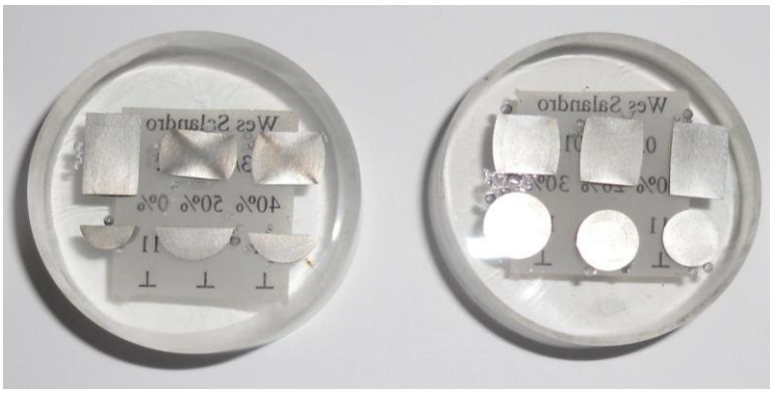

b.) Etched specimens

Figure 212. Percent cold work microstructure specimens. Each of the worked specimens were cut using an EDM, and were then cold-mounted and polished using a final alumina solution of 0.05µm.

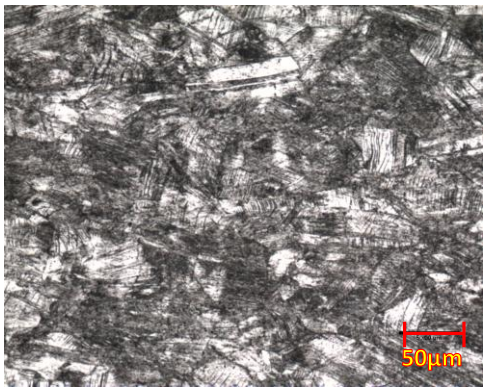

a.) 20%CW conv., 20x

b.) 20%CW conv., 50x

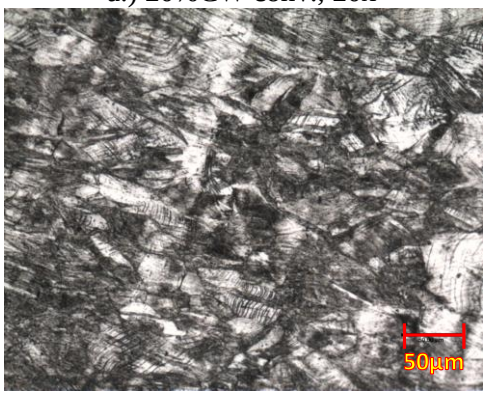

c.) 20%Annealed conv., 20x

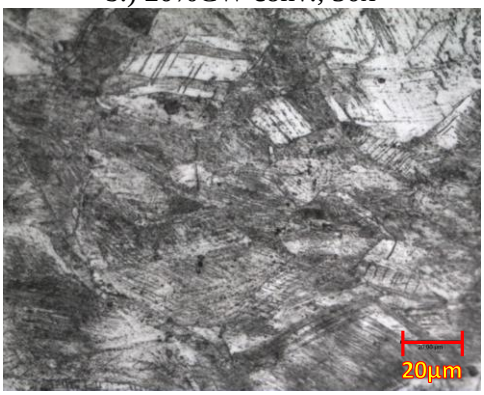

d.) 20% Annealed conv., 50x

e.) 20%CW EAF, 20x

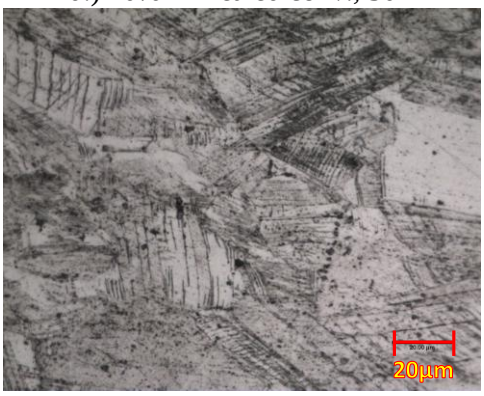

f.) 20%CW EAF , 20x

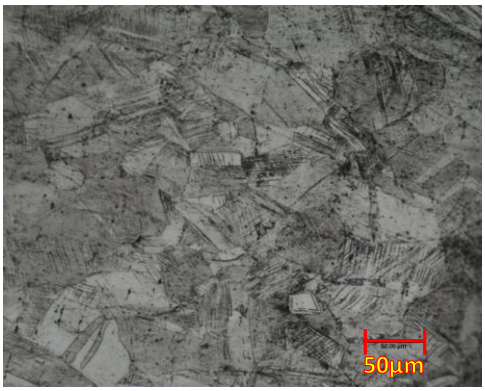

g.) 20% Annealed EAF, 20x

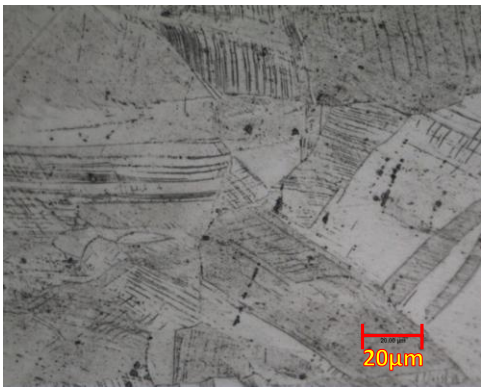

h.) 20% Annealed EAF, 50x

Figure 213. Worked/Annealed EAF post-forming micrographs. The figures show the microstructures at designated magnifications of pre-worked and annealed specimens deformed conventionally and using the EAF technique.

LIST OF ABBREVIATIONS

Abbreviation	Description
EAM	Electrically-Assisted Manufacturing
EEC	Electroplastic Effect Coefficient
EAF	Electrically-Assisted Forming
CU-ICAR	Clemson University – Intl. Center for Automotive Research
GDP	Gross Domestic Product
FLD	Forming Limit Diagram
EA	Electrically-Assisted
OEM	Original Equipment Manufacturer
CAFÉ	Corporate Average Fuel Economy
MPG	Miles Per Gallon
SMDI	Steel Market Development Institute
UHSS	Ultra-High Strength Steel
IF	Incremental Forming
SPF	Superplastic Forming
GBS	Grain Boundary Sliding
TWB	Tailor Welded Blank
CAE	Computer-Aided Engineering
HCP	Hexagonal Close-Packed
FEA	Finite Element Analysis
PNNL	Pacific Northwest National Laboratory
DC	Direct Current
FLIR	Forward Looking Infra Red
MSEC	Manufacturing Science and Engineering Conference
EDM	Electrical Discharge Machining
EAB	Electrically-Assisted Bending
SS	Stainless Steel
RMS	Root Mean Square
CA	Contact Area
CD	Current Density
CNC	Computer Numerical Control
EP	Extreme Pressure
IFOV	Instantaneous Field Of View
AMRL	Advanced Materials Research Laboratory
CW	Cold Work
FFT	Fast Fourier Transform
FCC	Face-Centered Cubic
HCP	Hexagonal Close-Packed
SCR	Silicon-Controlled Rectifier
OHTL	Overhead Transmission Lines
ACSR	Aluminum Conductor Steel Reinforced
AAC	All Aluminum Conductor
AAAC	All Aluminum Alloy Conductor
ANSI	American National Standards Institute
RBS	Rated Breaking Strength
MW	Mega-Watt

LIST OF NOTATIONS

Notation	Description
$\bar{\sigma}$	Flow stress
C	Strength coefficient
$\bar{\varepsilon}$	Effective strain
n	Strain hardening exponent
J^*	Upper bound on power
$\dot{W}_i$	Internal power of deformation
$\dot{W}_s$	Shear power given by the discontinuity of velocity
$\dot{W}_b$	Power to overcome opposing external forces
$\dot{W}_k$	Inertia power
$\dot{W}_p$	Pore opening power
$\dot{W}_\gamma$	Surface power
r_{inst}	Instantaneous workpiece radius
h_{inst}	Instantaneous workpiece height
$\dot{u}$	Velocity of the compressive die
r_0	Initial radius of the billet
F	Forming load
p	Pressure
$\sigma_z, \sigma_\theta, \sigma_r$	Principal stresses
$\varepsilon_z, \varepsilon_\theta, \varepsilon_r$	Principal strains
J_m^*	Mechanical component of power
J_e^*	Effective (usable) electrical power
ξ	Electroplastic Effect Coefficient
P_e	Power of electrical current passing through the workpiece
$\frac{\partial \rho U}{\partial t}$	Rate of change of the internal energy of the part
$\frac{\partial}{\partial x_j}\left(\dot{Q}_{cond}\right)$	Conductive component of the heat flux
$\frac{\partial}{\partial x_j}\left(\dot{Q}_{conv}\right)$	Convective component of the heat flux
Q_{rad}	Radiation heat
$(1-\xi)P_e$	Heat generated in the part from the electric energy dissipated
ρ	Density of the material
V_v	Volume of the part
C_p	Specific heat of the material

T	Temperature
t	Time
A_s	Lateral surface of the part
h	Convection heat transfer coefficient
T_∞	Surrounding temperature
k	Thermal conductivity of the die material
A_c	Cross-sectional area of the part
ε	Radiative emissivity for the part
σ_{SB}	Stefan-Boltzmann constant
V	Electric voltage
I	Intensity of the current
C	Strength of the material
$\dot{\bar{\varepsilon}}$	Effective strain rate
m	Strain rate sensitivity coefficient
C_d	Current density
πr^2	Area of a circle
ΔP_m	Mechanical power step
P_m	Mechanical power
P_{conv}	Mechanical power profile of a conventional compression test
P_{EAF}	Mechanical power profile of an EAF compression test
$\dot{E}_{part}$	The rate of change of the energy content in the part analyzed
$\dot{E}_g$	The rate of heat generation due to the electric resistive heating
$\dot{E}_{out}$	The rate of energy leaving the part due to conduction into the dies in the contact zone
$\dot{Q}_{cond}$	Conduction heat transfer
$\dot{Q}_{conv}$	Convection heat transfer
$\dot{Q}_{rad}$	Radiation heat transfer
ξ_0	Initial EEC value
ε	Material strain
$\dot{\varepsilon}$	Strain rate
b	Exponential term for thermal-based EEC determination
P_e	Electric power
P_{heat}	Amount of electric power that will dissipate into heat
P_{def}	The electrical power component that will aid the plastic deformation
μ	Friction coefficient
h_o	Starting specimen height
V_{Total}	Total voltage of the system
V_{Z1}	Voltage of Zone 1

V_{Z2}	Voltage of Zone 2
V_{Z3}	Voltage of Zone 3
L_c	Length of the die/workpiece contact zone
L_w	Length of the workpiece-only zone
L_{Total}	Total length of the specimen
$r_{NA} = \sqrt{r_p\left(r_p + t_b\right)}$	Air bending neutral axis relation
α	Bending angle
ε_x	Bending strain in the outer fiber
r_p	Punch radius
t_b	Thickness of the strip
dF_x	Internal force
wdz	Incremental element of cross section
M	Total bending moment
F_p	Punch force
a	Length of the arm (bending modeling)
$J_m^* = F_p\dot{u}$	Total power for plastic bending
Δt	Pulse duration
Δp	Pulse period
$C(T)$	Temperature-dependent strength coefficient function
A_d	Cross-sectional area of the dies
A_p	Cross-sectional area of the punch
$J^*_{classical}$	Mechanical power of a classical bending test
J^*_{EAF}	Mechanical power of an EAF bending test
$F_{p_{classical}}$	Mechanical load needed in classical bending
$F_{p_{EAF}}$	Mechanical load needed in EAF bending
wt_b	Cross-sectional area of sheet metal
ds	Movement increment for positioning of the bending punch
dt	Time increment
β	The angle at which the bending specimen was bent
β_r	The “real” bending angle
Red_{SB}	Reduction in springback
$SB_{classical}$	Springback for a classical bending process
SB_{EAF}	Springback for an EA-Bending process
$CA_{apparent}$	Apparent contact area
L_1	Length of the first cut (contact area section)
L_2	Length of the second cut (contact area section)
L_3	Length of the third cut (contact area section)

L_4	Length of the fourth cut (contact area section)
w	Width of each cut (contact area section)
R	Electrical resistance
L_{part}	Length of the part
$A_{contact}$	Actual contact area of the specimen/die interface
R_{total}	Total resistance of the system
$R_{electrical}$	Electrical resistance of the system
$R_{contact}$	Contact resistance of the system
r_{part}	Resistivity of the part material
r_{die}	Resistivity of the die material
n_{asp}	Number of asperities
a_{asp}	Radius of the contact points
D	Diameter of the region where the asperities are located
τ	Shear stress
k_{shear}	Shear strength
m	Friction factor
F_{EAF}	Average forming load for an EAF ring compression test
F_{conv}	Average forming load for a conventional ring compression test
r_T	Thermal resistivity
C_v	Concentrations of vacant lattice sites
C_I	Concentrations of interstitial ions
C_D	Density of dislocations
C_s	Area of stacking faults
P_v	Material-specific weighting for vacancies
P_I	Material-specific weighting for ions
P_D	Material-specific weighting for dislocations
P_S	Material-specific weighting for stacking faults
S_{cond}	OHTL sag
w	Conductor weight
L	OHTL horizontal span length
T_{cond}	Conductor tension
α_{exp}	Coefficient of thermal expansion
ΔL	Increase in length of the conductor
E	Coefficient of elasticity
$Amps_{Al}$	Amps in the aluminum portion of the OHTL
$Amps_{Steel}$	Amps in the steel portion of the OHTL

REFERENCES

[1] Hogan, B.J., Waurzyniak, P. (2007), "NAMRC 35 Demonstrates Manufacturing's Vitality," Manufacturing Engineering, v 139, n 1.

[2] Liewald, M., Held, C., Schleich, R. (2009), "Characterisation of sheet metal formability - A review and new approaches," Steel Research International, v 80, n 4, p 275-280. ISSN: 16113683.

[3] Roth J.T., I. Loker, D. Mauck, M. Warner, S.F. Golovashchenko, A. Krause (2008). "Enhanced Formability of 5754 Aluminum Sheet Metal Using Electric Pulsing." Transactions of the North American Manufacturing Research Institute of SME, 36, pp. 405-412.

[4] Kravchenko V. (1966). JETP (USSR) 51, 1676 (1966).

[5] Klimov, K.M. and I.I. Novikov (1982). "The "Electroplastic Effect"." A.A. Baikov Institute of Metallurgy, Academy of Sciences of the USSR, Moscow. Translated from Problemy Prochnosti, No.2, pp. 98-103.

[6] Conrad, H. (2000a). "Effects of Electric Current on Solid State Phase Transformations in Metals." Materials Science & Engineering, A287, pp. 227-237.

[7] United States Department of Labor. "Motor Vehicle and Parts Manufacturing." Bureau of Labor Statistics. (Accessed 02 Oct 2011), http://www.bls.gov/oco/cg/cgs012.htm.

[8] Keith, D., (2010), "HSS, AHSS and aluminum jockey for position in the race to cut auto curb weight." American Metal Market Monthly. February 1.

[9] Pfestorf, M., (2009), "Multimaterial lightweight design for the body in white of the new BMW 7 series." BMW Group. Innovative Developments for Lightweight Vehicle Structures. Wolfsburg. May 26-27.

[10] Krinke, S., (2009), "Life cycle assessment and recycling of innovative multimaterial applications." Volkswagen AG. Innovative Developments for Lightweight Vehicle Structures. Conference proceedings. Wolfsburg. May 26-27.

[11] Ford, H., (1924), "My Life and Work." In collaboration with S. Crowther. Kessinger Publishing Co., Montana, 2003.

[12] U.S. Environmental Protection Agency (U.S. EPA), (2009a), "Light-Duty Automotive Technology and Fuel Economy Trends: 1975 through 2008". EPA420-R-08-015.

[13] Glennan, T.B., (2007), "Strategies for Managing Vehicle Mass throughout the Development Process and Vehicle Lifecycle." Society of Automotive Engineers. 2007-01-1721.

[14] www.NHTSA.gov

[15] Kleiner, M., M. Geiger, A. Klaus, (2003), "Manufacturing of Lightweight Components by Metal Forming", CIRP Annals - Manufacturing Technology, Volume 52, Issue 2, Pages 521-542, ISSN 0007-8506, 10.1016/S0007-8506(07)60202-9.

[16] Friesen, F., Schwarz, D., Cunat, P.-J., (2002). "Lightweight Design with Stainless Steel". Proceedings DYNAmore LS-DYNA Forum, Bad Mergentheim, D.

[17] Friebe, E. et al, (2001) "Hydro mechanical deep drawing of passenger car fuel tanks." In, Siegert, k. (Ed.), Hydroforming of tubes, extrusions, and sheets, Vol. 2, MAT-INFO, Frankfurt, D. 193-213.

[18] Taub, A., Krajewski, P., Luo, A. and Owens, J. "The evolution of technology for materials processing over the last 50 years: The automotive example." JOM Journal of the Minerals, Metals and Materials Society, 2007, 59(2), 48-57.

[19] American Iron and Steel Institute: 2009 Press Releases. http://www.steel.org/.

[20] www.mckinnesrolledrings.com

[21] Ross, C.D., T.J. Kronenberger, and J.T. Roth (2009). "Effect of DC on the Formability of Ti-6AL-4V." Journal of Engineering Materials and Technology, 131(3), pp. 11.

[22] Golovashchenko, S.F., A. Krause, and A.J. Gillard (2005). "Incremental Forming for Aluminum Automotive Technology." 2005 ASME – Int. Mech. Engr. Cong. and Exp., IMECE2005-81069, pp. 7.

[23] www.meslab.org

[24] Kalpakjian, S. (1997) "Superplastic Forming." Manufacturing Processes for Engineering Materials, Third Edition, pp. 421-422.

[25] http://asm.informz.net

[26] Kinsey, B. and J. Cao (2003). "An Analytical Model for Tailor Welded Blank Forming." Journal of Manufacturing Science and Engineering, 125, pp.344-351.

[27] http://www.twbcompany.com

[28] Center for Automotive Research. (2011). "Automotive Technology: Greener Products, Changing Skills, Lightweight Materials & Forming Report." Driving Change Project.

[29] Bandivadekar, A., K. Bodek, L. Cheah, C. Evans, T. Groode, J. Heywood, et al. (2008). "On the Road in 2035: Reducing Transportation's Petroleum Consumption and GHG Emissions." Massachusetts Institute of Technology.

[30] Machlin, E. S. (1959). "Applied Voltage and the Plastic Properties of "Brittle" Rock Salt," J. Appl. Phys., 30(7), pp.1109-1110.

[31] Nabarro, F.R.N. (1967). “Theory of Crystal Dislocations,” chapter IX.

[32] Troitskii, O.A. (1969). “Electromechanical Effect in Metals.” Pis’ma Zhurn. Experim. Teoret. Fiz., No. 10, pp. 18.

[33] Xu, Z.S., Z.H. Lai, and Y.X. Chen (1988). “Effect of Electric Current on the Recrystallization Behavior of Cold Worked Alpha-Ti.” Scripta Metallurgica, 22, pp. 187-190.

[34] Chen, S.W., C.M. Chen, and W.C. Liu (1998). “Electric Current Effects Upon the Sn/Cu and Sn/Ni Interfacial Reactions.” Journal of Electronic Materials, 27, pp. 1193.

[35] Chen, S.W., and C.M. Chen (1999). “Electric Current Effects on Sn/Ag Interfacial Reactions.” J. of Electronic Mat., 28, pp. 902.

[36] Conrad, H., (2000b). “Electroplasticity in Metals and Ceramics.” Mat. Sci. & Engr., pp. 276-287.

[37] Conrad, H., (2002). “Thermally activated Plastic Flow of Metals and Ceramics with an Electric Field or Current”, Mat. Sci. & Engr., A322, pp. 100-107.

[38] Heigel, J.C., J.S. Andrawes, J.T. Roth, M.E. Hoque, and R.M. Ford (2005). “Viability of electrically treating 6061-T6511 aluminum for use in manufacturing processes.” Transactions of the North American Manufacturing Research Institute of SME, Vol. 33, pp. 145-152.

[39] Andrawes, J.S., T.J. Kronenberger, J.T. Roth, and R. L. Warley (2007). “Effects of DC current on the mechanical behavior of AlMg1SiCu.” Material and Manufacturing Proceedings, 22 (1), pp. 91-101.

[40] Perkins, T.A., T.J. Kronenberger, J.T. Roth (2007). “Metallic forging using electrical flow as an alternative to warm/hot working.” Journal of Manufacturing Science and Engineering, 129 (1), pp. 84-94.

[41] Ross, C.D., D.B. Irvin, and J.T. Roth (2007). “Manufacturing aspects relating to the effects of DC current on the tensile properties of metals.” Journal of Engineering Materials and Technology, 129(2), pp. 342-347.

[42] Salandro W.A., Jones J.J., McNeal T.A., Roth J.T., Hong S.T., and Smith M.T. (2008). “Effect of Electrical Pulsing on Various Heat Treatments of 5xxx Series Aluminum Alloys.” International Manufacturing Science & Engineering Conference, MSEC 2008-72512, pp. 10.

[43] Salandro W.A., A. Khalifa, and J.T. Roth (2009). “Tensile Formability Enhancement of Magnesium AZ31B-O Alloy Using Electrical Pulsing.” Transaction of the North American Manufacturing Research Institute of SME, Vol.37.

[44] McNeal T.A., J.A. Beers, and J.T. Roth (2009). “The Microstructural Effects on Magnesium Alloy AZ31B-O While Undergoing an Electrically-Assisted Manufacturing Process.” International Manufacturing Science & Engineering Conference, MSEC 2009-84377, pp. 10.

[45] Green C.R., T.A. McNeal, and J.T. Roth (2009). “Springback Elimination for Al-6111 Alloys Using Electrically-Assisted Manufacturing (EAM).” Transactions of the North American Manufacturing Research Institute of SME, 37.

[46] Jones, J.J. and J.T. Roth (2009). “Effect on the Forgeability of Magnesium AZ31B-O When a Continuous DC Electrical Current is Applied.” International Manufacturing Science & Engineering Conference, MSEC 2009-84116, pp. 10.

[47] Salandro, W.A. and J.T. Roth (2009). “Formation of 5052 Aluminum Channels Using Electrically-Assisted Manufacturing (EAM).” International Manufacturing Science & Engineering Conference, MSEC 2009-84117, pp. 9.

[48] Siopis, M.S. and B.L. Kinsey (2009). “Experimental Investigation of Grain and Specimen Size Effects During Electrical-Assisted Forming.” International Manufacturing Science & Engineering Conference, MSEC2009-84137, pp. 6.

[49] Siopis, M.S., B.L. Kinsey, N. Kota, and O.B. Ozdoganlar (2010). “Effect of Severe Prior Deformation on Electrical-Assisted Compression of Copper Specimens.” International Manufacturing Science & Engineering Conference, MSEC2010-34276, pp. 7.

[50] Dzialo, C.M., M.S. Siopis, B.L. Kinsey, and K.J. Weinmann (2010). “Effect of current density and zinc content during electrical-assisted forming of copper alloys.” CIRP Annuals – Manufacturing Technology, 59(1), pp. 299-302.

[51] Salandro W.A. and Roth, J.T. (2010). “Ch19. Electrically-Assisted Manufacturing”, in Intelligent Energy Field Manufacturing: Interdisciplinary Process Innovations, ed. Zhang W. CRC Press.

[52] Bunget, C., W.A., Salandro, and L. Mears (2011). “Thermal Mechanical Predictive Algorithm for Electrically-Assisted Manufacturing Processes” (Provisional patented filed on May 25, 2011).

[53] US 7,302,821 – Techniques for Manufacturing a Product Using Electric Current During Plastic Deformation of Material.

[54] US 7,516,640 – Method and Apparatus for Forming a Blank as a Portion of the Blank Receives Pulses of Direct Current.

[55] Electrically Assisted Single-Point Incremental Forming (EA-SPIF), (non-provisional application, disclosure #3484).

[56] Electrically Assisted Metal Forging Process, (non-provisional application, disclosure #3314).

[57] Yao, L., C. Hong, G. Yunquo, and H. Xinbin (1996). “Effect of Electric Current Pulse on Superplasticity of Aluminum Alloy 7475.” Trans. Of Nfsoc, 6(1), pp.77-84.

[58] Antolovich S.D. and H. Conrad (2004). “The Effects of Electric Currents and Fields on Deformation in Metals, Ceramics, and Ionic Materials: An Interpretive Survey,” Materials and Manufacturing Processes, 19(4), pp.587-610.

[59] Kronenberger, T.J., D.H. Johnson, and J.T. Roth (2009). “Coupled Multifield Finite Element Analysis Model of Upsetting Under an Applied Direct Current.” Journal of Manufacturing Science and Engineering, 131.

[60] Salandro, W.A., T.A. McNeal, J.A. Beers, L. Mears, and J.T. Roth (2010). “Mechanical and Microstructural Effects Caused During Uniaxial EAM Tensile Deformation of MgAZ31B-O Sheet Metal.” To be submitted to the Proceedings of the Institution of Mechanical Engineers, Part B: Journal of Engineering Manufacture.

[61] Salandro W.A., Jones J.J., McNeal T.A., Roth J.T., Hong S.T., and Smith M.T. (2010). “Formability of Al 5xxx Sheet Metals Using Pulsed Current for Various Heat Treatments.” Journal of Manufacturing Science and Engineering. v132. pp11.

[62] MatWeb, “Aluminum 6061-T6; 6061-T651.” MatWeb Material Property Data, (Accessed 01 July 2012). www.matweb.com.

[63] MatWeb, “Magnesium AZ31B-O, Annealed Sheet.” MatWeb Material Property Data, (Accessed 01 July 2012). www.matweb.com.

[64] MatWeb, “304 Stainless Steel.” MatWeb Material Property Data, (Accessed 01 July 2012). www.matweb.com.

[65] MatWeb, “Titanium Ti-6Al-4V (Grade 5), Annealed.” MatWeb Material Property Data, (Accessed 01 July 2012). www.matweb.com.

[66] Bunget, C., W.A. Salandro, L. Mears, and J.T. Roth (2010), “Energy-based modeling of an electrically-assisted forging process”, Trans. of the North American Manuf. Research Institute of SME, 38.

[67] Lange, K. (1985). “Handbook of Metal Forming.” New York, McGraw-Hill.

[68] Backofen, W.A. (1972). “Deformation Processing.” Boston, Addison-Wesley Educational Publishers Inc.

[69] Kobayashi, S., S.-I. Oh, and T. Altan (1989). “Metal Forming and the Finite-Element Method.” New York, Oxford University Press.

[70] Wagoner, R.H. and J.L. Chenot (1996). “Fundamentals of Metal Forming.” Hoboken, NJ, John Wiley & Sons Inc.

[71] Avitzur, B. (1980). “Metal Forming: The Application of Limit Analysis.” New York, Dekker.

[72] Cengel, Y.A. (2007). “Heat and Mass Transfer: A Practical Approach.” McGraw-Hill, 3rd Ed.

[73] Cengel, Y.A. and M.A. Boles (2008). “Thermodynamics: An Engineering Approach.” McGraw-Hill, 6th Ed.

[74] Sprecher, A.F., S.L. Mannan, and H. Conrad (1983). “On the Temperature Rise Associated with the Electroplastic Effect in Titanium.” Scripta Metallurgica, 17, pp.769-772.

[75] Silveira, V.L.A., M.F.S. Porto, and W.A. Mannheimer (1981). “Electroplastic Effect in Copper Subjected to Low Density Electrical Current.” Scripta Metallurgica, 15, pp.945-950.

[76] Kopomev, A.A. (1991). “The Nature of the Electroplastic Effect in Metals.” Problemy Prochnosti, No.1, pp.47-51.

[77] Kiryanchev, N.E., O.A. Troitskii, and S.A. Klevtsur (1983). “Electroplastic Deformation of Metals (Review).” Problemy Prochnosti, No.5, pp.101-105.

[78] Troitskii, O.A. (1976). “Electroplastic Deformation of Metal.” Problemy Prochnosti, No.12, pp.88-93.

[79] Okazaki, K., M. Kagawa, and H. Conrad (1978). “A Study of the Electoplastic Effect in Metals.” Scripta Metallurgica, 12(1), pp. 1063-1068.

[80] Salandro, W.A., C. Bunget, and L. Mears (2011). “Thermo-Mechanical Investigations of the Electroplastic Effect.” International Manufacturing Science & Engineering Conference, MSEC2011-50250, pp.10.

[81] Salandro, W.A., C. Bunget, and L. Mears, (2011), “Several Factors Affecting the Electroplastic Effect During an Electrically-Assisted Forming Process," Journal of Manufacturing Science and Engineering, vol. 133.

[82] Salandro W.A., C. Bunget, and L. Mears (2011). “A Thermal-Based Approach for Determining Electroplastic Characteristics.” Proceedings of the Institution of Mechanical Engineers, Part B: Journal of Engineering Manufacture, January 5, 2012, DOI: 10.1177/0954405411424696.

[83] Salandro, W.A., C. Bunget, and L. Mears (2012). “Modeling the Electroplastic Effect During Electrically-Assisted Forming of 304 Stainless Steel.” International Manufacturing Science & Engineering Conference, MSEC2012-7241, pp.10.

[84] Salandro, W.A., C. Bunget, and L. Mears (2012). “Electroplastic Modeling of 304 Stainless Steel.” Under review for publication in the Journal of Manufacturing Science and Engineering.

[85] Bunget, C., W. Salandro, and L. Mears (2012). “Sensitivities When Modeling Electrically-Assisted Forming.” International Manufacturing Science & Engineering Conference, MSEC2012-7334, pp.9.

[86] Properties of Aluminum Alloys, Editor J.G. Kaufman, Pub. ASM and the Aluminum Association of America (1999) (Al6061).

[87] H.E. Dedman, E.J. Wheelahan and J.R. Kattus, WADC technical report 58-440, part 1, (1950) (Ti-G5).

[88] Allegheny Ludlum Corp., product data sheet (304SS).

[89] Salandro, W.A., C. Bunget, and L. Mears (2011). “Electroplastic Modeling of Bending Stainless Steel Sheet Metal Using Energy Methods.” Journal of Manufacturing Science and Engineering. 133(1), pp.10.

[90] Salandro, W.A., C. Bunget, and L. Mears (2010), “Modeling and Quantification of the Electroplastic Effect When Bending Stainless Steel Sheet Metal.” International Manufacturing Science & Engineering Conference, MSEC 2010-34043, pp. 10.

[91] Hill, R. (1950). “The mathematical theory of Plasticity”, Oxford University Press.

[92] Hosford, W.F. and R. M. Caddell (1993). “Metal forming: Mechanics and metallurgy”, Prentice Hall, 2nd Ed.

[93] Weinmann, K.J., and R.J. Shippell (1978). “Effect of tool and workpiece geometries upon bending forces and springback in 90° V-die bending of HSLA steel plate”, Proceedings of the 6th North American Metal Working Research Conference, pp. 220-227.

[94] Altan, T., G. Ngaile, and G. Sheng (2004). “Cold and hot forging; Fundamentals and applications”, ASM International.

[95] R. Holm, Electric Contacts, Theory and Applications, Springer-Verlag, Berlin, 1976.

[96] C. Bunget and Gracious Ngaile, (2008), “Ultrasonic Microforming.” ISBN: 978-3-639-00055-9, VDM.

[97] 1972 Proceedings of the Sixth International Conference on Electrical Contact Phenomena.

[98] Timsit, R.S. (2001). “Connector Lubricants Enhance Performance.” www.interconnectionworld.com, accessed 06 Jun 2011.

[99] Bowden, F.P. and D. Tabor (1939). “The Area of Contact Between Stationary and Between Moving Surfaces.” Proceedings of the Royal Society of London Series A, Mathematical and Physical Sciences, Vol. 169, 938, pp. 391-413.

[100] MS Thesis: 'Microforming and Ultrasonic Forming', North Carolina State University, 2006.

[101] Uppal, A.H. and S.D. Probert (1972). “Mean Separation and Real Contact Area Between Surfaces Pressed Together Under High Static Loads.” Wear, 23, pp. 39-53.

[102] Pullen, J. and J.B.P. Williamson (1972). “On the Plastic Contact of Rough Surfaces.” Proceedings of the Royal Society Mathematical, Physical, and Engineering Sciences, 327, pp. 159-173. DOI: 10.1098/rspa.1972.0038.

[103] Kragelsky, I.V. and N.B. Demkin (1960). “Contact Area of Rough Surfaces.” Wear, 3, pp. 170-187.

[104] Stewart, M. (1990). “A New Approach to the Use of the Bearing Area Curve.” International Conference on Honing Technologies andApplications, FC90-229, pp. 11.

[105] Uppal, A.H. and S.D. Probert (1972), “Considerations Governing the contact Between a Rough and a Flat Surface.” Wear, 22, pp. 215-234.

[106] Boyer, L. (2001). “Contact Resistance Calculations: Generalizations of Greenwood’s Formula Including Interface Films.” IEEE Transactions on Components and Packaging Technologies, 24, pp. 50-58.

[107] Bunget, C., W.A. Salandro, and L. Mears (2010). “Tribological Aspects in Electrically-Assisted Forming.” International Manufacturing Science & Engineering Conference, MSEC 2010-34249, pp. 8.

[108] Bunget C., W.A. Salandro, and L. Mears (2010). “Evaluation of Lubricants for Electrically-Assisted Forming.” Proceedings of the Institution of Mechanical Engineers, Part B: Journal of Engineering Manufacture, DOI: 10.1177/0954405411401267.

[109] J.A. Schey, “Tribology in Metalworking”, American Society for Metals, 1983.

[110] Gariety, M., Ngaile, G., and Altan, T. Evaluation of new cold forging lubricants without zinc phosphate precoat. Intr. J. of Machine Tools & Manufacture, 2007, 47, 673-681.

[111] Ngaile, G., and Botz, F. Performance of Graphite and Boron-Nitride-Silicone Based Lubricants and Associated Lubrication Mechanisms in Warm Forging of Aluminum. Journal of Tribology, 2008, 130, pp.7.

[112] Ngaile, G., Cochran, J., and Stark, D. Formulation of polymer-based lubricant for metal forming. Proc. IMechE Part B: J. Engineering Manufacture, 2007, 221, 559-568.

[113] Hall, E. O. (1951). “The Deformation and Ageing of Mild Steel: III Discussion of Results.” Proc. Phys. Soc. B 64, pp.747-753.

[114] Hansen, N. (2004). “Hall-Petch relation and boundary strengthening.” Scripta Materialia. 51, pp. 801-806.

[115] Meyers, M.A. and E. Ashworth (1982). “A model for the effect of grain size on the yield stress of metals.” Philosophical Magazine, Vol. 46, 5, pp737-759.

[116] Struers Application Notes, Metallographic preparation of stainless steel.

[117] Kalpakjian, S. (1997) Manufacturing Processes for Engineering Materials, Third Edition.

[118] United States Department of Defense (2003). “Department of Defense Handbook: Metallic Material and Elements for Aerospace Vehicle Structures, MIL-HDBK-5J.”

[119] Yilmaz, A. (2011) “The Portevin–Le Chatelier effect: a review of experimental findings.” Sci. Technol. Adv. Mater. 12, 063001 (16pp).

[120] http://www.es.anl.gov/Energy_systems/research/process_technology/process_tech_industrial.html.

[121] http://www.thefabricator.com/article/metalsmaterials/protecting-magnesium-alloys-from-corrosion.

[122] http://www.theregister.co.uk/2009/12/15/dreamliner_first_flight/.

[123] Public Service Commission of Wisconsin (2011). “Electricity: From Power Plants to Consumers”, Electric Transmission Lines notes, pp. 1-13.

[124] Castro, R.D. (1995). “Overview of the transmission line construction process.” Electric Power Systems Research, 35, pp. 119-125.

[125] Oncor Electric Delivery Company. (2011). “Index Section 9 Conductors.” pp.47.

[126] Castro, R.D. (1995). “Overview of the transmission line design process.” Electric Power Systems Research, 35, pp. 109-118.

[127] Ergon Energy Corp. (2012). “Network Lines Standard Guidelines for Overhead Line Design.” pp.20.

[128] Di Troia, G. (2000). “Effects of High Temperature Operation on Overhead Transmission Full-Tension Joints and Conductors.” pp.1-7.

[129] Bernauer, Christian, et.al (2007). “Temperature Measurement on Overhead Transmission Lines (OHTL) Using Surface Acoustic Wave (SAW) Sensors.” 2011 International Conference on Electricity Distribution, CIRED2007_0788, pp.4.

[130] Muhr, M., S. Pack, R. Schwarz, and S. Jaufer (2006). "Calculation of Overhead Line Sags." 51st Internationales Wissenschaftliches Kolloquium, pp.10.

[131] Clydesdale Ltd., "ABC, Copper, AAAC &ACSR Conductor Specifications." Conductor specifications Tables: Technical Specification for Aluminum Conductor Steel Reinforced (ACSR) to BS 215 Part 2: 1970. www.clydesdale.net.

[132] High-Temperature Property Data: Ferrous Alloys, Editor M.F. Rothman, ASM International (1988); and Engineering Properties of Steel, P.D. Harvery, ASM (1982).

[133] Aluminum Alloys for Cryogenic Applications, The Aluminum Association, Washington, DC (1999).

[134] Zocholl, S.E.. and A. Guzman (1999). "Thermal Models in Power System Production." report from Schweitzer Engineering Laboratories Inc., pp.16.

[135] Allegheny Ludlum Corp., product data sheet and A.F. Clark, G.E. Childs and G.H. Wallace, Cryogenics, v10, p295, August (1970) (304SS resistivity vs. temperature).

[136] http://www.tf.uni-kiel.de/matwis/amat/def_ge/kap_5/backbone/r5_2_2.html.

[137] http://www.ndted.org/EducationResources/CommunityCollege/Materials/Structure/linear_defects.htm.

[138] http://oregonstate.edu/instruct/engr322/Exams/AllExams/S98/ENGR322MT2.html.

[139] http://www.ndted.org/EducationResources/CommunityCollege/Materials/Structure/metallic_structures.htm.

[140] Callister, W.D. (2007). Materials Science and Engineering An Introduction, Seventh Edition.

[141] Askeland, D.R. and P.P. Phule (2006). The Science and Engineering of Materials, Fifth Edition.